CVD Diamant als Material für Teilchendetektoren

Dissertation
zur Erlangung des Doktorgrades
des Fachbereichs Physik
der Universität Hamburg

vorgelegt von
A. Oh
aus Hamburg

Hamburg, 1999

Gutachter der Dissertation:	Prof. Dr. A. Wagner Prof. Dr. W. Schmidt-Parzefall
Gutachter der Disputation:	Prof. Dr. A. Wagner Prof. Dr. R. Heuer
Datum der Disputation:	28.7.1999
Dekan des Fachbereiches Physik und Vorsitzender des Promotionsausschusses:	Prof. Dr. F.-W. Büßer

Particle Detection with CVD Diamond

A. Oh

II. Institut für Experimentalphysik
Universität Hamburg

June 1999

Abstract

In this study synthetic diamonds are investigated with respect to the applicability as a material for future particle detection systems. Different methods to characterise electrical and structural properties are employed and further developed to gain a deeper understanding of the charge collection process in the material. The investigations with spatially resolving and non-resolving methods show that the charge collection properties are non-uniformly distributed in the polycrystalline material, and depend on the stopping range of the ionising particle. Different methods measure a consistent degree of non-uniformity. The spread of the charge collection efficiency is typically of the order of 20% rms to the mean. Results obtained with a computer simulation, which incorporates the crystallite structure and describes the charge collection in terms of microscopic quantities, is in good agreement with the experimental findings.

To improve the detection properties a systematic study of the growth parameters of a chemical vapour deposition process (CVD) to produce diamond is performed. Correlations of growth conditions and detection properties are established. Material with a collection efficiency of as much as 38% is obtained.

The sensibility of diamond to irradiation with neutrons is tested up to a fluence of $6.5 \cdot 10^{15}$ n cm^{-2}. It is found that the charge collection efficiency of diamond deteriorates with increasing neutron fluence, varying in decrease for different samples. The experimental observations are explained by a damage model, which is used to predict the damage behaviour of a CVD diamond detector in a future high energy physics experiment.

Finally, a position sensitive strip detector is developed and successfully tested. The strip detector reaches a resolution of $\sigma_x = 8.4$ μm with a strip pitch of 50 μm and a strip width of 16 μm at a signal-to-noise ratio of ≈ 5. A computer simulation of the strip detector is qualitatively in good agreement with the experimental data.

Kurzfassung

Diese Arbeit befaßt sich mit den Eigenschaften von synthetischem Diamant als Teilchendetektor. Die elektrischen und strukturellen Eigenschaften werden mit unterschiedlichen Meßmethoden untersucht, um einen tieferen Einblick in das Ladungssammlungsverhalten zu bekommen. Die Untersuchungen mit teilweise ortsaufgelösten Meßverfahren zeigen, daß die Ladungssammlungseigenschaften ungleichmäßig verteilt sind, was auf die polykristalline Struktur des Materials zurückzuführen ist. Zudem hängt das Signalverhalten stark von der Eindringtiefe des ionisierenden Teilchens ab. Die Verbreiterung der Ladungssammlungseffizienz wird mit verschiedenen Methoden zu typischerweise 20% RMS relativ zum Mittelwert bestimmt. Ein Modell, das die polykristalline Struktur berücksichtigt und die Ladungssammlungseffizienz mit mikroskopischen Größen beschreibt, kann die experimentellen Befunde gut erklären.

Die Abhängigkeit der Detektionseigenschaften von den Wachstumsbedingungen der Diamantschichten wird in einer systematischen Studie untersucht, wobei Korrelationen festgestellt werden. Unter der besten Wachstumsbedingung wird eine Ladungssammlungseffizienz von 38% erreicht.

Die Auswirkung von Neutronen auf die elektrischen Eigenschaften wird bis zu einer Fluenz von $6.5{\cdot}10^{15}$ n cm^{-2} mit Proben von verschiedener Qualität überprüft. Alle Proben zeigen eine Verschlechterung des Ladungssignals mit steigender Fluenz, wobei quantitative Unterschiede im Verhalten der Proben festgestellt werden. Die experimentellen Resultate werden mit einem Schädigungsmodell erklärt, welches auch benutzt wird, um das Schädigungsverhalten von Diamant in einem Strahlungsszenario vorauszusagen, wie es an zukünftigen Beschleunigerexperimenten erwartet wird.

Schließlich wird der Entwurf, Bau und Test eines ortsauflösenden Streifendetektors aus CVD Diamant durchgeführt. Der Detektor erreicht eine Auflösung von $\sigma_x = 8.4$ μm bei einem Streifenabstand von 50 μm und einer Streifenbreite von 16 μm mit einem Signal-zu-Rausch Verhältnis von ≈ 5. Die Ergebnisse einer Computersimulation des Detektors befinden sich in guter qualitativer Übereinstimmung mit den experimentellen Daten.

Contents

1 Introduction **1**

2 Particle Detection with Solid State Detectors **3**
2.1 Passage of Ionising Radiation through Matter 3
2.1.1 Charged Particles 4
2.1.2 Photons 8
2.2 Principle of Operation of Solid State Detectors 9
2.3 Materials and Concepts of Solid State Detectors 11

3 CVD Diamond **13**
3.1 Properties of Diamond 13
3.2 Chemical Vapour Deposition of Diamond 15
3.3 Diamond Detectors and Signal Generation 21
3.4 Polarisation, Passivation and the Role of Defects 24

4 Characterisation Methods **29**
4.1 Scanning Electron Microscopy 30
4.1.1 Set-up 31
4.1.2 Results 31
4.2 Raman Spectroscopy 31
4.2.1 Results 33
4.3 X-Ray Diffraction 35
4.3.1 Principle 35
4.3.2 Set-up 36
4.3.3 Results and Discussion 37
4.4 Secondary Ion Mass Spectroscopy 45
4.4.1 Results 45
4.5 I-V-Characteristic 46
4.5.1 Results 47
4.6 Beta Particles 48
4.6.1 Set-up 49
4.6.2 Results 50
4.7 Synchrotron Radiation 55
4.7.1 Experimental set-up 55
4.7.2 Results and discussion 56
4.8 Alpha Particles 63
4.8.1 Set-up 63
4.8.2 Results 63
4.9 Proton Micro-beam 67
4.9.1 Set-up 67
4.9.2 Results 67

4.10 Electron Beam Induced Currents 72
4.10.1 Set-up 72
4.10.2 Results: Strip Electrode Configuration 73
4.10.3 Results: Sandwich Electrode Configuration 74
4.11 Thermally Stimulated Currents 78
4.11.1 Principle 78
4.11.2 Set-up 80
4.11.3 Results 81
4.12 Summary and Interpretation 89

5 Growth Studies of CVD Diamond 93
5.1 Preparation of CVD Diamond Films 93
5.2 Characterisation 93
5.3 Correlation of Growth Parameters with Charge Collection Properties 94
5.4 Summary and Interpretation 96

6 Radiation Tolerance 99
6.1 Radiation Damage 99
6.2 Experimental Set-up 101
6.3 Results 102
6.4 Comparison to Existing Data 104
6.5 Interpretation 106
6.6 Damage Model 107
6.7 Damage Projection for the LHC 111
6.7.1 Particle Fluxes of ATLAS at the LHC 111
6.7.2 Performance Projections 113
6.8 Summary 115

7 A Model of the Charge Drifting in CVD Diamond 121
7.1 A simple CVD diamond growth generator 123
7.2 Simulation of the Charge Carrier Drift Process 124
7.3 Implementation of Traps 125
7.4 Results 127
7.4.1 Material 127
7.4.2 Alpha Particles 128
7.4.3 Protons 130
7.4.4 Minimum Ionising Particles 131
7.5 Summary 134

8 A Prototype Detector Study 135
8.1 Principle of Operation 135
8.2 Detector Design 136
8.2.1 Pattern Design 137

8.2.2 Material . . . 138
8.2.3 Read-Out Electronics . . . 139
8.2.4 Quality Control, Device Assembly and Calibration . . . 140
8.3 Test Environments . . . 141
8.3.1 Table Top Set-up . . . 141
8.3.2 Test-beam Set-up . . . 142
8.4 Results . . . 145
8.4.1 Cluster Finding . . . 146
8.4.2 Charge Spectrum . . . 146
8.4.3 Charge Sharing . . . 150
8.4.4 Resolution . . . 153
8.4.5 Spatial Uniformity of the Charge Collection . . . 156
8.4.6 Systematic Deviation of Position Reconstruction . . . 162
8.5 Numerical Modelling . . . 164
8.5.1 Simulated Device . . . 165
8.5.2 Results of the Simulation . . . 165
8.6 Summary . . . 168

9 Summary **171**

A Appendix **175**
A.1 Classification Scheme of Natural Diamond . . . 175
A.2 Signal Amplification . . . 175
A.3 Weighting Field Method . . . 177

1 Introduction

Children and scientists may confront their environment and contemporaries with fundamental questions like: What is the world made of? And, what holds it together? Nuclear and elementary particle physics are devoted to addressing these questions. The current answer is the standard model of particle physics, a theory firmly supported by experimental data obtained with large particle colliders and multi component detectors. However, an important aspect of the theory, namely the mechanism to generate the masses of particles, awaits experimental confirmation. For this purpose new particle collider machines are being designed to reach unprecedented energies and luminosities[1]. Solid state particle detectors have become an important part of the complex detection apparatus. In current experiments silicon is widely employed to precisely reconstruct the tracks of particles emerging from the primary interaction point. In the most recently designed experiments the enormous number of particles produced will present a severe threat to the reliable operation of detector devices. The radiation fluence in the inner layer of the experiment will exceed 10^{15} particles per cm^2 over the projected time of operation, which is beyond the radiation tolerance of standard silicon technology. Thus the need for a more robust detector material was realized and efforts were started to improve the radiation hardness of silicon and to examine the radiation hardness of other materials - like diamond.

Diamond is the hardest natural substance on earth with many exceptional properties due to its high bonding strength. A high radiation resistance was expected from its stable lattice, and was demonstrated by irradiation experiments with various particle types. However, only the advent of a production technology capable of manufacturing coherent diamond films of good quality, the so called chemical vapour deposition (CVD) of diamond, made the employment of diamond as an alternative detector material conceivable.

The first reports of detector studies with CVD diamond appeared at the beginning of this decade [1, 2]. Since then a substantial improvement of the material quality was achieved [3], increasing the signal from a minimum ionising particle from a few hundred electrons to around 7200 electrons at present.

This thesis is concerned with the properties of CVD diamond as a particle detector, comprising investigations of the detection process of differently ionising particles, its radiation hardness, the optimisation of parameters of the CVD growth process, a performance study of a prototype CVD diamond detector and a computer simulation of CVD diamond to gain a deeper insight into the detection process.

The text is organised in eight chapters. In chapter 2 a discussion of the principle of operation and the basic physical processes important for particle detection in solid state detectors is given. A general introduction to diamond and

[1] The luminosity relates the event rate R and the interaction cross section σ_{int} by $\mathcal{L} = R/\sigma_{int}$.

the CVD production process is given in chapter 3. In chapter 4 the structural and electrical characterisation methods are presented together with results obtained from various samples. Systematic studies of the production process parameters needed to obtain detector grade CVD diamond are the concern of chapter 5. The radiation hardness is tested with neutrons in chapter 6 and the findings are parametrised with a proposed damage model. A new approach to model the charge drifting process in CVD diamond (chapter 7) taking into account the polycrystalline nature of the material explains many aspects of the experimental observations. Finally the development and test of a prototype strip detector with different strip geometries is presented in chapter 8.

2 Particle Detection with Solid State Detectors

The first experiments with solid state detectors were made as early as 1913 by W. C. Röntgen and A. Joffè [4]. The absence of sophisticated electronics and the lack of appropriate materials made the discovery of counting crystals difficult. In 1945 P. J. van Heerden [5] published his dissertation where he discussed crystal counters, and initiated a host of research in the field of solid state detectors. Van Heerden used silver chloride crystals detecting signals electrically. Many different materials were tried, including also diamond. The first observation of counting pulses initiated by charged particles in selected species of diamond were reported by G. Stetter in 1941 [6]. The poor availability and high costs of natural diamond with counting properties prevented the successful spread as a detector material. Nowadays the world of solid state particle detectors is dominated by silicon, assisted by the rapid development of a silicon industry since the late 1960s.

To detect a particle, it is necessary that the particle interacts with the detector to produce electric charge or light which can be interpreted as the signature of the particle. The physical processes allowing the detection are different for neutral and charged particles. Charged particles and photons as the mediators of the electromagnetic force interact electromagnetically with matter. Photons can produce charged particles via the photoeffect or Compton-effect which are detected directly. Neutrons interact via the strong force. The production of unstable isotopes which decay into a nucleus and a charged particle can be used to detect neutrons (e. g. the capture of a neutron by B and the subsequent emission of an alpha particle in the reaction $^{10}\mathrm{B}(n,\alpha)^{7}\mathrm{Li}$). Neutrinos are only weakly interacting particles. The interaction is mediated by a gauge boson which can produce charged secondaries.

While the neutral particles are not detected directly the charged particles interact via the electromagnetic interaction with the detector material and produce a direct signature.

In this chapter the basic physical processes of particle detection with solid state detectors are reviewed. The different processes by which charged particles interact with matter are discussed. The principle of operation for different detectors are explained. Particular emphasis is given to those mechanisms which are relevant for diamond based detectors.

2.1 Passage of Ionising Radiation through Matter

Electromagnetically interacting particles (photons and charged particles) are also called *ionising radiation* because of the production of free charge carriers when traversing matter. Ionisation means the liberation of a bound electron from an atom in the material by exchanging sufficient energy with an incoming particle. The atom is left in an ionised state and the kinetic energy of the liberated electron is $E = E_x - E_b$, when E_x is the transferred energy from the incoming particle

and E_b the binding energy of the electron. The vacancy in the atomic shell is called a hole and can also be mobile, e. g. if the atoms are arranged in a crystal lattice. In the following the specific processes for particle detection are discussed for charged particles and photons separately.

2.1.1 Charged Particles

The electromagnetic interaction of charged particles traversing matter can be divided into three processes: (a) ionisation, (b) Bremsstrahlung and (c) emission of Cherenkov light and transition radiation. For the loss of energy (a) and (b) are important, while (c) can also be used for the detection of particles but does not contribute significantly to the energy loss.

Ionisation

Ionisation processes are associated with the exchange of virtual photons between the incident particle and atoms of the medium. The energy spectrum extends from the soft infrared region up to hard X-rays, leading to large fluctuations in the energy loss of the incident particle. The energy loss can be described by the interaction cross section $\sigma(E, \vec{K})$ differential in the energy loss E and the momentum transfer $\vec{K}$ between incident particle and the medium. To calculate $\sigma(E, \vec{K})$ the cross sections for longitudinal and transverse excitations of different atomic shells, for large and small energy losses and momentum transfers have to be known [7].

For large energy losses and non-relativistic particles the Rutherford cross section

$$\sigma_R(E) = \frac{2\pi z^2 e^4}{m_e v^2 E^2} \tag{1}$$

represents a good approximation, where E is the energy loss of a particle with charge ze and velocity v, while e is the elementary charge and m_e the electron rest mass. As can be seen from eq. (1) the cross section rises with the inverse of the square of the particle velocity and is independent of the particle mass. Since the cross section describes the energy loss in a single collision with an electron the momentum transfer is solely to the electron and given by $|\vec{K}| = \sqrt{2mE}$.

When considering relativistic particles the cross section has to be modified and becomes

$$\sigma(E, \vec{K}) = \underbrace{\sigma_R(Q)}_{\text{Rutherford}} \; Z[\overbrace{\xi(E, \vec{K})}^{\text{longitudinal}} + \underbrace{\iota(E, \vec{K})}_{\text{transverse}}] \overbrace{(1 + \frac{Q}{mc^2})}^{\text{relativistic}} \tag{2}$$

where $\vec{K}$ is the momentum transfer, Q the energy transfer and Z is the number of electrons per atom as derived by Fano [8] and reviewed by Bichsel [7]. In

the case of ionisation the momentum transfer is not solely to the electron but also shared by the atom and no simple expression can be used to relate E and Q. The relation depends on the properties of the atom which are described by the longitudinal and transverse excitation terms ξ and ι. The longitudinal excitation term ξ represents the static Coulomb interaction and ι, the transverse term, describes the exchange of virtual photons. In the non-relativistic limit the transverse term vanishes and eq. (2) simplifies to

$$\sigma(E, \vec{K}) = \sigma_R(Q) Z \xi(E, \vec{K}). \tag{3}$$

The equation is composed of $\sigma_R(Q)$, the Rutherford term described above, the number of electrons in the atom Z and ξ representing the probability of excitation of the atom.

In the relativistic regime the transverse field component rises with $\beta\gamma$ because of Lorentz invariance and thus the energy loss increases with the particle speed. The relativistic rise saturates at a value of $\beta\gamma$ which depends on the density of the medium as the field starts to see the neighbouring atoms (*density effect*). For denser media the limit is reached for smaller values of $\beta\gamma$. If the media is a crystal, i. e. the atoms form a lattice, additional effects can be important since the transverse and longitudinal excitation functions can depend on the lattice orientation. However, for most applications these effects are negligible [8]. If the cross section $\sigma(E, K)$ is known, the energy loss per unit length $\mathrm{d}E/\mathrm{d}x$, can be obtained by suitable integration over Q and $\vec{K}$. The exact transverse and longitudinal excitation functions can be replaced by an effective ionisation potential I when calculating $\mathrm{d}E/\mathrm{d}x$. The effective ionisation potential represents an average of the excitation energies weighted with the corresponding oscillator strengths. This approximation was used by Bethe who obtained equation (4) [9].

$$-\left(\frac{\mathrm{d}E}{\mathrm{d}x}\right)_{Ion} = 4\pi N_A r_e^2 m_e c^2 z^2 \frac{Z}{A} \underbrace{\frac{1}{\beta^2}}_{\text{a}} \left[\frac{1}{2} \underbrace{\ln\left(\frac{2m_e c^2 \gamma^2 \beta^2 T_{max}}{I^2}\right) - \beta^2}_{\text{b}} - \underbrace{\frac{\delta}{2}}_{\text{c}} \right] \tag{4}$$

Equation (4) is composed of a part decreasing and a part rising with the particle velocity. The decreasing part (a) is produced by the Rutherford cross section and is dominating at low particle speeds, while the rise at relativistic particle velocities is caused by the transverse excitation term (b). Here T_{max} is the maximum energy transfer which a point-charge particle of mass M and momentum p can impart to a stationary free electron. T_{max} is given by:

$$T_{max} = \frac{2m_e p^2}{M^{-2} + 2\gamma m_e M + m_e^2}.$$

By introducing a term (c) accounting for the *density effect* mentioned above the relativistic rise is limited.

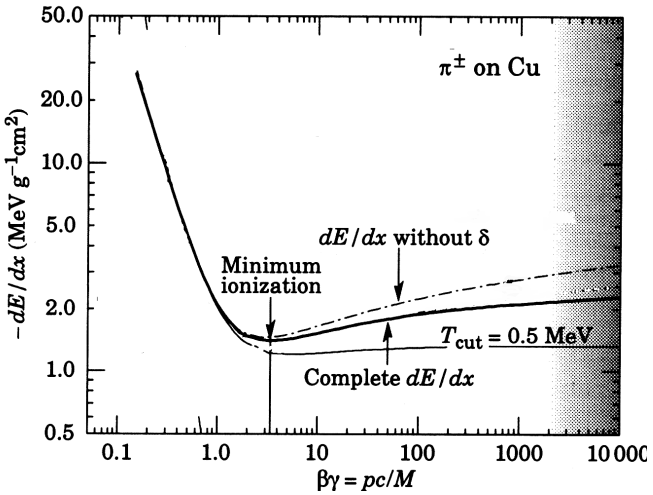

Figure 1: *Energy loss rate in copper taken from [9]. The functions with density correction and for the restricted energy are also shown.*

A plot of $\mathrm{d}E/\mathrm{d}x$ in copper is shown in fig. 1 [9]. It should be noted that the shape of $\mathrm{d}E/\mathrm{d}x$ is independent of the particle mass and can be well parametrised as a function of the particle velocity $\beta\gamma$. The energy loss has a minimum around $\beta\gamma \approx 4$. Particles in this regime are called minimum ionising particles (MIPs). For higher velocities the increase of the energy loss is small in dense media due to the density effect and $\mathrm{d}E/\mathrm{d}x$ stays approximately constant. Also depicted are the energy loss with density correction and for the restricted energy loss.

The so called restricted energy loss considers the energy deposited in the medium, which is the energy measured by the detector. It must be distinguished from the energy lost by the particle. Production of energetic secondaries (electron, photons) escaping the active volume lead to less energy deposited than actually lost by the particle. The restricted energy loss is given by:

$$-(\frac{\mathrm{d}E}{\mathrm{d}x})_{Ion,T<T_{cut}} = 4\pi N_A r_e^2 m_e c^2 z^2 \frac{Z}{A}$$
$$\underbrace{\frac{1}{\beta^2}}_{\text{a}} \left[\frac{1}{2} \underbrace{\ln\left(\frac{2m_e c^2\gamma^2\beta^2 T_{upper}}{I^2}\right) - \frac{\beta^2}{2}\left(1+\frac{T_{upper}}{T_{max}}\right)}_{\text{b}} - \underbrace{\frac{\delta}{2}}_{\text{c}} \right] \tag{5}$$

where $T_{upper} = min(T_{cut}, T_{max})$. The choice of T_{cut} for diamond can be motivated by the absorption length of photons. In [10] a value of $T_{cut} = 7.5$ keV was chosen, which is the energy at which photons have an absorption length of $\lambda \approx 500$ μm in diamond. If electrons are considered the stopping range of $S \approx 500$ μm leads to a value of $T_{cut} = 320$ keV [11]. Dependent on the value of T_{cut} the ionisation yield for MIPs becomes

$$\rho_{mip}^{T_{cut}=7.5 \text{ keV}} = \rho \frac{1}{E_{eh}} \frac{\mathrm{d}E}{\mathrm{d}x}_{Ion,T<T_{cut}} = 36 \frac{\text{eh}}{\mu\text{m}} \tag{6}$$

$$\rho_{mip}^{T_{cut}=320\ \mathrm{keV}} = 43\frac{\mathrm{eh}}{\mu\mathrm{m}} \tag{7}$$

where ρ is the density of diamond, E_{eh} the energy required to create an electron-hole pair and ρ_{mip} is the ionisation density in units of electron-hole pair per micrometer. In the literature the value of $\rho_{mip} = 36\frac{\mathrm{eh}}{\mu\mathrm{m}}$, although disputable, is established and it is also used in this work.

The Bethe-Bloch formula describes the average energy loss per unit length of a particle in a medium. Because of the statistical nature of the energy loss the actual deposited energy in the medium for a single event is subject to large fluctuations. Rare occurrences of scattering with high momentum transfer, which produce so called delta electrons, lead to an asymmetric spectrum with a tail towards higher energy losses. If the absorber is thin the number of scattering processes is small and an accurate description of the resulting broad asymmetric spectrum is difficult. Approaches have been made to describe the energy loss spectrum - also called straggling function - by Bohr, Landau [12], Vavilov, Shulek, Bichsel [7] and others. A comprehensive overview is given in reference [7]. Widely used is the Landau description and often the asymmetric distribution of deposited energy is called Landau spectrum. In a thick absorber the spectrum of the deposited energy approaches a Gaussian distribution because the number of scattering events is high.

Bremsstrahlung

The emission of bremsstrahlung occurs if the charged projectile is decelerated in the target material. Bremsstrahlung contributions are negligible for heavy projectiles but become important for highly energetic electrons and positrons. The energy loss through Bremsstrahlung can be described by

$$-\left(\frac{\mathrm{d}E}{\mathrm{d}x}\right)_{Brems} = 4\alpha_A\frac{z^2}{A}r_e^2 E\ \ln\frac{183}{Z^{\frac{1}{3}}} = \frac{E}{X_0} \tag{8}$$

where α is the fine structure constant, z the charge of the projectile in units of the elementary charge, Z the atomic number of the medium, and r_e the classical electron radius. Equation (8) is used define the radiation length X_0. The ratio of energy loss by ionisation and by Bremsstrahlung is given by:

$$R = \left(\frac{\mathrm{d}E}{\mathrm{d}x}\right)_{Brems} \Big/ \left(\frac{\mathrm{d}E}{\mathrm{d}x}\right)_{Ion} \approx \frac{ZE}{580\ \mathrm{MeV}}. \tag{9}$$

The critical energy is defined as the energy where the energy loss through ionisation equals the energy loss through Bremsstrahlung:

$$E_{crit} \approx \frac{580\ \mathrm{MeV}}{Z}. \tag{10}$$

For ultra-relativistic electrons and positrons the energy-loss through ionisation is negligible and $\mathrm{d}E/\mathrm{d}x = \mathrm{d}E/\mathrm{d}x_{Brems}$.

Cherenkov Light and Transition Radiation

Transition radiation occurs when the particle crosses the interface between two media with different optical properties. Cherenkov light[2] is emitted if the velocity of the incoming particle $v_0 = \beta c$ is greater than the phase velocity of the medium $v_\phi = \frac{c}{n}$ with n the refractive index of the medium. The light is emitted in a cone with the half angle

$$\theta_c = \arccos(1/n\beta).$$

The photon yield per unit path in the energy interval $\mathrm{d}E$ can be approximated by [9]

$$\frac{\mathrm{d}^2 N}{\mathrm{d}E\ \mathrm{d}x} \approx 370\ \sin^2\theta_c(E)\ \mathrm{eV}^{-1}\ \mathrm{cm}^{-1}$$

for a particle of charge $z = 1$.

2.1.2 Photons

The predominant interaction of photons with matter is dependent on the photon energy. The interaction can lead to absorption (photoelectric effect, pair production), coherent or incoherent scattering (Compton-effect) of the photon. For energies $E_\gamma < 100$ keV the predominant interaction is absorption via the photoelectric effect, from 100 keV to 2 MeV Compton scattering becomes more important and above the threshold for pair production of $E_{pair} = 1.02$ MeV at around 2 MeV the latter effect dominates the total cross sections. In figure 2 [9] the total photon cross section for carbon is shown together with the individual contributions. The photo absorption cross section has a substructure corresponding to the atomic shells and is falls with energy as $E_\gamma^{-3.5}$, while the cross section for Compton scattering (σ_{incoh}) falls with E_γ^{-1}. Explicitly the cross section for the photo-effect is given by [13]:

$$\sigma_{ph} = \frac{32\pi}{3}\sqrt{2}Z^5\alpha^4\frac{1}{\epsilon^{3.5}}r_e^2 \ \text{ for } \ \epsilon_\mathrm{K} < \epsilon < 1 \tag{11}$$

and

$$\sigma_{ph} = 4\pi r_e^2 Z^5\alpha^4\frac{1}{\epsilon} \ \text{ for } \ \epsilon > 1 \tag{12}$$

with $\epsilon_K = E_k/(m_e c^2)$ the normalised K shell binding energy and $\epsilon = E_\gamma/(m_e c^2)$ the normalised photon energy. $r_e = 2.8$ fm denotes the classic electron radius. The strong energy dependence is seen in the $1/\epsilon^{3.5}$ term in eq. (11). In carbon the photo effect dominates over the Compton effect up to a photon energy of about 11 keV.

Pair production of electrons and positrons arises after the threshold of two times the electron mass ($2m_e = 1.02$ MeV) is crossed. The conversion of a photon

[2]For a comprehensive discussion of this process the reader is referred to [13, 14].

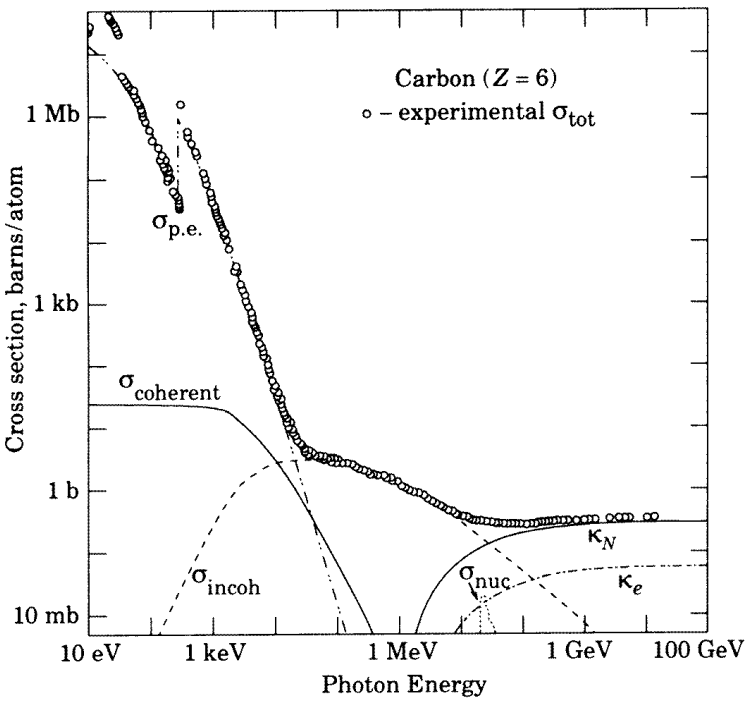

Figure 2: *Total cross section [9] of photons as a function of energy in carbon. The different contributions to the cross section are shown.*

into a lepton pair is constrained by momentum conservation and requires the field of an atom, thus pair conversion only occurs in matter. The cross section per nucleus, σ_p, is given by [13]

$$\sigma_p = 4r_e^2 \alpha Z^2 \left(\frac{7}{9} \ln 2\epsilon - \frac{109}{54} \right) \tag{13}$$

for $1 < \epsilon < 137/Z^{1/3}$. For high photon energies $\epsilon \gg 137/Z^{1/3}$ the cross section becomes energy independent and asymptotically reaches

$$\sigma_p = 4r_e^2 \alpha Z^2 \left(\frac{7}{9} \ln(183/Z^{1/3}) - \frac{1}{54} \right). \tag{14}$$

2.2 Principle of Operation of Solid State Detectors

Solid state charged particle detectors are usually composed of a sensitive volume and an amplification stage. The sensitive volume is characterised by a low intrinsic carrier density and an external field applied to it by adequate contacts. In the case of semiconductors, for example silicon, the sensitive volume is defined by the depleted region in a reversed biased diode. In the case of diamond, an insulator, the resistivity of the material is of the order $> 10^{11}$ Ω cm and the sensitive volume is essentially given by the geometry of the applied field, i. e. the shape of the electrodes. A diagram with the principal components is shown in fig. 3.

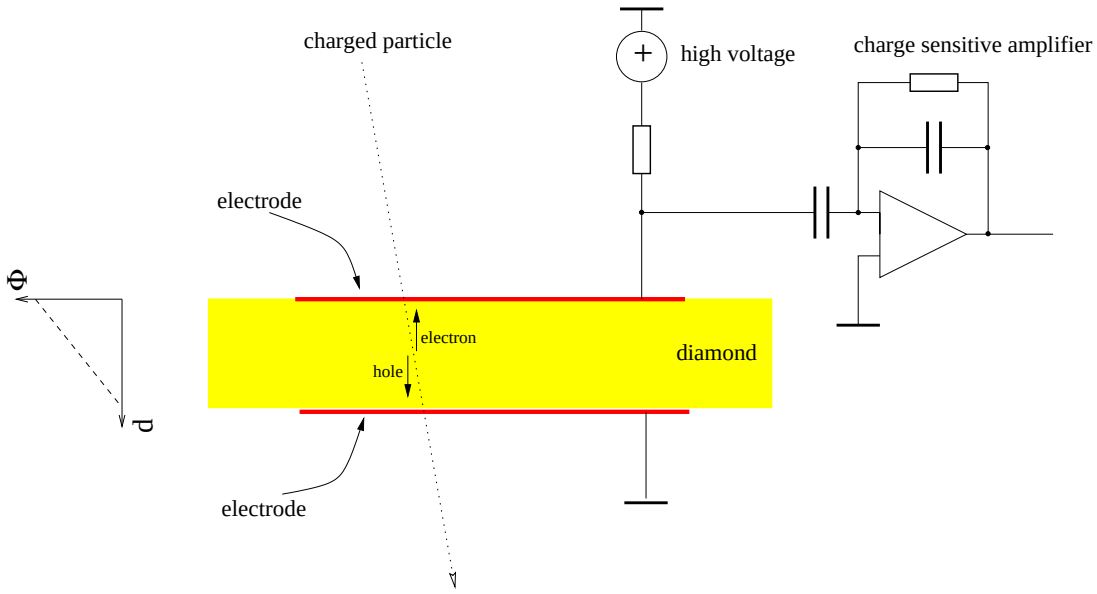

Figure 3: *Principle of operation of a charged particle detector made with diamond.*

If a charged particle enters the sensitive volume, the secondary free charge carriers produced by ionisation processes in the bulk start to drift because of Coulomb interaction in the electric field. The change of charge distribution induces an image charge on the electrodes which is compensated by the flow of charge in the external circuit to balance the potential difference. The resulting current in the external circuit is integrated by a charge sensitive amplifier and the signal can be detected. The drift of charge is limited by the lifetime and the mobility of free charge carriers and defines together with the amount of electron hole pairs the total charge induced on the electrodes. If the lifetime sets no limit on the signal generation, as in the case of silicon, the total charge seen on the electrodes equals the number of created electron hole pairs.

The amount of charge created by an ionising particle is given by the energy deposition and is a characteristic of the material. To obtain a clear detection signal it is thus important to optimise the carrier lifetime. In diamond the carrier lifetime is the limiting factor of the signal yield. The signal generation will be discussed in section 3.3 in greater detail.

As the signals from CVD diamond detectors are typically in the order of $O(10^3)$ electrons it is important to have a low noise level in the amplifier. A brief discussion of noise sources is given in appendix A.2.

2.3 Materials and Concepts of Solid State Detectors

Materials

Silicon is the most widely used material for semiconducting solid state detectors. The advantages of silicon are its high availability, the relativly low cost and the good understanding of the material. Moreover it can be run at room temperature and the charge collection is practically complete. Besides silicon some other materials may become important for detector applications including germanium, gallium arsenide, amorphous silicon and, of course, diamond.

Germanium has the disadvantage that it must be cooled to be able to operate it as a detector. However more charges are produced than in silicon for a given amount of deposited energy, allowing a more precise determination of energy or track position. Because of its high resolution germanium is used for spectroscopic studies, where it is superior to silicon.

Gallium arsenide attracted much attention in recent times due to the belief in its potential radiation hardness. The advantages of the material stem also in its high atomic number which makes it interesting for medical applications as X-ray detectors. However, the disadvantages are the high cost and low availability compared to silicon. Moreover, it has been found [15] that the radiation resistance to neutrons is superior to silicon, but that in fact the material suffers under charged hadronic radiation more severely than silicon, which makes its application impractical in environments common to the experiments at particle accelerators.

Amorphous silicon is a relatively new material for detector applications, the advantage being its potential for high cost effectiveness. The material is a binary alloy (a-Si:H) of silicon and hydrogen [16] and highly disordered. The disadvantages are the low carrier mobilities and lifetimes which are related to the disordered structure. Moreover, the amorphous layers are produced in a deposition process on a glass substrate and are typically thin in thickness (5-50 μm) making the detection of single MIP impossible due to the insufficient signal yield. Amorphous silicon detectors have been successfully employed in photon detection systems where active layers of only a few microns are required.

Concepts

The principle of a solid state detector was discussed in section 2.2. In all technologies the charge produced by the ionising particles is passed to an amplification stage. Different concepts exists for the read-out of the charge and the associated reconstruction of position information. Three concepts, namely segmented electrode, charge coupled device, and drift chamber represent the main approaches to the charge read-out issue.

The segmented electrode concept is the simplest approach. Here an array of electrodes is placed on the detector material with each electrode connected to a separate amplifier. Strip-like segmented electrodes are widely used in conjunc-

tion with silicon to obtain a spatially sensitive device [16]. The segments can also be arranged in the form of small pixels. Appropriate read-out is achieved by customised pixel read-out chips which are bonded on top of the detector and provide each electrode with its individual amplifier. The charge in the detector material is initially localised at the track of the traversing particle. An external electric field is applied to the detector material and the charge cloud starts to drift towards the electrodes and is widened by thermal diffusion. Only the electrode(s) nearest to the track will collect the charge and thus position information is obtained.

Especially in the case of pixel segmentation the number of read-out channels can be enormous because each pixel requires a unique channel. If a number of pixels can share one channel the number of channels is reduced. In the case of a charge coupled device (CCD) a very fine segmentation is achieved while the number of read-out channels is kept small by serial read-out of pixel rows. The segmented electrodes are replaced by potential pockets formed with an appropriate electrode structure. The charge of a traversing particle will accumulate in such a well defined pocket. By changing the potential on the electrode structure in a certain scheme the pocket and thus the charge can be shifted towards a read-out node of an analogue shift register at the end of each row. The shift register is used to sequentially read out the charges of each row with an amplifier. This technique requires only one read-out channel but maintains the fine segmentation. The disadvantage is the relatively long read-out time compared to individual pixel elements.

An example of a detector concept for applications where the goal is low noise, but fast read-out and position resolution are not important (i. e. X-ray imaging applications), is the so called "drift chamber" approach. Here an ultra low capacitance is needed to achieve an optimum noise performance. The read-out node is thus a very small structure which serves a larger cell structure. The charges produced in the cell drift through the volume to the read-out node by an appropriately shaped field. The field shape is obtained by a number of field electrodes. The cell can be of the order of millimetres while the read-out node size is a couple of micrometers.

For the application as vertex detectors in colliding beam experiments the former two approaches are adequate and currently a field of active research and development. The charge coupled device approach has until now been realized only with silicon, while segmented electrode detectors have been realised with all the detector materials discussed including diamond.

3 CVD Diamond

This chapter is concerned with the general properties of diamond. Emphasis is put on the comparison of the electrical and mechanical properties of diamond with standard semiconductor materials.

A second issue will be the discussion of diamond synthesis. The diamond samples investigated in this study were synthetically produced by means of the chemical vapour deposition method (CVD). A brief introduction to the growth mechanism and the production chemistry will be given.

Finally, the current status of diamond detectors and the theory of operation will be discussed.

3.1 Properties of Diamond

Diamond is constituted of carbon atoms. Each carbon atom has four sp^3 hybridised covalent bonds and is arranged in a tetraedical lattice - two face centred cubic fundamental cells offset by a $(\frac{1}{4}, \frac{1}{4}, \frac{1}{4})$ lattice vector with a lattice constant of 3.56 Å and a nearest neighbour spacing of 1.54 Å. This lattice arrangement is also called the *diamond structure* and is typical for elements of the IV group of the periodic table (e.g. silicon, germanium, tin).

The strong σ-type bonds of the diamond configuration have an ionic character and are the origin of many of the exceptional properties of diamond like its excellent hardness and its heat conductivity. The latter is five times that of copper at room temperature, although diamond is an electrical insulator. The band gap of diamond is 5.5 eV [17] at room temperature and is compared to silicon (1.1 eV) and germanium (0.76 eV) [18] relatively high. As in silicon, the minimum of the conduction band and the maximum of the valence band are separated and thus the band transition can occur only with participation of a phonon to satisfy momentum conservation. The direct transition requires $E_{g,direct} = 7.3$ eV.

The band gap is related to the bonding properties and reflects the energy difference of the bonding and anti-bonding state. The carbon-carbon bond strength is estimated to be of the order of 5 eV from theoretical calculations and cleavage experiments [19] and almost twice as large as the Si-Si bond strength.

Carbon can also arrange in staggered hexagonal lattice planes with sp^2 bonds forming graphite. The triangular σ-bonds involve three valence electrons while the fourth electron is in a delocalized p-state perpendicular to the hexagonal planes giving rise to the electrical conductivity of graphite. The lattice structures of diamond and carbon are shown in figure 4.

The transition of the carbon ground configuration $1s^2 2s^2 2p^2$ (graphite) to the exited configuration $1s^2 2s^1 2p^3$ (diamond) requires an energy of 4 eV [20]. The diamond configuration of carbon at room temperature and normal pressure is meta-stable but the transition to graphite in normal conditions is very unlikely.

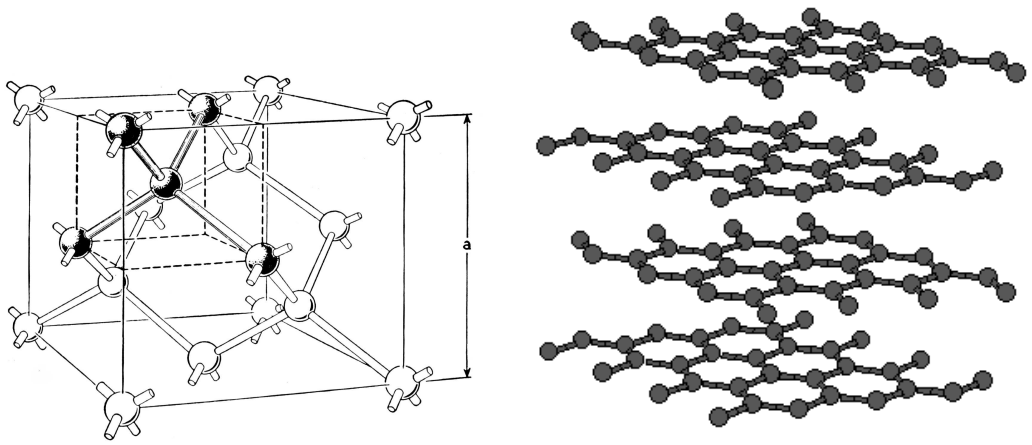

(a) The fcc $(\frac{1}{4}, \frac{1}{4}, \frac{1}{4})$ lattice structure of diamond.

(b) The staggered hexagonal plane structure of graphite.

Figure 4: *Possible crystal structures of carbon.*

The difference in free energy is only 0.03 eV per atom, thus of the order of kT, but a huge activation energy barrier exists between the two phases [21].

Although the fcc$(\frac{1}{4}, \frac{1}{4}, \frac{1}{4})$ structure is relatively empty, diamond possesses by virtue of its small lattice constant the highest atomic number density ($1.77 \cdot 10^{23}$ cm^{-3}) of any material at normal pressure.

The large band gap makes pure diamond an insulator at room temperature with a resistivity of $> 10^{14}$ Ω cm. However if impurity atoms acting as dopants are introduced it can also be a semiconductor. Successful p-type doping with the introduction of substitutional B atoms has been achieved artificially and has been observed in nature. The III group element boron acts as an acceptor on a substitutional lattice site. The activation energy has been experimentally determined to be 0.37 eV [22] in natural diamond, which is in good agreement with the calculated value of 0.36 eV [23]. Successful n-type doping has not yet been achieved. The V group element N, a potential donor, is an abundant impurity in both natural and CVD diamond but its activation energy of ≈ 1.7 eV [24, 23, 25] is too high for effective n-type doping. Other candidates like P or Li have been tried [26] but no convincing doping effect has been achieved.

The abundance of the impurities B and N in natural diamond were used for a classification scheme of natural diamond. The scheme was introduced phenomenologically by distinguishing different absorption lines. The absorption characteristics were later assigned to impurity concentration and aggregation of N and B. Very pure diamond with impurity concentrations of a few ppm are classified as type II while most diamonds found in nature have a high N content and are

classified as type I (see appendix A.1 for details).

Compared to Si the mobility of electrons and holes in diamond at low electric fields ($E < 1$ kV cm^{-1}) and room temperature is higher (values are given in table 1) [27]. This can partially be explained by the high Debye temperature and the relative stiffness of diamond. The saturation velocity of electrons was calculated to be $v_{sat} = 2.3 \cdot 10^7$ cm s^{-1} [28] at fields above 30 kV/cm. An actual measurement of v_{sat} for electrons and holes gives values of v_{sat} of $1.5 \cdot 10^7$ cm s^{-1} for electrons and $1.05 \cdot 10^7$ cm s^{-1} for holes [29] for fields above 30 kV/cm at room temperature.

The energy required to create an electron hole pair is in diamond $E_{eh} \approx 13$ eV and therefore much higher than in silicon ($E_{eh} = 3.6$ eV at room temperature). This leads to fewer charge carriers generated per deposited energy and reduces the signal from an ionising particle. The energy E_{eh} is higher than the bandgap ($E_g = 5.5$ eV) because of the additional production of phonons in the wake of the ionising particle. The theoretical value of E_{eh} has been calculated to 13.6 eV [30] and has experimentally been determined to 13.19 eV as reported in [31]. However the experimental data for E_{eh} in diamond varies from 10 eV to 25 eV as noted in [32], hence the uncertainty about this quantity is substantial. However, commonly accepted is a value of $E_{eh} = 13$ eV [10, 32, 33] which is also used in this work.

To summarise the properties of diamond, important parameters are listed in table 1 and compared to the other IV group semiconductors Si, Ge and the III/V group semiconductor GaAs.

3.2 Chemical Vapour Deposition of Diamond

Chemical vapour deposition (CVD) is widely used in industry for the production of thin films, semi-conducting or otherwise. The growth of diamond with a CVD process was long thought to be impossible because of the phase diagram of carbon shown in figure 5. At the relatively low temperatures and pressures used for the CVD process diamond is the thermodynamically unstable phase and only graphite is expected to be produced.

Traditionally the synthesis of diamond is achieved by processes operating in the stable diamond regime of the phase diagram, for example high temperature high pressure processes (HPHT) near equilibrium or processes involving a catalyst allowing diamond to be grown at less extreme conditions and thus more economically. The synthesised diamond crystals are typically small in size and have a high impurity concentration of nitrogen and the catalyst metal. The product is used for grinding applications in industry but fails to serve electronic applications because of size and crystal quality.

For electronic applications large dimensions and the highest crystal quality are essential. These properties can be achieved by means of CVD, if the physical difficulties presented by the phase diagram can be overcome. Growth of diamond

Property	Diamond	Si	Ge	GaAs
Atomic number	6	14	32	31/33
Atomic weight	12.0	28.1	72.6	144.6
Density [g cm^{-3}]	3.51	2.33	5.32	5.32
Crystal structure	Diamond	Diamond	Diamond	zincblende
Lattice constant [$\AA$]	3.57	5.43	5.64	5.63
Thermal conductivity [W cm^{-1} K^{-1}]	10-20	1.5	1.05	0.45
Dielectric constant	5.7	11.9	16.0	13.1
Band gap [eV]	5.5 indirect	1.1 indirect	0.6 indirect	1.4 direct
Energy to create e-h pair [eV]	13	3.6	2.9	4.3
Radiation length [cm]	18.8	9.4	2.3	2.3
Average $\frac{dE}{dx}$ for a MIP [MeV g^{-1} cm^{-2}]	1.75	1.66	1.37	1.45
Average ionisation density for a MIP [$e-h/\ \mu$m]	36	110	260	130
Electron mobility [$cm^{-2}V^{-1}s^{-1}$]	2150 ± 200	1450	3900	8500
Hole mobility [$cm^{-2}V^{-1}s^{-1}$]	1700 ± 280	450	1900	400
Intrinsic carrier density [cm^{-3}]	$< 10^3$	$1.1 \cdot 10^{10}$	$2.4 \cdot 10^{13}$	$1.8 \cdot 10^6$
Intrinsic resistivity [Ω cm]	$> 10^{11}$	$3.1 \cdot 10^5$	47	10^8
Saturation field [V cm^{-1}]	$3 \cdot 10^4$	$2 \cdot 10^4$	$8 \cdot 10^3$	$3 \cdot 10^3$
Electron saturation velocity [10^6 cm s^{-1}]	23	10.5	5.5	8.0

Table 1: *Structural and electronic properties of diamond, silicon, germanium and gallium arsenide at room temperature [16, 27, 28, 34].*

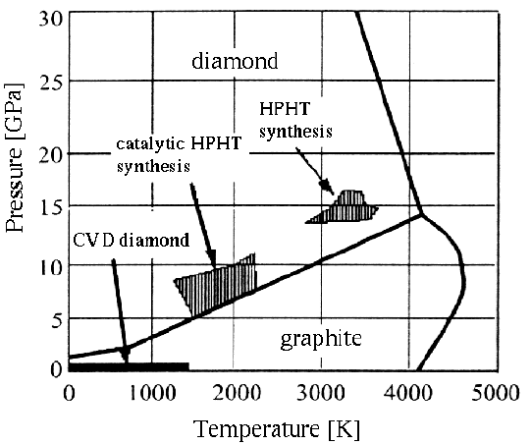

Figure 5: *Phase diagram of diamond. Indicated are the regions of stable diamond growth for high pressure high temperature processes (HPHT) in the diamond phase and the CVD process in the graphitic phase.*

with a CVD process was first shown in the 1950s and published in the 1960s by Eversole [35], Liander [36] and also by Angus et al. [37]. It was shown that at CVD conditions the mass of a sample of diamond grit could be increased by flowing methane over the grit at elevated temperatures and that a fraction of the mass increase was due to the formation of diamond.

The breakthrough came in the mid-seventies, when Deryagin et al. [38, 39] introduced the concept of super-equilibrium of atomic hydrogen to minimise the co-deposition of graphite and allow deposition of diamond on non-diamond substrates. Since then a rapid development of the deposition techniques and an improved understanding of the physics of the process was achieved by research groups and commercial manufacturers. To date films of several hundred microns thickness have been grown on up to 4 inch wavers with excellent crystal quality [40, 41].

The principle of diamond growth in a CVD process is based on the higher bonding energy of sp^3-bonds relative to sp^2-bonds. In the gas phase highly reactive atomic hydrogen and carbon species (e. g. CH_3 radicals) are present. The H-H bond energy is greater than the C-H bond strength and thus continuous abstraction of H from the surface and addition of H to vacant surface sites takes place [21]. The exothermic reactions will provide a steady-state concentration of vacant surface sites which can be filled by a carbon carrier. The higher bonding energy of sp^3-bonds will lead to a preferential growth of diamond over graphite despite the latter being thermodynamically the favoured phase. The weaker bonded graphite will be etched away by atomic hydrogen. The mechanism of diamond growth in a CVD reactor is sketched in figure 6.

A generic CVD reactor consists of a carbon carrier source, e. g. methane, a hydrogen source and possible admixture of oxygen to enhance growth rates. Further components are an excitation source and a cooled substrate. With the excitation source the molecules of the gas mixture are dissociated into CH_3 radicals and atomic hydrogen.

The substrate on which the CVD diamond film is formed can be either diamond in the case of homo-epitaxial growth or other materials. Silicon is widely used as a substrate material because it has the same lattice structure, the lattice mismatch is acceptable ($a_C/a_{Si} = 0.67$) and the availability is good. To increase the nucleation site density the substrate surface is pretreated with ion bombardment [42] or scrubbed with diamond powder. Diamond films grown on non-diamond substrates are typically polycrystalline. The films growth starts with randomly oriented micro-crystallites at the nucleation sites. The lateral growth of a crystallite is limited by its neighbouring crystallites and a columnar growth morphology develops. The growth speed is depending on the crystal orientation and parameters of the gas phase. Crystallites of slow growth can be overgrown by faster developing neighbouring crystallites. The resulting film consists of many columnar structured crystallites. Due to the overgrowth of neighbours the width of the crystallites becomes larger with the film thickness, and the faster growth

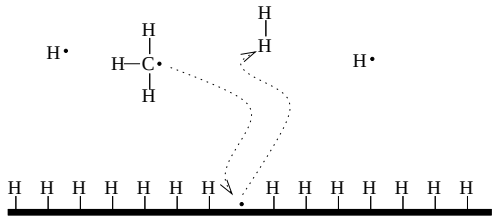

(a)

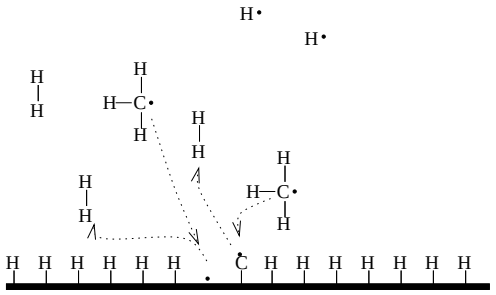

(b)

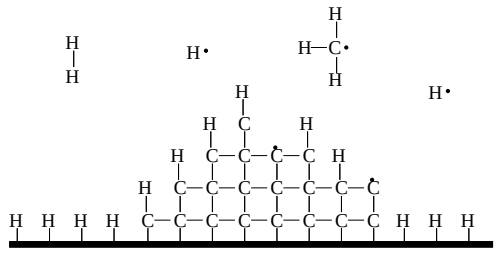

(c)

Figure 6: *Schematic of the growth principle of diamond in a CVD reactor: The initially hydrogen saturated surface reacts with atomic hydrogen radicals in the gas phase. Abstraction of hydrogen from the surface leaves a free surface site (a) which can be occupied by hydrogen or a carbon growth species (b). By continuous abstraction of hydrogen and replacement with carbon carriers a diamond lattice is formed (c).*

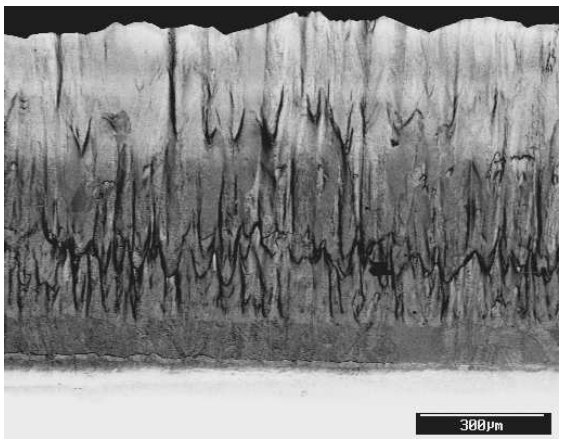

Figure 7: *Cross section of a typical polycrystalline CVD diamond with the substrate side on the bottom and the growth side on the top. The columnar structure of the film is clearly visible.*

of certain crystallographic directions generally leads to a texture[3] [43].

A typical cross section of a polycrystalline CVD diamond is shown in figure 7. The columnar structure of the film and the increase of the crystallite size by overgrowth of neighbouring crystallites can be clearly seen (see section 7 for a growth model of CVD diamond). The side attached to the substrate is called substrate side while the side facing the growth species is termed growth side. The crystal quality of the substrate side is generally poor due to the small crystallite size and the high density of grain-boundaries. The quality increases with thickness of the diamond film and the best quality is observed on the growth side.

Both on diamond and non-diamond substrates highly oriented films can be deposited. When a complete orientation of the crystallites is reached no grain boundaries are present and the obtained film is virtually a single crystal. The completely orientated growth in one crystallographic direction on a diamond substrate is called homo-epitaxial growth. The growth on non-diamond substrates (hetero-epitaxy) is more difficult due to the lattice mismatch of substrate and diamond. Nevertheless highly oriented growth has been reported on silicon substrates [44]. The result of oriented growth is a very smooth and uniform film (see figure 8 taken from reference [44]). Hetero-epitaxial material is a good candidate to reach a single crystal film with advantage that the disturbing influence of grain boundaries on thermal and electrical transport properties would vanish. However, the production of such films involves the intentional addition of impurities to steer the direction of growth which can deteriorate the electrical quality.

A number of reactor types have been used, which can be classified by the excitation source of the gas mixture. Different reactor types and their advantages and drawbacks are summarised in table 2 taken from reference [45]. The bulk of the samples investigated in this work was produced with a *microwave-plasma*

[3]Texture means the preferred crystallite orientation in one crystallographic plane with a rotational degree of freedom about the surface normal of the film.

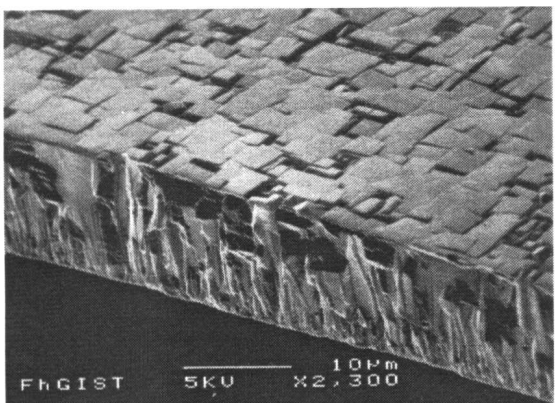

Figure 8: *SEM micrograph of (001) oriented hetero-epitaxial diamond film taken from [44].*

Method	Rate [μm]	Area [cm^2]	Quality [Raman]	Substrates	Advantages	Drawbacks
Flame	30-100	1	+++	Si, Mo, TiN	Simple	Area, stability
Heated filament	0.3-2	100	+++	Si, Mo, silica, etc.	Simple, large area	Contaminations, stability, no O_2
DC discharge (low pressure)	< 0.1	70	+	Si, Mo, silica, etc.	Simple, large area	Quality, rate
DC discharge (med. pressure)	20-250	< 2	+++	Si, Mo, alumina	Rate, quality	Area
DC plasma jet	930	< 2	+++	Mo, Si	Highest rate, quality	Area, stability, homogeneity
RF (low pressure)	< 0.1	?	-/+	Si, Mo, Ni silica, BN	Scale-up	Quality, rate, contaminations
Microwave (0.9-2.45 GHz)	1-30	40	+++	Si, Mo, silica, WC	Quality, stability	Rate, area

Table 2: *Comparison of the properties of different diamond deposition methods from [45].*

reactor (MWPR) of which the basic design is illustrated in figure 9.

The MWPR uses a standing micro-wave fed by a magnetron to actuate a plasma over a cooled substrate. The resonance of the cavity can be adjusted by a movable plunger at the end of the wave guide. The active reactor volume is separated from the wave guide by a quartz tube through which a constant flow of a gas containing the reactive species is maintained. A typical microwave frequency of 2.45 GHz and microwave power of typically 1 to 5 kW is used. Power and frequency are chosen according to the commercial availability of magnetrons. Depending on the growth parameters growth rates up to 30 μm h^{-1} are achieved. A detailed study of the dependence on growth parameters of the detection properties of CVD diamond is presented in section 5.

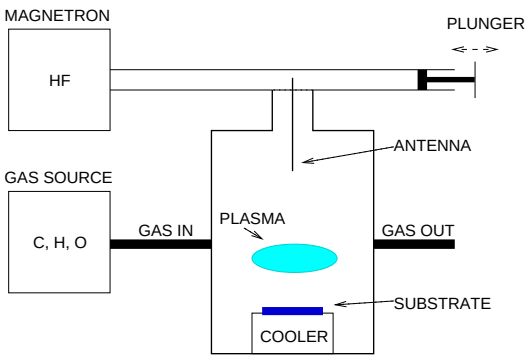

Figure 9: *Basic set-up of a microwave-plasma reactor for CVD diamond growth.*

3.3 Diamond Detectors and Signal Generation

The first reports about detector studies with CVD diamond appeared at the beginning of this decade [1, 2]. The material employed was produced in a DC-arc-jet reactor and typically had a signal of arround 1500 e for a minimum ionising particle (MIP). In recent years a substantial improvement of signal yield has been achieved to about 7200 e on selected samples to date [46].

The high resistivity of diamond makes the fabrication of diamond detectors simple. No depletion zone is needed to reduce the intrinsic carrier density. Diamond can be used as a solid state ionisation chamber. It is sufficient to apply two electrodes accross the material and supply a sufficiently high potential difference to create a electric field inside the diamond. The high resistivity prevents the occurence of significant currents. In figure 3 on page 3 the principle components were shown. In the following, the important concepts of collection distance, δ_Q, and collection efficiency, ϵ_Q, are explained in the context of signal generation.

To discuss the signal formation in CVD diamond, the simple case of one free electron at point $\vec{r}$ in a two dimensional diamond of thickness d and infinite length is considered. The electrical contacts are placed over the full length and the electrical field is thus equal to that of an ideal plate capacitor with strength $E = U/d$ and the direction of the field pointing perpendicular to the surface. Because of Coulomb interaction with the electric field the electron drifts towards the anode. The displacement of the charge causes a change of the potential on the electrodes. To maintain the potential difference U a current flows in the external circuit which is equal to [47, 48]

$$I = \frac{ev}{d} \tag{15}$$

with v the drift velocity of the electron. The induced charge is given by the time integral of equation (15). The time the electron can drift is limited by the lifetime (i) and by the distance to the anode (ii). Condition (ii) is void in the case of re-injection of charge carriers at the contact. This process is termed *photo-conductive-gain* and has been observed in a range of materials but not yet in diamond. The carrier lifetime (i) is a material property and independent of the

electric field. The lifetime τ is infinite for an ideal crystal. For real crystals defects in the form of impurity atoms, dislocations, stacking faults and grain boundaries distort the band structure by introducing additional energy levels in the forbidden band gap. The additional levels can act as recombination-generation centres or as trapping centres, limiting the lifetime of the free carriers.

If the lifetime τ is known, the induced charge for one electron can be calculated by

$$Q_m = \frac{e}{d}\int_0^\tau v \ \mathrm{d}t = \frac{e}{d}v\tau \equiv e\frac{\delta}{d} \tag{16}$$

with the condition $\tau \leq \frac{z}{v}$ if the distance to the anode is z. In equation (16) the drift length δ, also called Schubweg [49], is introduced. It describes the distance between the point of creation and point of stopping by trapping or recombination of the electron. The induced charge from one electron is proportional to the ratio of the Schubweg and the distance of the electrodes, i. e. the thickness of the detector. The Schubweg is given as the product of the lifetime and the drift velocity. The drift velocity is calculated by the product of the electric field and the carrier mobility. Thus the Schubweg δ can be expressed as

$$\delta = v\tau = \mu(E)E\tau \tag{17}$$

with $\mu(E)$ the mobility and E the electrical field strength. The mobility μ depends on E and decreases for high field strengths (> 1 kV/ cm). If E approaches the saturation field ($E_{sat} \approx 2 \cdot 10^4$ kV cm^{-1}) the mobility scales with $1/E$ making the product $\mu(E)E$ independent of E and defining the saturation velocity v_{sat}. The decrease of mobility at high fields is caused by the enhanced production of optical mode phonons when the energy gained by the charge carrier in the electric field becomes non-negligible compared to the thermal equilibrium of $3/2kT$ [27].

The capture of an electron is a statistical process and τ denotes the characteristic lifetime. If an ensemble of n_0 free electrons at time t_0 and distance z from the electrode is considered, the amount of free electrons after a time Δt is given by

$$n(\Delta t) = n_0 \ \exp(-\Delta t/\tau) \tag{18}$$

or expressed in terms of Schubweg and drifted distance Δz:

$$n(\Delta z) = n_0 \ \exp(-\Delta z/\delta). \tag{19}$$

To calculate the induced signal from an ensemble of n_0 electrons expression (16) is modified to

$$\begin{aligned} Q_m &= \frac{e}{d}\int_0^{z/v} n(t)v \ \mathrm{d}t \\ &= n_0\frac{e}{d}\tau\left[1 - \ \exp\left(-\frac{z/v}{\tau}\right)\right] \\ &= n_0 e\frac{\delta}{d}\left[1 - \ \exp\left(-\frac{z}{\delta}\right)\right]. \end{aligned} \tag{20}$$

For $z \gg \delta$ the exponential term becomes small and the approximation $Q \approx n_0 e\delta/d$ can be made. If the electrons are distributed with $\rho_e(z), \int_0^d \rho_e(z)\ \mathrm{d}z = n_0$, in the detector the expression for Q becomes

$$\begin{aligned} Q_m &= \frac{e}{d}\int_0^d \rho_e(z) \int_0^{(d-z)/v} \frac{n(t)}{n_0} v\ \mathrm{d}t\ \mathrm{d}z \\ &= \frac{e}{d}\int_0^d \rho_e(z)\tau \left[1 - \exp\left(\frac{(z-d}{v\tau}\right)\right]\ \mathrm{d}z \\ &= e\frac{\delta}{d}\int_0^d \rho_e(z) \left[1 - \exp\left(\frac{z-d}{\delta}\right)\right]\ \mathrm{d}z. \end{aligned} \tag{21}$$

Until now τ was assumed to be a constant of the material and independent of the position. This is not the case in a polycrystalline material like CVD diamond, where the lifetime τ is dependent on the position z in the material. Two different models of $\tau(z)$ are discussed in section 7. One approach [10] proposes a linear variation of $\tau(z)$ with the thickness of the CVD diamond. The other approach assumes a $(1 - \exp(r/r_0))$ dependence of τ on the distance to the nearest grain-boundary r with r_0 being a characteristic distance, and uses a generic CVD diamond growth morphology. The life-time and the Schubweg are related by equation (17) defining the position dependent Schubweg $\delta(z) = \mu(E)E\tau(z)$. For a varying $\delta(z)$ the integral of equation (21) is modified to[4]

$$Q_m = \frac{e}{d}\int_0^d \delta(z)\rho_e(z) \left[1 - \exp\left(\frac{z-d}{\delta(z)}\right)\right]\ \mathrm{d}z. \tag{22}$$

Expression (22) simplifies for $\delta(z) \ll d$ and constant $\rho_e(z)$ to

$$Q_m \approx Q_i \frac{\bar{\delta}}{d} \tag{23}$$

with $Q_i = e\int_0^d \rho_e(z)\ \mathrm{d}z$ and $\bar{\delta} = \frac{1}{d}\int_0^d \delta(z)\ \mathrm{d}z$.

Up to now The discussion was restricted to electrons contributing to Q. A similar expression can be derived for holes. The total induced signal is the sum of the hole and the electron contribution

$$\begin{aligned} Q_m &= Q_e + Q_h \\ &= \frac{e}{d}\int_0^d \left[\delta_e(z)\rho_e(z)\left[1 - \exp\left(\frac{z-d}{\delta_e(z)}\right)\right] + \delta_h(z)\rho_h(z)\left[1 - \exp\left(\frac{-z}{\delta_h(z)}\right)\right]\right]\ \mathrm{d}z \\ &\approx Q_i \frac{\bar{\delta}_e + \bar{\delta}_h}{d} \equiv Q_i \frac{\delta_Q}{d} \end{aligned} \tag{24}$$

[4]The discussion is restricted to one dimension z for the sake of simplicity. The general case of three dimensional distributions of δ and ρ_e is obtained by replacing z with $\vec{r} \stackrel{\mathrm{def}}{=} (x, y, z)$ and integrating over the active detector volume.

with the introduction of δ_Q as the *collection distance* [32], and the assumption $\rho_e(z) = \rho_h(z) \equiv \rho_Q(z)$ which is true for ionisation processes. To measure the collection distance in CVD diamond the values of Q_i, Q_m and $\rho_Q(z)$ have to be known. For $\rho_Q(z) = const.$, the approximation in equation (24) can be made and δ_Q can be written in analogy to equation (17) as

$$\delta_Q = E \cdot (\mu_e \tau_e + \mu_h \tau_h). \tag{25}$$

For MIPs the generated free carrier density is approximately constant. If free charge carriers are created in a thin surface layer only one charge carrier type can contribute to the signal because the drift length is zero for the other type. In this case the van Hecht [49] relation applies to approximate the drift length (eq. (26)), with $\delta = \delta_e, \delta_h$ at the surface).

$$Q_m \approx Q_i \frac{\delta}{d} \tag{26}$$

Equation (26) can be used in an experimental situation where particles with a short range relative to the detector thickness are used, i.e. alpha particles of a few MeV or electrons in the keV range.

A more pragmatic quantity is the collection efficiency defined as

$$\epsilon_Q = \frac{Q_m}{Q_i} \approx \frac{\delta}{d}. \tag{27}$$

The charge collection efficiency, ϵ_Q, is determined only by the measured charge Q and the produced charge Q_i, and is thus independent on the distribution of ρ_Q. This quantity is more exact as no approximation needs to be used to determine it.

3.4 Polarisation, Passivation and the Role of Defects

In the previous section the signal generation process was discussed and the importance of the collection distance δ_Q was emphasised. The ideal case that all charge is collected is only given for $\delta_Q \gg d \Leftrightarrow \epsilon_Q = 100\%$. In CVD diamond ϵ_Q is typically well below 50%, and charge carriers remain in the crystal. The trapping of charge occurs in levels established in the forbidden band gap by various defects of the diamond. The defects can be displaced carbon atoms in interstitial or vacancy positions, or impurity atoms (typically O and N [50]) forming so called point defects. Figure 10 taken from [51] presents an overview of the possible configuration of point defects.

At grain-boundaries the defect density is found to be very high [44]. Here many point defects are agglomerated and clusters or layers of defects (planar defects) [51] are produced.

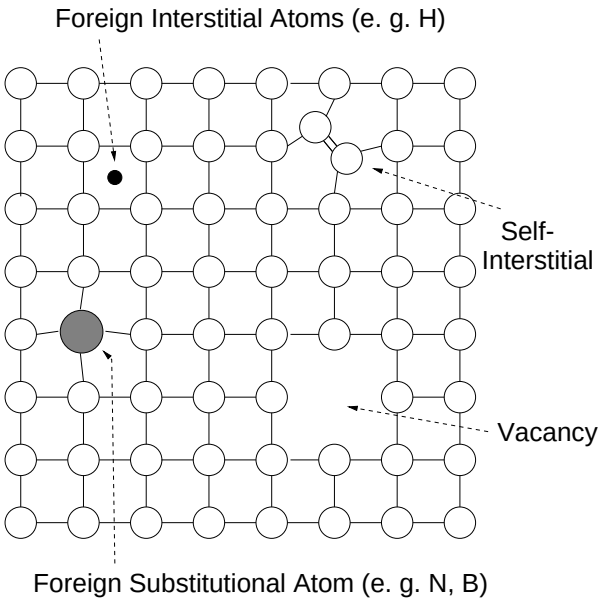

Figure 10: *Possible configurations for point defects in diamond.*

Defects are characterised by their position in the band-gap and their cross section to capture a charge - a negatively charged electron or a positively charged hole. The energy of the trap (E_t) determines together with the temperature T and the Fermi level E_f the occupation state

$$F(E_t) = \frac{1}{1 + e^{\frac{E_t - E_f}{kT}}}$$

with k being the Boltzmann constant. Trap levels with $(E_t - E_f)$ of a few eV (deep traps) are therefore practically not occupied at room temperature ($kT \ll (E_t - E_f)$) but can be filled by excess carriers generated by e. g. ionisation.

Traps can act via three processes: (a) trapping, (b) recombination and (c) generation of charge carriers. The mechanism is depicted in figure 11. Traps can capture a free carrier (a) from the valence or conduction band. The rate per volume for this process is given by the density of not occupied traps, n_t, and the density of free carriers, n_c, the capture cross section, σ_t and the thermal velocity of the carrier, v_{th}, as

$$r_t = n_t n_c \sigma_t v_{th}. \tag{28}$$

An occupied trap can capture a carrier of opposite sign which recombines (b) with the trapped charge. The rate is

$$r_r = n_r n_c \sigma_r v_{th} \tag{29}$$

with n_r the density of occupied traps and σ_r the capture cross section for charges of opposite sign. In the case of quasi-equilibrium with $n_t \gg n_c$ and $n_r \gg n_c$ a life-time τ can be defined as

$$\tau = \frac{n_c}{r_t + r_r} = \frac{1}{v_{th}(\sigma_t n_t + \sigma_r n_r)}. \tag{30}$$

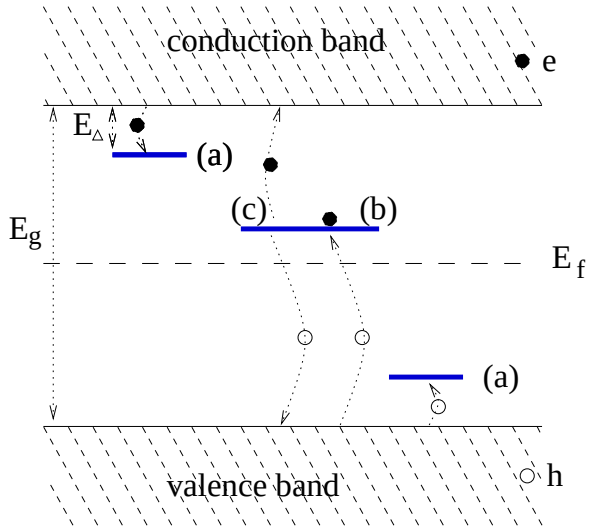

Figure 11: *The mechanism of trapping (a), recombination (b) and generation (c) of charge carries. E_f is the Fermi-level, e electron, h hole, E_g the bandgap and E_Δ the distance of the trap level to the band edge.*

A trapped charge can be emitted thermally. The probability for thermal emission is dependent on the activation energy E_Δ defined by the distance of the trap level to the conduction or valence band in the case of electrons or holes respectively. The temperature dependence of the emission rate per volume is given by

$$r_e = s \cdot n_f \cdot \exp\left(-\frac{E_\Delta}{kT}\right) \tag{31}$$

with n_f the density of occupied traps and s the frequency factor. Typically s is in the range 10^{12} s^{-1} to 10^{14} s^{-1}. The inverse s^{-1} is a measure of the characteristic emission time. The thermal emission rate is for deep defect levels ($E_\Delta \gg kT$) very low and the charge is stored for a long time in the trap.

If an electric field is present electrons and holes generated by ionisation will be separated. The trapped charges create an internal electric field which is opposed to the applied external field. This *polarisation field* lowers the effective field strength in the crystal and can completely compensate the external field with the effect that the particle detection signal is lost. The persistence of the polarisation is dependent on the energy level of the participating traps. Spectroscopic methods (see section 4.11) indicate that the relevant states are located deep in the band-gap at around 1 to 2 eV. Consequently the polarisation is stable at room temperature. The non-polarised state is reestablished after heating the sample to above $T = 540$ K or after illumination with visible light. Both treatments enable the emission of trapped charge into the allowed bands.

While polarisation deteriorates the signal of a counter, the same mechanism of trap filling can lead to the opposite - the signal enhancement. If traps are occupied the lifetime of free carriers increases due to the lower free trap density. The well established effect of passivation [52, 50] is generally called *priming* or also *pumping* [46].

Trap filling leads to polarisation if the initial ionisation density distribution

$\rho_Q(x)$ is non-uniform. In this case the charge clouds are effectively separated and in the region of charge deposition a strong polarisation field develops. If the ionisation density is uniform a less pronounced polarisation field develops. A computer simulation presented in section 7 reproduces the effect of priming and polarisation in agreement with experimental observations with different ionising particle types.

Although the picture is simplified in the sense of not considering traps with different energies, cross sections and charge states, it can explain the experimentally observed behaviour rather well. Additionally, comprehensive spectroscopic data of electronically active defects in detector grade CVD diamond is not yet available.

4 Characterisation Methods

This chapter describes the characterisation methods used to investigate various properties of CVD diamond samples. The methods are grouped into those concerned with the characterisation of electrical properties and those dealing with structural properties. Electrical properties are the resistivity (section 4.5), defect states (section 4.11) and charge collection properties for different ionisation sources (sections 4.6, 4.7, 4.8, 4.9 and 4.10). The structural properties include the surface morphology (section 4.1), lattice quality (section 4.2), lattice orientation, crystallite shape (section 4.3) and element purity (section 4.4). Some characteristics of the different methods are listed for comparison in table 3.

Method	Section	Class	Probe	Bulk	Surface	Property	Spatially resolved
SEM	4.1	st.	e^-, 20 keV		$\surd$	topology	$\surd$
Raman	4.2	st.	γ		$\surd$	structure	
X-diff	4.3	st.	γ, 10 keV	$\surd$		orientation	$\surd$
SIMS	4.4	st.	Ar		$\surd$	chemical impurities	$\surd$
IV	4.5	el.		$\surd$		ρ	
MIPs, ^{90}Sr	4.6	el.	$\beta, < 2.8$ MeV	$\surd$		ϵ_Q , Φ_0 , R_p	
MIPs, testbeam	8	el.	e^-, 5 GeV	$\surd$		ϵ_Q	$\surd$
photon beam	4.7	el.	γ, 10 keV	$\surd$		ϵ_Q	$\surd$
alphas	4.8	el.	α , 5.8 MeV		$\surd$	(ϵ_Q)	
proton micro-beam	4.9	el.	p, 2 MeV		$\surd$	(ϵ_Q)	$\surd$
EBIC	4.10	el.	e^-, 20 keV		$\surd$	(ϵ_Q)	
TSC	4.11	el.		$\surd$		defect levels	($\surd$)

Table 3: *Summary of methods of investigation. Given are the abbreviated method names, in which section the method is described, whether it investigated structural (st.) or electrical (el.) properties, the probing particle, whether the bulk or the surface is probed, the accessible properties and the ability of a spatially resolved measurement.*

The structural methods provide both spatially resolved and unresolved data. Standard scanning electron microscopy (SEM) was used to investigate surface morphologies and profiles of CVD diamond samples. The SEM was extended to measure electron beam induced currents (EBIC) which allowed qualitative measurements of electrical transport properties with a high resolution.

The overall orientation of crystallites in polycrystalline CVD diamond samples were determined by X-ray diffraction measurements. Spatially resolved X-ray diffraction measurements were employed to obtain information about the shapes of single crystallite and to verify the columnar growth morphology.

The chemical impurity concentration of a typical CVD diamond sample was

determined with spatially resolved secondary ion mass spectroscopy (SIMS) measurements. As well as the absolute concentration values, the spatial distribution of impurities was investigated.

For the development of particle detectors the charge collection properties are of primary interest. Thus emphasis was put on the investigations with ionising radiation. The peculiarities of CVD diamond in view of its charge collection were already mentioned when discussing the theory of operation of CVD diamond detectors in section 3.3. In particular the non-uniform and high trap density in the bulk should be emphasised. It is thought to be the origin for many of the observed phenomena. The methods using ionising radiation can be grouped into spatially resolved measurements and non-resolved measurements as listed in table 3. The spatially resolving methods are directly sensitive to the non-uniform properties of the material, while the non-resolving methods can be used to measure the average bulk properties, or to make qualitative predications about the uniformness of the material.

The ionisation sources have different ionisation characteristics. Two classes are distinguished: those resulting in a uniform distribution of free charge carriers along a traversing particle track, called *uniform ionisation*, and those giving a Bragg distribution of free charge carriers along the track of a particle stopping in the bulk, called *Bragg ionisation*. Uniform ionisation was obtained with electrons above $E > 1.1$ MeV where they become minimum ionising, and photons within an energy range where the absorption length is large compared to the material thickness ($E \approx 10$ keV). The response to Bragg ionisation was tested with protons ($E = 2$ MeV) and alpha particles ($E = 5.8$ MeV).

The chapter starts by presenting the structural methods, continues with the electrical methods and closes with an interpretation and a summary of the structural and electrical data obtained.

4.1 Scanning Electron Microscopy

Scanning electron microscopy was used to obtain topographic images of the surface and the profile of selected CVD diamond samples. The advantage of the SEM technique over conventional light microscopy is the enhanced resolution due to the use of electrons rather than light. The theoretical resolving power is governed by the Abbe formula

$$\upsilon = \frac{0.61\lambda}{n \sin(\alpha)} \tag{32}$$

with λ being the de Broglie wavelength, n the refractive index of the medium and α defining the semi-angle of the cone of useful rays emerging at some point from the object, i. e. the angular aperture. Taking the difference in λ between optical and electron microscopes alone the resolving power should be five orders of magnitude better for the electron microscope.

In practice no perfect lenses exist for electron optics. The aperture is rather small and further mechanical and electrical imperfections of the construction prevents the resolving power from reaching the theoretical value. Typical values for υ at a beam energy of 15 keV are of the order of $\upsilon \approx 1$ nm.

The beam electrons will interact with the surface layer of the specimen and produce secondary electron emission and backscatter. The electron yield is dependent on the specimen and the topology of the surface. By measuring the intensity of the secondary emission as a function of the beam position, a topographic image of the specimen is obtained.

4.1.1 Set-up

A scanning electron microscope of type Philips SEM505 at the Institut für Experimentalphysik[5], Universität Hamburg was used. The SEM505 had a magnification range of 30 to 240.000, offering a electron beam spot size between 10 nm and 500 nm with adjustable energy between 1 keV and 30 keV. Electrostatic lenses were used to focus the beam. The secondary electron detector consisted of a scintillator and a photo-multiplier. The images were digitised with an analogue-to-digital converter (ADC) and read out by a computer.

4.1.2 Results

A view of a typical polycrystalline CVD diamond surface at the growth side is depicted in figure 12a. The crystallites are randomly oriented. The typical grain size in this particular sample with a thickness of $d = 123$ μm is about 30 μm.

In figure 12b the side view of an approximately 1 mm thick CVD diamond sample is shown. Clearly distinguishable is the columnar growth morphology of the single crystallites. Moreover the lateral increase of the crystallites during growth is apparent. The weak two step structure along the profile is produced by the laser cutting of the sample.

These pictures introduce two important features of CVD diamond: its crystalline structure and the lateral growth of crystallites with increasing thickness of the material. The investigation of the role this structure plays for the use of CVD diamond as a detector material is a central topic of this thesis.

4.2 Raman Spectroscopy

Raman spectroscopy was used to determine the lattice perfection of crystals. Raman observed in 1928 that light scattered by a crystal solid or molecule contained small red-shifted and blue-shifted components in the spectra relative to the incident monochromatic light. The so called Raman scattering occurs if the

[5]The author wishes to acknowledge the support of Prof. Anton, Inst. f. Exp. Physik, Universität Hamburg.

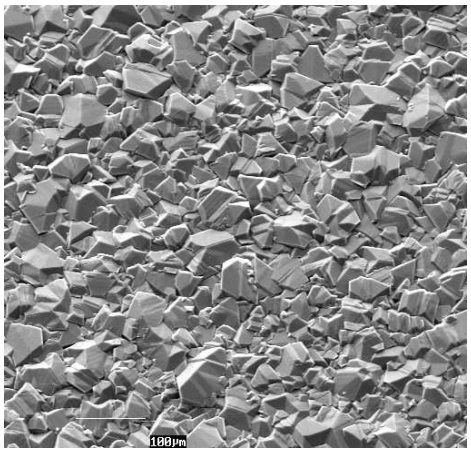

(a) Growth side of a polycrystalline CVD diamond.

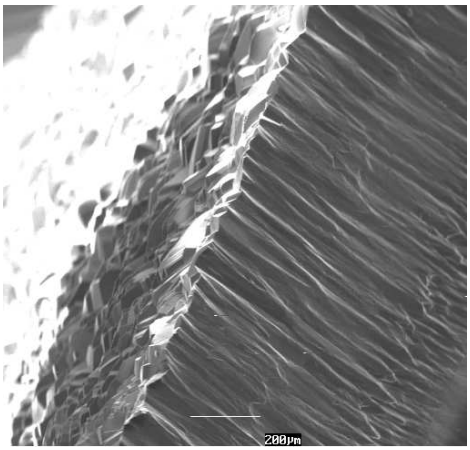

(b) Side view of a polycrystalline CVD diamond sample.

Figure 12: *Examples of typical topologies of polycrystalline CVD diamond samples.*

incoming photon produces or absorbs an optical mode phonon. The energy and momentum of the phonon are related to the lattice properties of the material and mainly determined by the electrical polarisability. The conservation of energy and momentum requires

$$h\nu' = h\nu \pm E_p \tag{33}$$

$$\vec{k} = \vec{k} \pm \vec{q_p} \tag{34}$$

where $h\nu$, $h\nu'$ and $\vec{k}$, $\vec{k'}$ are the energy and momentum of the incoming and scattered photon, and E_p and $\vec{q_p}$ are the energy and momentum of the optical phonon. In case of phonon absorption the quantities are added, in the case of the production of a phonon they are subtracted. The processes are called Anti-Stokes-scattering and Stokes-scattering after the Stokes rule, that the wavelength of fluorescent light must be equal or larger than that of the inducing light. In the case of absorption the wavelength is smaller than the incident light, hence the process is called Anti-Stokes-scattering.

Typically, visible light is used and the frequency shift is only a few percent of the initial frequency. The *Raman shift* is expressed in wavenumbers in units of cm^{-1} and is a characteristic of the material. Diamond has a characteristic Raman shift of $1332\ \mathrm{cm}^{-1}$. The full width at half maximum (FWHM) of the Raman peak is an indicator for the abundance of randomly oriented stress and strain in the specimen. If the lattice is under stress or strain the characteristic energy of the phonon and thus of the Raman line is shifted. If stress is non-uniformly distributed the line width is broadened.

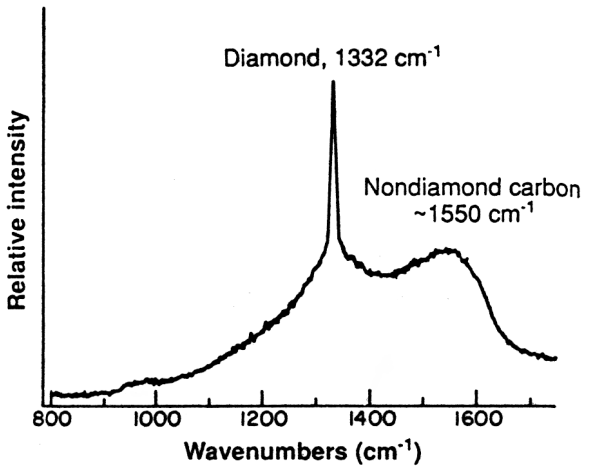

Figure 13: *Example of a typical Raman spectrum of a polycrystalline CVD diamond with a substantial amount of non-diamond carbon from [53].*

Graphite can be detected by a broad line at about 1580 cm^{-1}. A mixture of sp^2 and sp^3 bonds yields broad bands around the diamond and graphite Raman line indicating the presence of disordered structures as seen in DLC (diamond like carbon) material.

A typical Raman spectrum of a polycrystalline CVD diamond taken from [53] with substantial amount of non-diamond carbon is shown in figure 13. Clearly visible is the diamond peak at 1332 cm^{-1} and the broad band around the graphite peak indicating the non-diamond contribution.

4.2.1 Results

Raman spectra were recorded at the Fraunhofer Institut für Schicht- und Oberflächentechnik (FhGIST) in Braunschweig. For samples produced by FhGIST in the framework of systematic studies of the growth parameters for detector grade CVD diamond (see section 5), the crystal quality was routinely investigated using the FWHM of the diamond Raman peak. The apparatus had an intrinsic resolution of about FWHM ≈ 4 cm^{-1}. It has been found that all CVD diamonds with a detectable charge collection efficiency had a FWHM of the Raman line width equal or better than the intrinsic resolution of the apparatus. No sign of graphitic phases could be detected.

Typical Raman spectra for growth and substrate side of a polycrystalline CVD diamond of detector grade quality are shown in figure 14. The maximum is at 1337.2 cm^{-1} wavenumbers and slightly shifted relative to the expected value of 1332 cm^{-1}. The reason can be internal stress in the sample. The maximum value is the same for substrate and growth side. No indication of a graphitic phase (broad band at around 1580 cm^{-1}) is seen.

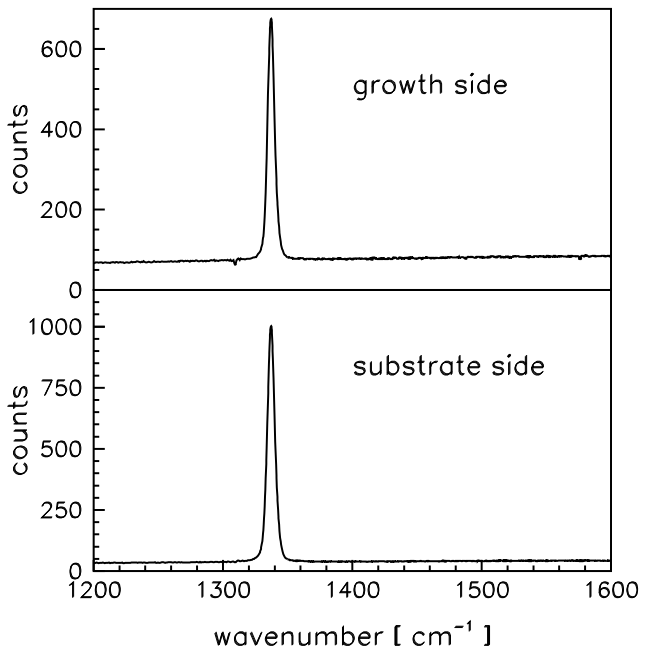

Figure 14: *Typical Raman spectra of a polycrystalline CVD diamond of detector grade quality. The spectra measured at the growth (upper) and the substrate side (lower) are plotted.*

4.3 X-Ray Diffraction

In this study the orientation of crystallites was measured on different samples with a X-ray diffractometer[6], allowing the detection of preferential growth orientation. Furthermore by using a set-up with synchrotron radiation and a CCD camera[7] the shape of single crystallites was spatially resolved with a resolution of 24 μm.

4.3.1 Principle

As with a grating the uniform arrangement of equally spaced crystal planes reflects light with a wavelength shorter than twice the inter-plane distance. The reflection occurs only for certain angles of incidence, which allows the identification of the participating crystal plane and thus the crystal orientation.

In the case of polycrystalline materials with randomly oriented crystallites the orientation distribution of the sample is extracted by looking at the reflected intensity of a certain plane as a function of the Euler angles ω and ϕ which set the orientation of the sample relative to the incident light.

The Bragg condition given by equation (35) determines the incident angle θ on a crystal plane for which constructive interference of elasticly scattered light is given, with d_{hkl} the distance of the (hkl)-crystal planes, λ the wavelength of the incident light and n an arbitrary integer number. The wavelength is constrained to $\lambda < 2d$ to meet the Bragg condition.

$$2d_{hkl}\,\sin\theta = n\lambda \tag{35}$$

The scattering amplitude for a crystal plane (hkl) is related to the structure factor S of the lattice by

$$I \;\propto\; N^2 S^2 \tag{36}$$

$$S \;=\; \sum_j f_j e^{i\vec{r}_j\cdot\vec{G}} \tag{37}$$

where the sum is over all atoms j at $\vec{r}_j$ in one unit cell with the atomic form factor f_j. The vector $\vec{G}$ is the reciprocal lattice vector to the scattering plane (hkl) and N is the number of participating unit cells. The atomic form factor f_j is defined as

$$f_j = \int n_j(\vec{r}) e^{i\vec{G}\cdot\vec{r}}\;\mathrm{d}^3\vec{r} \tag{38}$$

with n_j the electron concentration of the atom.

The arrangement of atoms in the unit cell of the diamond lattice leads to selection rules of allowed diffraction patterns. The rules can be deduced [20] from equation (37) and the structure of the lattice. The selection rules are

[6]The author likes to thank M. Zeitler from the Universität Augsburg, Germany, for providing the measurements

[7]The author wishes to acknowledge T. Wroblewski, HASYLAB, for providing the technical infrastructure and support.

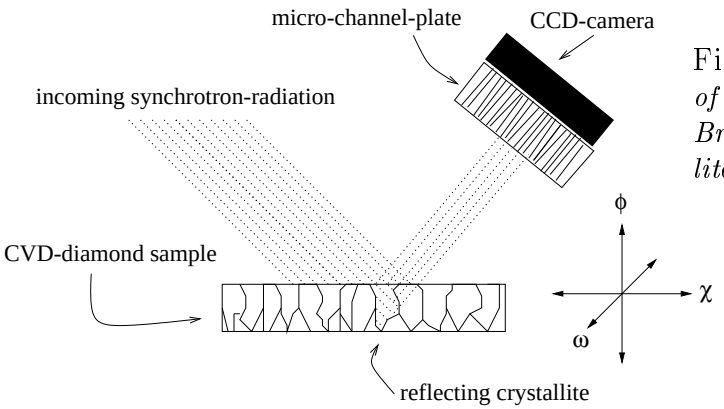

Figure 15: *Schematic view of the set-up to measure Bragg reflections and crystallite shapes spatially resolved.*

- $h + k + l = 4m$, h, k, and l are even, m is an integer.
- h, k and l are odd.

where a reflection occurs if one of the two rules is satisfied.

In the experiment the [220]-reflection, allowed according to the first selection rule, was used. The [220]-reflection has a 12-fold symmetry given by the four-fold symmetry of the plane diagonal $(++, +-, -+, --)$ in each of the three planes [220], [202], [022].

4.3.2 Set-up

A schematic view of the setup for measuring spatially resolved Bragg-reflections is shown in figure 15. A parallel white beam from a synchrotron light source passes through a silicon monochromator, resulting in a monochromatic beam with an energy width of $\approx 0.1\%$. The beam is directed at the diamond sample and will be reflected by crystallites fulfilling the Bragg condition. The reflections are detected with a resolution of 24 μm by a combination of a CCD-camera and a micro-channel-plate sitting on a movable arm [54]. The image in the CCD-camera is a direct projection of the single crystallite reflecting the light. The absorption length for 10 keV photons is about 1.4 mm, therefore thin samples are almost transparent and the whole crystallite in the sample can be seen. The method allows information of the shape of single crystallites within the sample to be obtained non-destructively.

The sample is mounted on a goniometer and can be moved in the angles ϕ, ω and χ, so the reflections in different solid angles can be recorded. The angle θ of the Bragg condition is set by adjusting the CCD camera position relative to the beam. The exposure time to obtain an image of the reflections is about 2 seconds. The cycle time of exposing, saving the image and setting the new position of the goniometer is about 10 seconds. The angular resolution of the setup is approximately 0.0025°, dominated by the diameter of the capillaries of the micro-channel-plate. The distance between camera and the sample was about

Name	d[μm]	shape	A[cm^2]	N[#]
DS1	315	□	0.5	88
DS2	312	□	0.5	98
NDF01	300	□	1	118
A3132A	123	◯	1.5	617
MC	300	-	-	999

Table 4: *Some characteristics of the investigated diamond samples, with d the thickness, A the area and N the number of individual crystallites found in [220] reflection within the scanned region in ω and χ as described in the text. The sample MC is a Monte Carlo data sample.*

$l = 10$ cm. The capillaries are arranged in a grid with 24 μm spacing which is large compared to the angular error on the spatial resolution of $l \cdot \cos(0.0025^\circ) = 4.3$ μm.

Since it would take several days to scan the necessary solid angle to get at least one reflection of every crystallite using the 12-fold symmetry of the [220] reflection the scan was limited to a smaller angular region. To be sure that the recorded data sample is of statistical relevance, it was checked with an X-ray diffractometer measurement over half the solid angle that the investigated diamond samples have no preferred orientation.

The set-up of the X-ray diffractometer is in principle the same as for the measurement of spatially resolved Bragg reflections. The beam source was an X-ray tube providing 8 keV photons with a beam spot size of 1 mm. The scattered light was detected with a scintillator and a photo-multiplier tube. A full scan of π in the Euler angle ϕ and 2π in ω could be recorded in less than 10 h.

4.3.3 Results and Discussion

Statistical samples of reflections from crystallites were obtained for four samples, allowing their shape, size and width to be investigated. Table 4 lists the samples with some of their properties.

A typical picture recorded with the CCD camera on a polycrystalline CVD diamond sample on the [220] reflection is shown in figure 16. The grey areas correspond to single crystallites which fulfil the Bragg condition. The shape of the areas are a direct image of the crystallite shape. The projection angle of the crystallites is given approximately by the Bragg angle, being in this arrangement ($E = 10$ keV, $d_{220} = 1.26$ $\mathring{A}$) $\theta = 23.3^\circ$.

A systematic error is introduced by over-exposure of the CCD camera. Over-exposure leads to cross-talk of pixel elements in the same row. As a result the structure seems to be wider along the row direction, which is perpendicular to

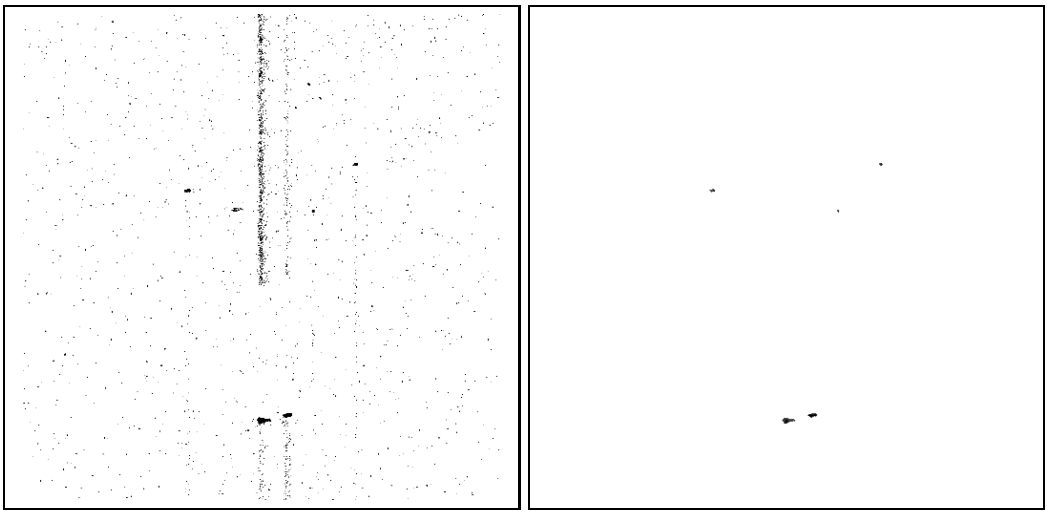

(a) Raw image. (b) Filtered image.

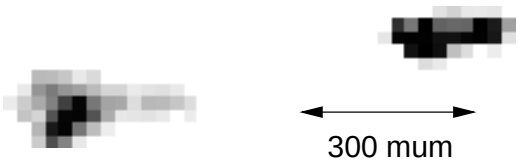

(c) Enlarged view of two crystallites.

Figure 16: *Typical data recorded with set-up to measure spatially resolved Bragg reflections on a polycrystalline CVD diamond sample NFD01 in the [220] reflection.*

the direction of crystallite growth. The effect could be reduced by cutting out extended stripes but was not eliminated.

An angular range of 1.525° in the angle ω and 0.704° in χ has been scanned with a step size of 0.025° and 0.064°, respectively. For each position an image of the reflections was recorded and analysed for cluster structures, which were interpreted as reflections of single crystallites. Typically the same crystallites appeared on a series of pictures due to the finite reflection width, which allowed the intensity to be traced and the optimum position for the cluster reconstruction to be selected.

After the identification of clusters the data were corrected for the projection angle which was equivalent to the Bragg angle. The projection correction required the assumption that the crystallites are growing perpendicular to the surface. SEM studies (section 4.1) showed the validity of this assumption. The discrete clusters were extracted from the image data and the shape was analysed. In

addition to the experimental data a Monte Carlo data sample from a simulation of crystal growth (see section 7.1) was used for comparison.

In figure 17 the distribution of the crystallite lengths is shown for the four samples investigated. A broad distribution is measured for all samples. The maximum length of a crystallite is restricted by the sample thickness. The end-points of the distributions, i. e. the largest length of a single crystallite, are within the measurement precision compatible with the thickness of the samples. Crystallites near the endpoint are likely to have continuously grown from substrate to growth side as their length is approximately equal to the sample thickness.

The distribution of the width is also shown in figure 17. The end-point of the width distribution is affected by artifacts of the measurement discussed above. The width distribution has thus a long tail towards unphysical high values.

To obtain information about the characteristic shape of crystallites a cut was introduced to retain only crystallites with a length of greater than 90% of the sample thickness. This cut ensured the selection of crystallites which were likely to have continously grown throughout the growth process and were not overgrown by neighbouring crystallites. Clusters passing this cut were further analysed, studying the dependence of the cluster width on the position along the cluster length.

The clusters were normalised to their width and length. The width dependence on the length was averaged over all clusters. For continously growing crystallites an increase of the width along the length (i. e. thickness of the film) from substrate to growth side is expected because of lateral over-growth of neighbours. The average dependence of the normalised width on the position along the normalised crystallite length was determined by

$$\langle \Delta x'(z') \rangle = \frac{1}{N} \sum_{i=1}^{N} \Delta x(z' \cdot d^i) \cdot \frac{1}{w^i}, \tag{39}$$

with $\langle \Delta x'(z') \rangle$ the averaged dependence of the normalised width on the normalised length z', N the number of crystallites, $\Delta x(z)$ the width at z of the i-th crystallite, d^i and w^i the length and width of the i-th crystallite. The definition of variables is illustrated in figure 18. In the simple case of a triangular shape $\langle \Delta x'(z') \rangle$ would be linear with $\langle \Delta x'(0) \rangle = 0$ and $\langle \Delta x'(1) \rangle = 1$, while in the case of a box $\langle \Delta x' \rangle = 1$ would be a constant and independent of z'.

The result is depicted in figure 19. For three samples an increase of the normalised width with increasing length is observed for $z' < 0.7$. For $z' > 0.7$ a sharp drop of $\langle \Delta x'(z') \rangle$ is present. This is primarily due to the finite resolution of the experiment but also due to the tilt of the crystallite. A reliable determination of the gradient of $\langle \Delta x'(z') \rangle$ is difficult because of the poor resolution of ≈ 24 μm and the systematic uncertainty introduced by the artifacts. The different behaviour of $\langle \Delta x'(z') \rangle$ for sample A3132A is explained by its thickness of only 123 μm which decreases the significance of the measurement.

The analysis of a Monte Carlo (MC) data sample generated by an algorithm discussed in section 7.1 with $\kappa_l = 0.2$ resulted in similar features, as depicted in figure 20. The $\langle \Delta x'(z') \rangle$ dependence is monotonically increasing from 0 to 1 as a result of the model assumptions and the "perfect measurement" of the crystallite structure without systematics and a resolution of 1 μm. Furthermore the projected crystallites in the MC sample are not tilted and have a flat top.

The distributions of d^i and w^i show a similar shape to the experimental data. When comparing d^i of the MC sample with experimental data the lowest bin containing $d^i < 50$ μm has to be neglected, because crystallites of this small size were not detected since the reflection intensity was too weak.

Conclusion

A method was presented to determine the shape of single crystallites within a CVD diamond sample non-destructively. In conclusion, evidence for a pyramidally shaped columnar structure of CVD diamond has been demonstrated. The experimental data agrees within the uncertainty of the measurement with a growth model proposed in section 7.1.

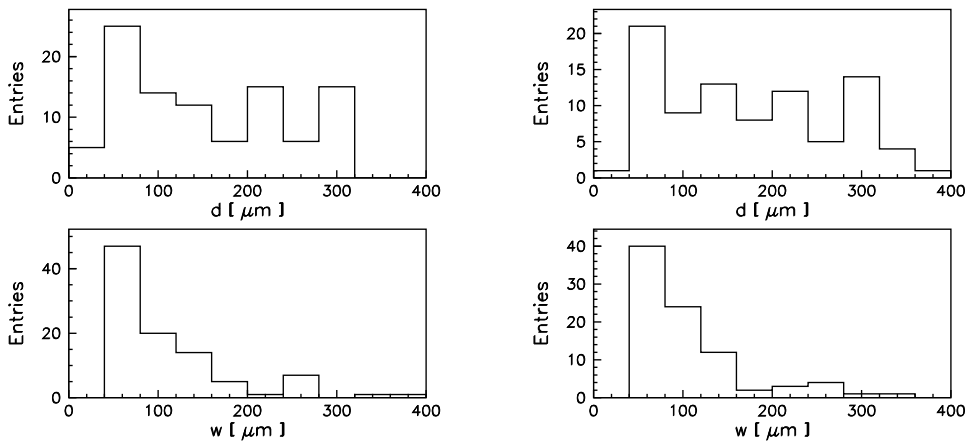

(a) Sample DS1

(b) Sample DS2

(c) Sample NFD01

(d) Sample A3132A

Figure 17: *Distribution of the length, d, and width, w, for the four investigated samples.*

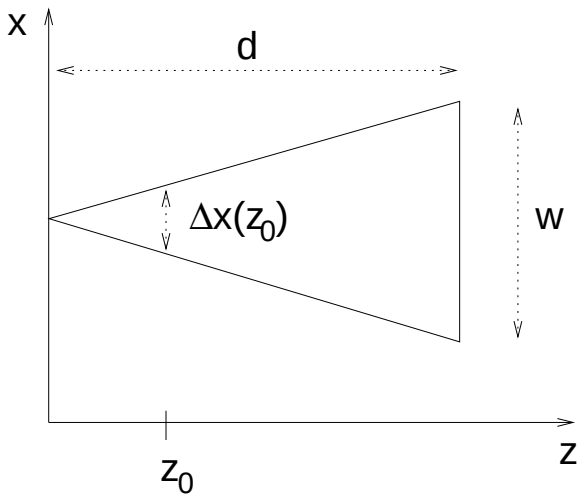

Figure 18: *Definition of the variables used for the shape analysis of crystallites.*

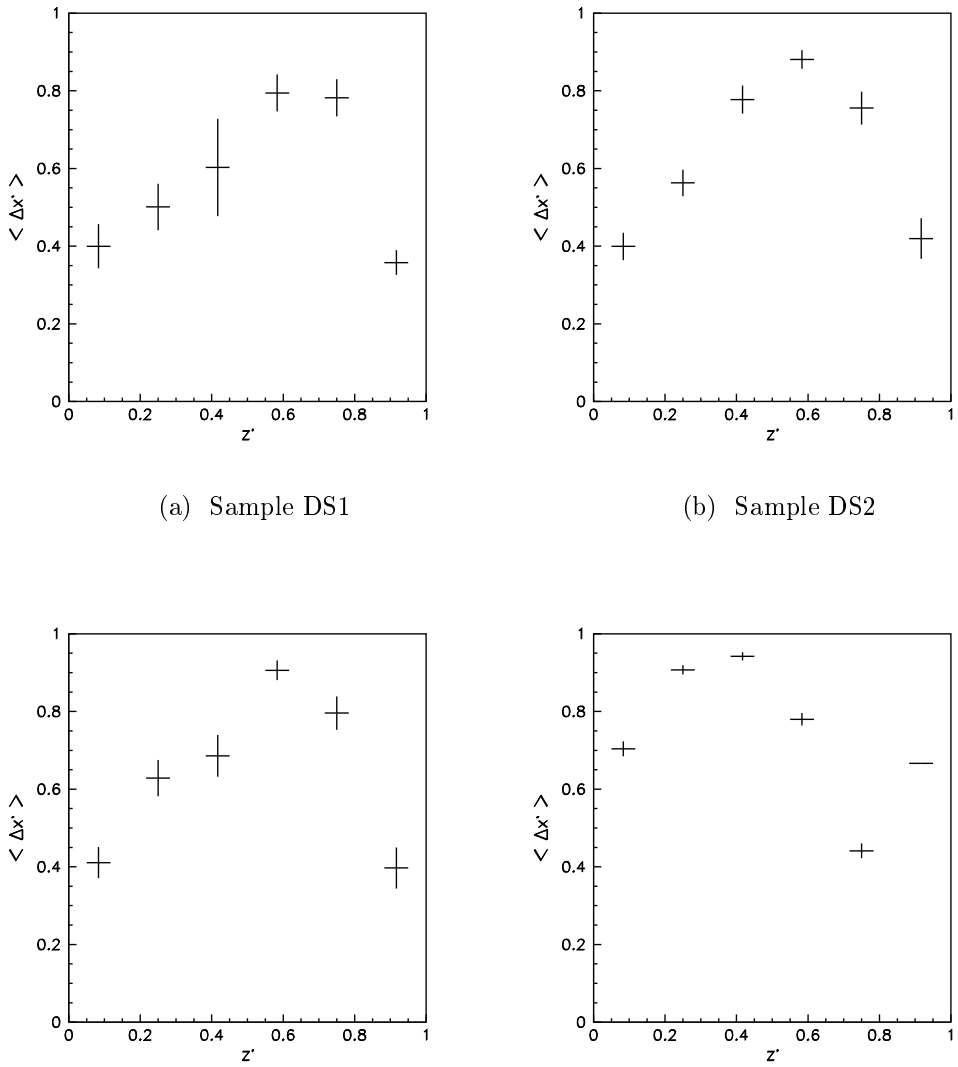

(a) Sample DS1

(b) Sample DS2

(c) Sample NDF01

(d) Sample A3132A

Figure 19: *Averaged dependence of the normalised width* $\langle \Delta x'(z') \rangle$ *on the normalised length* z' *for the four investigated samples.*

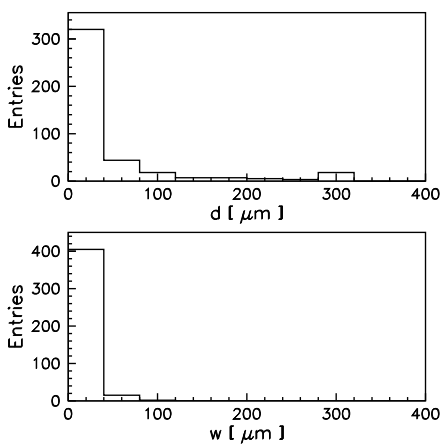

(a) Distribution of the length, d, and width, w for the MC sample.

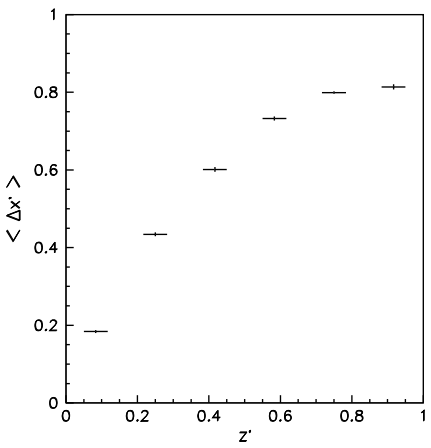

(b) Averaged dependence of the normalised width $\langle \Delta x'(z') \rangle$ on the normalised length z' for the MC sample.

Figure 20: *Results obtained with a Monte Carlo sample (MC) generated with an algorithm discussed in section 7.1.*

4.4 Secondary Ion Mass Spectroscopy

In collaboration with the Fraunhofer Institut für Schicht- und Oberflächentechnik (FhGIST), Braunschweig, secondary ion mass spectroscopy (SIMS) was used to investigate the concentrations of chemical impurity on diamond samples produced by FhGIST for detector applications. Chemical impurities can act as trapping and recombination centres. Thus the determination of impurity levels and distributions in the presence of grains and grain boundaries is important for the application of CVD diamond as a detector material.

The SIMS technique uses an ion beam, e. g. Ar, to sputter atoms off the specimen. A small part of the sputtered atoms are ionised and detected with a mass spectrometer. The method is inherently destructive but allows to determine impurities at the ppm level. As well as the possibility to measure depth profiles of impurity concentration by sputtering over a long period, the beam spot size can also be reduced to a few μm and scanned across the sample to obtain impurity concentrations spatially resolved.

4.4.1 Results

For some samples the impurity concentrations were determined by secondary ion mass spectroscopy (SIMS) depth profiles with a detection spot size of 120 μm and a detection depth of 700 nm. To exclude surface contributions to the SIMS signal pre-sputtering with a depth of 80 nm to 100 nm was used. Typical impurity levels were 2000 ppmat O, 1000 ppmat H and 30 ppmat N. The concentration of O and H atoms was relatively high.

A spatially resolved SIMS profile recorded on one sample with a lateral resolution of about 10 μm and a detection spot size of about 10 μm showed that O and H impurities at grain boundaries are at least ten times higher than within grains. The N concentration at grain boundaries is even more enhanced by a factor of at least 30 compared to the in-grain N concentration. A SIMS profile for the growth side of the detector material sample with calibrated SIMS signals is shown in figure 21 together with that of a reference sample for which the average grain size is 5 μm and therefore smaller than the spatial resolution of the SIMS scan. The scan of the reference material shows a flat distribution while the SIMS profile of the detector material sample is characterised by significant variations of the impurity concentration. The variations have a distinct peak structure. The peaks of the N, H, O concentration are highly correlated and the typical distances between two peaks corresponds to the typical grain size of 70 μm as determined with SEM-pictures. However no direct correlation of the SIMS signal with the surface topography could be made. The findings agree with results reported in [55], where a higher concentration of impurities was found in the region between grains than within grains.

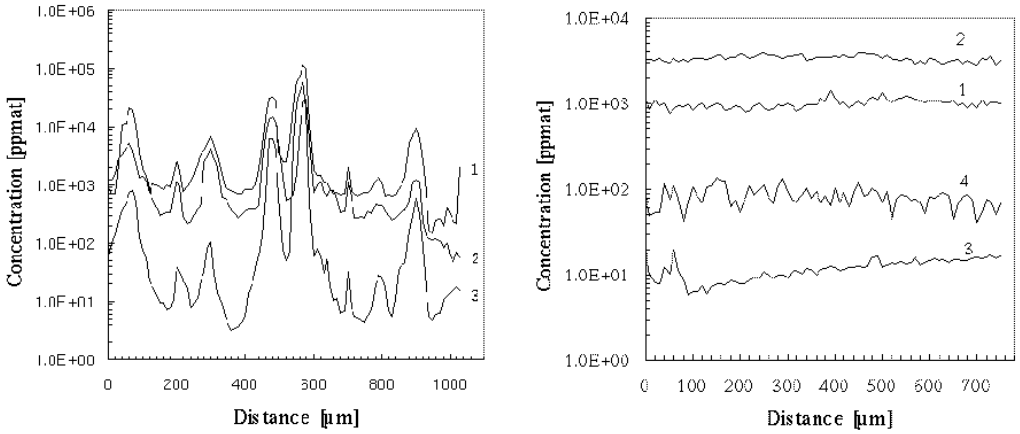

(a) Detector material (b) Reference material

Figure 21: *Spatially resolved SIMS of a detector material (a) and a reference sample (b) with calibrated SIMS signal. Impurity levels detected in the detector material are oxygen (1), hydrogen (2) and nitrogen (3). For the reference sample additionally boron (4) levels are shown. The spatial resolution is about* 10 μm.

4.5 I-V-Characteristic

The measurement of the current-voltage-characteristic (I-V-characteristic) was used to determine the contact properties of metallised CVD diamond samples and their electrical resistivity. The measurement of other electrical properties such as the collection efficiency and the priming behaviour was only possible if the resistance of the sample was above $\approx$ 1 GΩ. For smaller resistances the leakage current introduced excessive noise preventing a meaningful measurement. The I-V-characteristic served as a first quality check of the samples, which were metallised on the growth and substrate side.

The I-V-characteristics were measured at room temperature in the dark. The typically high resistance of the samples required a settle time (about 2 min.) after the voltage was applied to get a stable and reproducible measurement and discard fake current measurements caused by the charge-up of stray capacitance in the system. Since no guard ring structure was applied, no distinction was possible between current flowing through the bulk and over the surface.

Ohmic I-V-characteristics are governed by Ohm's law

$$\vec{j} = \rho^{-1}\vec{E} \tag{40}$$

with $\vec{j}$ the current density, $\vec{E}$ the electric field and ρ the resistivity. The current is linearly dependent on the electric field. Typically ohmic I-V-characteristics

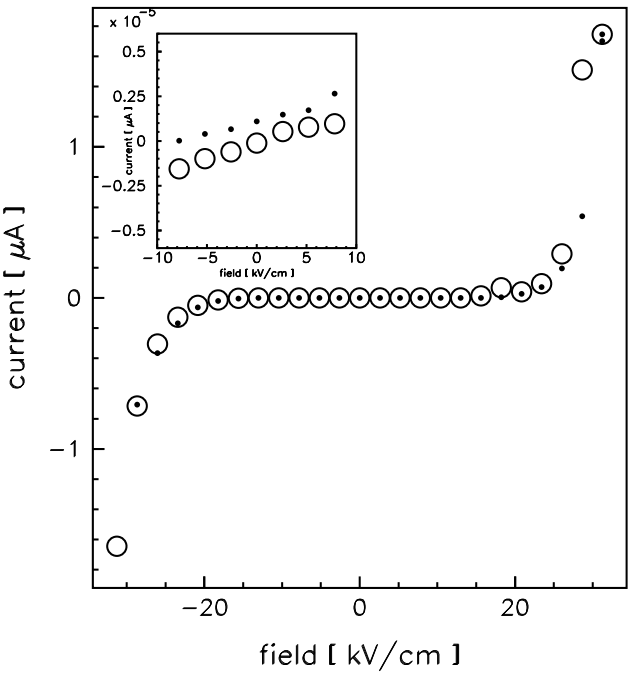

Figure 22: *Typical I-V-characteristic of a CVD diamond sample with dot contacts on growth and substrate side. Dots denote the measurement for ramping the voltage up and open circles for ramping down. The linear low-field region ($E < 10$ kV cm^{-1}) is used for determination of the resistivity ρ. The insert shows the low field region.*

were observed in the low field regime ($E < 10$ kV cm^{-1}) from which the values for ρ were deduced. At high electrical fields a supra-linear I-V-characteristic is commonly observed with CVD diamond. The origin of this effect is not clear.

4.5.1 Results

A typical I-V-characteristic of a CVD diamond sample with dot contacts on growth and substrate side is shown in figure 22. The I-V curves were measured a first time by ramping from negative to positive voltage (upward) , and a second time by ramping the voltage from positive to negative values (downward). A slight off-set for upward and downward measurement was observed, which is probably due to stray capacitances. A linear behaviour of the I-V-curve for the low field region ($E < 10$ kV cm^{-1}) is observed. From this part the resistivity has been determined for this particular sample to be $\rho = 12 \cdot 10^{12}$ Ω cm, which represents a typical value. Towards the high field region the curve shows a supra-linear behaviour, similar to a soft breakdown. Some samples were found to emit blue light visible with the naked eye at field $E > 10^4$ kV cm^{-1}. This phenomenon has been also been reported in [55] and is attributed to radiative recombination of injected charge carriers at defect sites.

Samples with a symmetric I-V-characteristic as shown in the plot are generally defined to have *ohmic* contacts, although two rectifying contacts would also result in a symmetric I-V-characteristic.

An example of a non-ohmic, i. e. asymmetric, I-V-characteristic is shown in

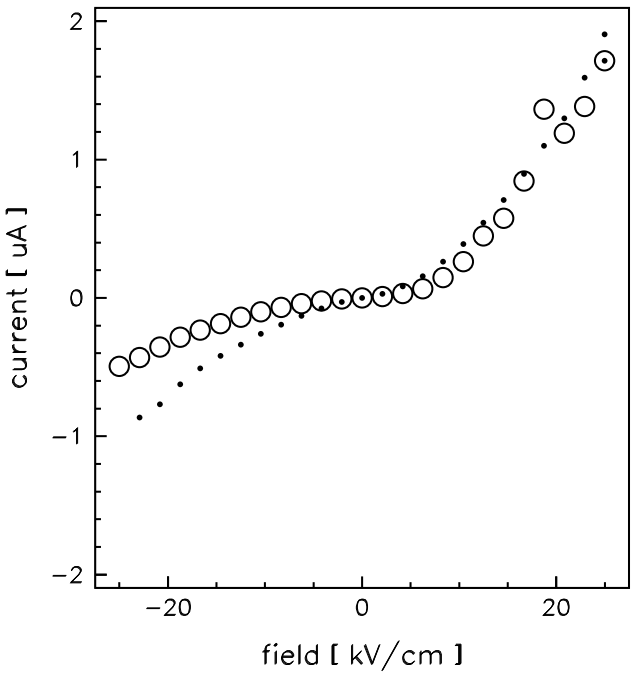

Figure 23: *Asymmetric I-V-characteristic of a CVD diamond sample with a high sp^2 content.*

figure 23. The particular sample had a grayish colour pointing to a high content of non-diamond phases. The I-V-curve is typical for a rectifying contact. A possible explanation is that the contact properties at growth and substrate side are different due to different sp^2 concentrations.

4.6 Beta Particles

The average charge collection properties of the diamond samples have been investigated using beta particles. Since they traverse the detector, they probe the charge collection efficiency, ϵ_Q, along the particle trajectory, and allow for a measurement averaged over the detector thickness. This method is widely used to characterise diamond samples, since it corresponds most closely to the situation of a position sensitive vertex detector application in a collider experiment.

The collection efficiency ϵ_{Q} is given by

$$\epsilon_{\mathrm{Q}} = \frac{Q_{\mathrm{m}}}{\rho_{mip} \cdot d}, \tag{41}$$

where d is the diamond thickness in μm, Q_{m} the average charge induced on the electrodes of the diamond detector, and $\rho_{mip} = 36$ eh $\mu\mathrm{m}^{-1}$ the ionisation density of a MIP. The collection efficiency ϵ_Q can also be expressed with the quantity collection distance, δ_Q, as

$$\epsilon_Q = \delta_Q / d \tag{42}$$

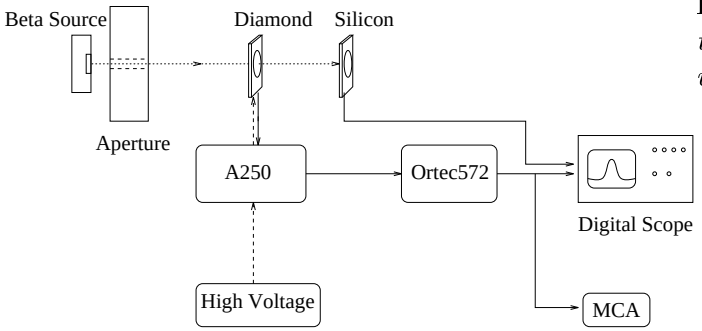

Figure 24: *Schematic view of the set-up for measurements with beta particles.*

with the detector thickness d. The dependence of the quantities δ_Q and ϵ_Q on the electric field strength E (see section 3.3) and the saturation values have been studied.

The signal distribution of the collected charge is governed by statistical fluctuations of the deposited charge and by variations of the charge collection efficiency, ϵ_Q, on the sample. If the statistical fluctuations of the charge deposition are known it is possible to obtain information about the variation of ϵ_Q. The method is shown for one sample and compared to results of other methods to measure the same quantity.

The dependence of ϵ_Q on the absorbed radiation dose has also been studied. The priming effect of uniformly ionising radiation has been established, and the characteristic priming dose constant Φ_0 has been derived.

4.6.1 Set-up

A ^{90}Sr beta source (114 μCi) provided beta particles with a maximum energy of 2.28 MeV. The beta particles were collimated by a 1 mm aperture in a Plexiglas block. The diamond was placed in the collimated beam of beta particles followed by a silicon detector which was used as a trigger device. A diagram of the experimental set-up is shown in figure 24.

The aperture ensured that all beta particles traversed the sensitive region of the diamond-detector. After having traversed the diamond, the beta particles had to deposit sufficient energy ($>$ 100 keV) in the silicon-detector to be accepted as an event. The trigger-rate was limited by the data acquisition system to about 15 Hz.

The charge was measured with a charge-integrating amplifier Amptek A250 followed by a shaping-amplifier Ortec 572 with a shaping-time constant of $\tau =$ 3 μs. The signal was read out with a digital scope and averaged over 3000 events. Additionally, the signal was recorded with a multi channel analyser (MCA).

The characteristic energy-loss of the beta particles in the diamond is approximately that of minimum ionising particles (MIPs) which on average produce $\rho_{mip} = 36$ electron-hole-pairs μm^{-1} in diamond (see section 2.1.1). The difference

in ionisation density between beta particles from ^{90}Sr and MIPs was estimated by convoluting the energy spectrum of the beta particles with the average charge deposited in a $d = 300$ μm thick diamond according to the Bethe-Bloch formula using in the restricted energy loss mode (equation 5 on page 6). The energy loss for electrons in diamond was modelled after experimental values for $\mathrm{d}E/\mathrm{d}x$ from [56], including radiative energy losses. Multiple scattering was not included in the estimation. As in the experimental set-up only beta-particles which retained an energy of greater than 100 keV were considered. The estimation gave an average ionisation density of $\rho_{mip}(^{90}\mathrm{Sr}) = 37.9$ electron-hole-pairs $\mu\mathrm{m}^{-1}$, which is about 5% higher than the value for MIPs of 36 electron-hole-pairs $\mu\mathrm{m}^{-1}$. It is reported in [33] that the signal induced by beta particles is on average 8% higher than that of MIPs, which is in qualitative agreement with the calculation.

It is known that the exposure of diamond to ionising radiation and UV-light can substantially increase ϵ_Q. This phenomenon is called priming [52] (see section 3.4). To measure the change of ϵ_Q under ionising radiation, i. e. the priming behaviour, a dedicated experiment was done where samples could alternately be exposed to a strong ^{90}Sr source (1300 μCi) without applying a voltage and to the ^{90}Sr source (114 μCi) described above to measure ϵ_Q. In this set-up the sample was mounted on a movable stand which drove the sample to the radiation position and the measurement position.

4.6.2 Results

The discussion will concentrate on two typical samples A and B. Basic properties of the samples are listed in table 5.

Producer	Name	Process	v_g[μm/ h]	d [μm]	ρ [Ω cm]
Norton	A	DCAJ	no information	300	7×10^{13}
FhGIST	B	MWP	1.3	123	6.4×10^{14}

Table 5: *Properties of the investigated samples. v_g stands for growth rate, d for film thickness and R for the resistivity. DCAJ stands for* direct current arc jet process *and MWPR for* micro wave plasma reactor process.

The charge collection efficiency ϵ_Q as a function of the field strength E (fig. 25) typically exhibits a sharp rise with E up to about 1 kV/cm. At higher field strengths, the curve flattens. This effect is also seen in natural type IIa diamond and is attributed to enhanced phonon creation, resulting in a decreased mobility (see section 3.3). Above an applied voltage of $U_\mathrm{b} = 250$ V, the signal became noisy for these particular samples, because the leakage current increased. As the corresponding field strengths differ by a factor 2.4 this is taken as an indication of surface currents.

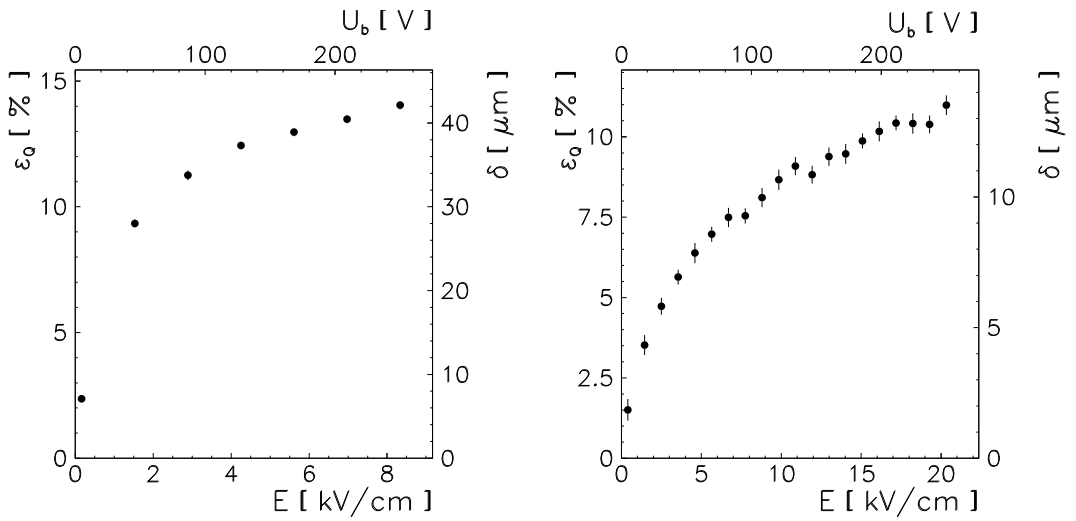

Figure 25: *The dependence of charge collection efficiency ϵ_{Q} on the electric field E for unprimed sample A (a) and sample B (b). The equivalent collection distance δ_Q is given on the right scale, the bias voltage U_b on the upper scale.*

The Priming Effect

Priming was observed when samples were irradiated with beta particles. In fig. 26, ϵ_{Q} is shown as a function of the absorbed dose for three different field strengths at a dose rate of $\mathrm{d}\Phi/\mathrm{d}t = 14.3$ rad h^{-1} for two samples A and B. The initial drop of ϵ_{Q} on sample B is suspected to be due to polarisation effects. The same behaviour has been observed for sample A at 0.4 kV/cm and 4.3 kV/cm. A function of the form

$$\delta_Q(\Phi) = \delta_{Q,0} + \delta_{Q,+}\left(1 - \exp\left(-\frac{\Phi}{\Phi_0}\right)\right) \tag{43}$$

was fitted to the monotonically rising part of the data. The parameters are $\delta_{Q,0}$ the unprimed value of the collection distance, $\delta_{Q,+}$ the increment of the collection distance through priming and Φ_0 the *priming-dose constant.*

The primed ($\epsilon_p = (\delta_{Q,+} + \delta_{Q,0})/d$) and unprimed ($\epsilon_u = \delta_{Q,0}/d$) efficiencies, the ratio of primed over unprimed efficiency ($R_p = \epsilon_p/\epsilon_u = 1 + (\delta_{Q,+}/\delta_{Q,0})$), and Φ_0 for the two samples are summarised in tab. 6. The errors given are statistical. The value of $\mathrm{R_p}$ is compatible for the two samples, whereas Φ_0 is significantly different.

The primed state of the diamonds was found to be stable for days. The diamonds can be reset to the unprimed state by illumination with visible light

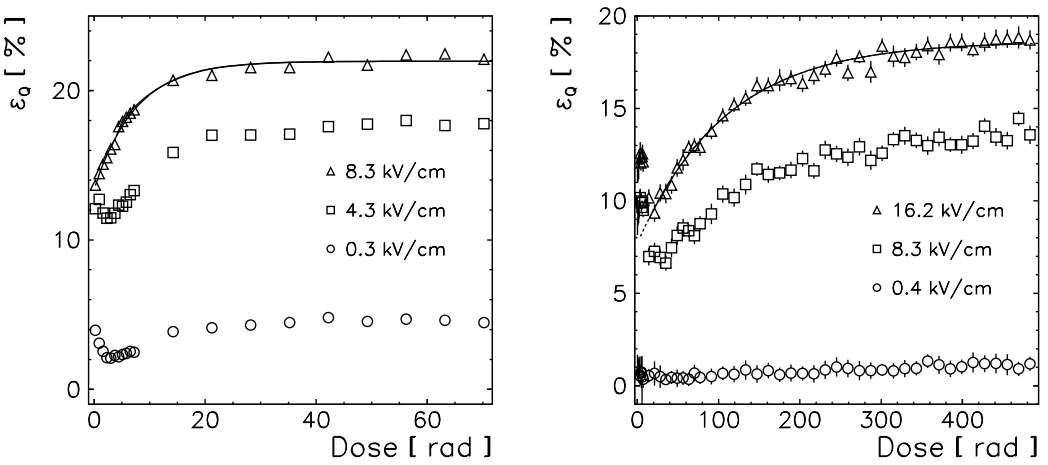

(a) (b)

Figure 26: *The charge collection efficiency ϵ_Q as a function of the absorbed dose for sample A (a) and sample B (b) at different field strengths. The fit function (43) is also drawn.*

name	$\epsilon_u[\%]$, unprimed	$\epsilon_p[\%]$, primed	Φ_0 [rad]	ratio ϵ_p/ϵ_u
A	13.7 ± 0.3	22.3 ± 0.4	7.4 ± 0.5	1.63 ± 0.04
B	11.4 ± 0.4	18.7 ± 0.5	108.6 ± 8.8	1.64 ± 0.06

Table 6: *Summary of the collection efficiencies measured in the primed and unprimed state as well as the priming dose Φ_0 and the ratio of the collection efficiency in the primed to unprimed state.*

or heating to about 540 K. IR-light was found to have no effect on the primed state. UV-light with a spectrum extending to about 5 eV did not show this reset effect, but instead a caused priming effect on the diamonds. The observations are in accordance with spectroscopic defect investigations presented in section 4.11.

Uniformity of the Charge Collection Efficiency

The method discussed provides no spatial information and thus does not allow to measure ϵ_Q spatially resolved. As an alternative the width of the pulse spectrum in conjunction with theoretical predictions were used to estimate the uniformity of ϵ_Q.

A pulse-spectrum of sample A in the primed state, recorded at $E = 8.3$ kV/cm, is shown in fig. 27. By fitting the spectrum with a function, which is based upon the theoretically expected shape and allows for a Gaussian distribution of ϵ_{Q}, information about the width of ϵ_{Q} can be obtained.

The Landau distribution is a description for the pulse spectrum of MIPs in thin detectors. It does not place a limit on the maximum energy transfer and thus is only a rough approximation for beta particles with a maximum energy of 2.28 MeV as used in this experiment. A description with a finite maximum energy transfer was derived by Vavilov [11], taking into account the particle velocity, β, and the ratio of the mean energy loss of the particle in the target and the maximum allowed energy transfer, κ, in a single collision with an atomic electron.

To fit the pulse spectrum, an implementation of this more accurate Vavilov distribution [57], $V(ax' + b, \kappa, \beta)$, was used where a is a scaling parameter and b is an offset parameter. To account for electronic noise and possible intrinsic variations of ϵ_{Q}, the Vavilov distribution has been folded with a Gaussian, $P(a(x - x') + b, a\sigma)$, with a width σ. The complete fit function is given by

$$f(x) = A \int V(ax' + b, \kappa, \beta) P(a(x' - x) + b, a\sigma)\ \mathrm{d}x' \tag{44}$$

with A being a normalisation factor. For the fit, $\kappa = 0.09$, and $\beta = v/c = 0.95$ were used. The values are motivated by the assumption that the average energy of the beta particles contributing to the spectrum was $\bar{E}_\beta = 1.7$ MeV. The maximum energy transfer was taken to $E_{\max} \approx 1.6$ MeV since an energy of about 100 keV is required to trigger an event in the silicon detector. The mean energy loss in the diamond is approximately given by the specific energy loss of a MIP in diamond. For a diamond with a thickness of $d = 300\ \mu$m, the mean energy loss is $E_{\mathrm{mean}} \approx 140$ keV.

The width of the Gaussian, as well as the mean b, the normalisation A and a scaling parameter a are free variables in the fit. The fit results in a width of the Gaussian of $\sigma_{\mathrm{tot}} = 490$ e with χ^2/dof of 1.02. To determine the systematic uncertainty of the fit κ and β were varied for $0.07 < \kappa < 0.15$ and $0.86 < \beta < 0.96$ to cover the energy range for 1.0 MeV $< \bar{E}_\beta <$ 2.0 MeV. This resulted in a systematic uncertainty on σ_{tot} of $(^{+30}_{-76})$ e. The electronic noise was determined to be $\sigma_{\mathrm{elec.}} = 250$ e, thus, the intrinsic broadening of ϵ_{Q} is given by

$$\sigma_Q = \sqrt{\sigma^2_{\mathrm{tot}} - \sigma^2_{\mathrm{elec}}} = (421^{+30}_{-76})\ \mathrm{e}$$

or expressed in charge collection efficiency

$$\sigma_Q = \frac{(421^{+30}_{-76})\ \mathrm{e}}{\rho_{mip} \cdot d} = (4.0^{+0.3}_{-0.7})\%$$

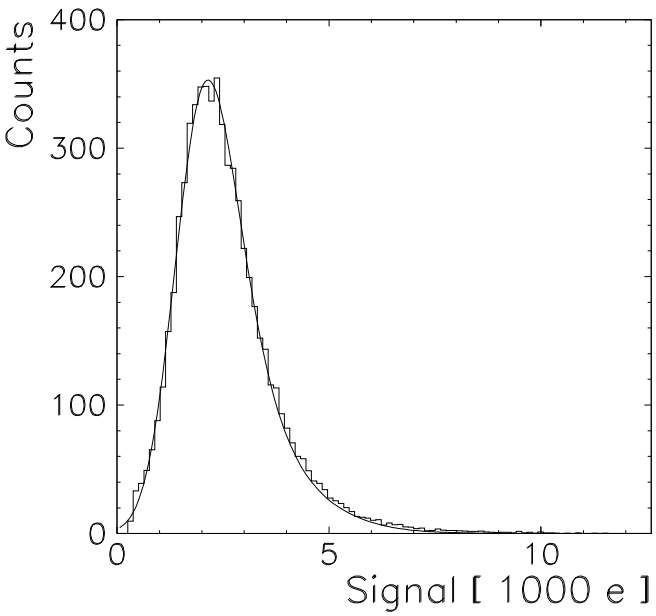

Figure 27: *Pulse spectrum recorded with sample A. Superimposed is a smeared Vavilov distribution fitted to the data as discussed in the text.*

assuming a Gaussian distribution of the broadening. When translated into collection distance using equation (27) on page 24, the width of the intrinsic Gaussian describing the distribution of the collection distance is $\sigma_Q = (11.9^{+0.8}_{-2.1})\ \mu$m.

The computation indicates a relative variation of the collection efficiency, i. e.} collection distance, from its average of 18% at the 1σ level, which cannot be explained by the uncertainty of the fit. This is evidence that ϵ_Q is not a constant of the sample but has a broad distribution. As will be shown in section 4.7 the obtained value for σ_Q is in good agreement with results obtained with spatially resolved measurements.

Conclusion

A method to measure ϵ_Q with beta particles from ^{90}Sr was discussed. The dependence of ϵ_Q on the electrical field strength was shown, and the priming effect was established and parametrised by the priming fluence Φ_0 and the priming ratio R_p. Furthermore the variance of ϵ_Q was determined by fitting the signal spectrum with smeared Vavilov distribution.

4.7 Synchrotron Radiation

For this investigation synchrotron radiation is used in a novel approach to measure the uniformity of the bulk ϵ_Q with a resolution of ≈ 100 μm. To create a uniform ionisation density a narrow beam of 10 keV photons was used. By scanning with the photon beam over the active detection area of CVD diamond samples the average charge collection efficiency ϵ_{Q} is measured spatially resolved. This allows a study of the uniformity of ϵ_{Q} on a scale of about 100 μm.

Photons with an energy of 10 keV interact with diamond predominantly via the photo-effect. When averaged over many photons the ionisation density distribution is given by $\rho_Q(x) = A_0 e^{-\frac{x}{\lambda_0}}$ with λ_0 being the absorption length, x the distance in the material, and A_0 a constant. In diamond $\lambda_0 = 1300$ μm for 10 keV photons and is therefore larger than the thicknesses of the investigated samples of 300 μm $< d <$ 500 μm. In good approximation the resulting ionisation density distribution can be taken as uniform.

4.7.1 Experimental set-up

A 10 keV photon beam from the HASYLAB synchrotron light source at DESY was used to study the charge collection properties of CVD diamond. Monochromatic photons with an energy of $E = (10 \pm 0.5)$ keV were selected using a graphite monochromator. The beam size was reduced with a variable aperture to a spot size of typically 100 μm $\times$ 100 μm.

The beam clock of the synchrotron provided an external trigger source marking the arrival of a photon pulse every 500 ns. The duration of the photon pulses was of the order of picoseconds. The flux per bunch of the monochromatic synchrotron beam was calculated to be in the order of 10^4 γ mm^{-2}. The expected charge deposited in a 300 μm thick diamond was of the order of 10^{-1} pC mm^{-2} per bunch.

The sample was mounted on a movable stand behind the aperture. An electrical field was applied to the diamond sample and the photo-induced signals were amplified and read out with the same read-out chain as described in section 4.6, except that the shaping time was reduced to 500 ns with a shaping amplifier (Ortec 454). The chain was calibrated by injecting a known charge using a test-pulser and a capacitor. The signals of the amplifier chain were averaged over 2048 bunches to improve the signal-to-noise ratio and read-out by a digital oscilloscope controlled by a computer and a customised control program. The same program was used to control a movable stand and monitor the beam-current in the storage ring for off-line correction of the photon fluence. A schematic view of the set-up is shown in fig. 28.

A variety of CVD diamond samples were investigated with this method. For comparison a silicon detector was studied. All measurements were taken at room temperature.

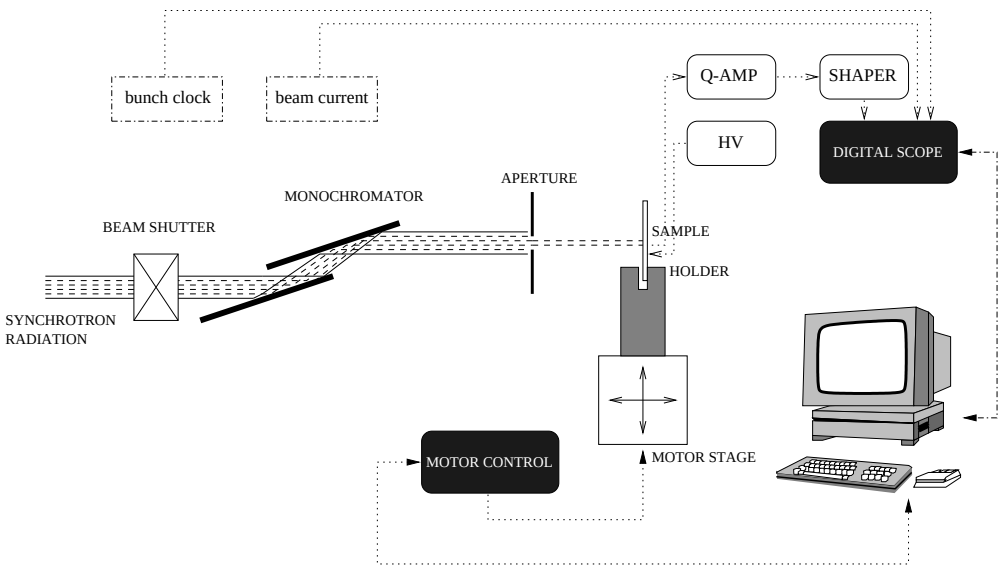

Figure 28: *Schematic view of the set-up for the measurement with synchrotron radiation.*

4.7.2 Results and discussion

The charge signals for different electrical field strengths and for different aperture openings were measured. Fig. 30a shows the induced signal as a function of the applied field for sample A. The dependence is very similar to the results obtained with MIPs (see section 4.6). A steep rise of the signal at small values of E is followed by a flattening of the curve at higher field strengths. However the behaviour is not identical to the shape observed with MIPs which could be due to the five orders of magnitude higher charge production rate.

Three different aperture sizes of approximately 300 μm $\times$ 300 μm, 300 μm $\times$ 100 μm and 100 μm $\times$ 100 μm were used. Within the precision of the aperture adjustment, a linear scaling of the signal with the spot size has been observed (fig. 30b). The signal height is compatible with the magnitude calculated from the photon flux and the charge collection efficiency measured with MIPs (ratio of measured over expected charge signal of ≈ 0.7 at $E = 10$ kV cm^{-1} with $\epsilon_Q = 22.3\%$ as determined in section 4.6). Although no precise absolute values of ϵ_Q could be determined due to the uncertainties in the absolute photon flux, accurate measurements of relative changes of ϵ_Q across the surface of the detector were possible. To translate the charge signal into the quantity ϵ_Q the assumption was made that the charge collection behaviour is similar for 10 keV photons and MIPs. The assumption is plausible since the ionisation density distribution of 10 keV photons is similar to the distribution created by MIPs. Therefore, the mean of the measured distribution of the charge signal was defined to be equal

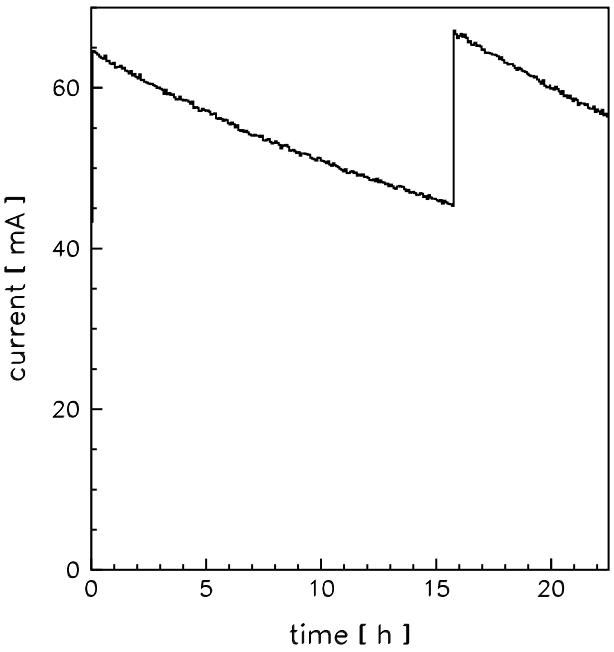

Figure 29: *Example for the change of the current in the storage ring of the synchrotron with time during a measurement period.*

to the ϵ_Q value measured with beta particles, and in this way the set-up was calibrated.

To obtain a spatial map of ϵ_Q, a part of the active area of the samples was scanned with a typical spot size of $\approx 100\ \mu\text{m} \times 100\ \mu\text{m}$ and with a step sizes ranging from 50 μm to 100 μm. At each point, the signal was measured and corrected for the change of photon flux with time, deduced from the beam current in the electron storage ring. A typical example for the development of the current in the storage ring is shown in figure 29.

An example of a map obtained with sample (A), 300 μm thick, is displayed in fig. 31a. The signal heights are encoded using a grey-scale. High signals are represented by dark grey, areas of low signals are marked with a light grey. The metallised part of the sample gives a clear signal, while the non-metallised area shows only the pedestal noise. The light-grey areas on the lower left and right side are caused by absorption from silver paint, which has been used to make an electrical contact to the sample. The spectrum of the signal response on the metallised area is shown in fig. 31b. It represents the distribution of the measured ϵ_Q on the metallisation folded with a contribution due to noise. As discussed above the uncertainties in the photon flux allowed only relative measurements. To translate the signal to the quantity ϵ_Q, the mean of the charge spectrum was set equal to $\epsilon_Q = (22.3 \pm 0.4)\%$ as measured with MIPs (see sec. 4.6). The priming effect, i. e. the increase of ϵ_Q under irradiation, was assumed to have fully saturated. The expected radiation absorption in the photon beam is of the order of 1 krad s^{-1} while the priming dose constant was determined to $\Phi_0 = 7.4 \pm 0.5$ rad (see sec. 4.6), thus the sample should be fully primed in less than 0.1 second. To verify the reproducibility of the measurement

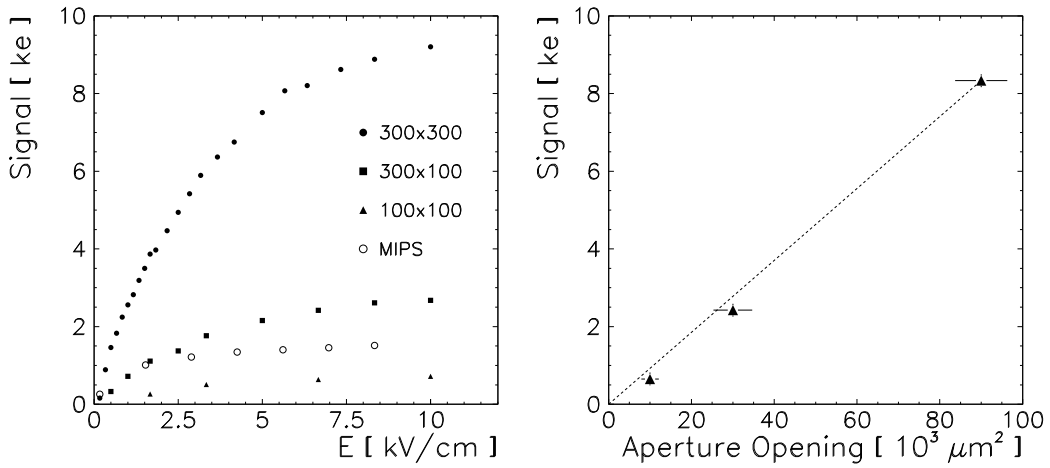

(a) (b)

Figure 30: *(a) X-ray induced signal of the diamond detector vs electrical field strength for three different aperture openings (*300 μm $\times$ 300*mum,* 300 μm $\times$ 100 μm *and* 100 μm $\times$ 100 μm*). For comparison, the signal obtained with MIPs is depicted too. (b) Signal for* $E = 10$ kV/ cm *as a function of the aperture opening. The dashed line indicates the expected progression for a linear behaviour.*

the sample was scanned a second time and a shift was found in the mean of the spectrum by a factor 1.05 which is assigned as a systematic error. The second scan was performed with a step size of 50 μm on a smaller part of the sample and is depicted in figure 32. The reproducibility of the ϵ_Q structure with a higher resolution is clearly visible.

The noise distribution has been estimated from the data by dividing the data sample for each measurement point into 8 subsamples and looking at the spread of the 8 amplitudes determined from the subsamples. The average of the spread is $\sigma_{\text{noise}} = (0.67 \pm 0.03)\%$. To determine the total width of the signal, a Gaussian has been fitted to the distribution. A width of $\sigma_{\text{m}} = (4.37 \pm 0.21)\%$ is obtained from the fit. To extract the intrinsic width of the ϵ_{Q} distribution, the contributions of the noise and the intrinsic variations of ϵ_{Q} were assumed to be Gaussian and the intrinsic width of the ϵ_{Q} distribution was calculated by

$$\sigma_Q = \sqrt{\sigma_{\text{m}}^2 - \left(\frac{\sigma_{\text{noise}}}{\sqrt{8}}\right)^2} = (4.32 \pm 0.22)\%.$$

This value has to be compared with the one obtained with MIPs as discussed in section 4.6, which was $\sigma_Q = (4.0^{+0.3}_{-0.7})\%$. The two methods give values of

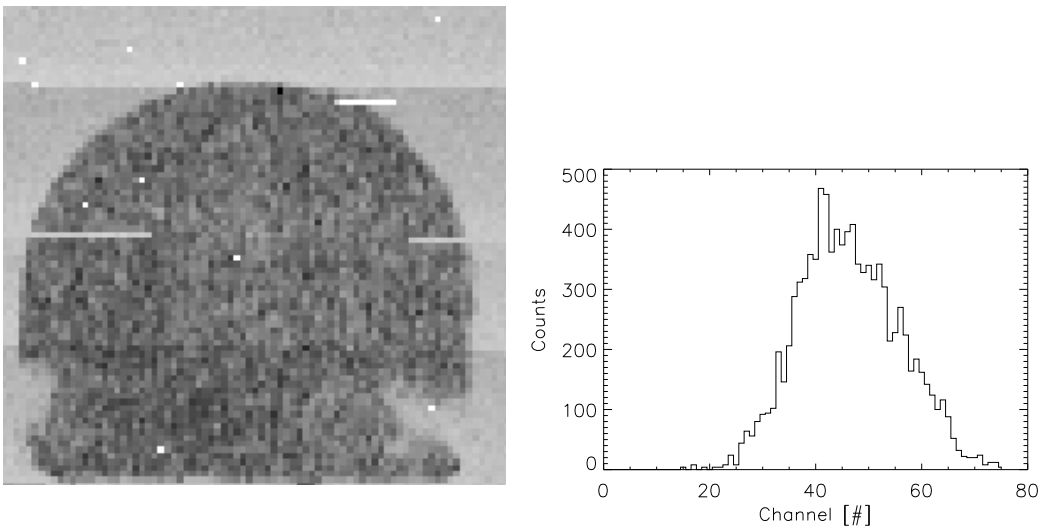

(a) (b)

Figure 31: *(a) Spatially resolved representation of the photo-induced signal measured on sample A at a field strength of E=9 kV/cm at room temperature with a step size of* 100 μm. *The picture represents a region of* 8 mm $\times$ 8 mm. *The white spots and stripes are failures of the DAQ system. (b) Distribution of the photo-induced response signal from the metallised region of the diamond detector.*

σ_Q which are in good agreement. Another way to quantify the degree of non-uniformity is the dimensionless charge collection significance, which is defined as the ratio of the mean ϵ_Q over the width σ_Q,

$$S_Q = \frac{\langle \epsilon_Q \rangle}{\sigma_Q}.$$

It allows to compare the non-uniformity of different samples with different mean charge collection efficiencies. The higher the value of S_Q is the better is the uniformity. Taking this quantity a value of $S_Q = 4.32$ is calculated for sample A. This value is compatible to the values obtained with other CVD diamond samples.

As the measurement with beta-particles was performed with an aperture of 1 mm the variation of σ_Q was calculated as a function of the position of a 1 mm $\times$ 1 mm box, which contained the events used for the calculation of $\sigma_{Q,box}$. Within the statistical error no deviation from the result calculated with full statistics was observed.

A typical result for the spatial variation of ϵ_Q for another 500 μm thick polished CVD diamond (sample DS7) is shown in figure 33a. Two scans of the same

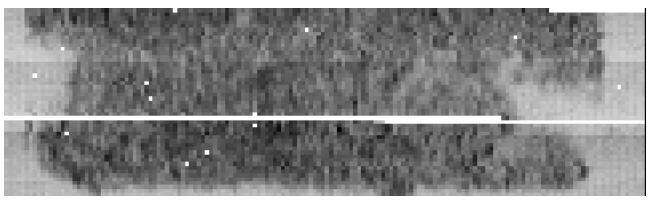

Figure 32: *(a) Spatially resolved representation of the photo-induced signal measured on sample A at a field strength of E=9 kV/cm at room temperature with a step size of* 50 μm. *The picture represents a region of* 8 mm $\times$ 2 mm.

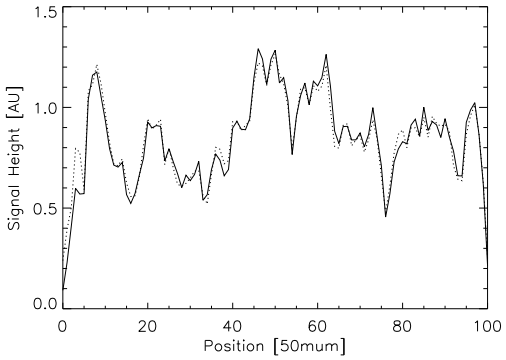

(a) Variation of the signal heights across a line-scan on a 500 μm thick diamond. Two scans of the same area are overlaid. The reproducibility is very good.

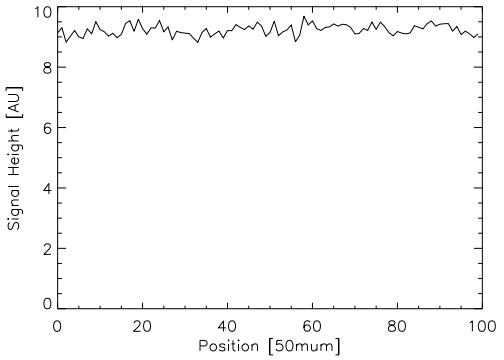

(b) Variation of the signal heights across a line-scan on a 300 μm thick silicon detector.

Figure 33: *Comparison of the variation of the induced signal across the surface for a CVD diamond sample and a silicon sample.*

area are overlaid. The variations of ϵ_Q are very well reproducible. A reference scan over a 300 μm thick silicon detector, as shown in figure 33b, produced no significant variations of ϵ_Q. The charge collection significance was determined to $S_Q(Si) = 50.7$ for the silicon sample.

A two dimensional map of ϵ_Q for the diamond sample DS7 is shown in figure 34a. The picture is again grey-scale encoded. The patterns appear to be irregular and the typical structure sizes are comparable to typical grain sizes of the sample of the order of 100 μm. To check the validity of the assumption of a uniform ionisation density the sample was turned around. If the ionisation was uniform the same pattern should be measured regardless of which side was exposed to the beam. In figure 34b a scan of the backside is depicted. The area corresponds partly to the area of the first scan in figure 34a. The measurement of the backside has been mirrored to facilitate a comparison. The circular shape

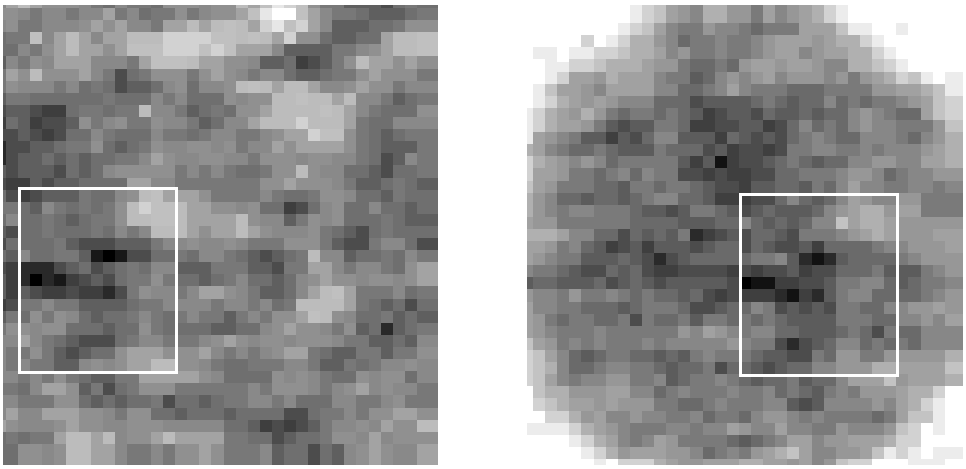

(a) Front side exposed to beam.

(b) Back side exposed to beam. The circular shape is the hole of the ceramic holder.

Figure 34: *Comparison two spatial scans of ϵ_Q with changed beam direction on approximately the same surface area on a* 500 μm *thick sample. The frame indicates the same surface area on the sample; the backside measurement has been mirrored to facilitate comparison. The step size is 50*μm .

is caused by the ceramic holder on which the sample was mounted: the backside had a circular opening of 1.5 mm in diameter which determined the area of measurement. The white frame in figure 34a and 34b denotes the same location on the sample. A comparison shows that the same characteristic pattern is seen on both measurements. This can only be explained by the uniformity of ionisation density. If charge would be deposited only in a shallow layer the patterns should be quite different as the crystallite structure of CVD diamond is very different on substrate and growth side (see section 3). Thus the result confirms that the ionisation density can be taken as uniform.

Quantifying the degree on non-uniformity with the mean charge collection efficiency significance, which was introduced above, sample DS7 has a value of $S_Q(DS7) = 5.03$. It is much lower than the value of $S_Q(Si) = 50.7$ obtained for the silicon sample but compatible to $S_Q(A) = 4.32$ of CVD diamond sample A.

Conclusion

A method was presented to measure the charge collection efficiency, ϵ_Q, spatially resolved with a resolution of ≈ 100 μm. The investigated CVD diamonds showed a non-uniform distribution of ϵ_Q over the active area. The non-uniformity was

expressed with the charge collection significance, S_Q. Typical values for CVD diamond samples were in the order of $S_Q \approx 5$. The typical size of the non-uniformities was comparable with the typical grains size of the samples. The strong non-uniformity of ϵ_Q in CVD diamond can affect the performance of a position sensitive detector device build from the material. An investigation of the influence of the non-uniformity on the spatial resolution and detection efficiency of a CVD diamond strip detector prototype is presented in section 8.

4.8 Alpha Particles

Because of growth process of CVD diamond the crystallites are larger on the growth side than on the substrate side. This leads to different charge collection properties and it is important to study the charge collection on both sides separately. This was done with mono-energetic alpha particles from a ^{244}Cm source with an energy of 5.8 MeV. The stopping range of 5.8 MeV alpha particles in diamond is about 14.3 μm [58]. Most of the kinetic energy is deposited via ionisation at the end of the track (Bragg-peak). The deposition of charge therefore takes place in a shallow layer close to the surface, so that the charge collection properties are not measured as an average of the bulk but are determined by the local drift lengths at the deposition layer. Thus, the response to alpha particles can be used to extract information about the difference of ϵ_Q on growth and substrate side. The discussion will concentrate on two typical samples A and B.

4.8.1 Set-up

The alpha-source and the diamond were placed in a vacuum-chamber at a pressure of 10^{-5} mbar. The AC-coupled amplifier chain was connected to the side which was exposed to the alpha-particles. The polarity of the electrical field is defined relative to the exposed side of the diamond, i. e. a negative potential on the exposed side is a negative field. The detector signal was amplified by a Canberra 2022 charge sensitive preamplifier, followed by an Ortec 572 shaping-amplifier with a time constant of $\tau = 3$ μs and an Ortec 444 gated biased amplifier. Since the range of the alpha particles is much smaller than the thickness of the diamond no external trigger could be used. The signal from the diamond itself had to be used as a trigger, which required to set a threshold to discriminate events from noise. The signal for a diamond detector with 100% charge collection efficiency is expected to be $4.46 \cdot 10^5$ e. The noise from the system was determined to be 590 e. The threshold was set to 6700 e. The signals were recorded with a multichannel-analyser. A silicon detector was used to calibrate the set-up, assuming 100% collection efficiency of the silicon detector and an energy of 3.6 eV to create an electron-hole-pair at room temperature in silicon.

4.8.2 Results

Alpha-spectra for different electrical field strengths were recorded, exposing the growth as well as the substrate side of the diamond samples. During the irradiation with alpha particles, the counting rate and the pulse height of the diamond detectors were decreasing. The change of the counting rate with time for a fixed threshold can be seen in fig. 35a. The decreasing counting rate indicates the build-up of a polarisation field which compensates the externally applied field. This can be clearly deduced from the fact that after removing the voltage, signals of opposite polarity were observed for some time indicating that the diamond

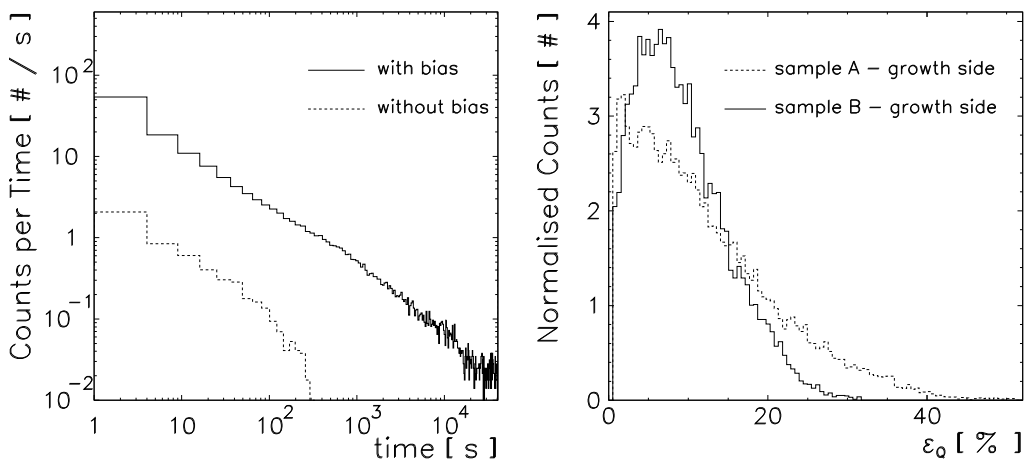

(a) (b)

Figure 35: *(a) Counting rate as a function of time for applied voltage ($U_b = 250$ V) and polarisation field ($U_b = 0$ V), measured with sample A. (b) Typical alpha-spectra obtained with CVD diamond.*

remained polarised.

Since the polarisation decreases the signal over the exposure time, the measured ϵ_Q depends on the history of the sample. To have reproducible results the following procedure was applied to obtain alpha spectra: The diamond was first exposed to alpha particles for a period of 300 s with an applied electrical field. Then the field was reversed and the response was measured for another period of 300 s. This procedure ensured a well-defined initial condition of the sample, independent of the initial polarisation state.

The two samples, A and B, show different responses. The 300 μm thick sample A exhibits a steeply falling spectrum with no visible peak when irradiated with mono-energetic alpha particles, while the 123 μm thick sample B produces a very broad peak. Typical spectra are shown in fig. 35b. As already pointed out in [55], the interpretation of spectra in terms of ϵ_Q is difficult due to the influence of polarisation, which disturbs the intrinsic electronic properties of the crystallites. The method is especially sensitive to polarisation because of the thin layer in which most of the charge is deposited. The measurements of the ϵ_Q distribution using methods which are less sensitive to polarisation (beta particles, 10 keV photons, multi GeV test-beam) show a much narrower distribution of ϵ_Q.

Nevertheless, the data can be used to compare the response of growth and substrate side at different field strengths and polarities. To extract a value of ϵ_Q

from the alpha spectra two methods were used. On the one hand the average of the entries in the spectrum was taken as a measure of ϵ_Q. Since a noise cut was applied, the observed average ϵ_Q for alpha particles should be systematically higher than the true ϵ_Q. On the other hand the mean of a Gaussian was taken as another measure of ϵ_Q in the case of spectra recorded with sample B, which contained a broad peak.

The field strength dependence of ϵ_Q is shown for both samples in fig. 36. The dependence is similar to that observed in the measurements with beta particles. Furthermore, ϵ_Q is higher for negative fields than for positive fields on both growth and substrate side indicating a higher mobility lifetime product for electrons.

The charge collection efficiency is higher on the growth side than on the substrate side, as expected from the better crystalline quality on the growth side. The results from growth and substrate side can be compared to verify the linear model proposed in [10], which predicts a linear increase of the collection distance with the film thickness. If this model is applied to sample A, the linear model predicts a ratio of growth side to substrate side collection distance of $R = 500\ \mu\text{m}/200\ \mu\text{m} \approx 2.5$, taking into account that sample A was lapped on the substrate side from an original thickness of 500 μm to 300 μm. The measured values vary between 2.4 at $E = 13.3$ kV/cm and 5.2 at $E = 3.3$ kV/cm, with a mean value of $R_\text{m} = 3.7 \pm 0.4$.

The average ϵ_Q for negative and positive polarity at a field of $E = 10$ keV/cm is $\langle\epsilon_Q\rangle = 10.1\%$ for sample B and $\langle\epsilon_Q\rangle = 7.1\%$ for sample A. Using the van Hecht equation (26), the average collection distance for sample A is approximately $\delta_Q = 43\ \mu$m and for sample B $\delta_Q = 25\ \mu$m. Comparing these values with measurements of δ_Q obtained with beta particles, the agreement is reasonable for A and poor for B. Complications due to polarisation and priming effects may account for the disagreement. Beta particles enable a more precise measurement of δ_Q since polarisation effects are negligible.

Conclusion

CVD diamond exhibits a very broad signal spectrum when irradiated with monoenergetic alpha particles with a stopping range of a few microns. The development of a strong polarisation field was observed. A comparison of growth and substrate side showed a better response of the growth side due to the better crystalline quality. The signal was found to be dependent on the polarity of the electric field which can be explained by a lower mobility lifetime product of holes than for electrons.

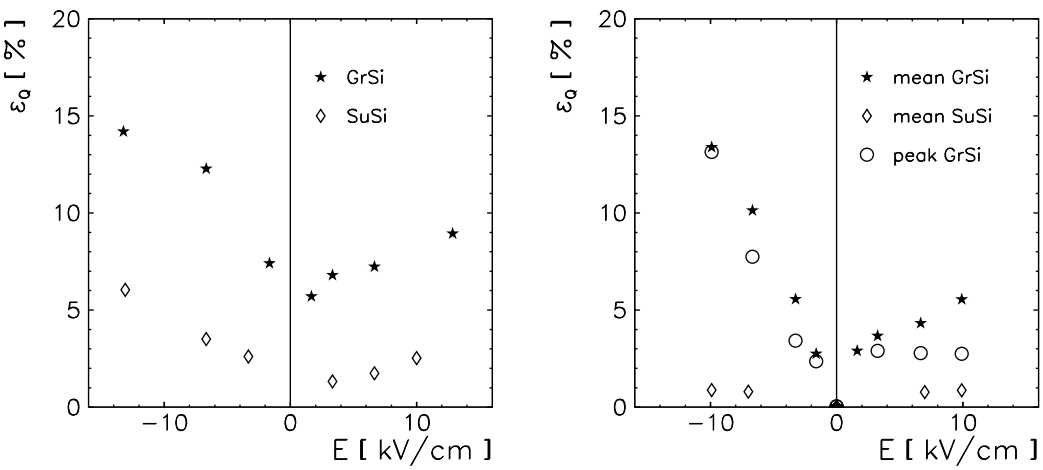

Figure 36: *Field dependence of the collection efficiency measured at the substrate (SuSi) and growth sides (GrSi) for sample A (a) and B (b), determined with alpha particles by taking the mean of the spectrum. In the case of sample B, a Gaussian fit was performed in addition if a peak was visible.*

4.9 Proton Micro-beam

A beam of protons with a diameter of ≈ 1 μm and an energy of 2 MeV (proton micro-beam) was used to investigate the lateral distribution of ϵ_Q on the growth and substrate side. The penetration depth of 2 MeV protons in diamond is about 30 μm [59] and therefore much smaller than the thickness ($d = 300$ μm) of the investigated sample. The ionisation density has a characteristic Bragg peak at the end of the trajectory. Only a shallow layer of the diamond of a few microns thickness is probed, similar to the investigations using alpha-particles which had a stopping range of 14.3 μm. Thus information about the ϵ_Q distribution and uniformity is disturbed by a strong polarisation field. The spatially resolved response behaviour of growth and substrate side was recorded. The map of the signal response was correlated with the surface topography by matching with SEM pictures. Only one sample (A) was investigated with this method.

4.9.1 Set-up

The PIXE (proton induced X-ray emission) facility at the I. Institut für Experimentalphysik[8], Universität Hamburg, provided a proton micro-beam with a proton energy of 2 MeV and a beam spot size of about 1 μm. The sample was mounted on a sample-holder in an evacuated chamber at a pressure of about 10^{-5} mbar.

The diamond signal was amplified by an Amptek A250 charge integrating amplifier. Then a shaping amplifier ($\tau = 1$ μs) and a gated biased amplifier, also used for the alpha particle measurements (section 4.8), further amplified the signal. The signal was again self-triggered with the threshold set to 2400 e. The set-up has been calibrated with a silicon-detector.

4.9.2 Results

The response spectrum of the diamond sample to 2 MeV protons at $E = 5.7$ kV/cm is displayed in fig. 37 for the substrate and the growth side.

The shapes of the spectra are similar to those seen with alpha particles. As with the results obtained with alpha particles the substrate side is less efficient than the growth side. The ratio of the average pulse heights of growth and substrate side is $R = 1.8$, which is smaller than the ratio observed with alpha particles (see section 4.8). The difference could be due to the lower threshold and the larger stopping range of 2 MeV protons compared to 5.8 MeV alpha particles.

Unlike the alpha measurements, measurements with the proton micro-beam allowed the signals to be spatially resolved thus obtaining a map of ϵ_Q.

[8]The support and collaboration of Dr. Fretwurst, Dr. Niecke and Dipl. Phys. Henkel is acknowledged.

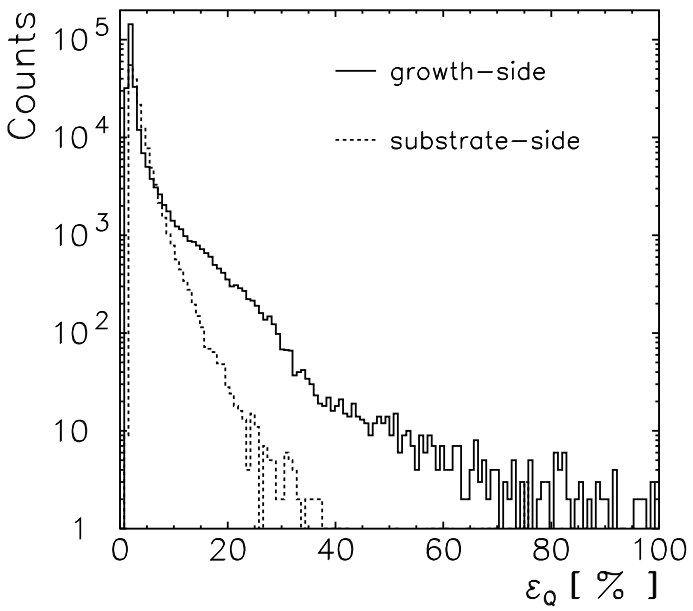

Figure 37: *Response spectra of sample A to 2 MeV protons at* $E = 5.7$ kV/ cm *for growth and substrate side.*

The edges of the metallisation were clearly visible, and some spot-like structures of high response with typical dimensions of 50 μm to 100 μm and a spot density of about 1 mm^{-2} were observed. The most of the sample did not show a signal above the applied threshold of the read-out system.

The centres of high response, which are referred to as *hot spots*, were partly not stable in time, indicating polarisation phenomena. Some remained localised and constant under continuous irradiation, others tended to disappear, while a third type seemed to appear only after some irradiation. Measurements with a proton micro-beam from [55] are in agreement with the observations presented here.

The fact that the regions at the edges of the metallisation gave a higher response is attributed to the higher field strength due to the non-uniformity of the electric field. This effect was used to correlate proton micro-beam measurements with SEM pictures of the topography of the surface. The metallisation structure visible in the signal map and in the SEM picture allowed to both measurements to be matched and hot spots to be localised. A correlation of both measurements is shown in fig. 38. Taking into account alignment and scaling uncertainties a matching resolution of 100 μm was estimated.

Hot spots were found preferentially on cloven structures between grains. A remarkably large hot spot (see the arrow in fig. 38), which was stable under continuous irradiation, was located in the middle of the metallisation strip. The structure of this single hot spot X is displayed in fig. 39 for different field strengths. The counting rate was reduced when the applied field was lowered and the corresponding spectra (fig. 40a) show a decrease in pulse height for lower fields. Two distinct peaks in the spectrum are observed, which are attributed to two different

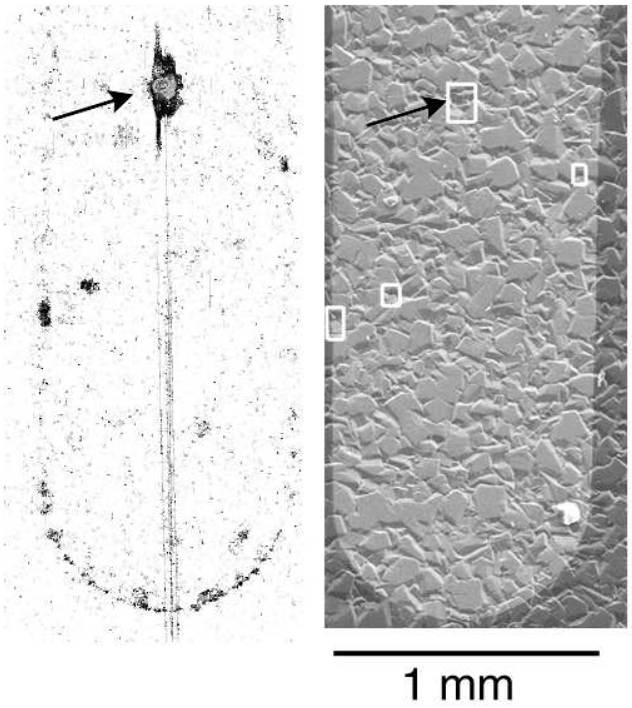

Figure 38: *Correlation of the map obtained with protons (left) and the SEM picture (right). Dark areas correspond to a high response (hot spots). Vertical stripes are artifacts of the measurement. The framed areas on the SEM mark the locations of the hot spots. The arrow points to the hot spot X discussed in the text.*

areas in the hot spot. Fig. 40b shows the full spectrum of the hot spot and the spectra of area A and B at $E = 5.7$ kV/cm as shaded histograms. Both spectra show clearly separated peaks. Area B is less efficient than area A. The peak position of A corresponds to a collection efficiency of about 25%.

Within the accuracy of the matching of the SEM-picture and the ϵ_Q map, the highlighted area shown in fig. 41 was assigned to this hot spot. The size of the highlighted area includes the estimated error on the matching. It shows that the hot spot is most likely to sit on the cloven structure as indicated in the picture.

The substrate side of the diamond was also scanned. The results of the substrate side gave a similar picture. Again the edges of the metallisation showed significantly higher counting rates and hot spots appeared also on the substrate side. However, the population of hot spots was denser on the substrate side (spot density of about 2.5 mm^{-2}) and they were smaller in size (typically 5 μm to 20 μm) than on the growth side. This can be explained by the fact that the average grain size is smaller on the substrate side than on the growth side. Furthermore, the existence of hot spots on the substrate side indicates that the surface roughness is not responsible for this phenomenon, since the substrate side was polished.

Attempts were made to correlate ϵ_Q maps of the growth side and the substrate side. If hot spots would appear at the same locations on the growth and on the substrate side it could indicate that continuous crystal columns of high collection efficiency are present at these locations. However, a spatial correlation was not observed between hot spots from the substrate and the growth side.

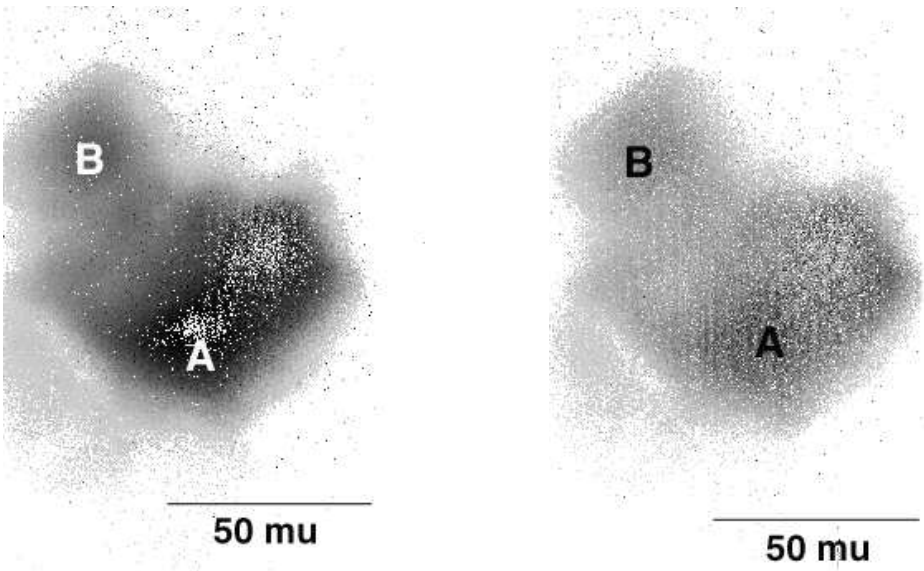

(a) (b)

Figure 39: *Hot spot X on the growth side at field strength of (a)* $E = 5.7$ kV/ cm *and (b)* $E = 4.7$ kV/ cm.

Conclusion

The investigations with a proton micro-beam show a strongly non-uniform charge signal. The observed signal spectrum is similar to spectra obtained with 5.8 MeV alpha particles. Maps of ϵ_Q were obtained and correlated with the surface topography. Hot spots of enhanced activation were found preferentially between grains and no correlation of hot spots on growth and substrate side was observed. The instability of some hot spots indicate a close link to polarisation phenomena as proposed in [55]. The results favour the interpretation of a complex polarisation phenomenon at grain boundaries [55]. This view is supported by the spatially resolved measurement of ϵ_Q with 10 keV photons (see section 4.7), which ionise uniformly in the bulk and suppress polarisation. No enhancement of ϵ_Q was seen with photons at the hot spot locations found with protons.

The detection capability of CVD diamond for particles with short stopping ranges compared to the sample thickness is strongly affected by polarisation of the bulk. The polarisation passivates most of the active detector region and only a few areas retain their detection capability.

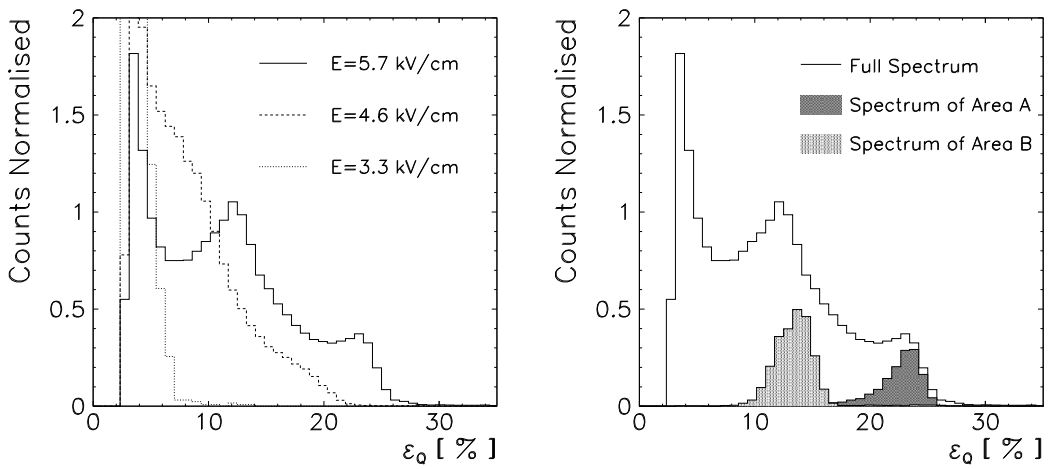

(a) (b)

Figure 40: *(a) Spectra of hot spot X described in the text at different electrical field strengths and (b) spectra of area A and B and full spectrum at* $E = 5.7$ kV/cm.

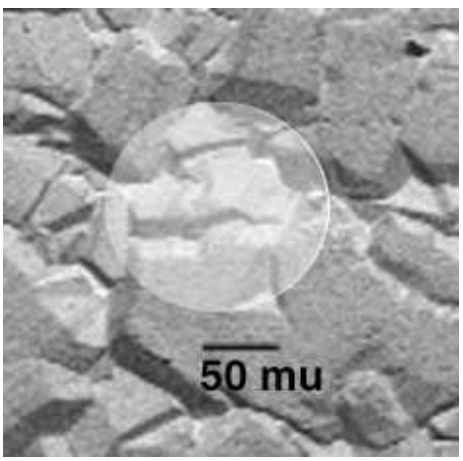

Figure 41: *Region of the crystal where the hot spot X is located.*

4.10 Electron Beam Induced Currents

The method of **e**lectron **b**eam **i**nduced **c**urrents (EBIC) is widely employed for the characterisation of semiconductors but has rarely been used to characterise the electronic properties of CVD diamond [60, 61], and has never been applied to detector grade CVD diamond before. The EBIC measurement allows information of the distribution of traps in a thin surface layer to be deduced. The resolution of the measurement is comparable to the resolution obtainable with SEM (better than 1 μm).

The EBIC method uses the focused electron beam of a Scanning Electron Microscope (SEM) to generate excess charge carriers in the sample. The sample is contacted with electrodes and an electric field is generated by applying a bias voltage. The electron beam continously generates excess carrier, which drift towards the electrodes and induce a detectable current, which is measured as a function of the position of the beam. The current is composed of the dark current and the excess current. The excess current is given by

$$\Delta I \approx e \frac{\mathrm{d}N_\Delta}{\mathrm{d}t} \frac{\mu E \tau}{d} \tag{45}$$

where e denotes the elementary charge, $\mathrm{d}N_\Delta/\mathrm{d}t$ the production rate of excess charge, E the electrical field strength, and d the spacing of the electrodes. The quantities E and τ are generally dependent on the position of the beam. Traps and recombination centres will determine the lifetime of the excess carriers and the induced current allows to deduce information about the lifetime at the position of the electron beam.

The high charge production rate makes the method very sensitive to polarisation effects, which will distort the electric field E. Especially if electrodes on the growth and substrate side are used (sandwich configuration), the polarisation can be very effective and completely compensate the external field as seen with alpha particles (section 4.8) and protons (section 4.9). The polarisation can be minimised using a strip configuration, where the electric field develops between two adjacent strips. Because the electron beam sweeps across the surface between the strips, charge carriers are generated throughout the field region and the build up of a polarisation field is reduced. A determination of the drift length δ_Q by this method is difficult due to the systematic effect of polarisation. Thus only qualitative results were obtained.

Samples with sandwich and with strip configuration have been investigated at different field strength and polarities. EBIC pictures were correlated with SEM pictures which were recorded in parallel to the EBIC data.

4.10.1 Set-up

The SEM set-up described in section 4.1 was also used to record EBIC data. The principle of the set-up is shown in figure 42. To provide electrical connections to

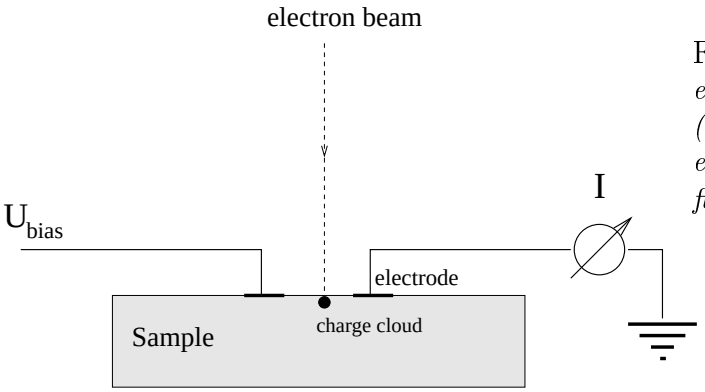

Figure 42: *Schematic of the electron beam induced current (EBIC) measurement. The electrodes are in the strip configuration.*

the sample in the vacuum chamber of the SEM, a special sample holder and a flange with BNC connectors was prepared. The sample was connected to the bias voltage and a current-voltage amplifier (Ortec 5002). The output signal was fed to the internal video control unit of the SEM. It allowed the current to be used to control the intensity of the video signal and thus the current to be displayed as a function of the beam position. The SEM was equipped with a image digitiser which could also be employed for the digitisation of EBIC images.

The input source of the video circuit could be switched from EBIC signal to secondary electron detector signal used to obtain SEM pictures. Thus a correlation of EBIC images with SEM images was possible by recording sequentially SEM and EBIC data without changing the sample position.

A beam energy of 20 keV with a beam spot-size of 100 nm was used to scan the samples. A slight dependence of the results on the scan frequency was observed due to the build up of polarisation fields and the resulting decrease of the current signal. The effect was minimised by selecting the highest possible scan frequency allowed by the bandwidth of the current amplifier.

4.10.2 Results: Strip Electrode Configuration

A strip electrode configuration designed for a prototype detector on a CVD diamond with good detection properties (sample DS8, see section 8) was investigated with the EBIC method. Two adjacent strips were contacted to the bias voltage and the current amplifier. The strip-pitch was 100 μm and the width of the metallised strip was 66 μm. From the strip area SEM and EBIC pictures at different bias voltages were obtained. Figure 43 shows the SEM and the corresponding EBIC images, recorded at $U_b = +40$ V and $U_b = -40$ V.

The strip electrode can be clearly recognised in the SEM and in the EBIC images. In the SEM picture (figure 43a) the strips which were connected to U_b and the current amplifier are indicated. The EBIC images are grey-scale encoded and show the current amplitude on the sample. The current signal for negative and positive U_b is white for negative bias and white for positive bias since the current changes its sign. Because the grey-scale was mapped after the measurement to

the maximum and minimum value of the current to enhance the contrast the dark current level is white in figure 43b and black in figure 43c. Surprisingly the structure is very different for positive and negative bias voltage. The areas of response do not match for negative and positive bias voltage. With the naive assumptions that the transport process is equal for electrons and holes the EBIC images should be equivalent except for the sign of the EBIC current. However the results suggest that the transport properties are quite different. While for a negative bias voltage most activity is observed under the bias strip, for a positive bias the activity is shifted to the edge and to the inter-strip region between bias and sensing strip. This could be explained if the mobility was significantly lower for holes than for electrons. This speculation is supported by the measurement with alpha-particles (see section 4.8).

For both polarities the coherent areas of response are of the typical grain sizes. A sharp drop of induced current is seen between the areas. Since the investigated sample was polished, a correlation to the surface topography was not possible. However the result is interpreted as a clear evidence for a significantly decreased life-time of charge carriers at grain-boundaries.

4.10.3 Results: Sandwich Electrode Configuration

The sandwich electrode configuration is very sensitive to polarisation effects because trapped charge can effectively establish a compensating field. The mechanism is the same as observed with alpha-particles (section 4.8) and protons (section 4.9). Consequently the observed signals were very small. SEM and EBIC images of the 300 μm thick sample NDF01 with a strip on the substrate side for $U_b = -350$ V is shown in figure 44. The granular area on the bottom part is silver-paint used for contacting the sample. The vertical stripes across the EBIC images are caused by noise from the video circuit.

It was observed that the signal response was initially very low. After a 1 min. exposure time to the electron beam, a dot-like structure appeared (b) and the response was more enhanced for longer exposure times (2 min. (c), 4 min. (d)). The response activation through radiation has also been observed with a proton micro-beam (section 4.9) where hot-spots of activity were found. The mechanism is probably related to the trapping of charge and the creation of complex polarisation fields guided by the grain structure.

Conclusion

Spatially resolved measurements of the electron beam induced current indicate a low lifetime of charge carriers at grain boundaries. The areas of uniform response have a comparable size to typical grain sizes and are dependent on the polarity of the electrical field. The polarity dependence can be explained by a higher drift length for electrons than for holes. This is in accordance with results obtained

with alpha particles (see section 4.8). A CVD diamond with sandwich electrode configuration showed hot-spots of response only after activation through radiation. More work is needed to fully understand the underlying mechanisms of the observed phenomenon.

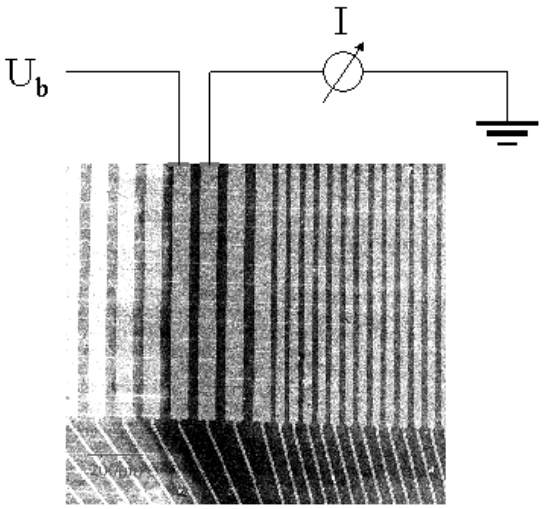

(a) SEM image of the strip electrode configuration. The contacted strips for the EBIC measurement are indicated.

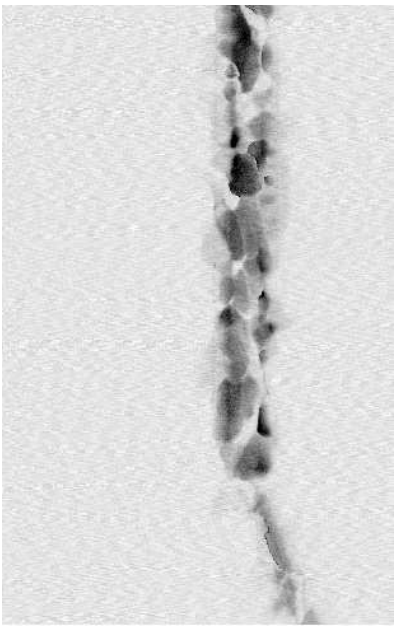

(b) EBIC image at $U_b = +40$ V.

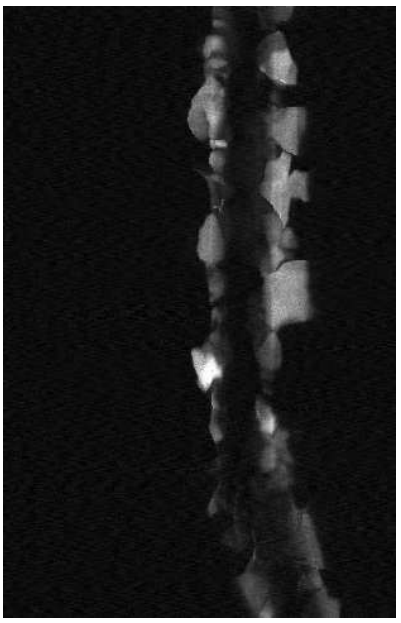

(c) EBIC image at $U_b = -40$ V.

Figure 43: *SEM and EBIC images of the strip electrode configuration on sample DS8. The drawing in (a) indicates the strips connected to U_b and the current amplifier. The EBIC image are grey-scale encoded and show the current amplitude on the sample. The images for negative and positive U_b use inverse grey-scale mapping of the current signal because the current changes its sign, i. e.à current signal is black in (b) and white in (c). Furthermore, the grey-scale was mapped after the measurement to the maximum and minimum value of the current to enhance the contrast, thus the dark current level is white in (b) and black in (c).*

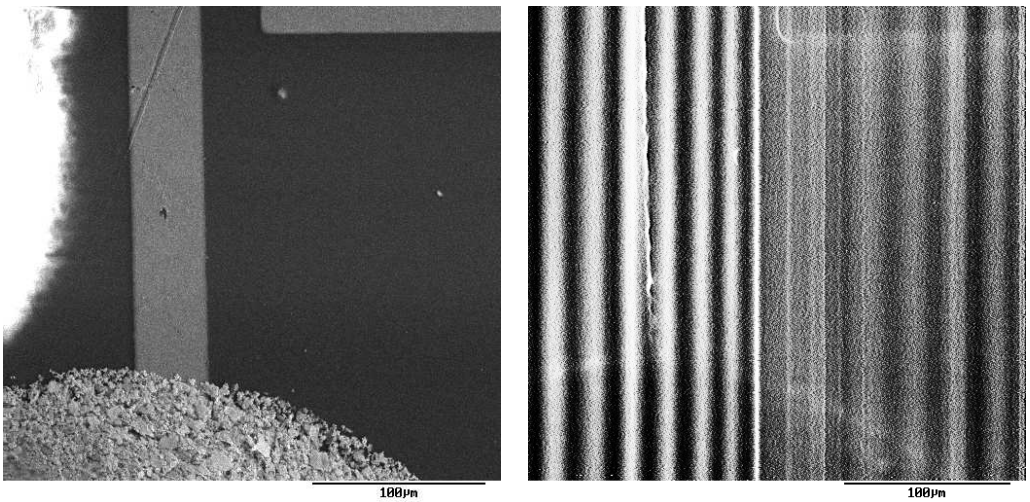

(a) SEM image.

(b) EBIC image, 0 min. irradiation time.

(c) EBIC image, 1 min. irradiation time.

(d) EBIC image, 4 min. irradiation time.

Figure 44: *SEM and EBIC images of the* 300 µm *thick sample NDF01 with a strip on the substrate side for* $U_b = -350$ V. *The EBIC images are taken at different times of pre-irradiation by the electron beam. The electric field was applied between growth and substrate side (sandwich configuration).*

4.11 Thermally Stimulated Currents

The method of thermally stimulated currents (TSC) has been widely used for the characterisation of defect states in semiconducting [62] and insulating materials [63]. The method has been particularly successful for the investigation of radiation induced defects in silicon and reliable determinations of defect concentrations and their characteristics were obtained [64].

In this study, high temperature TSC ($T > 300$ K) is used to extract information about defects in polycrystalline detector-grade CVD diamond. In addition a technique to obtain spatially resolved defect concentrations is presented.

4.11.1 Principle

A sample at temperature T_0 is irradiated with ionising radiation or light. The generated excess carriers will be trapped at defect states in the bandgap. The sample is then heated and the current as a function of temperature is measured. The excess current is defined as the current above the dark or leakage current and is called *thermally stimulated current*.

The excess current originates from charges being thermally emitted from defect sites with a characteristic energy separation E_Δ from the valence or conduction band. If the re-trapping of emitted charge carriers is neglected (first order kinetics) the emission rate of of charge carriers into the conduction band (in the case of electrons) is [63]

$$-\frac{\mathrm{d}n_t}{\mathrm{d}t} = s \cdot n_t \cdot \exp\left(-\frac{E_\Delta}{kT}\right), \tag{46}$$

where n_t is the density of trapped charge, E_Δ is the separation from the conduction band and s the frequency factor. The inverse of the frequency factor gives the characteristic time of emission of the trap. The TSC current is then given by $I_{TSC} = e \cdot A \cdot \delta \cdot \mathrm{d}n_c/\mathrm{d}t$ with A the electrode area and δ the carrier drift length. Substituting in equation (46) for $\mathrm{d}n_c/\mathrm{d}t$ it follows that

$$I_{TSC} = e \cdot A \cdot \delta \cdot s \cdot n_t \cdot \exp\left(-\frac{E_\Delta}{kT}\right). \tag{47}$$

For the theoretical discussion a constant heating rate is assumed. Then the time dependence of the temperature is given by $T(t) = T_0 + \beta t$ where T_0 is the initial temperature and β the heating rate. Using the time dependence of T, equation 46 can be solved to express n_t as a function of T. Substituting n_t in equation 47 it follows

$$I_{TSC} = e \cdot A \cdot \delta \cdot s \cdot n_{t0} \cdot \exp(-\frac{E_\Delta}{kT}) \cdot \exp\left[-s \int_{T_0}^{T} \frac{1}{\beta} \exp\left(-\frac{E_\Delta}{kT'}\right) \mathrm{d}T'\right], \tag{48}$$

where n_{t0} is the initial density of trapped carriers.

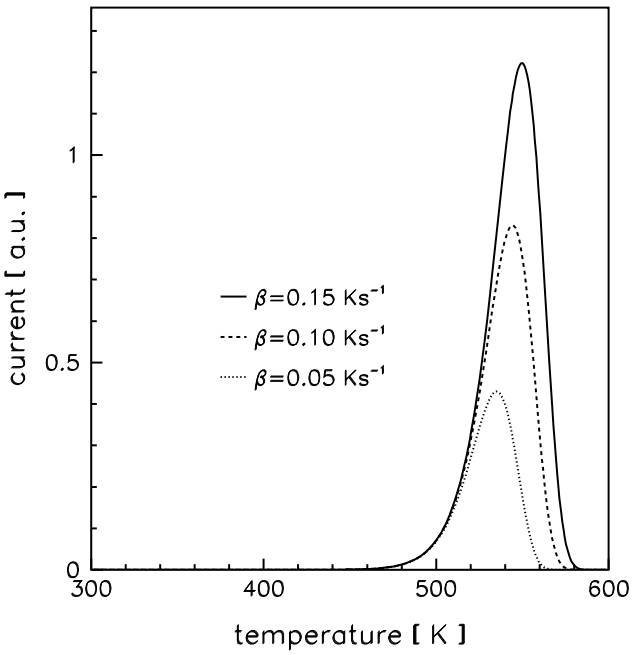

Figure 45: *Theoretical curves of the thermally stimulated current for* $E_\Delta = 1.8$ eV, $s = 3 \cdot 10^{14}$ s^{-1} *and three different heating rates calculated using equation (48).*

The theoretical shape of I_{TSC} for a single trap level at $E_\Delta = 1.8$ eV below the conduction band and $s = 3 \cdot 10^{14}$ s^{-1} [63] is shown in figure 45 for different heating rates β. The TSC curve has an asymmetric shape. The peak value scales linear with the heating rate and the peak position is shifted to higher temperatures for increased heating rates.

By integrating the TSC current a measure of the total trapped charge can be obtained:

$$Q \approx 2 \int \frac{1}{\beta} I_{TSC}(T)\, \mathrm{d}T. \tag{49}$$

The factor of 2 accounts for the displacement current, i. e. the released charge carriers are assumed to be approximately uniformly distributed in the bulk and thus on average a released charge will induce 1/2 elementary charge. The maximum of the current, $I_{TSC}(T_{max})$, is obtained by differentiating equation 48 with respect to T and equating the result to zero:

$$\frac{\beta E_\Delta}{k T_{max}^2} = s \exp\left(-\frac{E_\Delta}{k T_{max}}\right). \tag{50}$$

The peak position of the TSC current, T_{max}, determines E_Δ if s is known. The frequency factor s can be obtained by varying the heating rate β. With two measurements at the heating rates β_1 and β_2 the value of E_Δ is given by

$$E_\Delta = k \frac{T_{max,1} T_{max,2}}{T_{max,1} - T_{max,2}} \ln\left(\frac{\beta_1 T_{max,2}^2}{\beta_2 T_{max,1}^2}\right) \tag{51}$$

and insertion of E_Δ in equation (50) yields s.

4.11.2 Set-up

Two set-ups were used to measure TSC currents. A table-top set-up using β particle for trap-filling provided TSC information on trap parameters of the bulk material. A second set-up used a narrow photon beam to also obtain spatial information of the distribution of traps in the bulk.

Table-top Set-up

The sample was glued on a ceramic holder and clamped to the inside of a brass box with a wall thickness of about 3 cm. A thermometer probe was mounted next to the sample. Contacts were made with silver paint using Teflon cables and a cable holder. For heating the whole assembly was put into an oven which was preheated to 573 K. Due to this arrangement the heating rate was not linear but ranged from $\beta \approx 0.16$ K s^{-1} for $T < 430$ K to $\beta \approx 0.03$ K s^{-1} for $T > 510$ K. The actual heating rate was determined for each measurement as a function of T and used to fit the data to the theoretical expected shape, replacing the constant β in equation (48) with the function $\beta(T)$. The current was recorded at a field of $E = 0.5$ kV cm^{-1} with a computer controlled Keithley 6517A ammeter.

To occupy vacant trap sites the samples were irradiated with beta particles from a ^{90}Sr source with a dose rate of ≈ 14 rad h^{-1} without applied bias voltage. The uniform ionisation ensured trap filling throughout the bulk.

Photon-Beam Set-up

The set-up was designed to measure spatially resolved trap densities. To fill traps a 10 keV photon beam from a synchrotron light source as already described in section 4.7 was used. The absorption length of 10 keV photons is $\lambda_0 = 1300$ μm and therefore the trap filling is approximately uniform along the traversing beam. The lateral dimension of the filled volume is given by the beam diameter of ≈ 30 μm. The small volume allowed to measure spatially resolved the trap concentration by scanning the sample with the photon-beam and obtaining TSC spectra as a function of the beam position. The intensity of the photon-beam was of the order of 1 krad s^{-1} and therefore five orders of magnitude higher than the ^{90}Sr source in the table-top set-up.

The sample was inserted into a slit of a copper rod together with a thermometer probe and fixed mechanically. The copper rod was mounted on a soldering iron used as a heating element. The low mass of the copper rod ($m \approx 100$ g) allowed rapid heating of the sample from room temperature to 573 K with a heating rate of ≈ 10 K s^{-1}. After the heating cycle the copper rod was flushed with liquid nitrogen to minimise the cooling time. The assembly was mounted on a movable stand to position the sample relative to the beam. During the heating period the current, temperature and time was monitored with a Keithley 6517A ampere meter and a computer, which also controlled a beam shutter to switch off

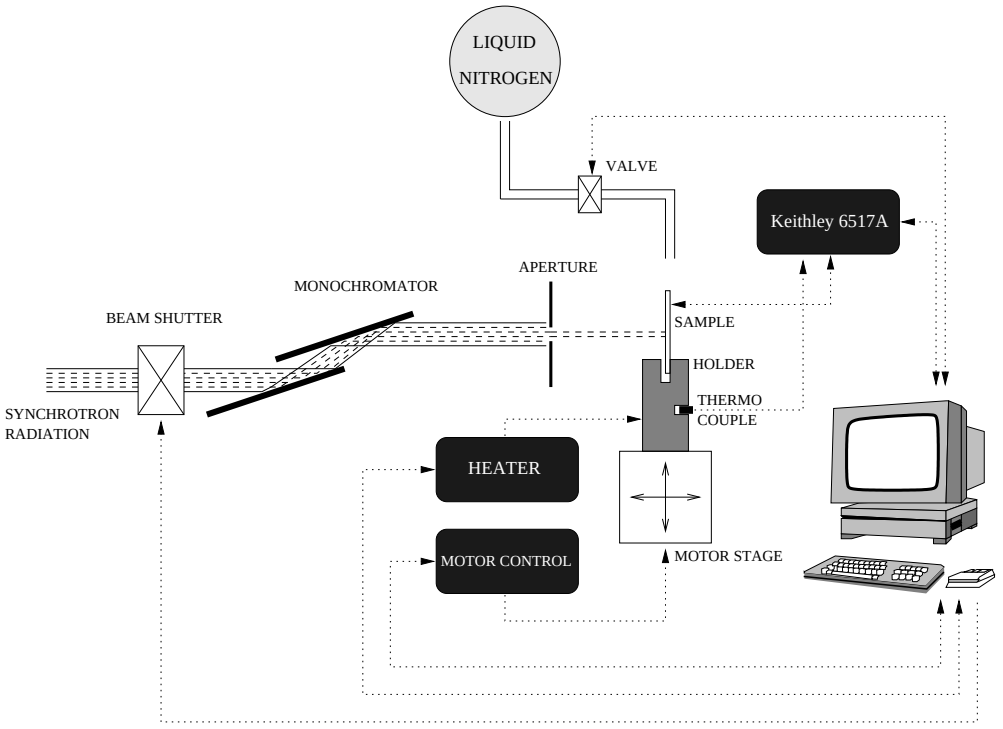

Figure 46: *Schematic of the set-up to measure spatially resolved TSC spectra.*

the beam during the TSC measurement and monitored the current in the storage ring of the synchrotron to be able to correct for changes of the photon flux by adjusting the irradiation time. During irradiation no bias voltage was applied to the sample, while for the TSC measurement a field of $E = 0.5$ kV cm^{-1} was used.

A full measurement cycle consisting of positioning the sample, trap filling by irradiation, heating and recording the TSC signal and finally cooling with liquid nitrogen required about 120 s $+ \tau_{irr}$ with τ_{irr} being the irradiation time. A schematic of the set-up is shown in figure 46.

Besides measuring the TSC signal the set-up could be reconfigured in situ to measure ϵ_Q as described in section 4.7. This was used to measure both ϵ_Q and the spatially resolved TSC signal of the same area, and to correlate trap densities with ϵ_Q.

4.11.3 Results

Table-top Set-up

Four samples were investigated, of which the properties are summarised in table 7. TSC spectra for different irradiation times of the samples A3132B and DS3 are

Name	A[mm^2]	d[μm]	ϵ_Q[%]	Φ_0[rad]	R_p	E_Δ[eV]
A3132B	38.5	123	9.5	108.	2.0	1.63 ± 0.02, 1.83 ± 0.04
A3134B	38.5	90	6.6	117.	4.4	1.65 ± 0.02, 1.87 ± 0.04
A3177B	38.5	370	6.7	45.	1.7	1.66 ± 0.02, 1.77 ± 0.04
DS3	19.6	545	8.9	5.5	1.8	1.78 ± 0.02

Table 7: *List of some properties of the samples investigated with TSC. The symbols are A the electrode area, d the thickness, ϵ_Q the collection efficiency, Φ_0 the priming fluence, R_p the priming ratio and E_Δ the activation energy of the observed TSC peaks.*

shown in figure 47. It was observed that samples of the A3 series contained two clearly visible peaks in the spectra while the DS3 sample only showed one peak. Moreover the observed TSC shapes were wider than the theoretical shape for all samples. A typical TSC shape together with the fit for sample DS3 is shown in figure 48. In the insert the raw signal prior to dark current subtraction is shown. The TSC peak on top of the dark current can be clearly seen.

The larger width of the experimental data indicates a broad distribution of trap levels instead of a sharp single trap level. This is in accordance with data reported in [63]. The peak maximum was used to extract E_Δ. Since the heating rate could not be changed a value of $s = 3 \cdot 10^{14}$ s^{-1} as reported by Gonon et al. in [63] for a E_Δ compatible with the values found here was used to fit the data.

The single trap level of sample DS3 was determined to $E_{\Delta a} = (1.78 \pm 0.02)$ eV. The two peaks of sample A3177B were found to have $E_{\Delta b} = (1.66 \pm 0.02)$ eV and $E_{\Delta c} = (1.83 \pm 0.05)$ eV. The errors on E_Δ do not account for the uncertainty in s. Qualitative similar results were found among the samples of the A3 series, namely the presence of the two peaks "b" and "c" with compatible values for E_Δ.

The intensity of the TSC signal scales approximately linear with the irradiation time as depicted in figure 49. The second peak "c" of sample A3177B could not be fitted above two hours irradiation time because it was completely swamped by peak "b". Interestingly no saturation of the TSC signal was achieved even after 67 hours of irradiation. Thus a determination of the absolute defect concentration was not possible.

The origin of the trap levels found is unclear. In the literature a broad trap level at $E_\Delta = (1.86 \pm 0.05)$ eV is reported by Gonon et al. in [63] for CVD diamond. A study of natural type IIa diamond reported three levels [65], where the dominant contribution to the TSC signal is found to have an activation energy of $E_\Delta = (2.0 \pm 0.3)$ eV. The level is commonly attributed to nitrogen impurities in the crystal. Since SIMS studies on A3 series samples (see section 4.4) show a high level of N impurity this explanation is also applicable here. However, more work is needed to understand the origin of the trap levels.

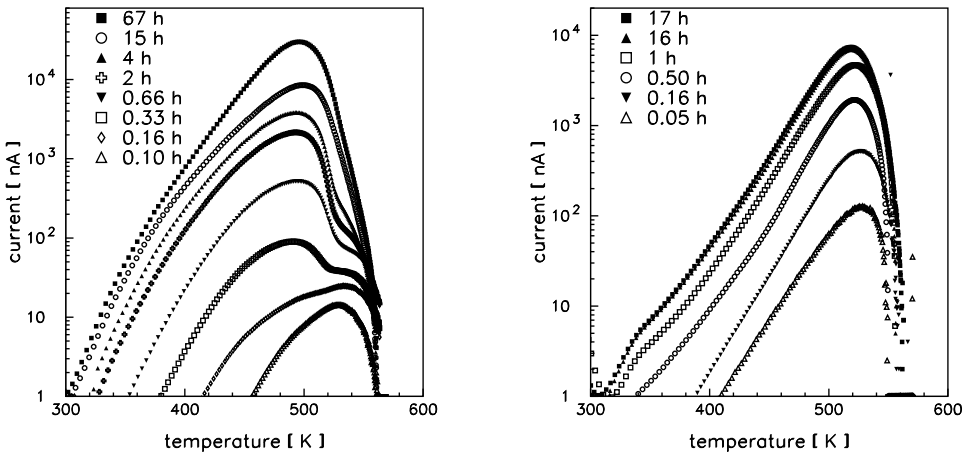

(a) Sample A3177B (b) Sample DS3

Figure 47: *TSC spectra of samples DS3 and A3177B for different irradiation times.*

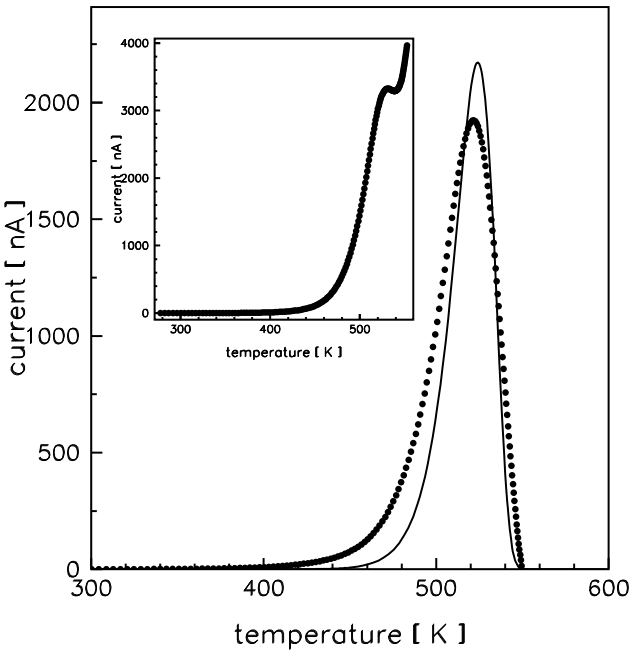

Figure 48: *Experimental data (dots) of sample DS3, irradiation time 30 min., and the fit curve (solid line) based on the theoretical shape. With* $s = 3 \cdot 10^{14}\ \mathrm{s}^{-1}$ *a value of* $E_\Delta = 1.78$ eV *is found. In the insert the raw data are depicted. The TSC peak on top of the dark current is clearly visible.*

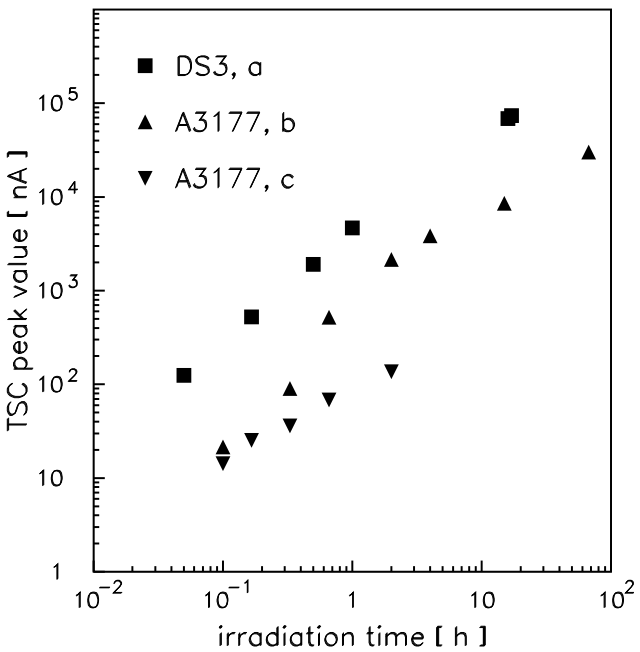

Figure 49: *Dependence of the TSC peak value for peaks "a", "b" and "c" on the irradiation time for samples DS3 and A3177B.*

Photon-Beam Set-up

Two sample (DSL2, $d = 379$ μm and DS7, $d = 500$ μm) were investigated with the photon-beam set-up. A first result obtained with sample DSL2 of a scan on an area of 1050 μm $\times$ 1050 μm with a step size of 70 μm and an irradiation time of $\tau_{irr} = 180$ s is shown in figure 50a. The graph shows the grey-scale encoded TSC intensity, where black corresponds to a high intensity and white to a low intensity. The TSC intensity varies over the scanned area due to a varying trap density.

The TSC intensity has been determined from the maximum of the TSC peak. A typical TSC curve is depicted in figure 50b. Due to the high heating rate the peak is significant and can be easily analysed despite the small volume of filled traps, which is about a factor 10^{-5} smaller than in the table-top set-up. It is noted that, in good agreement with the table-top set-up measurements, only one peak is visible of which the activation energy was determined to $E_{\Delta a} = 1.79$ eV by fitting the peak region. The noise around 550 K to 570 K is due to imprecise measurement of the dark current caused by the rapid heating rate of $\beta = 10$ K s^{-1} and the latency of the thermometer probe.

The dependence of the peak amplitude on the irradiation time is depicted in figure 51. It is found that the peak value increases non-linearly with irradiation time. However no saturation was achieved even at a irradiation time of $\tau_{irr} =$ 600 s although the intensity of the photon-beam was of the order of 1 krad s^{-1}. The behaviour could be due to carrier diffusion from the radiated volume and the exposure of the surrounding by additional radiation due to the less intense beam halo.

In a second measurement period sample DS7 was prepared with a irregular metallisation pattern to match a measurement of the TSC intensity with a measurement of ϵ_Q . The accuracy of the matching was estimated by repeative scans over the same area to 100 μm. The metallisation pattern of the investigated area is shown in the SEM picture in figure 52. A radiation time of $\tau_{irr} = 30$ s was chosen in order to complete the measurement in a reasonable time. The result is show in figure 53. It is noted that as expected both method give no signal beyond the edge of the metallisation. However besides that no clear correlation was observed.

For future studies the accuracy of the measurement could be improved by irradiating the sample for a longer time thus obtaining a higher signal. Furthermore, scanning over a greater area would improve the matching precision by using defined metallisation patterns.

Conclusion

A spectroscopic investigation of defect levels in CVD diamond by means of thermally stimulated current measurements was presented. Four samples were inves-

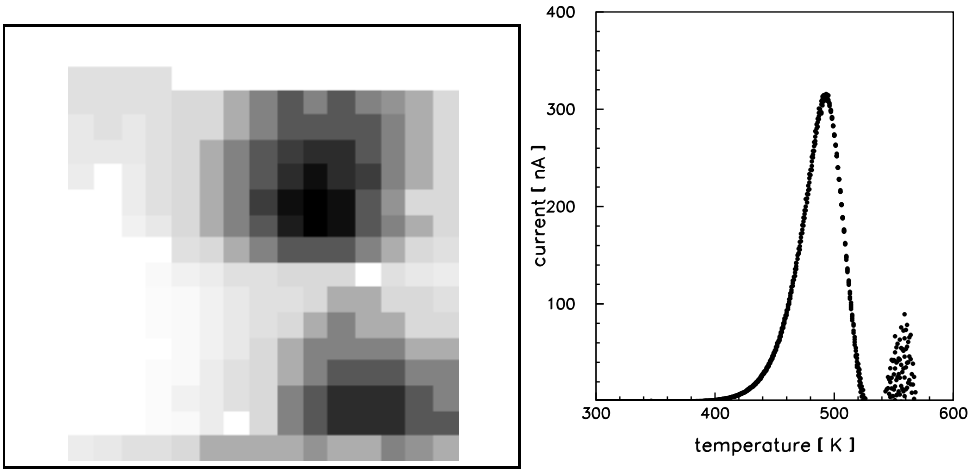

(a) First spatial resolved measurement of the TSC intensity on an area of 1050 μm × 1050 μm and a step size of 70 μm on the unpolished sample DSL2. The irradiation time was 180 s, the sample thickness was 380 μm.

(b) Typical TSC spectra obtained with the photon-beam set-up. The irradiation time was τ_{irr} = 180 s. The noise at 550 K to 570 K is due to imprecise subtraction of the dark current.

Figure 50: *Spatial representation of the TSC intensity as measured on sample DSL2 and a typical TSC spectrum for a single measurement point.*

tigated and a common defect level around 1.8 eV was found, which probably due to substitutional nitrogen. In some sample a second level at 1.66 eV of unknown origin was found. The higher width of the TSC peaks compared to the theoretical prediction is explained by a broad distribution of trap levels around the centre energy. Additionally a new method to measure TSC spectra spatially resolved was presented and a first measurement provided a proof of principle and showed a non-uniform trap concentration in CVD diamond.

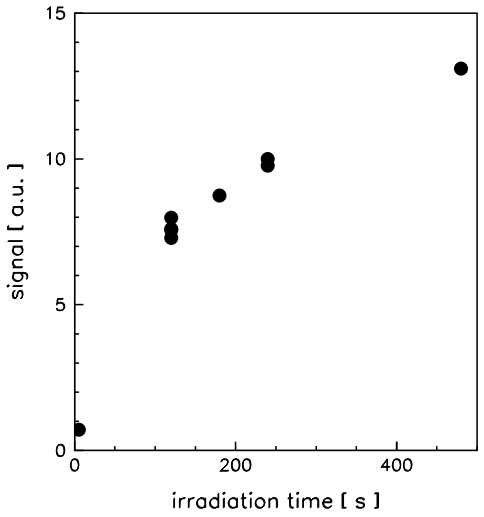

Figure 51: *Dependence of the peak amplitude of the TSC signal on the irradiation time.*

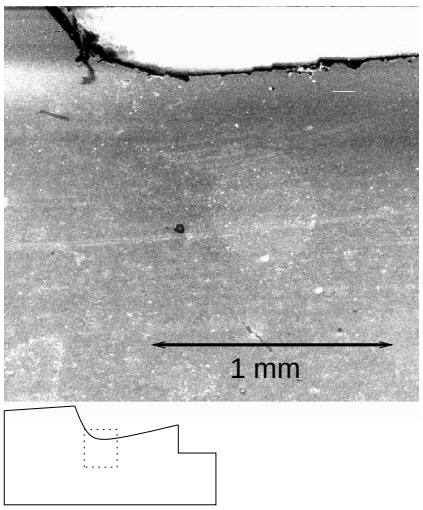

(a) SEM picture of the scanned area. The drawing below shows the shape of the full metallisation pattern.

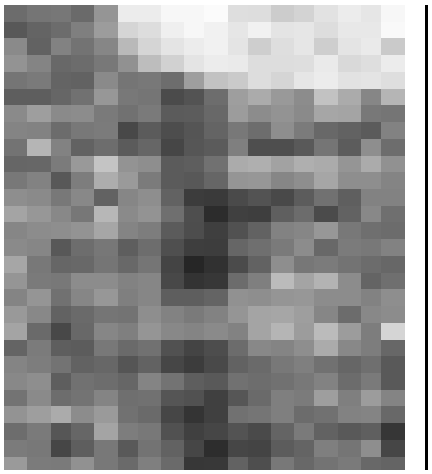

(b) ϵ_Q measurement.

Figure 52: *SEM picture (a) of the area scanned with the photon-beam to measure the TSC intensity and ϵ_Q (b). The step-size of the ϵ_Q measurement is* 50 μm.

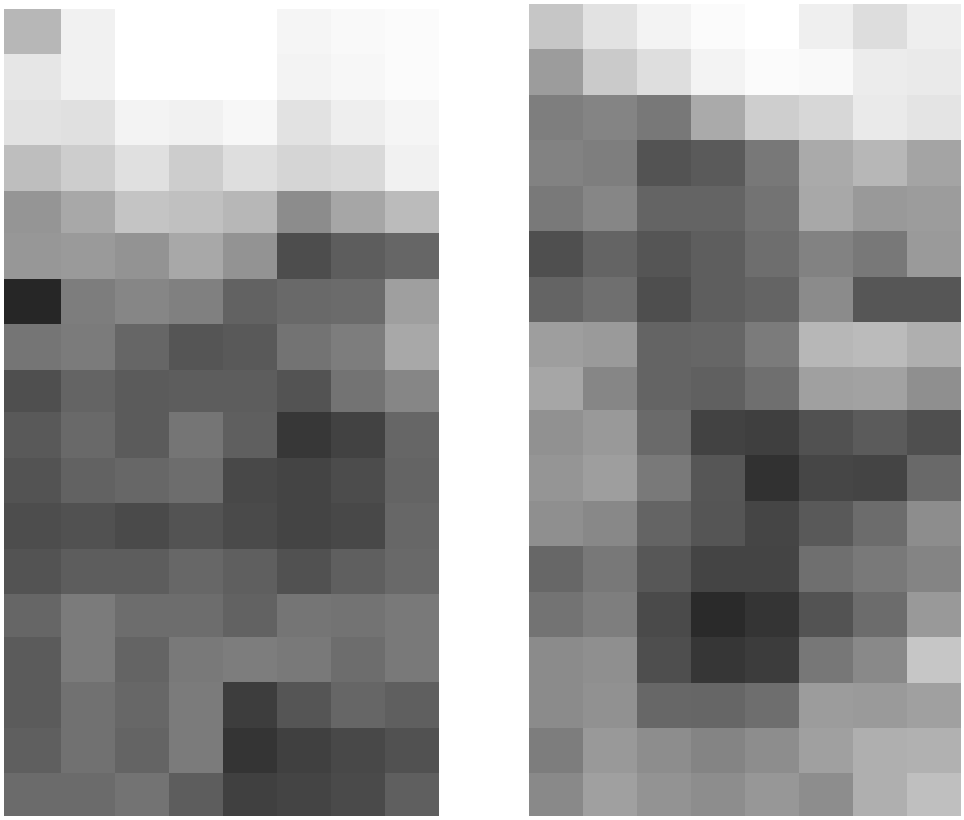

(a) TSC measurement. (b) ϵ_Q measurement

Figure 53: *Spatially resolved measurement of the TSC intensity,* $\tau_{irr} = 30$ s, *and of* ϵ_Q *on the same area with a step-size of* 70 μm.

4.12 Summary and Interpretation

Polycrystalline CVD diamonds have been characterised with various methods. The information about structural and electrical properties provides the foundation for a picture of CVD diamond as a polycrystalline material with heterogeneous distributed characteristics. The aim was to understand the particle detection abilities of the material. Emphasis was put on the investigation of the electrical properties. Structural information could partly be correlated to electrical entities and helped to understand the influence of grains and grain-boundaries on the charge carrier transport. The most important findings about structural and electrical properties are summarised in the following.

Structural Properties

Topographic pictures obtained with scanning electron microscopy verified the polycrystalline structure of the investigated samples. Moreover the data was used to correlate topographic and electrical properties.

The phase purity was investigated with Raman spectroscopy and the investigated samples showed a phonon-line typical for diamond while no graphitic phases were present. The line-width was in the order of the intrinsic resolution of the apparatus.

Information about the crystallite orientation and the typical shape of singular crystallites was obtained with spatially resolved X-ray diffraction. The experimental data was verified to be compatible with a growth model proposed in section 7.

The chemical impurity concentration of a typical CVD diamond sample was determined with spatially resolved SIMS measurements. Besides the absolute concentration values of N, H, and O impurities the spatial distribution was measured and significant variations of the impurity concentration were observed and interpreted as enhanced contamination at grain boundaries.

Electrical Properties

The charge collection efficiency, ϵ_Q, and charge collection distance, δ_Q, have been studied with uniformly ionising radiation (β particles, 10 keV photons) and particles with stopping ranges of a few micron (α particles, protons, and 20 keV electrons). Some methods (10 keV photon beam, proton micro-beam, EBIC) provided spatial information. The increase of the charge collection efficiency under irradiation with ionising particles, the so called priming effect, has been established. The priming behaviour was parametrised and the quantities priming ratio, R_p, and priming dose, Φ_0, were introduced.

In general it was found that the charge collection properties are non-uniformly distributed. A determination of the non-uniformity with a spatially resolved

measurement employing a photon-beam and an indirect method by fitting the signal spectrum of the response to MIPs were in good agreement.

While the non-uniformity measured with uniformly ionising particles was determined to be typically of the order of 20% (relative variation to the average charge collection efficiency at the 1σ level), the non-uniformity was found to be extremely enhanced for particles with a stopping range of a fraction of the samples thickness (Bragg-like ionisation density). In particular the response behaviour of the CVD diamond samples to mono-energetic alpha-particle and protons with ranges between 15 and 30 microns indicates a much higher broadening of the collection efficiency compared to the response to uniformly ionising radiation. The particles produce a very broad pulse distribution with an exponential fall-off towards large pulse-heights. A polarity dependence of the induced signal was observed with alpha particles, which was explained by a lower mobility lifetime product of holes relative to electrons. The spatially resolved measurement of the charge collection efficiency with a proton micro-beam reveals single spots (hot spots) in the material with a high response embedded in passive areas. Contrary to the priming effect seen with uniformly ionising particles, a strong polarisation build-up was found to decrease the average value of the charge collection efficiency during irradiation with Bragg-like ionising particles.

A measurement of the electron beam induced current (EBIC) provided information about the charge collection with a spatial resolution of ≈ 1 μm. The results obtained with a strip electrode configuration indicate poor charge collection between grains, while the signal on grains was reasonably high. Moreover, a strong dependence on the polarity of the electric field was observed. The finding is in agreement with the polarity dependence of the signal seen with alpha particles. It corroborates the explanation of a lower mobility lifetime product for holes than for electrons. An EBIC measurement with a sandwich electrode configuration showed small hot-spots which were activated through irradiation. Similar hot spots were seen in measurements with the proton micro-beam.

Finally, TSC measurements were presented and activation energies of trap levels were determined. The results are in agreement with data reported in the literature and show a broad level at about $E_\Delta = 1.8$ eV, commonly attributed to nitrogen impurities. In some samples a double peak structure in the TSC spectrum was observed, indicating the presence of a second trap level of unknown origin at about 1.66 eV. Additionally a method was described to measure spatially resolved TSC spectra. The first measurements gave a proof of principle and indicated a non-uniform distribution of traps.

Interpretation

The combination of the data allows important properties of CVD diamond as a particle detector to be deduced. The charge carrier lifetime in CVD diamond is limited by a high trap concentration. Activation energies well above room

temperature ($E_\Delta \gg kT$) were observed. The compositeness of the material from individual crystallites of different quality is the reason for the non-uniform properties of CVD diamond. The data strongly indicates that the grain boundaries are regions of enhanced impurity concentration and trap density, and thus limit, together with the defects within individual grains, the lifetime of charge carriers.

The high activation energy prohibits the re-emission of trapped charge, thus giving rise to persistent polarisation of the material. At the same time this lowers the density of active traps, which is established by the priming effect. The observed increase of the charge collection efficiency under irradiation with MIPs and the decrease of the charge collection efficiency observed under irradiation with protons and alpha particles is not contradictory. In the former case traps are filled throughout the bulk, thus increasing the charge collection efficiency due to the decrease of active trap levels (priming). However, because of the rather uniform distribution of the trapped charge, no effective polarisation field is produced. In the latter case the majority of the charge is deposited in a shallow layer. In the electric field the charge carriers are separated and trapped and thus create a strong polarisation field. The polarisation is dominating over the increase of the charge collection efficiency from trap passivation and thus the signal yield decreases. The plausibility of this explanation was verified with a detailed computer simulation (see section 7).

The applicability of CVD diamond as a particle detector depends on the radiation to be detected. For radiation which deposits charge non-uniformly as in the case of alpha-particles with a stopping range much less than the sample thickness, the charge collection efficiency varies strongly and the stability is very poor. For uniform ionisation as produced by MIPs, the primed charge collection efficiency is stable and shows typically a 20% variation relative to the mean over the sample. Thus, CVD diamond has the potential of being used as a stable detector for uniformly ionising particles. However, the relatively strong non-uniformity of the charge collection efficiency limits the achievable resolution and detection efficiency of a position sensitive device. This is investigated in section 8.

5 Growth Studies of CVD Diamond

This section reviews a study of the dependence of charge collection properties on growth parameters of a microwave plasma CVD process. The charge collection efficiency, ϵ_Q, and the priming parameters of several deposition experiments are studied and their correlation to growth parameters are investigated.

5.1 Preparation of CVD Diamond Films

The CVD diamond samples were prepared by the Fraunhofer-Institut für Schicht- und Oberflächentechnik [66] in Braunschweig with a microwave-plasma CVD process (see section 3.2 for a description of the CVD process).

The microwave power was 4.7 kW and the reactor was operated at a pressure of 150 mbar with H_2 diluted CH_4 and O_2 as source gases. Diamond was grown on 2 inch Si-substrates of 3 mm thickness. To facilitate and enhance the nucleation the substrates were pretreated with diamond powder in an ultrasonic bath.

The diamond films were grown to thicknesses between 50 and 215 μm . The growth rates varied between 0.3 μm h^{-1} and 4.0 μm h^{-1}, depending on gas composition and substrate temperature. To investigate the growth conditions for high collection efficiency material the substrate temperature (790 °C to 900 °C) and the gas composition were varied. Twelve different parameter-sets were processed and two samples of each process were investigated. The process parameters are summarised in table 8.

After etching off the Si substrate the free standing layers were cut into circular shaped pieces of 14 mm diameter and metallised with a dot of 5 mm diameter on both growth and substrate side. For metallisation 50 nm Ti was evaporated onto the sample which was subsequently heat treated for carbide formation. Then a diffusion barrier of 30 nm Pt followed by 60 nm Au layer was added. After metallisation the samples were etched in oxygen plasma to reduce the surface conductivity.

5.2 Characterisation

The phase purity was determined with Raman spectroscopy (see section 4.2). For all samples the FWHM of the Raman-peak at ≈ 1333 cm^{-1} was equal to or better than 6 cm^{-1}, which was the resolution of the apparatus, indicating a high diamond phase purity.

The collection properties of the samples were characterised with the set-ups and methods described in section 4.6. The measured parameters were the charge collection efficiency, ϵ_Q, the priming ratio, R_p, and the priming dose, Φ_0.

The values of ϵ_Q, R_p and Φ_0 varied significantly between samples of different deposition processes, however samples from the same process showed good agreement between each other. A typical example of $\delta_Q(E)$ for two samples of the

Name	T_{substr}[°C]	gas flow [cm^3 h^{-1}]	c/o	v_{gr}[μm h^{-1}]	d[μm]
121	800	803	3	1.1	80
132	830	803	3	1.3	123
133	885	750	5	2.8	110
134	832	500	5	2.3	90
135	819	803	3	1.5	108
141	820	803	3	2.2	145
144	808	545	4	3.9	215
157	822	-	2	1.7	70
158	762	-	2	1.6	70
177	830	-	3	1.57	370
178	829	-	2	0.73	118
179	829	-	1.5	0.31	50

Table 8: *Growth parameters of the twelve deposition experiments. The symbols are T_{substr} the substrate temperature, c/o the ratio of molecular carbon to oxygen, v_{gr} the growth velocity and d the film thickness. For some experiments no information on the gas flow was available.*

same wafer is shown in figure 54. The data taken on two samples are consistent with being equal. The samples were always cut out of the centre region of the wafer, where the crystalline quality is highest.

5.3 Correlation of Growth Parameters with Charge Collection Properties

The charge collection efficiency, ϵ_Q , was determined for all samples and exhibits a clear correlation with the growth rate, as shown in figure 55. To compare different samples the saturation value of ϵ_Q was taken. The trend in the data of higher collection efficiencies for lower growth rates is in accordance with data published in reference [10]. A best value of $\epsilon_Q = 38\%$ is found for a growth speed of 0.31 μm h^{-1}. The finding indicates that the growth rate plays an important role for the formation of lattice defects. However the impurity concentration given by the gas composition should not be affected.

If ϵ_Q is plotted versus the priming ratio R_p, a trend of low values of R_p for high values of ϵ_Q can also be observed (see figure 56). This observation corroborates the correlation found with the growth rate, namely the fraction of defects capable of passivation is minimised in the highest quality material.

The correlation of ϵ_Q with the priming dose, Φ_0 , is shown in figure 57. Low dose constants $\Phi_0 < 20$ rad are observed for high quality samples ($\epsilon_Q > 20\%$), and significantly higher constants of up to 160 rad for the lower quality samples

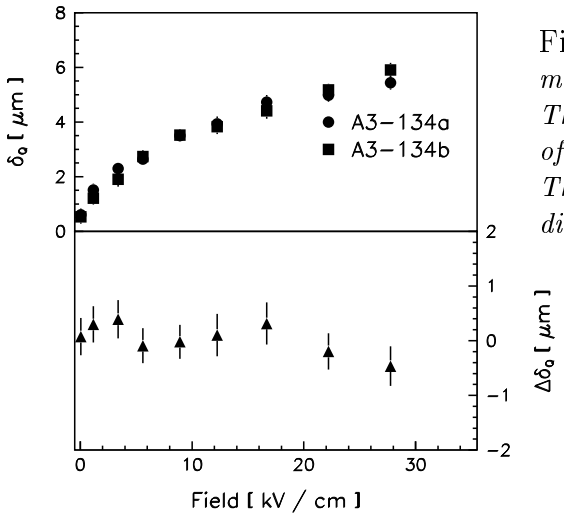

Figure 54: *Typical result for a measurement of samples from the same process. The $\delta_Q(E)$ dependence for two samples of the same wafer agree well (upper plot). The difference (lower plot) in collection distance ($\Delta\delta_Q$) is consistent with* 0 μm.

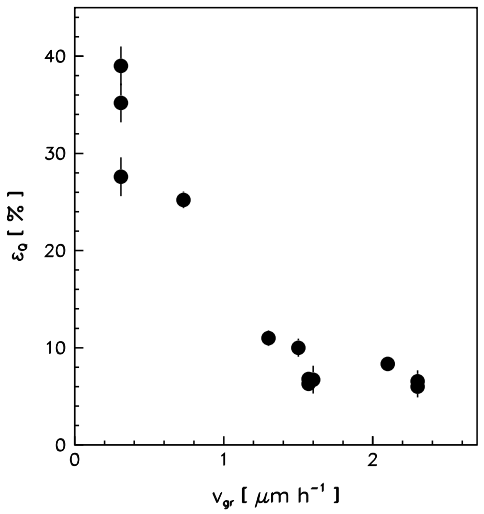

Figure 55: *The dependence of the unprimed charge collection efficiency on the growth rate of the diamond films.*

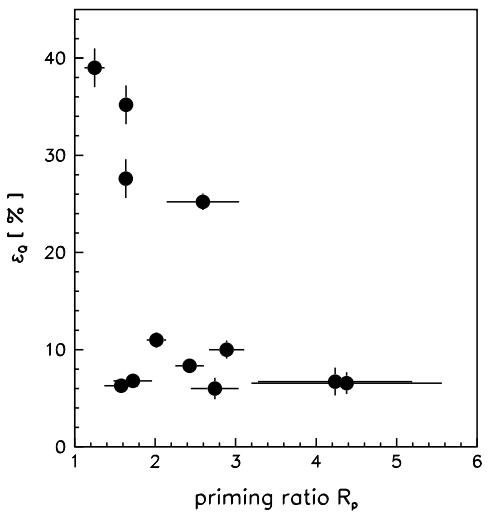

Figure 56: *The dependence of the priming ratio,* R_p*, on the charge collection efficiency,* ϵ_Q*, of the diamond films.*

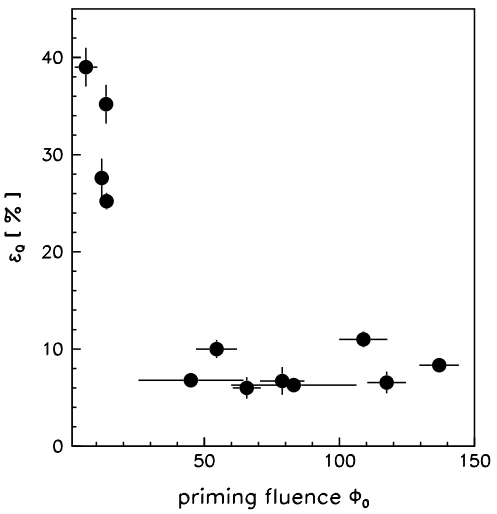

Figure 57: *The dependence of the priming dose, Φ_0 , on the charge collection efficiency, ϵ_Q , of the diamond films.*

($\epsilon_Q < 15\%$). It shows that the trap density is lower for high quality material in agreement with the other correlations.

5.4 Summary and Interpretation

Free standing layers of CVD diamond have been grown in a microwave plasma CVD process under different growth conditions in order to optimise the charge collection efficiency ϵ_Q. It has been found that high values of ϵ_Q are obtained with low growth rates of the diamond films. All samples showed an increase of ϵ_Q under irradiation with β particles, which is known as the priming effect.

The priming dose constant, which is proportional to the electrically active density of traps which can be passivated, varied between the samples from 7 rad to 160 rad, while the priming ratio was found in a range of $1.2 < R_p < 4.2$. A correlation between the charge collection efficiency, priming ratio and priming dose was established. The long lifetime of the primed state at room temperature points to trap levels with activation energies $E_\Delta \gg kT$ being responsible for the priming effect. The existence of two broad trap levels at energies around $E_{\Delta a} \approx 1.66$ eV and $E_{\Delta b} \approx 1.83$ eV in samples prepared in this study was shown in section 4.11.

Higher growth rates lead to the incorporation of more electrically active defects in the crystal. The defects form deep trap levels, which can be deactivated by filling with charge carriers produced by ionising radiation. The low priming dose constants for high quality material indicates a low intrinsic trap density. The priming yield is consequently significantly lower than for low quality material. However the priming yield of low quality material is not sufficient to achieve the ϵ_Q values of the low defect density high quality material.

Further studies are needed to identify the defects limiting the charge collection efficiency and to increase the growth rate for high quality material, thus

minimising the growth time and with it the costs. A possible solution would be to operate at a higher micro-wave power to enhance the growth rate while maintaining the crystal quality. Microwave reactors operating at a power of 50 kW, which is an order of magnitude higher than the power of the reactor used for this study, have been build recently [67] and should be considered for future studies.

6 Radiation Tolerance

Some high energy physics experiments are listed in table 9 with challenging radiation environments and the expected damage fluences of charged and neutral particles in the inner most layer of the vertex detector in units of 1 MeV neutron equivalents in silicon. All these experiments will produce radiation levels at which successful operation detectors made with standard silicon technology[9] will be critical until the end of the detector lifetime.

The term radiation tolerance refers to the amount of radiation a device can absorb without loss of functionality. It is thus clear that for different applications the radiation tolerance varies. This work concentrates on vertex detector devices[10] for colliding beam experiments.

Diamond is reputed to be extremely radiation hard. However, it is important to verify the radiation tolerance of detector grade CVD diamond, since earlier investigations made with CVD diamond were mostly restricted to material of poorer quality. The radiation tolerance has been investigated with neutrons in this study[11]. A decrease of the charge collection efficiency with increasing neutron fluence is found and a damage model is proposed.

Name	r[cm]	damage fluence [1 MeV n cm^{-2} y^{-1}]	Lifetime [y]
HERA-B	1	$3 \cdot 10^{14}$	4
LHC-B	1	$1 \cdot 10^{14}$	> 1
ATLAS	11.5	$6.2 \cdot 10^{13}$	10

Table 9: *List of HEP experiments with high radiation environments. Set out are the radius of the inner layer of the vertex detector, the damage fluence normalised to* 1 MeV *neutrons in silicon and the operational lifetime of the experiment [64, 69, 70].*

6.1 Radiation Damage

Radiation can introduce damage to the crystal lattice by scattering of the projectile off the lattice atom followed by a displacement of the atom from its original lattice site. Depending on the energy transfer the primary knock on atom (PKA) will travel some distance through the bulk before coming to rest at an interstitial lattice site. Along its path the PKA can produce secondary PKAs, creating additional vacancies and interstitials. About 80% of the vacancies are produced in

[9]Strong efforts are currently being undertaken to substantially improve the radiation hardness of silicon [68] to operate at the radiation levels quoted in table 9.

[10]For the description of such devices see chapter 8

[11]The neutron irradiations were carried out in close collaboration with the nuclear measurement technique group at the II. Institut für Experimentalphysik, Universität Hamburg.

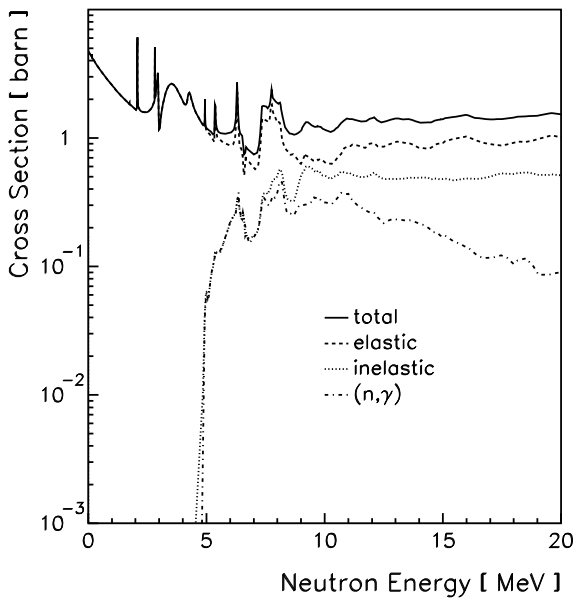

Figure 58: *Total cross section and its composition of inelastic and elastic cross sections for neutrons and carbon up to* 20 MeV. *Also shown is the (n,γ)-reaction dominating the inelastic cross section [72].*

the last third of the primary PKA's track lengths. The greater damage produced can lead to the formation of complex defects in addition to point defects [71].

The total inelastic cross section for nuclear processes in the dominant energy range of about 5 MeV of the neutrons used in this irradiation study is negligible compared to the damage introduced by PKAs. In figure 58 the total and elastic cross sections for neutron interaction in carbon [72] can be seen. Clearly the elastic contribution dominates by orders of magnitude up to about 7 MeV. The contribution of inelastic processes sets in at about 5 MeV with the predominant (n, γ) reaction. For higher neutron energies the inelastic cross section becomes significant but is still smaller than the elastic cross section.

The defect introduction rate is dependent on the particle type and its energy. To facilitate the comparison of the radiation damage introduced by various particle types at different energies the NIEL scaling hypothesis was introduced at first for silicon. It states that the bulk damage depends exclusively on the **n**on **i**onising **e**nergy **l**oss (NIEL). The NIEL value is postulated to scale with the damage yield [68]. By obtaining the NIEL value for different particle types in a large energy range it is possible to calculate the damage produced by different particle sources relative to another. Typically the radiation damage is normalised to the damage produced by one 1 MeV neutron. For silicon the NIEL function is modelled for various particle types (neutrons, protons, pions and electrons) in the energy range of 10^{-7} eV to 10^{7} eV. The situation for diamond is not as advanced and comprehensive damage functions are not yet available.

The method used here to scale the radiation damage to the damage of 1 MeV neutrons is to consult the NIEL for silicon as a rough estimate. This is motivated by findings of a comparative Monte Carlo study [71] on the damage produced by

Name	Source	d[μm]	ϵ_Q[%]	δ_Q[μm]
A3-179a	FHGIsT	50	44.8	22.4
A3-134a	FHGIsT	90	15.4	13.9
DS3	DeBeers	545	14.7	80.1

Table 10: *List of important properties of the samples used for the irradiation experiments. The symbols are d, the sample thickness, ϵ_Q and δ_Q, the primed maximum charge collection efficiency and charge collection distance before irradiation.*

neutrons in silicon and diamond. The energy dependence of the mean number of elastic interaction in diamond and silicon provided by this study shows an energy independent constant ratio between silicon and diamond in the energy range between 1 MeV and 10 MeV within 7%. This suggests that the NIEL scaling for diamond and silicon for neutrons in this energy range is quite similar.

6.2 Experimental Set-up

In this work the radiation resistance to fast neutrons was tested up to a fluence of $6.5 \cdot 10^{15}$ n cm^{-2} with a set of three CVD diamond samples of different quality. Important properties of the three samples are summarised in table 10. The neutron source at the PTB[12] Braunschweig provided fast neutrons with an energy spectrum extending up to 17 MeV and a pronounced peak at 5 MeV. The neutrons are produced by an intense deuteron beam (up to 30 μA) impinging on a Be disc housed in a collimator. The mean neutron energy of the spectrum is approximately 5.1 MeV at a distance of 5 cm from the target. The contribution of backscattered neutrons from the collimator to the total neutron fluence is about 2.6% at 5 cm distance and a maximum fluence rate of $1.8 \cdot 10^{10}$ cm^{-2} s^{-1} can be obtained [73]. The error on the fluence is dominated by the error on the distance from the sample to the neutron source and is typically of the order of 10% for a distance of 5 cm.

The samples were sealed in plastic foil and placed with plastic holders in the centre of the neutron beam and irradiated at room temperature. After each irradiation run the charge collection efficiency, ϵ_Q, the priming fluence, Φ_0, the priming ratio, R_p, and the electrical resistivity, ρ, were determined. Between irradiation runs and characterisation the samples were stored at room temperature. The time span between first and last irradiation run was 18 months.

[12]Physikalisch Technische Bundesanstalt

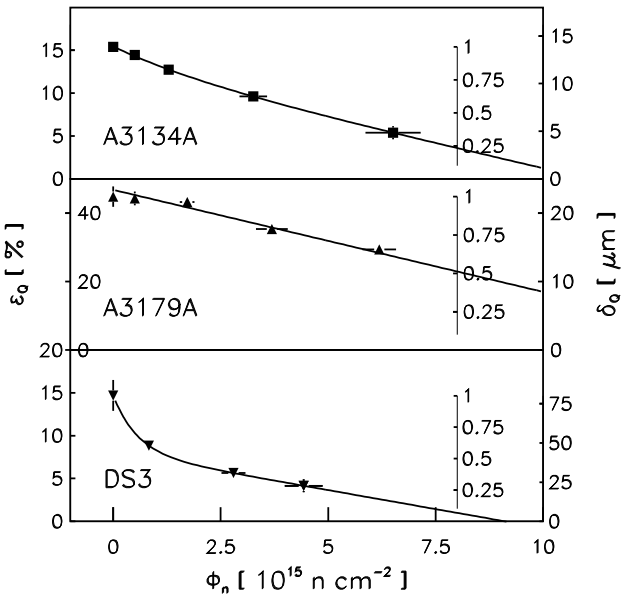

Figure 59: *Change of the average charge collection efficiency (ϵ_Q) vs neutron fluence (Φ_n) for the three investigated samples together with the empirical fit function described in the text. The right scale gives the collection distance (δ_Q) and the inner scale gives the relative change to the unirradiated value.*

6.3 Results

In the following ϵ_Q will denote the saturation value of the charge collection efficiency in the primed state. All samples show a decrease of ϵ_Q and an increase of Φ_0 under irradiation. In figure 59 the dependence of ϵ_Q measured in the primed state on the neutron fluence is depicted together with a fitted function discussed below. The general trend of decreasing ϵ_Q with increasing neutron fluence, Φ_n, is clearly observable but the relative change of ϵ_Q is different for the samples. The loss of ϵ_Q for the samples A3-179A and A3-134A can be parametrised by a linear fit, whereas the behaviour of sample DS3 shows a fast decaying exponential component and a linear component.

To achieve a reasonable description of the experimental data the dependence of ϵ_Q on Φ_n can be fitted with

$$\epsilon_Q(\Phi_n) = \epsilon_Q{}^{ini}\left[R_n\left(1-\frac{\Phi_n}{D_{n1}}\right)+(1-R_n)\left(1-e^{-(\Phi_n/D_{n2})}\right)\right] \qquad (52)$$

composed of a linearly decaying amplitude with the damage constant D_{n1} and an exponential decaying amplitude with damage constant D_{n2}. R_n expresses the ratio of charge collection efficiency loss due to the linear part and the total loss; $\epsilon_Q{}^{ini}$ denotes the value of ϵ_Q prior to irradiation. From figure 59 it can be seen that the proposed fit function 52 gives a reasonable description of the data. The fit parameters for the three samples are summarised in table 11. For sample A3179A the fit was constrained to $R_n = 1$ because of the relatively large errors on the first two data points. The fast decay of ϵ_Q with Φ_n for sample DS3 is reflected in the low value of R_n and D_{n2} relative to the other two samples. For sample A3134A an exponential component in $\epsilon_Q(\Phi_n)$ is clearly present but has

Sample	ϵ_Q [%]	δ_Q [μm]	D_{n1} [10^{15} n cm^{-2}]	D_{n2} [10^{15} n cm^{-2}]	R_n
A3134A	15.5 ± 3.0	13.9 ± 2.7	11.0 ± 3.5	2.1 ± 1.5	0.83 ± 0.13
A3179A	45.6 ± 0.9	22.8 ± 0.4	17.0 ± 1.8	no value	1
DS3	14.7 ± 0.5	80.0 ± 2.8	9.1 ± 0.9	0.6 ± 0.2	0.54 ± 0.02

Table 11: *Summary of the parameters D_{n1}, D_{n2} and R_n and their errors as extracted from the fit to the data. The significance of the symbols is explained in the text.*

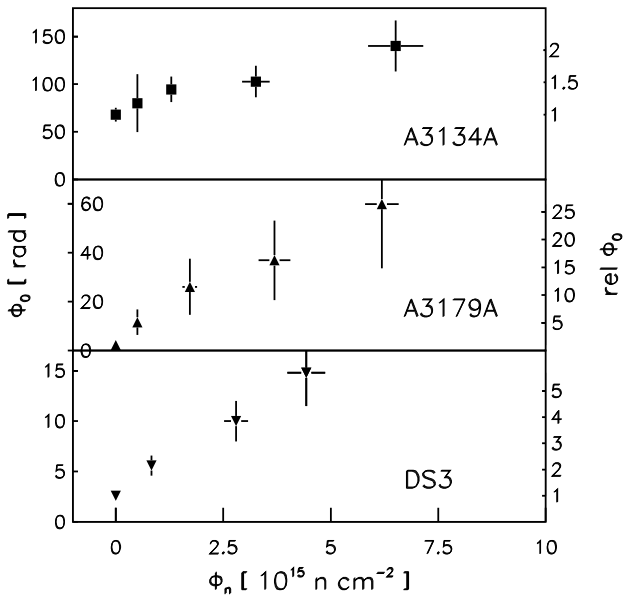

Figure 60: *Change of the priming fluence (Φ_0) vs neutron fluence (Φ_n) for the three investigated samples. The right scale gives the relative change to the unirradiated value.*

less impact on ϵ_Q as the major loss is due to the linear part ($R_n = 0.83 \pm 0.13$). With the assumption that the linear decay of ϵ_Q is a reasonable description also for higher fluences, one can estimate a complete loss of charge collection for all samples at fluences of the order 10^{16} n cm^{-2}.

The priming fluence (see section 4.6), Φ_0, has been determined after each irradiation step. A clear increase of Φ_0 with irradiation fluence, Φ_n, is observed for all samples (figure 60) caused by the introduction of radiation damage related new defect sites in the crystal. However, the behaviour of the priming ratio, R_p, defined as the ratio of unprimed over primed ϵ_Q, is qualitatively different between the A3 series sample and DS3. In figure 61 R_p is plotted versus Φ_n. For the A3 series R_p is increasing while for DS3 a sharp drop of R_p is observed. The remarkable radiation tolerance of the A3 series is a consequence of the increasing value of R_p with irradiation fluence.

Besides the characterisation of the charge collection properties the I-V-curves have been recorded after each irradiation run in the primed state at room temperature. From the linear part of the I-V-curves (see section 4.5) the electrical resistivities were determined. In figure 62 the resistivities of the samples are plot-

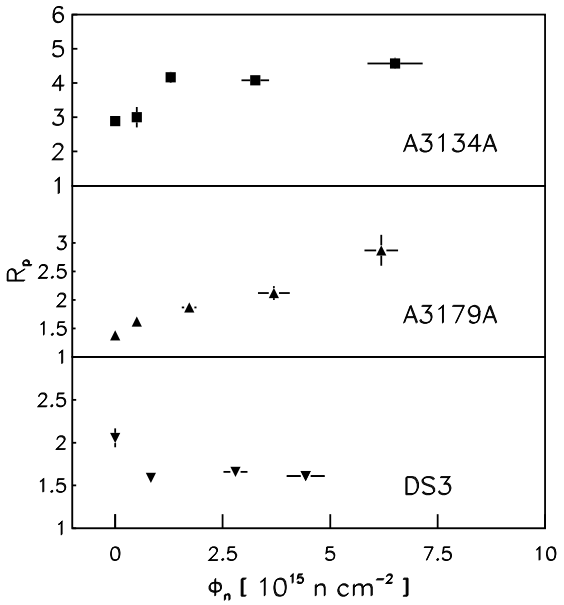

Figure 61: *Change of the priming ratio (R_p) vs neutron fluence (Φ_n) for the three investigated samples.*

ted versus the neutron fluence. A clear decrease in resistivity can be observed for all samples. This can be attributed to the introduction of new defect states increasing the free carrier concentration. The decrease of resistivity is not severe for the detector operation as the resistivity is above $5 \cdot 10^{11}$ Ω cm even at the highest irradiation fluence.

6.4 Comparison to Existing Data

With the advent of detector grade CVD diamond material a number of groups have investigated the impact of radiation on the charge collection efficiency, ϵ_Q. Many studies used neutrons for irradiation, but also data with pions, protons and electrons exist.

An early work from 1956 on the influence of neutron irradiation on the counting properties of natural IIa diamond is presented in [74]. The authors find a decrease of the response to alpha particles approximately proportional to the irradiation dose received. The fluence dependence of the maximum pulse height shows a steep initial decrease and a flattening for higher irradiation times. The pulse height distribution narrows with irradiation time.

In the context of the crystallite layer model[13] [75], a possible interpretation is that the larger crystallites are suffering more from the initial irradiation than the smaller crystallites. This view can be adapted to CVD diamond, consisting of differently sized crystallites separated by disordered regions, the grain boundaries. Results presented in [76] strongly corroborate this view. The paper presents

[13]The crystallite-layer model divides diamond into layers of varying thickness separated by disordered regions.

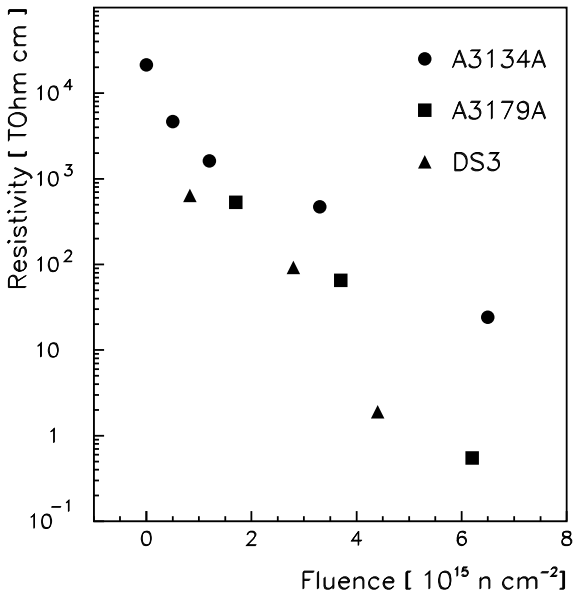

Figure 62: *Electrical resistivities vs neutron fluence for three CVD diamond samples.*

results from irradiation studies with protons (E = 24 GeV) on detector grade CVD diamond. The authors see a deterioration of ϵ_Q for proton fluences greater than 10^{15} p cm^{-2}. The measurement of ϵ_Q was done with MIPs in the fully primed state. The signal spectrum is narrowed with increasing proton fluence, and the average decreases, while the lower tail of the signal spectrum decreases less. For fluences less than 10^{15} p cm^{-2} the authors report an increase of ϵ_Q. However the quoted values of ϵ_Q are taken at a fixed field of E = 0.1 kV/cm despite the saturation value of ϵ_Q used here.

Results on neutron irradiation of detector grade CVD diamond and characterisation of the samples in a defined primed state can be found in [46] where similar results are reported as found in this study. The average value of ϵ_Q in fully primed samples degrades with increasing neutron fluence. The sensitivity of the samples to neutrons varies from no significant degradation to 50% loss of ϵ_Q at about 10^{15} n cm^{-2}. Additionally a narrower signal spectrum with increasing irradiation dose is measured supporting the views expressed in [75, 76]. The same group undertook studies with 300 MeV pions. It was found that a degradation of ϵ_Q is negligible up to a fluence of $5 \cdot 10^{14}$ π cm^{-2}. After a fluence of 10^{15} π cm^{-2} a degradation of roughly 30% was observed. In this study the samples were measured in a defined priming state and it was observed, that the exposure time to beta particles, which was needed to reach the fully primed state (pumping time) was longer for irradiated samples and scaled approximately linearly with the irradiation dose. The pumping time is proportional to the priming constant, Φ_0, used in this study and the behaviour is in qualitative agreement with results presented here.

Another study [77, 78] about radiation damage with neutrons up to the fluence

of 10^{15} n cm^{-2} reports on the increase of ϵ_Q by 30% in polycrystalline CVD diamond. Furthermore, an increase of the electrical resistivity by a factor of 50 after irradiation is observed. It was suggested that the increase of the resistivity and the increase of ϵ_Q is caused by the creation of deep donor and/or acceptor states compensating existing shallow acceptor/donor states and having a smaller trapping cross section. However, the priming effect was not systematically studied before and after irradiation and the priming state of the investigated samples is unclear.

A study with 5 MeV alpha particles [79] and polycrystalline CVD and natural type IIa diamond samples observed a degradation of the charge signal with irradiation fluence. By photoluminescence characterisations they found apparent lattice damage above fluences of $10^{14}\alpha$ cm^{-2} related to the nitrogen vacancy complex.

6.5 Interpretation

The following intermediate conclusions can be drawn:

- CVD diamond withstands radiation levels of 10^{15} n cm^{-2}, 10^{15} p cm^{-2}, $5 \cdot 10^{14}\pi$ cm^{-2} and $10^{14}\alpha$ cm^{-2} without significant loss of ϵ_Q except for single samples.
- Areas with better charge collection are more sensitive to radiation, leading to a uniformisation of ϵ_Q of the different crystallites.
- The radiation induced loss of ϵ_Q can partly be recovered by the priming effect.
- The spread of the present data is huge between different samples and the comparison of data between different groups is difficult due to different characterisation methods.

From the existing data and the data presented here it is evident that there is a qualitative disagreement between some data, namely data reporting on an increase of ϵ_Q with irradiation. However, the reliability of some data is affected by the inexact consideration of the priming effect which distorts the comparison of ϵ_Q before and after irradiation. Also the parameters Φ_0 and R_p have not been determined. Moreover, the spread of the data for different samples is quite large which makes the extraction of conclusive damage constants difficult. It is noticeable that in the data presented here the sample with the highest value of the collection distance, δ_Q, namely sample DS3, is the most sensitive to radiation damage. In the study with pions cited above it is also seen that samples with high values of δ_Q are seemingly more vulnerable to radiation. However, the number of samples is too small to deduce a general behaviour. More studies with the best material available have to be pursued to draw a final conclusion.

Detector type	12 cm strips	pixels
Lifetime [y]	10	10
n-Fluence [1 MeV n cm^{-2} y^{-1}]	10^{14}	10^{14}
Charged hadron fluence [1 MeV n cm^{-2} y^{-1}]	10^{14}	10^{14}
System noise [e]	≈ 5000	≈ 2000
Minimum resolution	digital	digital

Table 12: *Assumed parameters of operation for a vertex detector at LHC.*

The behaviour of a CVD diamond vertex detector in a future HEP scenario at the experiments at the LHC can be projected if typical parameters of operation as reviewed in table 12 are assumed. However the predictive power is questionable in view of the meagre data available, so that assumptions about damage constants and the damage mechanism have to be made. An appraisal to first order is presented in the following under the conditions that

- the damage constants found herein give a reasonable estimate for the sensibility of CVD diamond to radiation damage in general,
- the non-uniformity of the charge collection efficiency can be described by a log-normal distribution,
- regions with high collection efficiency are more sensitive to radiation then regions with low collection efficiency.

The last assumption requires an assumption for the non-uniform damage behaviour. A prediction is made with a damage model discussed in the next section.

6.6 Damage Model

A damage model of CVD diamond must incorporate the polycrystalline structure and the non-uniformity of the material. It is obvious that introducing new defects in material with a high defect concentration will alter the properties less strongly than in material with a low defect concentration. Thus the model must include the non-uniform distribution of ϵ_Q which is related to the non-uniform defect concentration, and predict the change of ϵ_Q with increasing defect density.

The relation between carrier lifetime and defect density is given by

$$\delta_Q \propto \tau \propto \frac{1}{(N_0 + \Phi_n g_n)}, \tag{53}$$

with N_0 the intrinsic defect density and $g_n \equiv \mathrm{d}N_n/\,\mathrm{d}\Phi_n$ the defect introduction rate. The relation follows from equations (25), (27) and equation (30) discussed in chapter 3.

In the following the term "defect" denotes an effective defect as various types of defects with different concentrations, cross sections and energy levels are present. The specific damage model proposed here must include the priming effect, and thus the defects are categorised into *residual defects* and defects which can be passivated by the priming process, called *primable defects*. This replaces the terms N_0 and g_n in equation (53) which becomes

$$\delta_Q \propto \tau_e + \tau_h \propto \frac{1}{(N_{r0} + N_{p0} + \Phi_n(g_{n,r} + g_{n,p}))}, \tag{54}$$

with τ_e and τ_h being the lifetime of electrons and holes, N_{r0} the residual defects, N_{p0} the primable defects, $g_{n,r} \equiv \mathrm{d}N_{n,r}/\,\mathrm{d}\Phi_n$ the introduction rate of residual defects and $g_{n,p} \equiv \mathrm{d}N_{n,p}/\,\mathrm{d}\Phi_n$ the introduction rate of primable defects. From equation (54) the priming ratio R_p can be predicted as

$$R_p = \frac{N_{r0} + N_{p0} + \Phi_n(g_{n,r} + g_{n,p})}{N_{r0} + \Phi_n g_{n,r}}. \tag{55}$$

The priming dose constant, Φ_0, was defined in section 4.6 by the fit function

$$\delta_Q(\Phi) = \delta_{Q,0} + \delta_{Q,+}\left(1 - \exp\left(-\frac{\Phi}{\Phi_0}\right)\right), \tag{56}$$

with $\delta_Q(\Phi)$ the collection distance as a function of the absorbed dose of ionising radiation Φ, $\delta_{Q,0}$ the unprimed collection distance and $\delta_{Q,+}$ the increase of the collection distance through the priming process. With equation (54) the collection distance and the defect concentrations can be related by

$$\begin{aligned} \delta_{Q,0} &\propto \frac{1}{N_r + N_p} \\ \delta_{Q,+} &\propto \frac{N_p}{N_r^2 + N_p N_r} \\ \delta_Q(\Phi) &\propto \frac{1}{N_r + c(\Phi) N_p} \end{aligned}$$

with $c(\Phi)$ a function describing the fraction of free primable traps and the effective residual and primable trap concentrations, $N_r(\Phi_n) = N_{r0} + \Phi_n g_{n,r}$ and $N_p(\Phi_n) = N_{p0} + \Phi_n g_{n,p}$.

For $\Phi \equiv \Phi_0$ according to equation (56) one can write

$$\frac{\delta_{Q,0} + \delta_{Q,+} - \delta_Q(\Phi_0)}{\delta_{Q,+}} = \exp(-1) \tag{57}$$

or expressed with defect densities

$$1 + \frac{N_r}{N_p}\left(1 - \frac{N_r + N_p}{c(\Phi_0)N_p + N_r}\right) = \exp(-1), \tag{58}$$

so if the function $c(\Phi)$ is known the priming dose constant Φ_0 can be calculated from N_r and N_p.

With the assumption that the probability of a free carrier to be trapped in a primable trap is given by the ratio of the free primable traps over all available traps the function c has to fulfil the differential equation

$$\frac{\mathrm{d}c}{\mathrm{d}\Phi} = -a\frac{1}{N_p + c^{-1}N_r} \tag{59}$$

with a a factor related to the number of charge carriers produced per absorbed dose Φ. In a model fit c has been implemented numerically. The data was normalised to the value of Φ_0 prior to irradiation to fit the relative change in Φ_0 and not the absolute values, thus cancelling the factor a.

To find realistic values for the parameters in equation (55), the experimental data of the three samples was fitted with the damage model. The fit was constrained to the measured unirradiated values of δ_Q and R_p for each sample, which determined the parameters N_{r0} and N_{p0}. The free parameters of the fit were the introduction rates of residual and primable defects, $g_{n,r}$ and $g_{n,p}$.

To account for the non-uniform distribution of δ_Q, which was related to the trap density by equation (54), the fit included an integration over the distribution of δ_Q. The shape of the distribution was assumed to be equal to the experimentally found shape of the distribution of the average signal over the active detector area (section 8.4.5). The shape is described by a log-normal distribution

$$f(x) = N \cdot \exp\left(-\frac{\log(a_0 \cdot x - x_0)^2}{\sigma_0^2}\right). \tag{60}$$

The parameters are N a normalisation factor, a_0 a scaling factor, x_0 an off-set and σ_0 the width. The log-normal distribution was fitted to the spatial distribution of the average signal over the active area of a CVD diamond detector. The mean of the spectrum is proportional to $\langle\delta_Q\rangle$ and the shape represents a typical distribution of δ_Q across the detector area. The fit of the log-normal shape to the data is shown in figure 63. In the damage model fit the shape was scaled to meet the unirradiated value of δ_Q for the sample.

The result of the simultaneous fit of the experimental values of ϵ_Q , R_p and Φ_0 for the three samples is depicted in figure 64. The description of ϵ_Q and R_p is good while the fit function gives a reasonable description of the relative change of Φ_0 for sample A3134A but is systematically higher for the other two samples DS3 and A3179A. The values of the total introduction rate of residual and primable traps and the fraction of introduced residual defects as determined from the fit are summarised in table 13.

The total introduction rate is similar for samples DS3 and A3179A, both samples of high quality, and is about a factor seven higher for sample A3134A. On the other hand the fraction of residual traps is similar for samples A3134A and

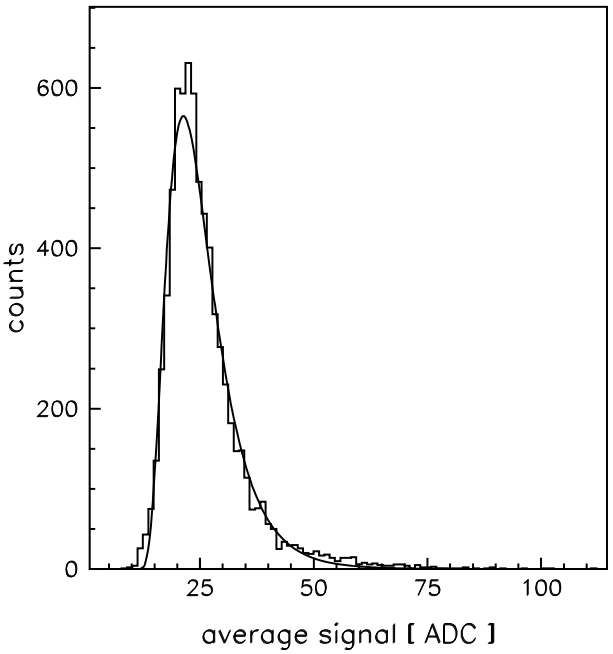

Figure 63: *Distribution of the average signal of* 50 μm $\times$ 50 μm *bins measured with* 5 GeV *electrons as described in section 8.4.5. The fit with function 60 is also shown.*

Sample	f_r	g_n	χ^2/dof
A3134A	$0.1566 \pm 0.23 \cdot 10^{-4}$	$18.895 \pm 0.624 \cdot 10^{-3}$	1.9
A3179A	$0.14807 \pm 0.21 \cdot 10^{-5}$	$2.591 \pm 0.933 \cdot 10^{-3}$	2.9
DS3	$0.69231 \pm 0.67 \cdot 10^{-5}$	$2.759 \pm 0.11 \cdot 10^{-3}$	11.5

Table 13: *Fit results for the fraction of residual traps,* f_r*, and the total introduction rate,* g_n*, obtained with the damage model described in the text and a simultaneous fit. The symbol* $f_r = \frac{g_{n,r}}{g_{n,p}+g_{r,p}}$ *denotes the fraction of introduced residual traps and* $g_n = g_{n,r} + g_{n,p}$ *is the total introduction rate of traps.*

A3179A and a factor three larger for sample DS3. Recalling that the definition of defect introduction rate used here is an effective introduction rate, the large variation can be interpreted as an evidence for a more complicated interplay of defects present and defects introduced. It is noticeable that the two samples with initial good collection properties DS3 and A3179A have a similar introduction rate. The variation of the fraction of introduced primable defects is less dramatic between the samples. Also here it is remarkable that the samples A3134A and A3179A, which were both produced by one manufacturer in the same reactor show a comparable value, while DS3 originating from another source and a different process has a higher value. This points to a process dependence of this property.

The number of samples is too limited to derive a general damage behaviour for CVD diamond, however to predict a damage scenario a bad case and a good case of damage behaviour is deduced from the data and compared. For the bad case scenario (A) the damage constant and the high fraction of introduced residual defects of sample DS3 are considered, while for the good case (B) the introduction rate and the low fraction of introduced residual defect of sample A3179A are taken. Very recently charge collection distances well above $\delta_Q > 200$ μm [46] for selected samples, equivalent to a signal of more than 7200 e on average for a MIP have been reported. The hypothetical CVD diamond detector in this damage projection is thus equipped with a most probable signal[14] $Q_{mp} = 7200$ e which seems a conservative estimate looking at the large progress made in CVD diamond fabrication during the last years (see chapter 1). It is further assumed that the non-uniformity of the charge collection properties is described correctly by the log-normal shape (equation 60) introduced above. The model presented here incorporates the non-uniformity of δ_Q typically found in CVD diamond. With the formalism discussed above a prediction about the change of the δ_Q spectrum with absorbed irradiation dose is possible by using equation 54. The complete sets of parameters for case (A) and case (B) are summarised in table 14. With these parameter sets the model is used to predict the spectrum and the average signal for a MIP as a function of the irradiation fluence, Φ_n, in the next section.

6.7 Damage Projection for the LHC

6.7.1 Particle Fluxes of ATLAS at the LHC

In the previous section a model was developed to predict the changes of charge collection properties with the fluence of 1 MeV neutrons. Two damage case scenarios (A) and (B) were defined to have a realistic estimate of the material quality of a CVD diamond vertex device. To make a projection of the damage behaviour of the device, when used at the LHC, the expected fluences of charged

[14] The average signal, Q_{ave}, is higher than the most probable signal, Q_{mp} due to the asymmetric shape of L and V_ϵ. The ratio is measured in CVD diamond to be typically $Q_{ave}/Q_{mp} \approx 1.3$.

Case	Q_{mp} [e]	f_r	g_n	σ_0	x_0
(A)	7200	0.69	2.76	0.7	0.95
(B)	7200	0.15	2.59	0.7	0.95

Table 14: *Parameter sets for case (A) and case (B) used to simulate the damage behaviour of CVD diamond. The symbols are Q_{mp} the most probable charge signal of a MIP, f_r the fraction of introduced residual traps, g_n the total trap introduction rate, σ_0 the width and x_0 the set-off parameter of the log-normal shape used to describe the non-uniformity of the charge collection properties.*

and neutral particles for a specific distance from the interaction point have to be normalised to 1 MeV neutron equivalents to be used in the damage model.

As mentioned above a NIEL function is not available for diamond and thus an approximation for the scaling of damage with particle type and energy has to be made. For a rough estimate the same NIEL scaling as for silicon is assumed. This allows to use calculations of the particle fluxes in the ATLAS SCT (Semiconductor Tracker) made for silicon by G. Gorfine as described in [64]. For the calculation a p-p cross section of 71 mb and a luminosity of 10^{34} cm^{-2} s^{-1} were assumed, the inner region is enclosed in a solenoidal magnetic field of 2 T and the operational year is defined by 10^7 s. Table 15 taken from [64] summarises the data of the annual expected fluences at different radii and averaged over the z-range quoted.

Radius [cm]	z [cm]	Neutron	Charged	Total
11.5	±35	12	50	62
14.5	±40	9.3	34	43
20.0	±55	8.2	19	28
30.0	±95	6.2	10	17
40.0	±95	6.0	6.5	12
50.0	±95	5.9	4.4	10
60.0	±95	5.0	3.1	8.1
69.0	±95	4.6	2.3	6.9

Table 15: *Annual equivalent damage fluences (*1 MeV n *in Si) in the ATLAS SCT for neutrons and charged particles in units of* [10^{12} n cm^{-2} y^{-1}] *from [64].*

At smaller radii the charged particles dominate the total damage fluence while for outer regions the omnipresent neutron background prevails.

The NIEL scaling factor of $\kappa = 1.4$ [80] to express the damage produced by the neutron spectrum of the irradiation experiment in 1 MeV n equivalents is used to adjust the damage parameters in table 14. The scaling factor was calculated

using the NIEL function for silicon.

6.7.2 Performance Projections

For the application as a vertex detector the hit detection efficiency, ϵ_r, as a function of the signal-to-noise threshold, S_{thr}, is an important figure when evaluating the applicability of CVD diamond. The signal spectrum of the detector is a convolution of the distribution of the deposited charge, L, the distribution of the collection efficiency, V_ϵ, and a Gaussian distribution from the amplifier noise, G. From the amplifier the constant noise term, σ_{ENC}, and the noise coefficient for the load capacitance, $\mathrm{d}\sigma_c/\mathrm{d}C$, must be known to determine the noise. If the signal spectrum and the amplifier noise is known, the relation between ϵ_r and S_{thr} is given by

$$\epsilon_r(S_{thr}) = \frac{1}{N_\epsilon} \int_{q_o}^{\infty} qV_\epsilon \otimes L(w_l, Q_{mp}) \otimes G \ \mathrm{d}q \tag{61}$$

with

$$\begin{aligned} N_\epsilon &= \int_{-\infty}^{\infty} qV_\epsilon \otimes L(w_l, Q_{mp}) \otimes G \ \mathrm{d}q \\ q_0 &= S_{thr} \cdot \sqrt{\sigma_{ENC}^2 + \left(\frac{\mathrm{d}\sigma_C}{\mathrm{d}C} \cdot C_{load} \right)^2} \end{aligned}$$

and $L(w_l, Q_{mp})$ being a parametrisation of the Landau distribution with the FWHM, w_l, and the most probable amount of deposited charge, Q_{mp}. The FWHM of the Landau is given by $w_l = 4.018 \cdot ZN_\alpha \frac{k}{\beta^2} d$ [7] where $Z = 6$, N_α the number of atoms per unit volume, $k = 2.55 \cdot 10^{-19}$ eV$/atom$ the extinction coefficient, $\beta = v/c$ and d the detector thickness.

An important parameter which has not been taken into account when calculating ϵ_r is the leakage current drawn during operation. However, in diamond the leakage current is negligibly small compared to silicon and it was shown that it does not increase critically with irradiation. As a consequence it is ignored.

The formalism is used to determine the damage behaviour of CVD diamond with the fluence projection for the ATLAS LHC experiment. The typical signal spectrum for a MIP is calculated as a function of the operational year at two different radii from the interaction point. As discussed above the figure of merit is the signal detection efficiency. In the following the threshold values for detection efficiencies of 99% and 95% respectively are deduced from the signal spectrum. The signal significance is calculated with a noise figure of the amplification device.

The simulated charge spectra for 0,1,5 and 10 years of operation at the LHC for two $d = 500$ μm thick CVD diamond detectors with properties as listed in tab. 14 of case (A) and (B), for two radii $r_1 = 30$ cm and $r_2 = 11.5$ cm are depicted in figure 65. For case(A) a clear shift of the most probable value for a

radius of $r = 11.5$ cm is observed, but the lower part of the Landau spectrum is less affected. For case (B) the change in the spectrum is marginal also for the smaller radius. In general the Landau spectrum gets narrower with increasing radiation in agreement with the experimental observations reported in [76]. The effect of radiation on the average signal and the detection threshold is shown in figure 66.

The calculations show that the average signal for case (A) at a radius of 11.5 cm will decreases in 10 operational years of LHC by 51% from 9329 e to 4547 e, while the threshold for 99% efficiency will decrease by 33% from 4229 e to 2843 e and the threshold for 95% efficiency will decrease by 37% from 5069 e to 3179 e. Thus the radiation damage on the threshold value is less severe than on the average signal. For a CVD diamond with the more optimistic damage constants of case (B) the effect of 10 years LHC at $R = 11.5$ cm is naturally less dramatic. The average signal will decrease by 18%, while the threshold for 99% efficiency will drop by 9% to 3851 e and for 95% efficiency by 12% to 4481 e.

Candidates for the read-out electronics for the LHC include the FELIX chip for a strip configuration and the BIER-PASTIS chip for a pixel configuration. The noise performance of the FELIX chip for fast read out (25 ns, deconvolution mode) is $\sigma_{ENC} = 698$ e + 101 e/pF. The BIER-PASTIS pixel chip operates in a digital mode, thus a threshold is set to discriminate amplifier noise from signal. Typical threshold values for this chip are about $\sigma_{thr} = 1750$ e.

The capacitative load of a strip detector is composed of the strip to backplane capacitance C_{bck} and the inter-strip capacitance C_{str}. The backplane capacitance C_{bck} is approximated by

$$C_{bck} = \epsilon_0 \epsilon A_{str}/d$$

with A_{str} the covered area of the strip and $\epsilon = 5.5$ for diamond. The inter-strip capacitance is estimated with an empirical formula from a study presented in [81]. There it was found in an investigation of silicon strip detectors with different geometries, that the inter-strip capacitance is dependent on the strip width to pitch ratio, $R_{w/p}$, and can be described by the empirical formula

$$C_{str}/L = (0.458 + 2.089 \cdot R_{w/p}) \text{ pF cm}^{-1}.$$

To adopt this formula to diamond, C_{str} is multiplied with $\epsilon(diamond)/\epsilon(Si) = 0.46$ under the assumption that the air contribution to C_{str} is small. For a typical ATLAS configuration of strips with 50 μm pitch, 25 μm width and $L = 12$ cm length for $d = 500$ μm thick diamond detector, the total capacitive load amounts to

$$C_\Sigma = C_{bck} + C_{str} = 0.29 \text{ pF} + 14.06 \text{ pF} = 14.35 \text{ pF}.$$

With this value the noise figure of the FELIX chip in this configuration is $\sigma_{ENC} = 2147$ e.

Taking these values, the performance can be calculated in view of the signal-to-noise (FELIX) and signal-to-threshold (BIER-PASTIS) ratios for 99% and 95%

Case	Read-Out	R [cm]	time [y]	95%	99%	ave.
A	FELIX	11.5	0	2.36	1.97	4.35
			10	1.48	1.32	2.12
		30	0	2.36	1.97	4.35
			10	2.03	1.73	3.37
	BIER-P.	11.5	0	2.90	2.42	5.33
			10	1.82	1.62	2.60
		30	0	2.90	2.42	5.33
			10	2.49	2.13	4.13
B	FELIX	11.5	0	2.36	1.97	4.35
			10	2.09	1.79	3.58
		30	0	2.36	1.97	4.35
			10	2.28	1.93	4.12
	BIER-P.	11.5	0	2.90	2.42	5.33
			10	2.56	2.20	4.39
		30	0	2.90	2.42	5.33
			10	2.80	2.37	5.06

Table 16: *Signal-to-noise (FELIX) and signal-to-threshold (BIER-PASTIS) projection for a CVD-diamond detector device (pixel and strip read-out, strip length 30 cm, 50*μm *pitch, 25*μm *strip width) for two damage scenarios case (A) and case (B) as discussed in the text.*

efficiency and the average ratio as summarised in table 16. The estimation can not be very precise as it does not include a possible change of the noise figure of the read-out electronics due to radiation damage nor the effect of charge-division (see chapter 8). However it seems that the pixel configuration will successfully operate after 10 year LHC at $r = 11.5$ cm in both damage scenarios. A safety margin of 0.6 σ_{thr} for case A and 1.2 σ_{thr} for case B over detection threshold for 99% efficiency is maintained. The strip detector configuration suffers from the additional load-capacitance and the inevitably higher noise. In case A the S/N ratio for 99% efficiency at $r = 11.5$ cm drops to 1.32, while for case B it drops to 1.79. A successful operation in this particular case study is dependent on the tolerable percentage of fake hits and the surrounding tracking environment. However if material with better collection properties is available the operation of a strip detector may become feasible.

6.8 Summary

The behaviour of the electrical properties of three CVD diamond samples of different qualities has been tested after irradiation with fast neutrons with fluences

up to several 10^{15} n cm^{-2}. The resistivity, the charge collection efficiency, the priming fluence and the priming ratios were recorded for different levels of irradiation. The change of the latter three properties can parametrised by a herein proposed damage model and simultaneously fitted with reasonable accuracy. The extracted damage constants were used to predict the change in the signal spectrum of a hypothetical CVD diamond detector with a most probable signal of 7200 e in the ATLAS environment for ten years operation at the LHC. The results show that operation of a pixel device is not likely to be critical while a strip detector configuration is restricted by its higher noise level.

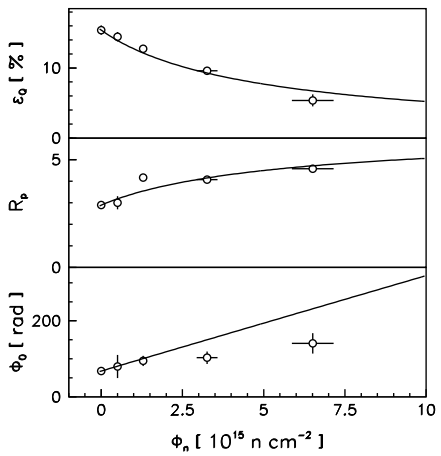

(a) Sample A3134A

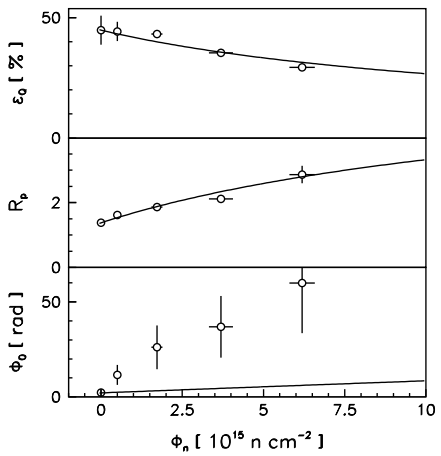

(b) Sample A3179A

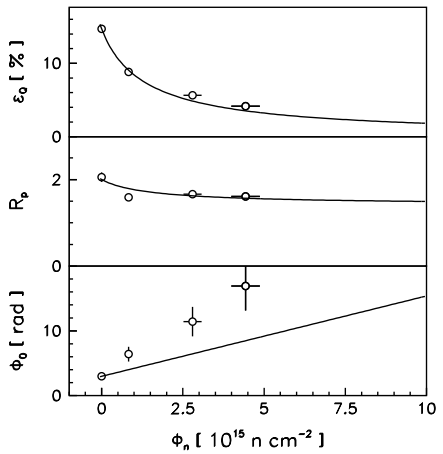

(c) Sample DS3

Figure 64: *Simultaneous fit of the damage model described in the text to the experimental values of the charge collection efficiency (ϵ_Q), the priming ratio (R_p) and the priming fluence (Φ_0) for the three investigated samples.*

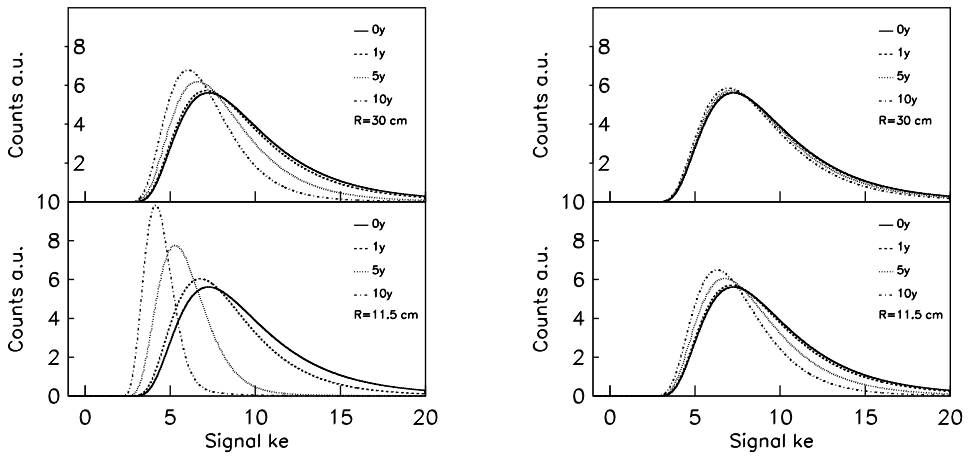

(a) (b)

Figure 65: *Simulated signal spectra for a* $d = 500$ μm *thick CVD diamond detector for two cases (A) and (B) of damage properties (see text) and at two radii* $r_1 = 30$ cm, $r_2 = 11.5$ cm *in the ATLAS experiment at LHC for 0, 1, 5 and 10 years of operation.*

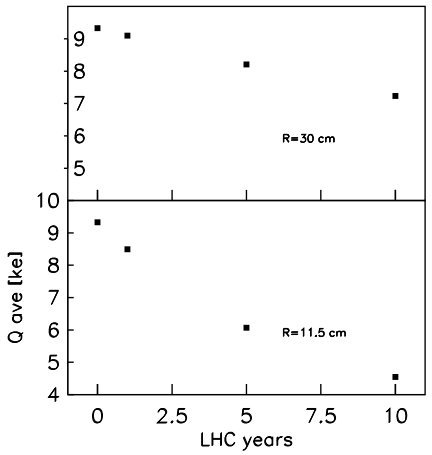

(a) Average signal for a MIP, case (A).

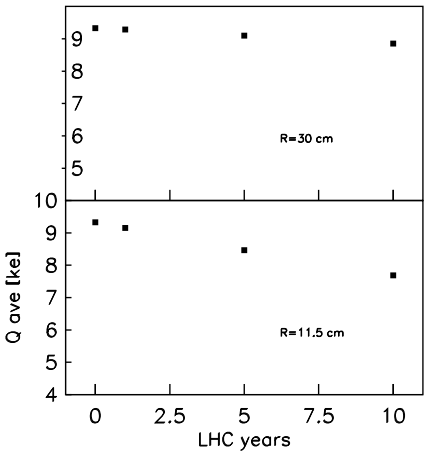

(b) Average signal for a MIP, case (B).

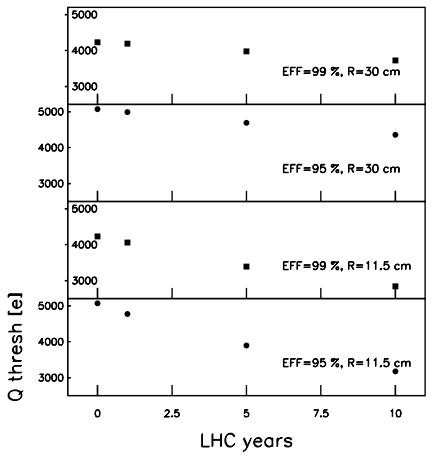

(c) Thresholds, case (A).

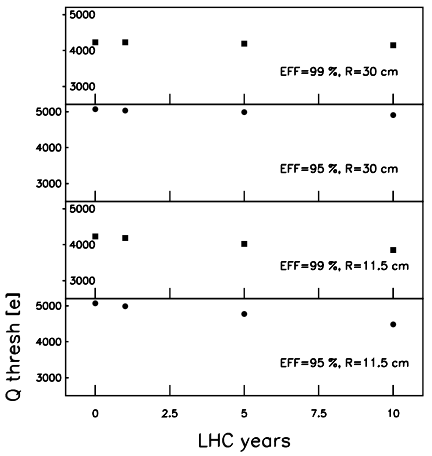

(d) Thresholds, case (B).

Figure 66: *Average signal and detection threshold for 99% and 95% efficiency as a function of operational year at the LHC in the ATLAS experiment at the radii* $r_1 = 30$ cm *and* $r_2 = 11.5$ cm *for a* $d = 500$ μm *thick CVD diamond detector for two cases (A) and (B) of damage properties (see text).*

7 A Model of the Charge Drifting in CVD Diamond

In this chapter a new model is proposed to describe the charge drifting process in CVD diamond and model calculations are compared with experimental data for different types of ionising particles.

The charge drifting process is determined by the properties of the CVD diamond film. On a microscopic scale the film is a heterogeneous composition of single crystallites of different sizes and orientations. At the boundaries of the crystallites the lattice is highly distorted and the electrical qualities are expected to be very different from the intra-grain regions. This is supported by observations showing that the impurity concentration is strongly enhanced at grain boundaries [55, 50] (see section 4.4). The role of grain boundaries in the carrier drift process has been subject of a lengthy and controversial discussion. On one side the opinion has been raised that the influence of grain boundaries is negligible for the carrier drift process [10]. It is argued that the carrier drift length is essentially the same when measured across multiple grain boundaries and when measured along the columnar direction of the grains.

Another opinion, which is favoured by the author, considers the grain boundaries as areas with a high trap density, where charge carriers are very likely to recombine or being trapped. This view is supported by Manfredotti and others in [82]. In the cited reference spatially resolved measurements of the charge collection efficiency on the surface of fracture perpendicular to the direction of growth of a CVD diamond sample gives evidence that the boundaries contain more electrically active defects than the intra-grain regions. The studies with EBIC presented in this work (see section 4.10) strongly corroborate this view.

It is desirable to find a model which can describe qualitatively and if possible quantitatively the charge drifting behaviour found in CVD diamond, while incorporating its typical structure of columnar growing crystallites. In the following a coordinate system (x, z) is used with z along the direction of growth, substrate side at $z = 0$ and growth side at $z = d$, and x perpendicular to z.

In a model proposed by Zhao [10], the charge collection distance, δ_Q, is linearly dependent on z:

$$\delta_Q(z) = \delta_0 + z \cdot \rho \tag{62}$$

with δ_0 the collection distance at the substrate side, i.e. at $d = 0$, and ρ a linear coefficient describing the increase of δ_Q with the film thickness. The analytical expression predicts an increase of the collection distance averaged over the thickness when material is removed from the substrate side. This is in qualitative agreement with observations made in [10, 46]. By calculating the induced charge using equation (24), the model can be used to predict the thickness of optimum signal for a given set of parameters ρ, d and δ_0. Examples are shown in fig. 67[15]

[15] The results shown here have been obtained by numerical methods. For a complete analytical

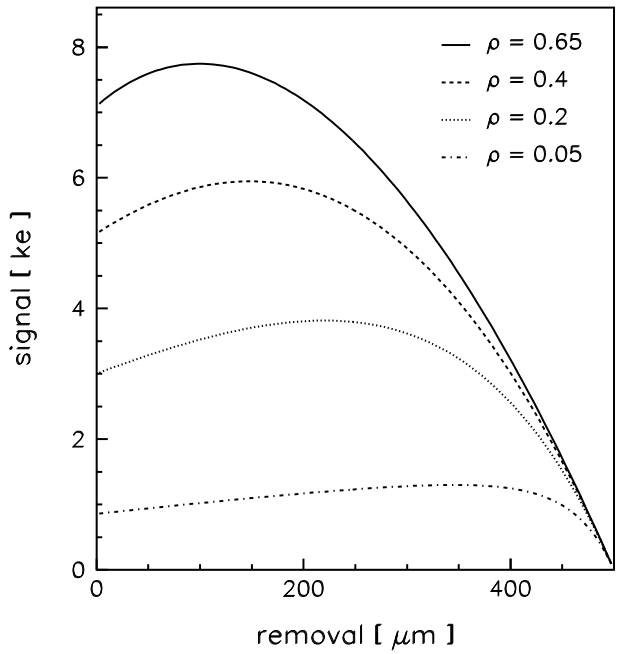

Figure 67: *Dependence of the charge signal of a MIP in a* 500 μm *thick CVD diamond detector on the amount of material removed from the substrate side. The calculation is based on a distribution of* δ_q *according to the linear model with different values of the parameter* ρ *as explained in the text.*

for 500 μm thick diamond with different values of ρ and $\delta_0 = 0$ μm. In the calculation no re-injection of charge carriers at the contact is assumed. The induced charge reaches a maximum which is dependent on ρ. The model seems to describe successfully the average charge drifting properties of the bulk. However, it does not incorporate structural information.

Another ansatz followed here is to take the structure of CVD diamond into account and to base the lifetime distribution of the charge carriers on microscopic rather than macroscopic assumptions. The two microscopic assumptions of the model are

A–I The impurity concentration is significantly enhanced at grain boundaries. Thus the lifetime at grain boundaries is assumed to be very low compared to intra-grain regions.

A–II The charge carrier lifetime, τ_x, is dependent on the shortest distance to the next grain boundary and is described by

$$\tau_x = \tau_0 \cdot (1 - e^{-\frac{r}{r_0}}) \tag{63}$$

with r the shortest distance to next grain boundary, τ_0 the maximum lifetime and r_0 the *lifetime length.*

Assumption A–I is supported by SIMS measurements presented in section 4.4. Furthermore measurements with alpha particles [55] (section 4.8), protons [55, 84] (section 4.9), and EBIC measurements (section 4.10) indicate, that the grain

approach the reader is referred to [83].

boundaries possess a high defect density which leads to preferred trapping and recombination in these areas.

Assumption A–II is motivated by the growth process of the crystallites. While the crystallites gain width the collision of differently oriented crystallites produces zones with a high lattice defect density and strain [85, 44]. The defect density and the strain decreases with distance from the zone of encounter. The lattice defects distort the band structure and form trapping and recombination centres [51] and thus the lifetime of the charge carriers should decrease in the vicinity of the grain boundaries. The defect density distribution near grain boundaries in polycrystalline CVD diamond has not yet been determined. The exponential used in the model to describe the lifetime dependence on the distance to the grain boundary is a plausible assumption.

7.1 A simple CVD diamond growth generator

The aim of the growth generator is to provide a realistic approximation of the crystal structure of CVD diamond. The model calculations were restricted, due to the available computing power, to two dimensions with a granularity of $\Delta x = \Delta z = 1$ μm. A coordinate system is chosen with z along the direction of growth, and the substrate side at $z = 0$; and x running parallel to the growth and substrate side. The space is divided into squares r_{ij} of 1 μm side length with the indices i and j determining the position $x = i \cdot \Delta x$ and $z = j \cdot \Delta z$ of the square.

To model the geometry of the grain boundaries in polycrystalline CVD diamond a simple algorithm has been used. The algorithm starts with a maximum seed density and gives each grain an equal probability to grow laterally (lateral growth probability κ_l) while increasing the film thickness. The resulting conflict between different grains claiming the same space element r_{ij} is solved by randomly assigning space to one of the grains. The probability for one grain to defeat another is weighted by the lateral width of the conflicting grains. This results in the behaviour that large grains become larger and small grains become smaller and finally get overgrown. The model is a simplification of the model of Van der Drift [86], who based the evolution of the crystal film on the initial distribution of the orientation of the seed crystallites. He then assigned different growth speed to the crystal planes. This results in different growth speeds for crystallites of different orientations. The crystallites with larger growth speed are overgrowing slower neighbours. Since the growth speed is dependent on the crystallite orientation the fastest growing orientation will prevail resulting in a texture in the film. In the end both growth models lead to similar results of the growth morphology. However, the model proposed here uses a stochastic growth-process leading to a more irregular pattern which comes closer to the actual pattern found in CVD diamonds.

Sample patterns generated with the algorithm for different lateral growth probabilities are shown in fig. 68. The growth model develops structures which

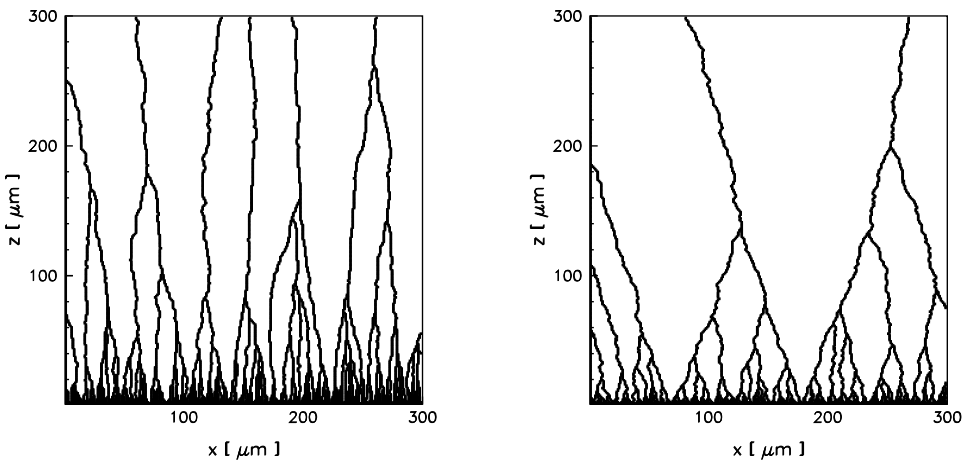

(a) $\kappa_l = 0.2$ (b) $\kappa_l = 0.5$

Figure 68: *Sample patterns produced by the growth algorithm for two different lateral growth probabilities* $\kappa_l = 0.2$ *(a) and* $\kappa_l = 0.5$ *(b). The grain boundaries are shown in black.*

are similar to structures seen on SEM pictures taken of the edge of CVD diamond samples (see section 4.1). The patterns define single grains with a resolution of 1 μm. In a second step each space element r_{ij} is assigned to a specific lifetime τ_{ij}. The lifetime is calculated according to equation (63).

7.2 Simulation of the Charge Carrier Drift Process

The charge carrier drift process is simulated by tracing the path of each charge carrier produced in an ionisation process in the bulk. The continuous drift process is described by calculating the drift path and trapping probability of each carrier in time slices of $\Delta t = 1$ ps. The bulk is modelled two dimensionally by a grid of space elements with spacing $\Delta x = \Delta z = 1$ μm. The drift direction is determined by the local electric field vector and thermal diffusion. The drift speed is derived from the local electric field strength and the mobility which is a function of the electric field (see chapter 3). The self-interaction of the free carriers is neglected. The lifetime is dependent on the position in the bulk as described by the growth generator. The probability of a carrier not to be trapped in the volume element at position $\vec{r} = (x, z)$ is given by

$$w_x = \exp\left(-\frac{\Delta t}{\tau_x(\vec{r})}\right) \tag{64}$$

with $\tau_x(\vec{r})$ being the lifetime of charge carrier type x at $\vec{r}$. The simulation stops when all charge carriers are trapped or reached the electrodes.

The induced signal on the electrodes is calculated with the weighting field method [87]. In the case of a plate capacitor configuration, the induced charge from one carrier is simply proportional to the drift distance in z. The weighting field method for a strip configuration is discussed in appendix A.3.

After each event charge is trapped in the bulk at various places, the amount depending on the lifetime distribution. The trapped charges create an electric field which is calculated and superimposed on the applied field after each event. On average the field of the trapped charges is opposed to the applied field leading to polarisation effects.

The code used for the simulation of the charge carrier drift process was based on a program written by David Fish, Rutgers University, NJ, USA. Additional routines for the calculation of the polarisation field due to trapped charge and the tracing of charge according to the local electric field vector under consideration of the field dependence of the mobility were added. The trap probabilities were calculated according to the lifetime distribution from the growth generator.

7.3 Implementation of Traps

Various trapping centres at different energy levels and with different cross section are present in diamond. From TSC measurements some peaks corresponding to different traps can be detected (section 4.11). The effect of traps on the lifetime was discussed in section 3.4. The priming effect (see section 4.6) demonstrates that traps can be passivated by ionising radiation. To accommodate the experimental facts an empirical approach was followed to implement trap densities and cross section. In the following all traps levels which might be present are described by an effective cross section σ_x and an effective trap density ρ_x. The trapping and recombination process was assumed to be independent of the charge carrier type, i. e. electrons and holes were assumed to be equivalent. Furthermore, thermal emission is neglected assuming that the activation energies of the relevant traps are well above the thermal energy $E_\Delta \gg kT$ at room temperature $T = 300$ K.

It is recalled that the charge collection distance δ_Q was defined as

$$\delta_Q = \delta_e + \delta_h = E \cdot (\mu_e \tau_e + \mu_h \tau_h). \tag{65}$$

The probability that a charge carrier (electron $x = e$ or hole $x = h$) will not be trapped after travelling a path length Δl can be written by reformulating equation (64) as

$$w_x = \exp\left(-\frac{\Delta l}{\delta_x}\right) = \exp\left(-\frac{\Delta t}{\tau_x}\right) \tag{66}$$

with δ_x the drift length of electron ($x = e$) or holes ($x = h$). As mentioned above, the lifetime τ_x depends in general on the location of the charge in the diamond

and is determined by the growth model. The lifetime of a charge carrier of type x is related to the density and cross section of trap levels by equation (30) of section 3.4:

$$\tau_x = \frac{1}{v_{th}(\sigma_t n_t + \sigma_r n_r)}$$

with n_t the density of free traps, σ_t the cross section of trapping and n_r the density of traps occupied with a charge carrier of opposite sign relative to x and σ_r the cross section for recombination.

The effect of priming suggests the existence of trapping centres which are passivated when occupied by a charge. However, in principle every trap can act as a recombination centre, so that the effect of priming can only occur if the cross section for a free trap to capture a charge carrier $\sigma_{t,x}$ is significantly higher than for the same trap to recombine carriers $\sigma_{r,x}$,

$$\sigma_{t,x} > \sigma_{r,x}. \tag{67}$$

In other words a defect level is supposed to have a higher cross section to trap e. g. an electron than for the recombination process of capturing a hole when already occupied by an electron. To parametrise the mixture of traps with different cross sections $\sigma_{t,x}$ and $\sigma_{r,x}$, the two extreme cases of pure recombination (rec) and pure trapping (tr) were defined, where

$$\sigma_{r,x}^{rec} = \sigma_{t,x}^{rec} \tag{68}$$
$$\sigma_{r,x}^{tr} = 0. \tag{69}$$
$$\tag{70}$$

The parameter α is introduced which is defined as

$$\alpha = \frac{n^{rec}}{n^{tr} + n^{rec}}. \tag{71}$$

The parameter α determines the ratio of traps with equal cross sections of trapping and recombination over all traps. Traps are only allowed to have either σ^{rec} or σ^{tr}. The parametrisation allows an arbitrary modelling of the priming effect in terms of the priming ratio $\mathrm{R_p}$ and the priming dose Φ_0.

The lifetime τ_{ij} provided by the growth generator for each space segment r_{ij} is recalculated in terms of an effective trap density n_{ij}. The trap density is divided into two components according to the α parameter:

$$n_{ij}^{rec} = \alpha n_{ij} \tag{72}$$
$$n_{ij}^{tr} = (1-\alpha) n_{ij}. \tag{73}$$

By the process of charge trapping, n_{ij}^{tr} becomes lower and results in an increase of the drift length and the lifetime τ_{ij}. This is the effect of priming.

κ_l	average $\epsilon_Q[\%]$	$l_{gr}[\ \mu\text{m}]$
0.1	35	29
0.2	48	51
0.5	66	126

Table 17: *Influence of the lateral growth probability κ_l on the average ϵ_Q and the average grain size on the growth side, l_{gr}, for a* 300 μm *thick simulated CVD diamond and the set of parameters discussed in the text.*

7.4 Results

In this section the results of the simulation are presented for different particle types and three different growth parameters of the growth generator. A sample with a thickness of $d = 300$ μm and a length of $L = 1000$ μm was simulated. The electrodes were taken to be a parallel plate configuration. Results with a strip electrode configuration can be found in section 8.5.

7.4.1 Material

A set of parameters was chosen for three variants of a CVD diamond with the following properties :

- lateral growth probability $\kappa_l = \{0.1, 0.2, 0.5\}$
- lifetime length $r_0 = 10$ μm.
- maximum lifetime $\tau_0 \cdot v_{sat} = 100$ μm (v_{sat}: saturation velocity) for electrons and holes.

The choice of different values for κ_l resulted in different values for the average ϵ_Q and the average grain size on the growth side, l_{gr}. These values are listed in table 17. The parameter sets represent growth processes with low ($\kappa_l = 0.1$), medium ($\kappa_l = 0.2$) and extremely high ($\kappa_l = 0.5$) lateral growth probabilities (see figure 68).

The morphological model and the linear model with $\delta_0 = 0$ μm (see equation (62)) predict that the collection distance approaches zero at the substrate side,

$$\lim_{z \to 0} \delta_Q(z) = 0$$

because the initial growth phase consists essentially only of grain boundaries. However the models differ for $z \to \infty$. The linear model predicts a linear change of the average collection distance, δ_Q , with film thickness d. For a CVD diamond of infinite thickness consequently

$$\lim_{z \to \infty} \delta_Q(z) = \infty.$$

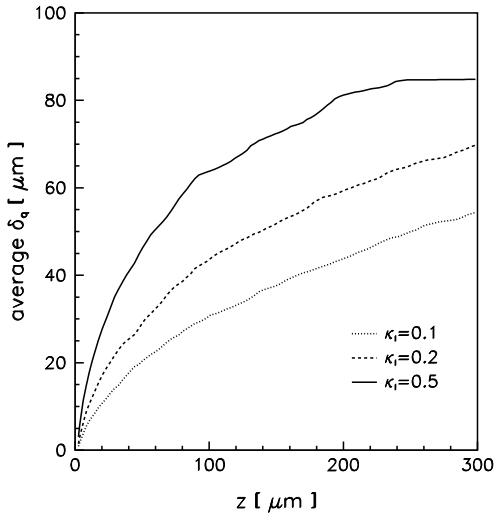

Figure 69: *Dependence of the laterally average charge collection distance, δ_Q, on the distance from the substrate side, z, as predicted by the morphological model for three different values of the lateral growth probability, κ_l.*

The morphological model also predicts an increase of δ_Q with film thickness but δ_Q is not linearly dependent on z as can be seen from figure 69. The slope decreases with the film thickness and tends to zero for an infinite film thickness with the average collection approaching the saturation value

$$\lim_{z\to\infty} \delta_Q(z) = \tau_0 v_{sat}.$$

Physically this corresponds to the situation of a CVD diamond film grown to a thickness where only one initial grain survives. The finite lifetime expresses the incorporation of lattice defect and foreign atoms which will occur for real growth processes.

The model can reproduce the priming effect via the distinction of pure recombination centres and pure trapping centres as explained in the previous section. The α parameter, defined by equation (71), was set to a value of $\alpha = 0.35$, resulting in a value of $\mathrm{R_p} = 1.5$, which will be shown in section 7.4.4. The choice of α yields a realistic value of $\mathrm{R_p}$. Experimentally $\mathrm{R_p}$ was found to vary between 1.2 and 4.3 with a trend of low values of $\mathrm{R_p}$ for high values of ϵ_Q (see section 4.6).

The next sections will discuss the response of the different materials to α - particles, protons and minimum ionising particles (sections 7.4.2, 7.4.3 and 7.4.4).

7.4.2 Alpha Particles

The α-particles in the simulation were set to an energy of $E = 5.8$ MeV corresponding to the decay of $^{244}\mathrm{Cm} \rightarrow {}^{240}\mathrm{Pu} + \alpha$ as used in experimental studies presented in section 4.8. The α-particle had a range of about 14.3 μm and produced 5.8 MeV$/E_{eh} = 44.6 \cdot 10^4$ electron hole pairs distributed according to the Bragg curve along the trajectory. The distribution of charge was calculated according to the analytical expression of $\mathrm{d}E/\mathrm{d}x$ for He nuclei in carbon from [58].

The relatively large number of charges per event (roughly 10^6) together with the available computing power limited the number of events. To reduce the

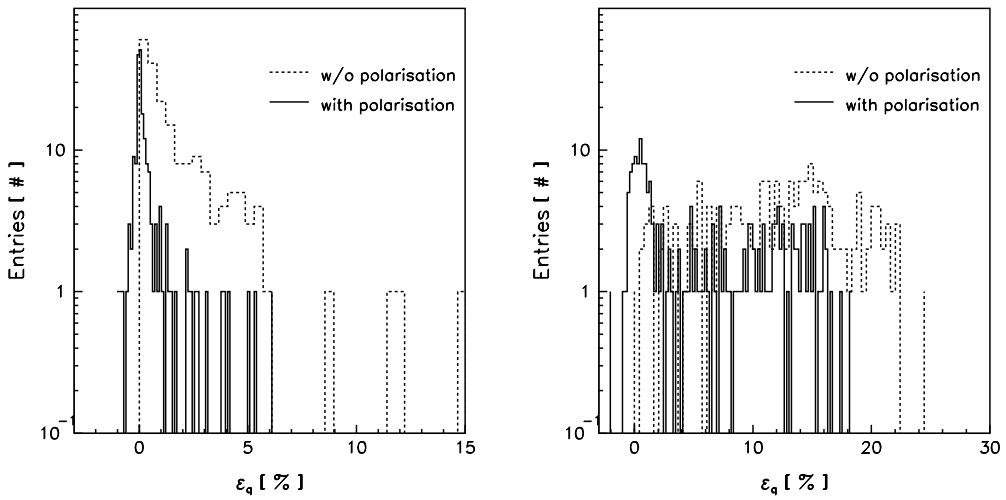

(a) Substrate side. (b) Growth side.

Figure 70: *Signal spectrum of* 5.8 MeV α*-particles in a simulated* 300 μm *thick CVD diamond detector with* $\kappa_l = 0.2$. *The response is shown for* α*-particles impinging on the substrate side (a) and growth side (b). The solid line shows the spectrum with activated polarisation field, the broken line represents the unphysical case of the absence of a polarisation field.*

computing time per event a charge multiplicity of 10 was given to the charge carriers. The simulation was restricted to 1000 events impinging randomly on a line of 500 μm width. The polarisation field created by trapped charge was recalculated after each event. The polarisation field could overcompensate the applied field since the self interaction of charge carriers during the drift process was neglected, leading to events with negative signals.

Two simulation modes were distinguished to clarify the influence of the polarisation field. In one mode the polarisation field was calculated and added to the external field. In another mode the polarisation field was neglected. The two modes yield qualitatively different results. A signal spectrum of the detector response for α-particles impinging on the substrate and growth side of a material with $\kappa_l = 0.2$ with and without activated polarisation field is shown figure 70.

The spectra of the substrate side show for both modes a steeply falling number of entries with increasing signal heights, while the introduction of the polarisation field further reduces the signal height. Moreover the spectrum with activated polarisation field also has entries for negative signals which are explained by the overcompensation of the external electric field.

The growth side response shows a very broad spectrum if the polarisation field is neglected. The spectrum is essentially determined by the distribution of ϵ_Q.

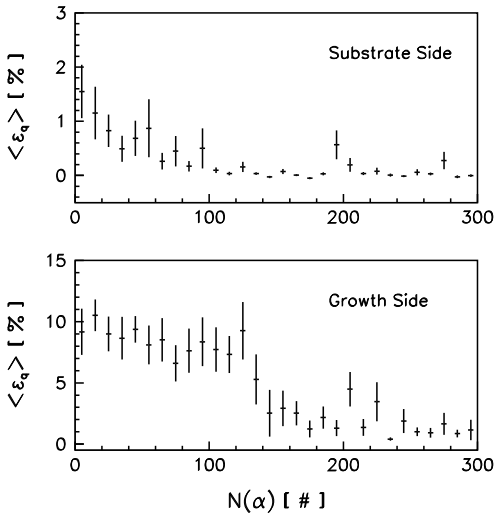

Figure 71: *The plot shows the simulated development of the average signal response ($\langle \epsilon_Q \rangle$) with the number of 5.8 MeV α-particles ($N(\alpha)$) applied on a 300 μm thick diamond detector with $\kappa_l = 0.2$ on the substrate (upper plot) and growth side (lower plot). The steady decrease of signal height is caused by polarisation.*

If the polarisation field is switched on, the effective compensation of the external field leads to a drastic decrease in pulse height and an accumulation of events near zero. Here negative signals also occur as a consequence of overcompensation.

The counting rate of α particles was observed to decrease as a function of time. This experimental finding (see section 4.8) is well reproduced by the simulation. The decrease of counting rate is equivalent to the decrease of the average signal height because a threshold was applied in the experiment to discriminate between α events and noise. In the simulation the signal height is found to decrease rapidly as a function of the number of α-particles applied, i. e. the exposure time to α-particles, as can be seen from figure 71. The decrease is found to be steeper for the substrate side than for the growth side in accordance with experimental observations. The higher trap density on the substrate side leads to a faster build up of a compensating polarisation field.

The distribution of the trapped charge demonstrates the consequences of the initial Bragg distribution of the free carriers. Electrons and holes are well separated in the external field as demonstrated in figure 72. The plot shows the number of charges trapped versus the location of trapping for electrons (negative) and holes (positive) for an α-particle impinging on the growth side. The separation leads to an effective compensation in the region of initial charge distribution.

7.4.3 Protons

Protons with $E = 2$ MeV have in principle the same ionisation characteristic as 5.8 MeV α-particles, i. e. the stopping range of $s \approx 30$ μm is low compared to the film thickness of 300 μm, and the ionisation distribution has the characteristic Bragg shape. Thus the results are qualitatively comparable with the results from 5.8 MeV α-particles. The signal spectrum containing 1000 events for 2 MeV protons impinging on growth and substrate side is shown in figure 73a. As the

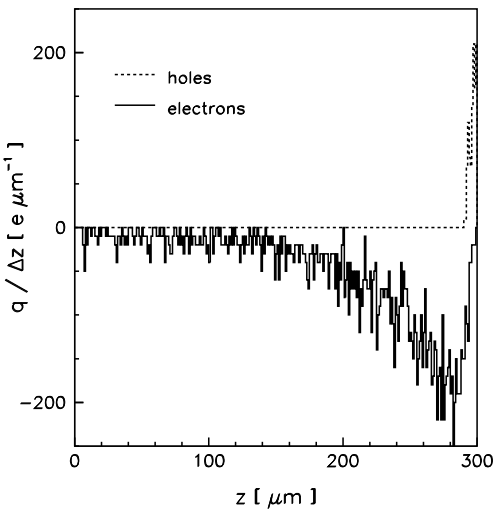

Figure 72: *Distribution of trapped electrons (negative) and holes (positive) for an α-particle impinging on the growth side of a CVD diamond detector. The electric field is applied in a manner such that electrons drift to the substrate side ($z = 0$) and holes to the growth side ($z = 300$).*

spectrum from 5.8 MeV α-particles, the signal spectrum for 2 MeV protons is broad and peaks at low signals. The average signal is higher on the growth side than on the substrate side.

The polarisation behaviour was found to be qualitatively similar to the results with α-particles in agreement with experimental observations. The development of the average signal with the event number is shown in figure 73b. As in the case of α particles the average signal decreases due to the effect of polarisation.

The spatially resolved measurements with a proton micro-beam (section 4.9) showed areas of enhanced response, the so called hot spots. The occurrence of hot-spots could not be reproduced with the simulation. Possible reasons could be the limited number of events processed and the restriction to two dimensions.

7.4.4 Minimum Ionising Particles

The ionisation density of minimum ionising particles (MIPs) is defined by $\rho_{mip} = \mathrm{d}E_{min}/\mathrm{d}x \cdot 1/E_{eh} = 36\ \mathrm{eh}\mu\mathrm{m}^{-1}$. This value represents the average. Fluctuations arise by the statistical nature of the ionisation process and the production of delta electrons. In the simulation the value of ρ_{mip} was fixed and fluctuations were neglected. Only tracks perpendicular to the surface were considered.

Priming

The priming effect was discussed in section 7.3. The effect is experimentally observable when measuring ϵ_Q with MIPs (see section 4.6). For ionising particles with stopping ranges less than the detector thickness, the build-up of a polarisation field screens the priming effect and makes it undetectable. To qualitatively verify the priming behaviour of the model, a simulation run with 5000 tracks distributed over 50 μm in x was performed.

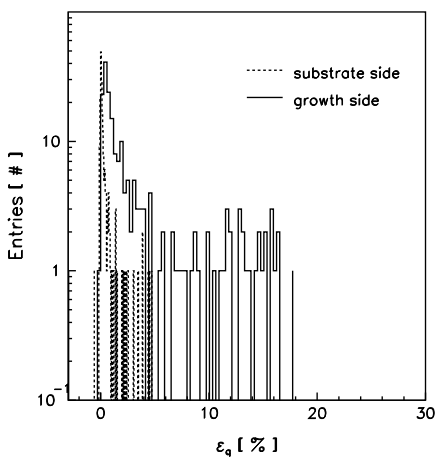

(a) Signal spectra for the growth and substrate sides. The polarisation field is calculated after each event.

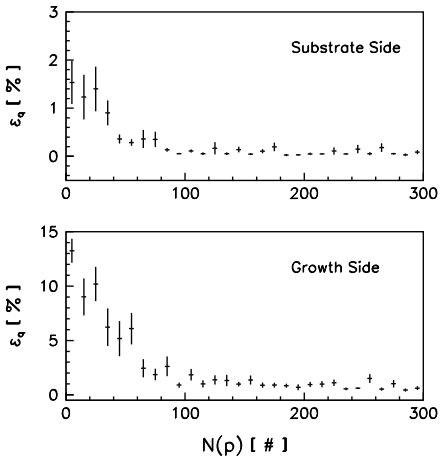

(b) Development of the average signal response (ϵ_Q) with the number of 2 MeV protons ($N(p)$) applied to the diamond on the substrate (upper plot) and growth side (lower plot).

Figure 73: *Response of a* 300 μm *thick simulated CVD diamond detector with* $\kappa_l = 0.2$ *to* 2 MeV *protons.*

The result is shown in figure 74. A clear increase of ϵ_Q with the number of tracks is seen. Moreover the shape of the increase reproduces very well the experimentally observed shape (see section 4.6). Also shown is the fit with function (43) used to fit the experimental data. The fit gives for the simulated data values of $\mathrm{R_p} = (1.5 \pm 0.2)$ and $\Phi_0 = (1425 \pm 44)\#$ with Φ_0 being in units of number of tracks. While $\mathrm{R_p}$ can be adjusted with the α parameter which has been chosen to $\alpha = 0.35$, the priming dose, Φ_0, i. e. the dose needed to achieve a fraction $\frac{1}{e}$ of the increase, is dependent on the total effective trap density n_x and the cross section σ_x given as parameters in the simulation.

Although the extraction of α , n_x, σ_x^{tr} and σ_x^{rec} from the data is possible, it does not access detailed microscopic information because the trap densities and cross section used in the model represent effective quantities and are in this sense only reformulations of ϵ_Q, $\mathrm{R_p}$ and Φ_0. However, the advantage of the model is that it explains the empirical quantities ϵ_Q, $\mathrm{R_p}$ and Φ_0 with the concept of traps, which is physically more meaningful. It reproduces the empirical quantities in terms of physical microscopic quantities.

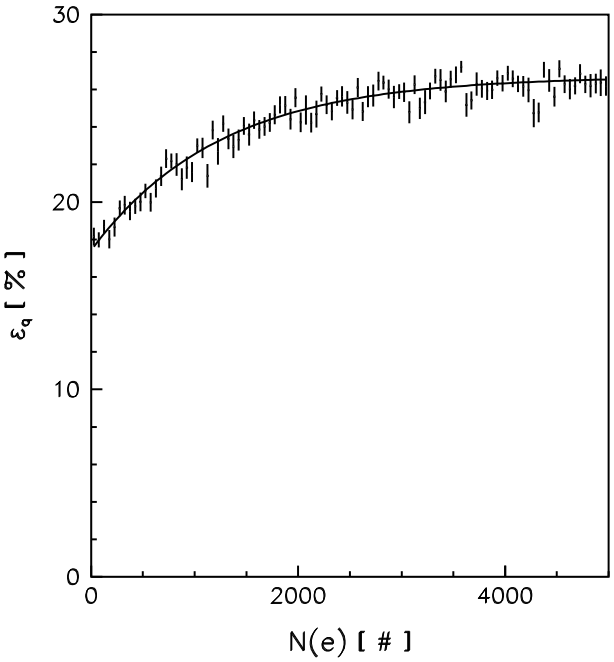

Figure 74: *Simulated priming process for a* 300 μm *thick CVD diamond with MIPs. The result is fitted with equation (43) on page 51.*

Uniformity

Various experimental methods show a very heterogeneous distribution of ϵ_Q. The direct spatially resolved measurements with 10 keV photons (section 4.7) and in the electron test beam (section 8.4.5) provide precise information of the non-uniformity of ϵ_Q. The model explains the non-uniformities by the introduction of crystallites.

An example of the non-uniformity of ϵ_Q as provided by the model and measured with MIPs is depicted in figure 75. The figure shows the spatial dependence of ϵ_Q for three different materials with different values of κ_l. The patterns vary with the parameter κ_l. For high κ_l, corresponding to the formation of large crystallites, the variations are more extended in structure than for small κ_l. If the patterns are compared with the experimental results obtained with photons (section 4.7) and electrons (section 8.4.5) the qualitative agreement is obvious.

To reach quantitative agreement the exact crystallite structure of the investigated samples is required to make model predictions accordingly to the crystallite geometry of the investigated sample. However, since data on the exact crystallite structure is very difficult to obtain and beyond the scope of the work presented here, a quantitative comparison can not be made. A new method to measure the crystallite geometry was discussed in section 4.3. However the resolution of the obtained data was not sufficient to be used for a comparison of model predictions and experimental data.

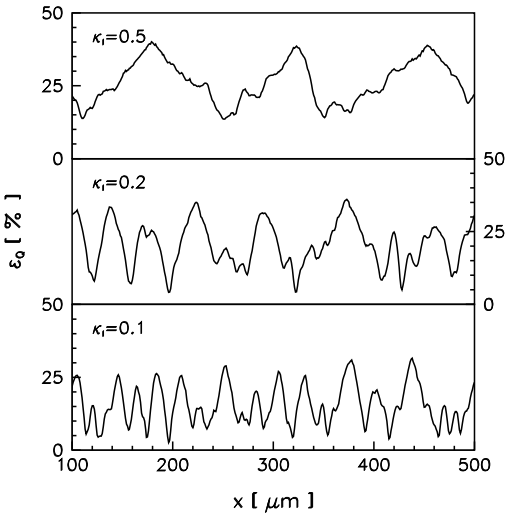

Figure 75: *Simulated spatially resolved measurement of the charge collection efficiency ϵ_Q with MIPs for three different materials with $\kappa_l \in \{0.1, 0.2, 0.5\}$.*

7.5 Summary

A new descriptive approach towards a model of the charge drifting process in CVD diamond was discussed. While the existing model [10] proposes a linear relationship between film thickness and the charge collection distance, δ_Q, the new model is based on the constituting crystallites and proposes a $(1 - e^{-x})$ dependence of δ_Q from the distance to the next grain boundary.

The model was implemented in a computer simulation including a reformulation of δ_Q in terms of traps and recombination centres. The computer simulation can qualitatively reproduce the experimentally observed phenomena of priming, polarisation and spatial non-uniformity of the charge collection. It explains the differences in response to particles with Bragg like ionisation distribution (5.8 MeV α-particles, 2 MeV protons) and particles with uniform ionisation distribution (MIPs, 10 keV photons).

8 A Prototype Detector Study

To demonstrate the functionality of CVD diamond as a material for a spatial resolving particle detector, a prototype micro strip detector was developed and tested. Performance characterisitcs, e. g. charge signal and resolution, of the device are influenced by the non-uniformly distributed charge collection properties of the polycrystalline material. The peculiar behaviour the device, partly due to the non-uniformity, has been studied and was qualitatively reproduced with a computer simulation accounting for the polycrystalline structure.

8.1 Principle of Operation

The detection principle of a plate capacitor field device is described in section 2.2. To achieve position resolution the electrode can be segmented into multiple strips with each strip connected to a separate amplifier as shown in figure 76. The electric field resembles closely by superposition of the individual strips the plate capacitor field. The potential of an individual strip, together with the drift path of the ionised charge carriers, determine the charge signal at the amplifiers. The signal generation process is discussed in greater detail in section 3.3.

If the charge collection is complete and the carrier diffusion is negligible compared to the strip pitch p, only one strip will give a signal and the spatial resolution of the device is given by $\sigma^2 = \int_{-p/2}^{p/2} x^2/p \, \mathrm{d}x = p^2/12$, called digital resolution. The position resolution can be improved if the carrier diffusion is significant or if the charge collection is incomplete. In this case the charge signal is shared by multiple strips and the position x' can be calculated by the centre of gravity (*cog*):

$$x' = \frac{\sum_{i=1}^{N} x_i \cdot Q_i}{\sum_{i=1}^{N} Q_i} \tag{74}$$

with x' the estimated hit position, x_i the i-th strip position, Q_i the charge signal on the i-th strip and N the number of strips. If the charge sharing is not a linear function of the hit position a systematic error on x' is introduced. The quantity η is defined as

$$\eta = \frac{Q(R)}{Q(R) + Q(L)} \tag{75}$$

with Q the signal of the strips L and R adjacent to the particle track [88]. If the charge sharing is linear then η is also linearly dependent on the impact point. However, in real detectors the charge sharing is non-linear and η may look as shown in figure 77. The figure was obtained from a simulation (see section 8.5) of a single crystal diamond detector with 100 μm strip pitch and 50 μm strip width. The charge is collected by mainly one strip if the particle penetrates through the strip. In the region between two strips the charge is shared.

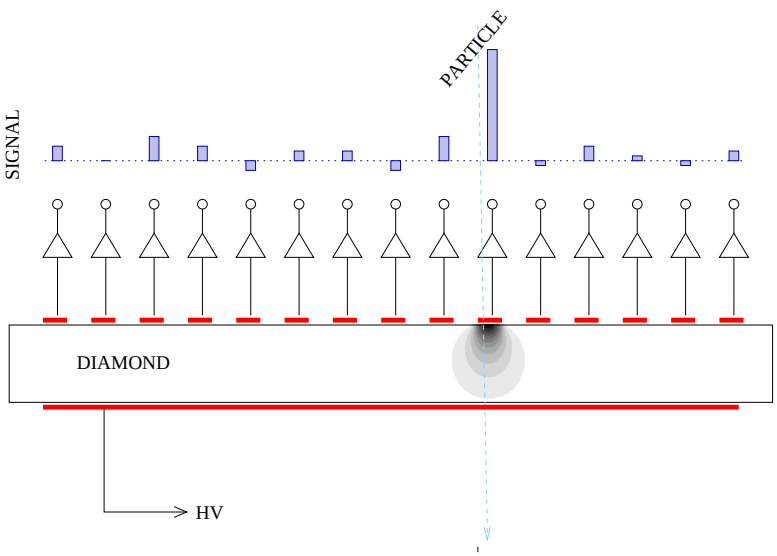

Figure 76: *Principle of operation of a strip detector. The cross section of a diamond strip detector with strips on top and a solid electrode on the bottom is depicted. The shaded region suggests the potential of a single strip. The electric field is given by the superposition of all strip fields and resembles closely a plate capacitor field. The free charge carriers created by a traversing charged particle drift in the field of the electrodes and induce a signal on the strip(s) near the particle track. Each strip is connected to an individual amplifier. By analysing the strip signals the hit position can be reconstructed.*

If the relation between η and the impact point x is known it can be used to improve the reconstruction of the track position [88]. The average impact point x for a given η is determined by

$$x = \frac{p}{N_0} \int_0^\eta \frac{\mathrm{d}N}{\mathrm{d}\eta}\, \mathrm{d}\eta - \frac{p}{2} \tag{76}$$

with p the strip pitch and $N_0 = \int_0^1 \frac{\mathrm{d}N}{\mathrm{d}\eta}\, \mathrm{d}\eta$ a normalisation factor.

The η algorithm is especially useful if intermediate strips are present, which are connected to the potential but are not read out. Through capacitive coupling between intermediate strips and read-out strips the charge accumulated on the intermediate strips are detected. Intermediate strips lead to additional peaks in the η distribution and enhance the spatial resolution significantly relative to the digital resolution of read out pitch over $\sqrt{12}$.

8.2 Detector Design

To successfully demonstrate the functionality of a position sensitive detector from CVD diamond the signal response should be reasonably high. Thus the material

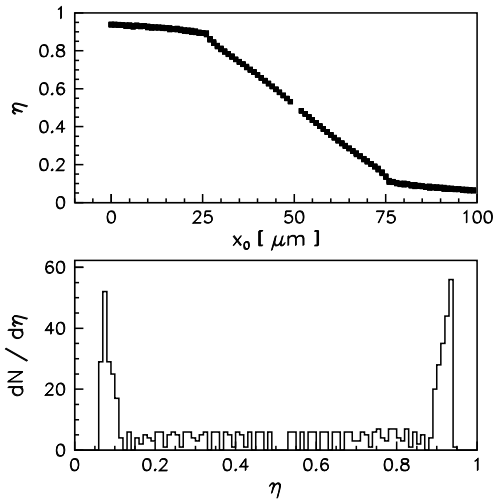

Figure 77: *Example of the dependence of η defined by equation 75 on the impact parameter x (top figure) and the distribution of η (bottom) from a simulation of a single crystal diamond detector with* 100 μm *pitch and* 50 μm *strip width.*

Name	Structure	channels [#]	pitch [μm]	width [μm]	length [μm]
S11	Strip	14	200	67	2000
S12				100	
S13				133	
S21		28	100	33	
S22				50	
S23				67	
S31		58	50	17	
S32				25	
S33				33	
P	Square	24	100	75	75

Table 18: *Geometrical data and naming scheme of the implemented structures on the test device.*

with the highest available charge collection distance, δ_Q, was chosen. To study the influence of different read-out geometries a variety of test structures were implemented on the device allowing the study of geometries with different strip pitches and strip widths.

8.2.1 Pattern Design

The metallisation pattern is shown in figure 78. It comprises nine different strip width/pitch combinations and a small pixel array. Each strip is connected to a fan-out line also patterned onto the diamond. The whole structure is surrounded by a guard-ring. An overview of the pattern data and naming scheme gives table 18.

The pattern allowed relevant detector parameters such as the resolution, the

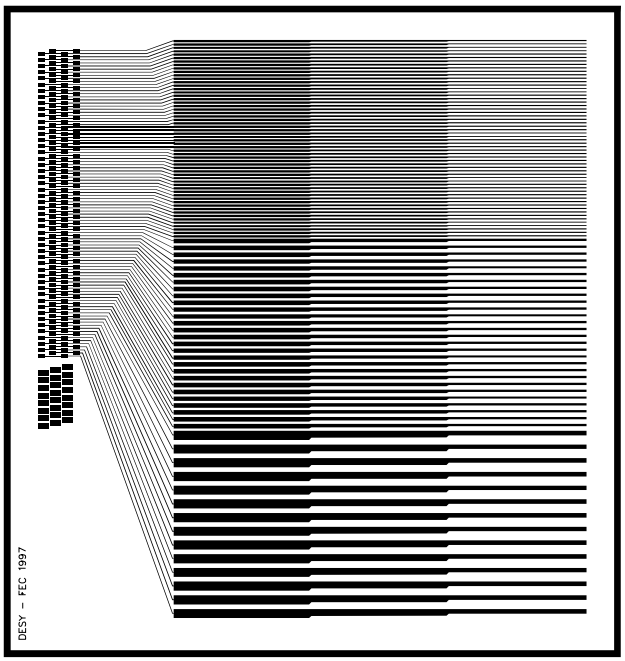

Figure 78: *Metallisation pattern of the test device.*

signal generation and charge sharing for a multitude of strip configurations to be studied on a single device. The structure was transferred onto the diamond with a lithographic process. The layout of the lithographic mask was designed with the help of the electronics engineering group at DESY (FEC). The mask itself was produced by Maskenzentrum für Mikrostrukturierung, Dresden, Germany (MZD). The structured metallisation was finally put onto the growth side of the diamond by the Fraunhofer Institut für Schicht und Oberflächentechnik, Braunschweig, Germany (FhGIST). By successive evaporation of Ti-Pt-Au and annealing at 700 °C in air the electrodes were formed. A solid electrode on the substrate side provided the backplane contact.

8.2.2 Material

The best sample in terms of collection distance, δ_Q, investigated in this study was sample DS8 provided by DeBeers [89], a commercial manufacturer. It was grown to an initial thickness of 1049 μm and lapped down to 480 μm from the substrate side. The growth side was polished to obtain a surface roughness below 1 μm. The rather small dimensions of 10.5 mm $\times$ 10.5 mm enforced the dense test structure discussed above.

The sample was characterised with a variety of methods to supply additional information. The experimental data on this sample are summarised in table 19. The experimental methods are described in the referenced chapters. The charge collection properties measured with ^{90}Sr were obtained with a planar dot contact configuration before patterning the detector.

Method	Chapter	Quantity	Value	Comment
^{90}Sr β	4.6	primed δ_Q	95 μm	$E = 5$ kV cm^{-1}
^{90}Sr β	4.6	Φ_0	4.5 rad	
^{90}Sr β	4.6	R_p	1.4	
7 GeV e^-	8	primed δ_Q	87 μm	$E = 5$ kV cm^{-1}
7 GeV e^-	8	S_Q	2.9	
γ, 10 keV	4.7	S_Q	3.3	

Table 19: *Summary of the experimental data on sample DS8 used for the prototype detector study.*

8.2.3 Read-Out Electronics

Low noise is an important requirement on the read-out electronics to clearly distinguish particle signals from background noise. In contrast to a real application in a colliding beam experiment, where the shaping time is determined by the bunch crossing frequency, the prototype was equipped with slow electronics facilitating the use of an ultra low-noise amplifier array chip, the VA3. The shaping time of the VA3 was $\tau = 2$ μs and it was optimised for low noise.

The VA3 provided 128 amplifier channels on a CMOS chip and an analogue read-out via a sample-and-hold circuit and an analogue shift register. The manufacturer quoted a noise figure of $\sigma_{ENC} = 40$ e$+C_{load} \cdot 12$ e pF^{-1} [90] for a shaping time of $\tau = 2$ μs.

If a trigger signal was provided, the output of the amplifier channels were sampled and stored. Then the values of the sample-and-hold circuits were read out sequentially by an analogue multiplexer. The maximum read out frequency was 10 MHz. The minimum read-out frequency was determined by the charge loss of the sample-and-hold circuit which could store the analogue signal for about 100 ms, so the minimum read out frequency was limited to about 1.3 kHz.

The VA3 could be operated in a test mode and a normal mode. In the normal operation mode each amplifier was connected to its input pad. In the test mode each amplifier was connected sequentially to a separate calibration pad via another analogue multiplexer. The calibration pad supplied a defined charge signal if, for example, a voltage step over a capacitor was used for charge injection. The test mode was useful for verifying the functionality and calibrating the single amplifier channels.

The VA3 chip was mounted on a G10 board together with additional electronics for filtering and drivers for digital lines (hybrid board). The detector device was glued next to the VA3. The supply voltages and reference currents were generated by an additional board, the repeater card [91], which also featured a differential output signal amplifier.

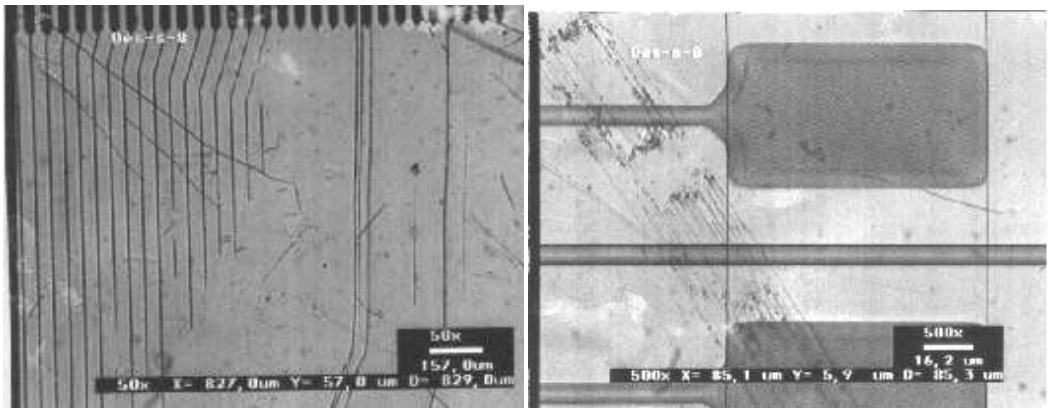

(a) Broken fan-out lines of an unsuccessful metallisation attempt.

(b) Successful metallisation.

Figure 79: *SEM pictures of an unsuccessful and a successful metallisation attempt.*

8.2.4 Quality Control, Device Assembly and Calibration

The structured metallisation process proved to be difficult and several attempts had to be made before a satisfying result was obtained. The fan-out structures with a width of only 7 μm in an early attempt can hardly be seen in figure 79a. After dispensing with a cleaning step in an ultra-sonic acetone bath and an additional hydrogenisation step before metallisation good patterning was achieved (see figure 79b).

After the structured metallisation was successfully produced the connectivity of bond pads to strip structures was tested. A typical pad to strip resistance of 300 Ω to 600 Ω was found. The inter-strip resistivities ranged between greater than 20 MΩ to a few hundred Ω. The low inter-strip resistivities accumulated in the 50 μm pitch region. This indicates, that the etch process had not removed all of the metallic layer or that remains of previous metallisations increased the surface conductivity. Strips with inter-strip resistances in the kΩ range and below could not be used because the noise was dramatically enhanced. This could be due to inter-gate currents of the input stage FETs.

Discarding strips with low inter-strip resistances, only 43% of the strips could be used in the analysis of the test-beam data. The percentage of working strips in the three pitch regions amounted to 100% for the 200μm pitch, 71% for the 100μm pitch and 14% for the 50μm pitch region. This means that 62% of the active area of the diamond detector could be used for the analysis.

After inspection the diamond was glued conductively onto the hybrid board close to the VA3 read-out chip and the fan-out was wire bonded to the input pads.

Previous tests with the same metallisation process ensured that the adhesion of the metal layer was strong enough to withstand the bonding procedure, and that the bond connection was sufficiently robust. This was a critical point since the normal metal layer thickness for bonding is in the μm range but the total thickness of the Ti-Pt-Au layer amounted to only ≈ 140 nm.

A capacitor $C_{test} = 1.6$ pF was connected to one channel of the VA3 to inject a defined charge $Q = U_{TP}/C_{test}$ with a test pulser providing a step signal U_{TP}. The other channels could then be calibrated relative to this channel using the test mode of the VA3. A 10% uncertainty in the calibration is assumed due to stray capacitance and the precision of the test capacitance. The average calibration constant of all working channel was to (73 ± 6.5) e per ADC count (#) with a rms of $\sigma_{rms} = 3.2$ e$\#^{-1}$. The average electronic noise of the amplifier channels used was determined from the data as $\sigma_{noise} = 190$ e, with a rms of 18 e.

The hybrid board and the repeater card were mounted into a common steel housing with thin Al entrance and exit windows of 50 μm thickness at the detector position. The assembly formed the *detector module*.

8.3 Test Environments

8.3.1 Table Top Set-up

The principal components of the set-up were the detector module, the interface module, the timing unit and the ADC. The task of the timing unit [92] was to generate the digital signals required for operation of the VA3. Additionally, it was able to generate a test-pulse and allowed single channel operation, i. e. to switch the analogue multiplexer to a defined channel while disabling the sample-and-hold. The ADC was integrated into a PC used for read-out, storing and analysis of the signals. The control program was written in LabView. The interface module provided additional amplification of the differential output signal of the repeater card and formed a single line output with adjustable offset and amplification. Moreover it provided interfacing of digital lines between the PC and the timing unit, which were used for synchronisation of the read-out cycle.

A ^{90}Sr β emitter housed in a collimator with an opening of 1 mm diameter was placed in front of the detector module. Traversing β particles were detected with a scintillator, which triggered the read-out cycle.

The table top set-up could only provide rough position information on the traversing particle, given by the aperture opening size of 1 mm. The set-up was only used to test the basic functionality of all system components of the prototype detector. The study of the detection properties required a multi GeV electron beam in conjunction with a silicon telescope, as provided by the test-beam set-up.

8.3.2 Test-beam Set-up

A necessary requirement of a test environment to study the spatial resolution and uniformity of response of the prototype device is to provide precise track information on the traversing particle and a sufficiently high event rate to acquire the statistics needed in a reasonable time. A multi GeV electron beam formed the particle source and a silicon telescope[16] was employed to obtain information on the track position.

The Particle Source

The electron test beam at DESY offered electrons in a selectable energy range from 450 MeV to 7 GeV. Positron packets (6×10^9 particles) were accelerated in the storage ring DESY II up to 8 GeV with a circulating frequency of 1 MHz. By driving a carbon fibre target of 10 μm thickness into the beam, impinging positrons were decelerated and emitted Bremsstrahlung. An Al plate of 3 mm thickness was placed in the energetic photon beam and electron-positron-pairs were created by photon conversion. With a magnet and a collimator, selecting particles with a bending angle of about 5.5°, electrons of a specified energy passed into the test area. The maximal rate of 1 kHz was reached at 4 GeV at a collimator opening of 5 mm $\times$ 5 mm [93].

The Silicon Telescope

The silicon telescope (figure 80) consisted of three x-y-planes[17] of strip detectors (Si-modules) with a read-out pitch of 50 μm and one intermediate strip. Each x-y-plane was build from two orthogonally oriented Si ladders with 640 read out strips and an active area of 3.2 cm $\times$ 3.2 cm size. The read-out was performed with a 128 channel low noise amplifier, the VA2, which has basically the same architecture as the VA3 used for the prototype device (section 8.2.3) but is optimised for a higher load capacitance.

The three Si-modules were freely movable with respect to the z-axis on a common guide rail. The detector module (section 8.2.4) was placed between the Si-modules on a support with a positioning mechanism in x and y.

Four scintillator finger counters, two in front and two in the back of the telescope, could be used to define an event. Typically a coincidence of the two front scintillators and the back scintillator oriented in x was used as trigger condition, resulting in an active area of about 1 cm $\times$ 1 cm.

[16] The Si-telescope and support in the test-beam was provided by the ZEUS Micro Vertex Detector group.

[17] A right handed coordinate system with Y pointing upwards and Z along the beam axis is used.

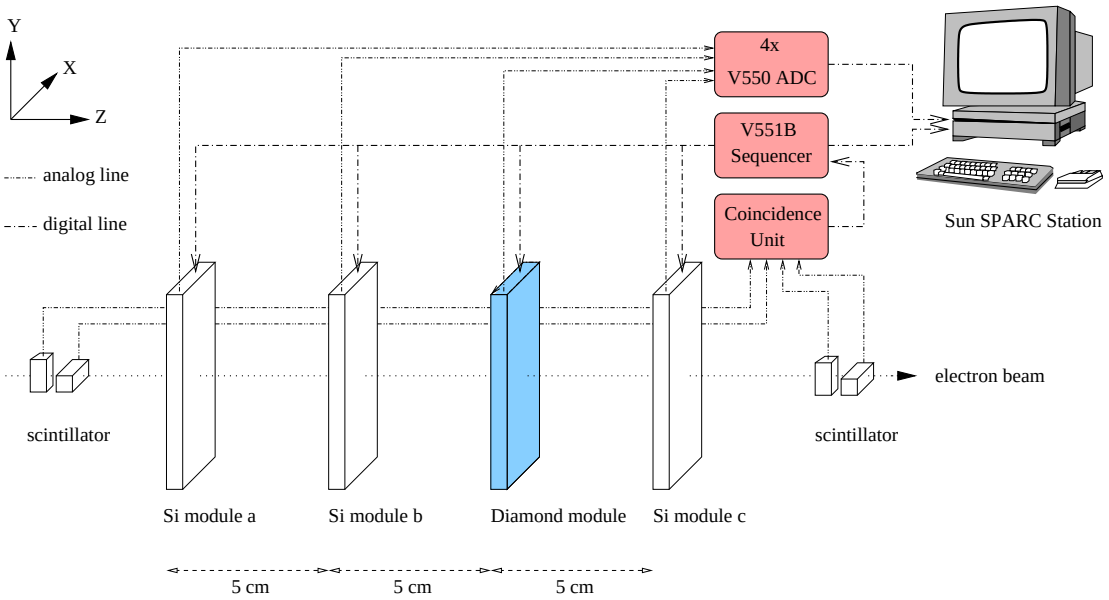

Figure 80: *Schematic view of the set-up in the multi GeV electron test-beam.*

Data Acquisition

The similarity of the VA3-chip chosen for the prototype device and the VA2-chip for the Si detectors allowed to use the same data acquisition system for both chips. Each module was connected to a digital sequencer (V551B) providing the control signals for sequential read-out at frequency of 2 MHz. The test module was hooked on the same digital bus as the Si modules. The analogue signals were digitised by four ADC's (V550), one for each module, with 10 bit precision. ADC's and the sequencer were controlled by a LabView program[18] running on a Sun SPARC Station.

The full data volume of one event is defined by the number of read-out channels and the precision of digitisation. For the set-up described with three Si modules with 4096 channels per module and one test module with 128 channels one event amounts to $3 \times 4096 + 128 = 12416$ words, about 24 kbytes. To reduce the amount of data empty channels defined by a 3 σ cut on signal-to-noise ratio of the Si modules were suppressed and not stored in the event data. This reduced the data volume to typically 10 channels for one Si module and resulted in a reduced event data size of about 300 bytes. The maximal acquisition rate was limited to approximately 50 Hz by the data transfer rate of the data acquisition system, depending on the data reduction.

[18]The control program was written by M. Milite, ZEUS, DESY.

Event Reconstruction

The track position on the test device was predicted using the hit information on the silicon planes. Only events with valid position information on all three silicon planes were accepted for the analysis. Offline reconstruction code[19] provided pedestal subtraction, calibration and cluster finding. The position information was obtained by the centre-of-gravity method. After alignment of the Si planes three measured space points were available for the track reconstruction. The intrinsic resolution on the space points were $\sigma_{x,y} = 2.8$ μm for the x and y components [94] and about $\sigma_z = 1$ mm for the z component.

The impact point at the test device was determined by fitting a line to three measured space points and adding the error introduced by multiple scattering in quadrature to the intrinsic errors. The error on the impact point was dominated by multiple scattering. If the angular distribution of the scattering is approximated by a Gaussian, the central 98% is contained within a Gaussian of width θ_0 [9]:

$$\theta_0 = \frac{13.6 \text{ MeV}}{\beta cp} \cdot \sqrt{x/X_0} \cdot (1 + 0.20 \cdot \ln(x/X_0)) \qquad (77)$$

where βc is the velocity and p is the momentum of the incident electron. x/X_0 is the thickness of the scattering medium in radiation length.

In the case of two Si modules in front (a, b) and one Si module behind (c) the test device (**d**evice **u**nder **t**est, *dut*) the total errors of the coordinates $(\sigma'_{x,y})$, comprising the intrinsic error $(\sigma_{x,y})$ and the error through multiple scattering, were estimated to be

$$\begin{aligned}
\sigma'_{x,y}(a)^2 &= \sigma^2_{x,y} + [(z_a - z_{dut}) \cdot tan(\theta_0^{dut})]^2 + [(z_a - z_b) \cdot tan(\theta_0^{Si})]^2 \\
\sigma'_{x,y}(b)^2 &= \sigma^2_{x,y} + [(z_b - z_{dut}) \cdot tan(\theta_0^{dut})]^2 \\
\sigma'_{x,y}(c)^2 &= \sigma^2_{x,y} + [(z_c - z_{dut}) \cdot tan(\theta_0^{dut})]^2
\end{aligned}$$

for the three modules a, b and c.

In the geometrical arrangement of the set-up (see figure 80) the error on the impact point at the test device was calculated to be $\sigma_{dut} = 7.5$ μm for a beam energy of $E = 5$ GeV for $\sigma_{x,y} = 2.8$ μm, while for $\sigma_{x,y} = 0$ μm the resolution would improve to only $\sigma_{dut} = 6.1$ μm. The resolution could be improved if the distance between the modules is decreased as shown in figure 81 or the particle energy is increased.

In order to determine the position of the test device relative to the coordinate system defined by the reconstructed tracks, the test device was aligned by fitting events passing a 3σ signal cut to a strip map. The strip map contained the expected hit position for individual strips according to the special metallisation pattern. The χ^2-fit of the alignment procedure considered translation and rotation in the x-y-plane.

[19] Offline code for the Si telescope was written by C. Burgard, ZEUS, DESY.

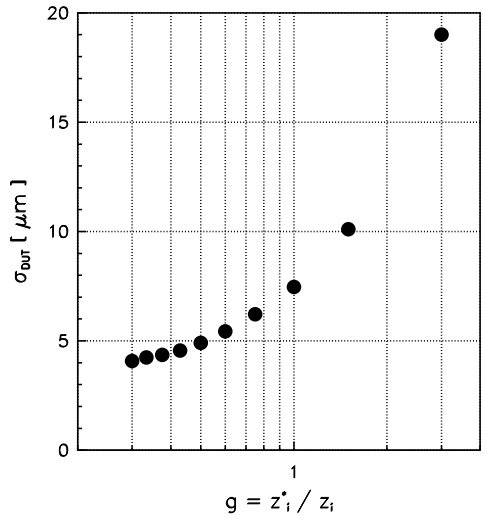

Figure 81: *The precision of the impact point prediction as a function of the distance between the modules of the telescope for $E = 5$ GeV. The geometrical factor on the abscissa is defined by $g = z_i'/z_i$ where z_i corresponds to the z-positions of the three Si modules as used in the set-up and z_i' denotes the assumed position to calculate $\sigma_{x,y}$.*

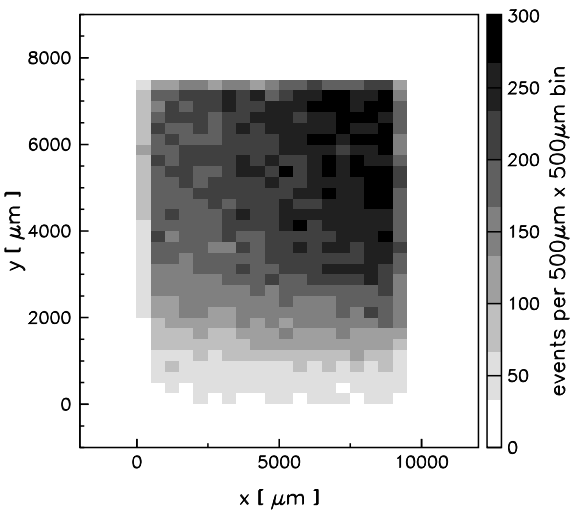

Figure 82: *Typical beam-profile for the multi GeV test-beam. The rectangular active area is defined by three scintillators in coincidence.*

8.4 Results

After the functioning of all system components was verified with the laboratory set-up, the detector module was moved to the test beam and a total of $3.1 \cdot 10^6$ events at different bias voltages were recorded. A typical beam profile of the test-beam is shown in figure 82. The active area defined by the scintillators render a rectangle with side length of 9.5 mm in x and 7.5 mm in y. The intensity is non-uniformly distributed with a maximum in the high x and high y region.

The detector noise was increased critically for bias voltages above about $U_b >$ 170 V due to surface currents. This led not only to an increase of the noise in individual channels but also to events with correlated base line shifts, i. e. common mode fluctuations. These events were discarded in the analysis.

8.4.1 Cluster Finding

A hit in the *dut* was recognised by excess charge on the strips surrounding the impact point. The strips contributing to the signal formed a cluster. Two cluster definitions, the transparent and the non-transparent cluster scheme, were used in the analysis. In the transparent cluster scheme the predicted impact point on the *dut* was used to find the strip closest to the incident particle track. The cluster was formed by a fixed number of n strips centred around the impact point.

In the non-transparent cluster scheme the strip with the most significant signal in the event is searched for. If it passed a defined threshold, the so called *seed strip significance cut*, s_0, the strip qualified to be a seed strip. The strips surrounding the seed strip were tested and added to the cluster if the signal exceeded the secondary strip significant cut, s_+. The overall signal-to-noise of the cluster was required to exceed a certain value, the *cluster sum significance cut*, s_{cl}. Typical values used for silicon strip detectors are $s_0 = 8$, $s_+ = 4$ and $s_{cl} = 12$ [95]. In this study the range of $1.5 \leq s_0 \leq 8$, $s_+ = \frac{1}{2}s_0$ and $s_{cl} = s_0 + \frac{1}{2}s_+$ were scanned to measure the dependence of the detection efficiency on the cluster cuts. These values are covering the range from cuts previously used for the analysis of a CVD diamond strip detector ($s_0 = 2$, $s_+ = 1$ and $s_{cl} = 2.5$) [33] up to typical values used for silicon strip detectors.

The transparent cluster scheme was used to study general detector properties such as the uniformity of signal formation and the charge sharing between strips, while the non-transparent scheme was used to assess the efficiency of hit recognition.

8.4.2 Charge Spectrum

Transparent Scheme

The transparent cluster widths of two, three and five strips were chosen to extract the signal. The 50 μm pitch region could not be used for three and five strip clustering as there at most two adjacent working strips were available.

The signal spectra for different numbers of strips used for the formation of the cluster are depicted in figure 83 for two, three and five strip clusters for 100 μm and 200 μm pitch. The average signal increases by about 5% from two strip to three strip clusters for 200 μm pitch, while no significant change between three strip and five strip clustering is observed. For 100 μm pitch the average signal increases by about 10% from two strip to three strip clustering, and by about 5% from three strip to five strip clustering. The dependence of the average signal on the number of strips used for clustering is shown in figure 84. The result indicates that the charge is shared mainly among two strips and the complete signal is included in three strips for the 100 μm and 200 μm pitch region. The signal-to-noise ratio, defined by the ratio of the average signal over the electronic noise, is determined to $S/N \approx 5$ for $U_b = 168$ V.

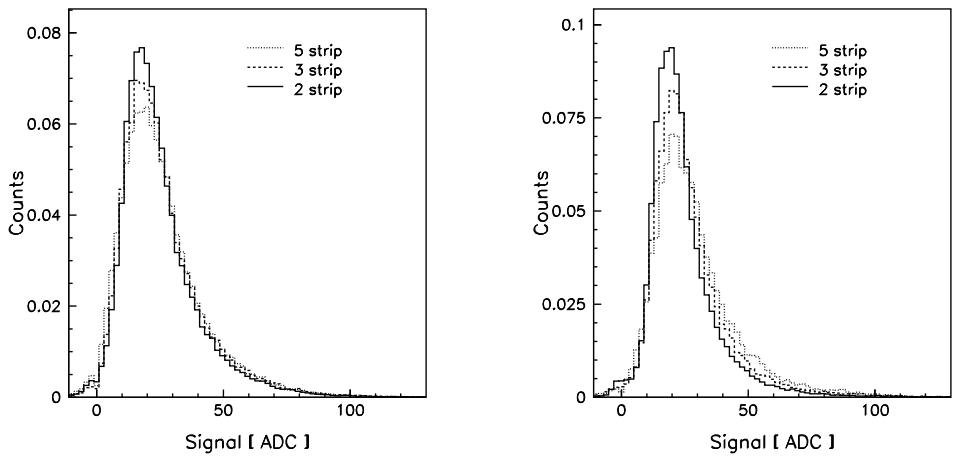

(a) 200 μm pitch, 100 μm width

(b) 100 μm pitch, 50 μm width

Figure 83: *Signal spectrum for transparent cluster formation with two, three and five strips for* 200 μm *and* 100 μm *pitch.*

The average signal of three strip clustering for different bias voltages is depicted in figure 85. The dependence of the average signal on the bias voltage shows about 10% lower values for the average signal then the measurement of the same quantity with ^{90}Sr and dot contact configuration. This discrepancy is attributed to the uncertainty of the calibration and the difference in ionisation density between 5 GeV electrons and ^{90}Sr beta particles (see section 4.6).

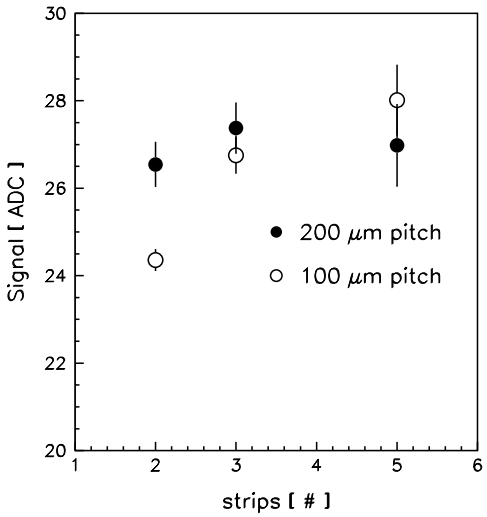

Figure 84: *Dependence of the average charge signal on the number of strips in a transparent n-strip cluster for* 200 μm *and* 100 μm *pitch and* $U_b = 168$ V.

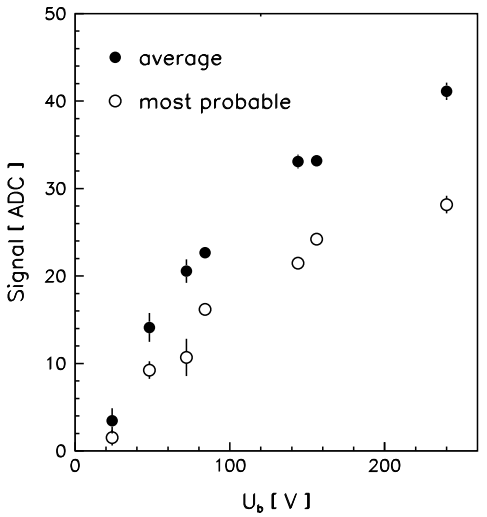

Figure 85: *Dependence of the average charge signal and the most probable signal of a three strip cluster on the bias voltage.*

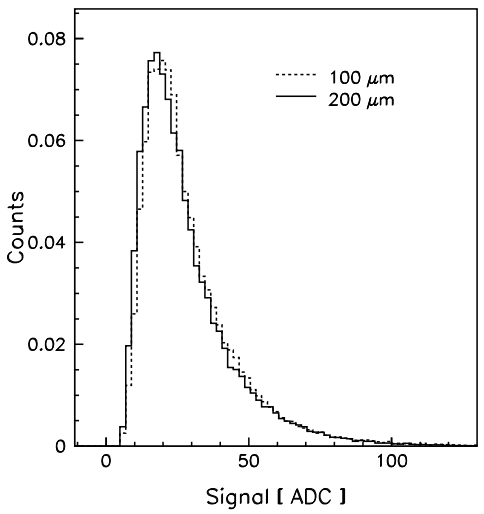

Figure 86: *Example of non-transparent cluster charge spectrum of the* 200 μm *pitch and* 100 μm *width region at* U_b = 168 V *with cluster cuts applied as explained in the text.*

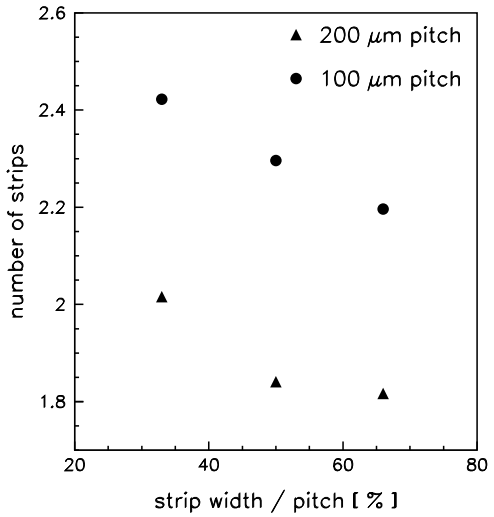

Figure 87: *Average number of strips included in a cluster for different strip width/pitch combinations (ratio of strip width over pitch is given in percent) with the cluster cuts defined in the text at* U_b = 168 V. *The* 50 μm *pitch region was not included as at most two adjacent working strips were found.*

Non-Transparent Scheme

In the non-transparent cluster scheme the seed strip was required to exceed a threshold value of signal significance and thus the spectrum is well separated from zero. In figure 86 a charge spectrum is shown for a pitch width of 200 μm and 100 μm at U_b = 168 V and a cluster significance cuts of $s_0 = 2$, $s_+ = 1$ and $s_{cl} = 2.5$. The separation from zero is clearly visible. The average number of strips included in a cluster as shown in figure 87 increases with decreasing strip pitch. It also shows a dependence on the strip width, namely for large strip widths fewer strips are included on average in the cluster formation than for small strip widths, reflecting the charge sharing profile discussed in section 8.4.3.

The reconstruction efficiency is defined as the ratio of reconstructed tracks N_r over all tracks N_0 passing through the fiducial volume, $\epsilon_r = N_r/N_0$. It is clearly a function of the cluster cuts applied in the clustering algorithm. The dependence of the efficiency on the seed strip significance, s_0, for U_b = 168 V is shown in

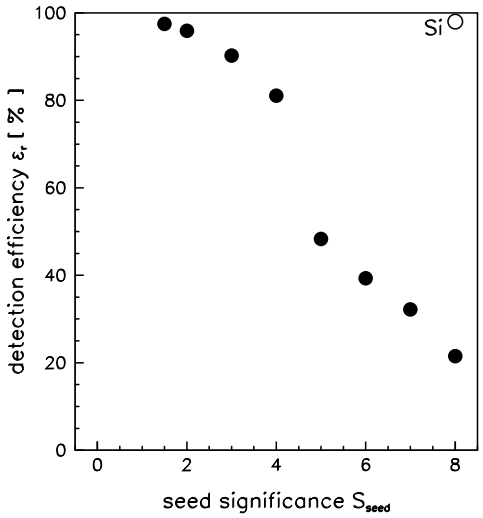

Figure 88: *Dependence of the detection efficiency, ϵ_r, on the seed significance, s_0, for $U_b = 168$ V. The open circle marks the position of a typical silicon detector.*

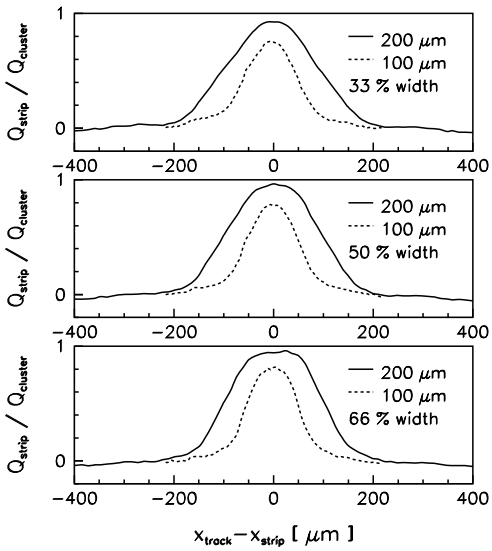

Figure 89: *Measured fraction of charge on one strip versus the position of the track relative to the strip position for* 100 μm *and* 200 μm *strip pitch and a strip width over pitch ratio of 33%, 50% and 66%.*

figure 88. Typical seed strip significances used at experiments with silicon vertex detectors are of the order of 8. The plot illustrates that the particular test device is inferior in competition with Si detectors where efficiencies of nearly 100% are reached. Moreover in this test-beam study the read-out electronics were optimised for low-noise for the sake of a relatively long shaping time.

8.4.3 Charge Sharing

The charge sharing between strips is dependent on the diffusion and drift length of the excess carriers, as well as on the strip width and pitch. Figure 89 shows the average fraction of the total charge induced on one strip versus the distance of the track from the centre strip position. The total charge was calculated by the sum of the five nearest strips.

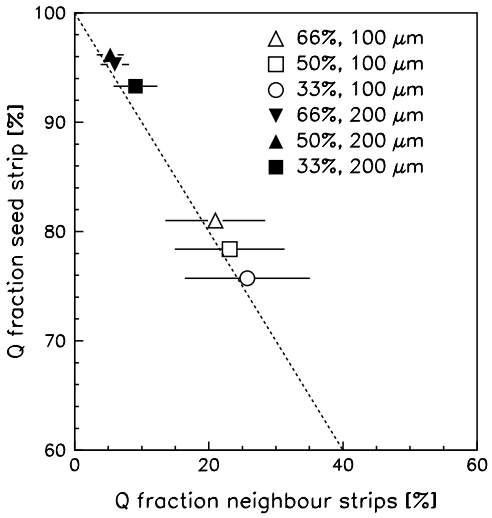

Figure 90: *Measured fraction of charge on the seed strip and on the two neighbouring strips for tracks going through the middle of the seed strip. Displayed are the data for* 200 μm *and* 100 μm *pitch. The dashed line indicates a sum of neighbour and seed strips of 100%.*

The general behaviour is similar for the 200 μm and 100 μm pitch region. As expected most of the charge is collected if the track is penetrating the strip. The decrease of the signal with increasing distance of the track position from the center of the strip is clearly dependent on the strip width. For 66% strip width a plateau of the fraction of collected charge centred at the middle of the strip is formed, while for 33% strip width the plateau is narrowed. The maximum fraction of collected charge, i. e. when the track penetrates the middle of the strip, shows a dependence on the strip width and pitch. The fraction of charge shared by the next two neighbouring strips is anti-correlated to the hit strip fraction, showing a consistent sharing of charge among three strips adding up to about 100% as shown in figure 90.

The η-value (defined by equation (75)) is another way to describe information about charge sharing. The distribution and the dependence of η on the position between two strips are shown in figure 91. The η-plots show that the linearity of the charge sharing is best at a small strip width over pitch ratio, while for 66% strip width the η over x dependence has a s-shape. A second thing to notice is that only 80% of the cluster charge (100 μm pitch) is collected on the seed strip if the track penetrates at the central position as already seen in figure 90. The change of shape is less pronounced for the 100 μm pitch region but still evident.

The corresponding distributions of η are shown in figure 92. At 33% strip width η is more uniformly distributed than for 50% and 66% strip width, where pronounced peaks near $\eta \approx 0$ and $\eta \approx 1$ are seen. The shape of the distributions is anticipated by the dependence of η on the track position. It is noted that negative values of η can occur due to noise fluctuations.

The results show that the charge is shared among the strips even for tracks penetrating the middle of a strip which is a consequence of the finite carrier drift length and thermal diffusion. Furthermore the charge sharing approximates a linear behaviour for small strip widths and becomes non-linear for wide strips.

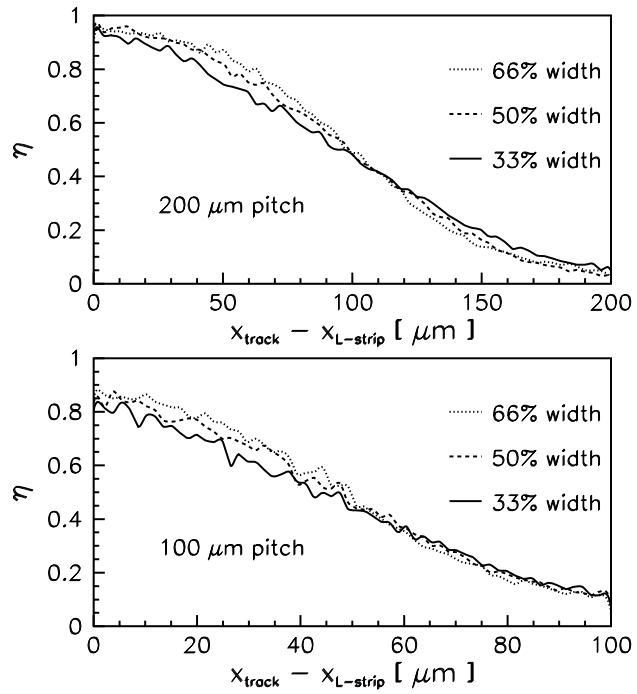

Figure 91: *Measured dependence of the η-value defined by equation 75 on the distance of the track to the nearest left strip for* 100 μm *and* 200 μm *strip pitch and 33%, 50% and 66% strip width.*

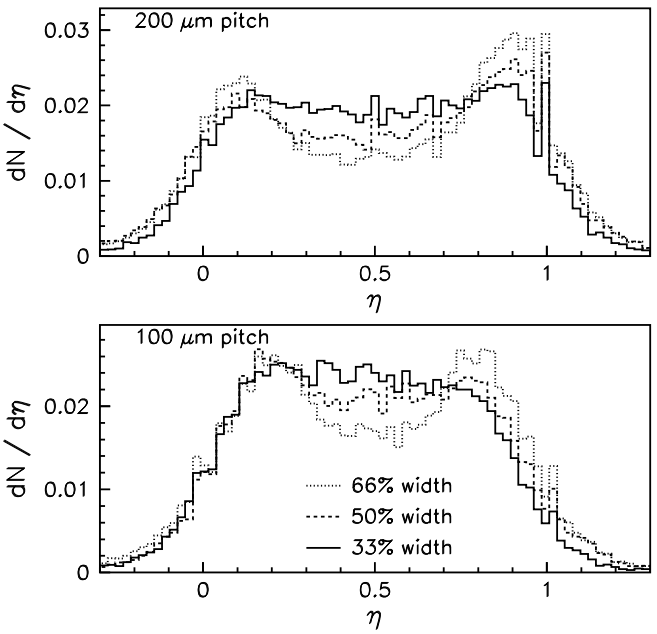

Figure 92: *Measured distribution of η as defined by equation 75 for* 100 μm *and* 200 μm *strip pitch and 33%, 50% and 66% strip width.*

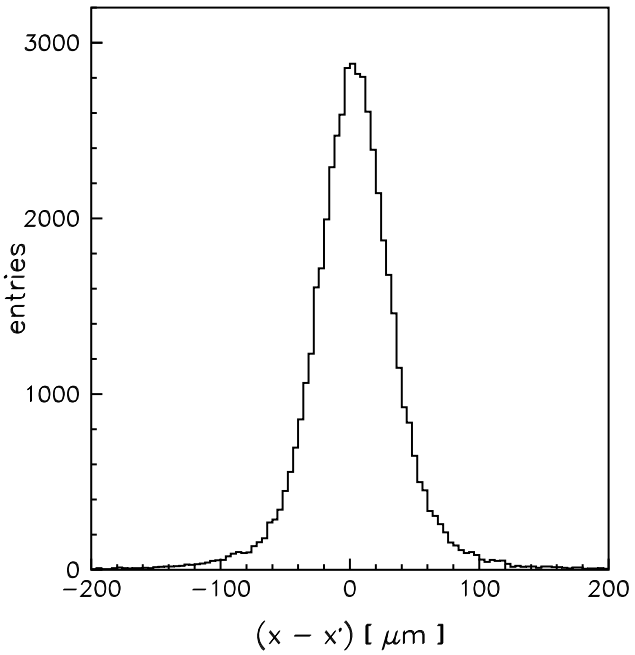

Figure 93: *Distribution of the difference between the predicted position and the reconstructed position* $(x - x')$ *for strips of* 200 μm *pitch and* 66 μm *width at* $U_b = 168$ V.

The impact on the resolution using the cog-method for position reconstruction will be discussed in the next section.

8.4.4 Resolution

The resolution is defined by the deviation of the reconstructed track position, x', from the true track position, x_{true}. The best approximation to the true track available is x, which is the track position predicted by the telescope. The error on x has to be taken into account when calculating the resolution of the test device. The total width of the residual distribution, i. e. the distribution of the deviation from predicted to reconstructed track, is given by adding the resolution of test device and the telecope in quadrature:

$$\sigma_{dut}^2 + \sigma_{x'}^2 = \frac{1}{N} \sum_{i=0}^{N} (x_i - {x'}_i)^2. \tag{78}$$

Here N is the number of events, $\sigma_{x'}$ the error on the reconstructed track position, $\sigma_{dut} = 7.5$ μm the error on the predicted track position, x_i the predicted track position and x'_i the reconstructed track position. An example for the distribution of $(x - x')$ is shown in figure 93 for strips with a pitch 200 μm of a width of 66 μm at $U_b = 168$ V.

The track position is reconstructed using the cog-method (see equation 74), which is optimised for linear charge sharing. To improve the resolution in the case of non-linear charge sharing the η-algorithm can be used [88] (see equation 76). The improvements are significant for extreme distributions of η as for example in silicon strip detectors with intermediate strips. Since in CVD diamond the

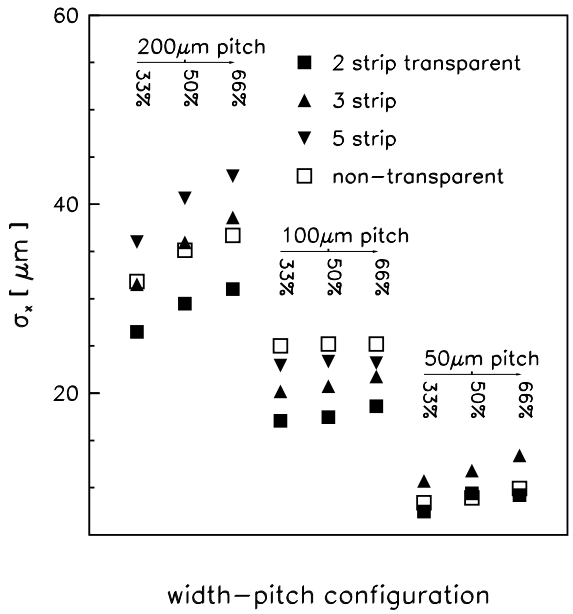

Figure 94: *Measured resolution $\sigma_{x'}$ of the test device for nine strip width configurations and two, three and five strip transparent clustering, as well as non-transparent clustering using the cluster cuts described in the text. A voltage of $U_b = 168$ V was applied.*

resolution is only marginally improved the cog-method will be used throughout the analysis to facilitate comparison between different geometries.

The resolution obtained, $\sigma_{x'}$, for the nine strip width/pitch combinations with a two strip clustering algorithm and a bias voltage of $U_b = 168$ V are plotted in figure 94. The resolution is clearly best for 33% strip width and degrades slightly for higher strip width as a consequence of the increasing non-linearity of charge sharing as seen in the η-value. The obtained resolutions are all better than the digital resolution due to charge sharing. The resolution for three strip and five strip clusters are displayed as well. Both methods have slightly worse resolution because of the increased noise contribution to the cluster signal.

The dependence of the average resolution of 100 μm and 200 μm pitch on the applied voltage is shown in figure 95. The decreasing signal for lower fields degrades the obtained resolutions due to the decreased signal-to-noise ratio.

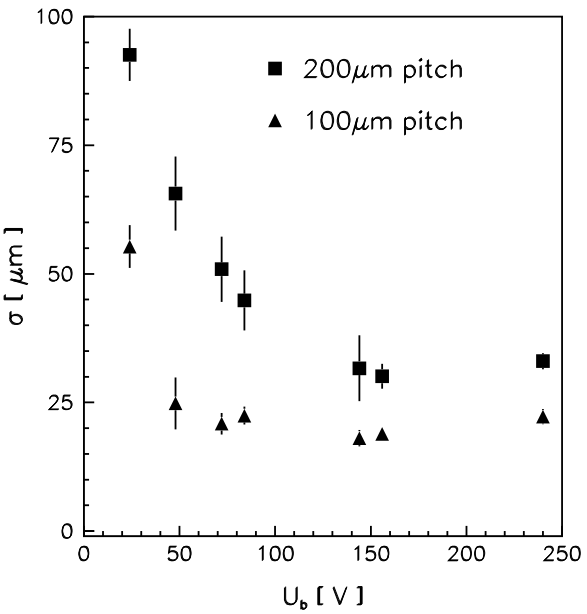

Figure 95: *The dependence of the average resolution for* 100 μm *and* 200 μm *on the bias voltage.*

8.4.5 Spatial Uniformity of the Charge Collection

One of the main results of the previous chapters was that the charge collection properties of CVD diamond are non-uniformly distributed due to the polycrystalline structure of the material. The knowledge of the position of the particle track provided by the silicon telescope allows to study the uniformity of the charge collection efficiency with MIPs.

For a study of the spatial uniformity a data set with a hit density of about 16000 tracks mm^{-2} was recorded at $U_b = 168$ V. To determine a spatially resolved ϵ_Q the average signal height of a group of events in a small area element (bin) was taken. The error on the measurement of ϵ_Q is given by

$$\sigma^2_{cce}(i,j) = \frac{\sigma_{ext}(i,j)^2}{N(i,j)} \tag{79}$$

with σ_{ext} the rms of the Landau fluctuation and the electronic noise, and N the number of events in the specified bin.

The value of σ_{ext} can not be obtained from the the rms of the signal spectrum, because it is a convolution of the ϵ_Q distribution, the electric noise, and the Landau fluctuation of the charge deposition. However, σ_{ext} must account for electronic noise and Landau fluctuations only. The average electronic noise contribution was $\sigma_{noise} = 190$ e, with a rms of 18 e. The contribution from the Landau fluctuation was estimated from the theoretical FWHM of the Landau distribution of $w_l = 4.018 \cdot ZN_\alpha \frac{k}{\beta^2} d = 1015$ e [7], where $Z = 6$, N_α the number of atoms per unit volume, $k = 2.55 \cdot 10^{-19}$ eV$/atom$ the extinction coefficient, $\beta = v/c$ and $d = 500$ μm the detector thickness. The theoretical value of w_l considers the fluctuation of the deposited charge. However, the fluctuation of the measurement is given by $w_l \cdot \epsilon_Q$. As a rough estimate a value of $w_l \cdot \langle \epsilon_Q \rangle = 136$ e was taken considering the average efficiency $\langle \epsilon_Q \rangle = 13\%$ of the samples at $U_b = 168$ V. To correctly take into account the asymmetric shape of the Landau distribution, a distribution with $w_l = 136$ e was numerically calculated and convoluted with a Gaussian with $\sigma = 190$ e to determine the error contribution of external sources to $\sigma_{ext} \approx 236$ e $= 3.2$ ADC counts. The dependence of the error σ_{cce} on the bin size Δx is depicted in figure 96 for the hit density in the data of 0.016 events per $\mu\mathrm{m}^2$.

For the analysis a bin-size of $\Delta x = \Delta y = 50$ μm was chosen resulting in an error of $\sigma_{cce} = 0.51$ ADC counts. Due to the non-uniform beam-profile and limited statistics σ_{cce} fluctuates for the different bins. The range of σ_{cce} where 98% of the bins were contained was determined to be 0.73 ADC $> \sigma_{cce} >$ 0.41 ADC.

The purity of events assigned to a specific bin is related to the spatial precision of the impact point determination. It can be approximated by

$$\xi \approx \frac{1}{1 + \frac{\sqrt{2\pi\sigma(dut)^2}}{\Delta x \Delta y}} \tag{80}$$

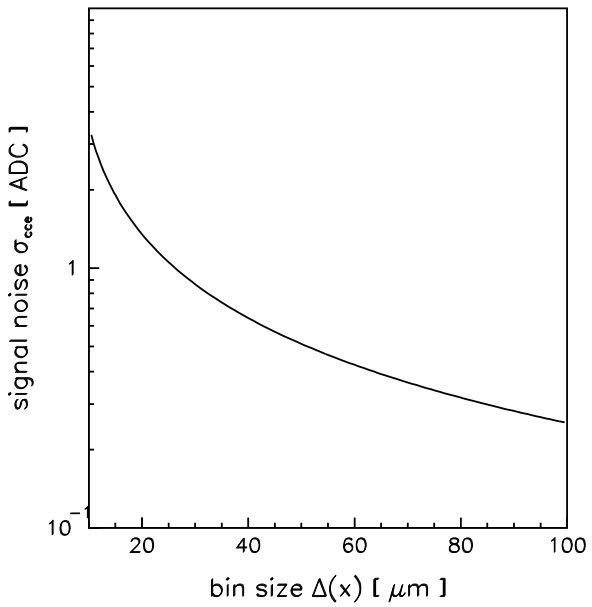

Figure 96: *The dependence of the the error σ_{cce} of the measurement of ϵ_Q on the bin-size Δx.*

with $\sigma(dut)$ the precision of the impact point prediction from the silicon telescope and $\Delta x \Delta y$ the bin size. For $\sigma(dut) = 7.5$ μm and $\Delta x \Delta y = (50\ \mu\text{m})^2$ the purity is $\xi = 0.73$.

A map of the average charge signal obtained with the transparent two and three strip clustering algorithm described in section 8.4.1 is displayed in figure 97. The map shows clustered non-uniformities of the detector response as seen with other methods (see chapter 4).

Each bin represents the average signal response of a volume element $\Delta V = (\Delta x, \Delta y, d)$ located at (x, y). The distribution of the average signal response of all bins for two and three strip clustering is shown in figure 98. The two-strip cluster algorithm produces a spectrum shifted to slightly lower values of the average signal response if compared to the three strip cluster algorithm. This is in agreement with the observation made in section 8.4.2 that enhanced charge collection is achieved for three strip clusters.

The distribution is a convolution of the intrinsic variation of ϵ_Q based on the material property, and the statistical fluctuation of the ϵ_Q measurement in each bin due to Landau fluctuations and the amplifier noise. To obtain the intrinsic variation of ϵ_Q the external contribution σ_{ext} discussed above has to be subtracted in quadarature. The results for σ_Q and the mean signal μ_Q is for 2 strip (index $2s$) and three strip (index $3s$) clustering given by:

$$\begin{aligned} \sigma_Q^{2s} &= 9.14 \text{ ADC} \Leftrightarrow \sigma_Q^{2s}(\epsilon_Q) = 3.7\% \\ \mu_Q^{2s} &= 26.02 \text{ ADC} \Leftrightarrow \langle \epsilon_Q^{2s} \rangle = 10.5\% \\ \\ \sigma_Q^{3s} &= 9.49 \text{ ADC} \Leftrightarrow \sigma_Q^{3s}(\epsilon_Q) = 3.8\% \end{aligned}$$

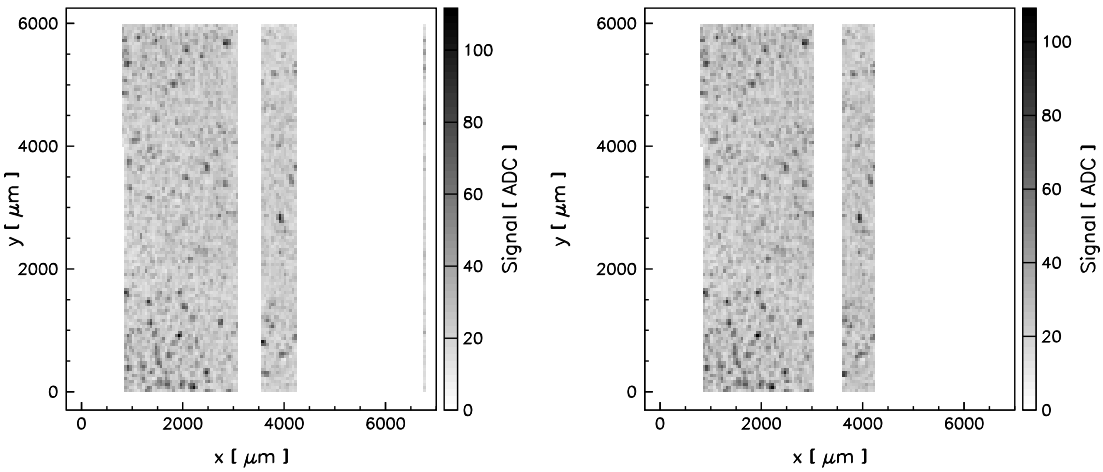

(a) Two strip clustering

(b) Three strip clustering

Figure 97: *Map of the average charge signal with a bin-size of* 50 μm *and an average of* $N = 40$ *entries per bin. The charge signal was obtained with the transparent two strip clustering algorithm. The empty areas stem from malfunction of the corresponding strips.*

$$\mu_Q^{3s} \quad = \quad 27.54 \text{ ADC} \Leftrightarrow \langle \epsilon_Q^{3s} \rangle = 11.2\%. \tag{81}$$

The results can also be expressed in terms of the charge collection efficiency significance, S_Q, expressing the uniformity of ϵ_Q. The charge collection efficiency significance was defined as the ratio of the mean over the variance, $S_Q = \mu_Q / \sigma_Q$. The results are $S_Q^{2s} = 2.84$ and $S_Q^{3s} = 2.9$ for two and three strip clustering. The value of S_Q was also determined by the method described in section 4.7 employing a 10 keV photon beam. The same sample was metallised with a circular pattern of 7 mm diameter for this measurement. The spatially resolved measurement of on an area of ≈ 20 mm^2 is shown in figure 102. Half of the metallised area was scanned. The circular shape is easily recognised. The signal spectrum is depicted in figure 99. The peak at zero is caused by the non-metallised area. When taking only the metallised area into account this measurement yields a value of $S_Q = 3.3$, which is close to the values quoted for the electron beam. The slightly higher S_Q measured with photons may be a result of the poorer resolution of ≈ 100 μm.

Structure Scale

To characterise the structure scale of the non-uniformities a simple algorithm (*structure algorithm*) was applied to merge bins by searching for clusters in

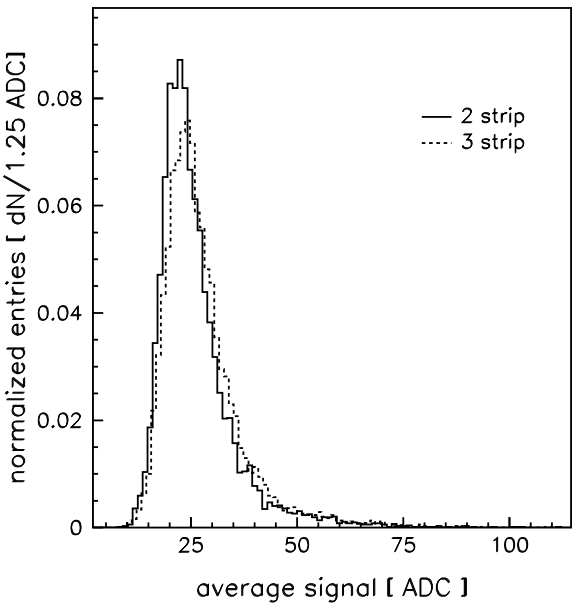

Figure 98: *Distribution of the average signal response for two and three strip clustering in bins of* $\Delta x = \Delta y = 50$ μm.

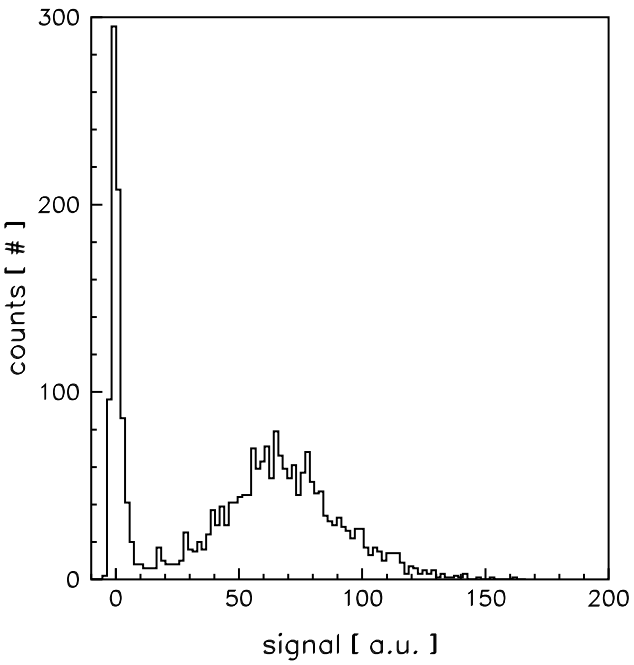

Figure 99: *Signal spectrum obtained with a 10 keV photon beam on the sample DS8 metallised with a circular pattern of 7 mm diameter.*

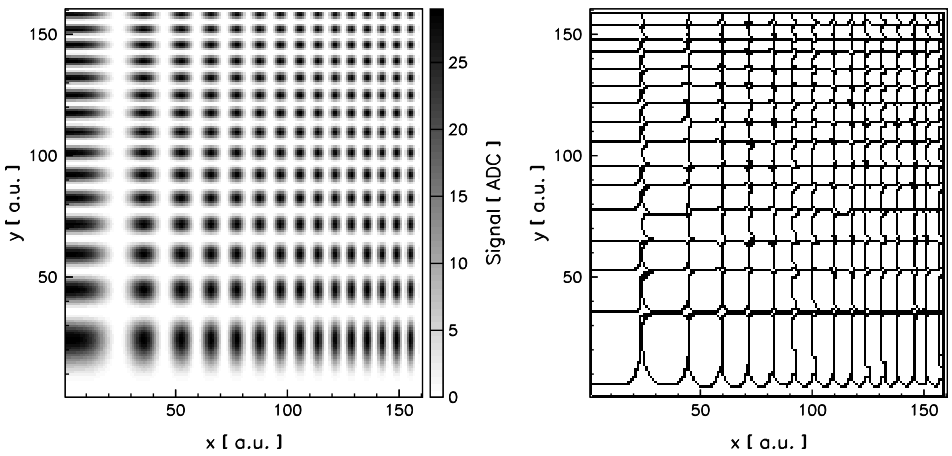

(a) Generated sample data.

(b) Clusters found by the structure algorithm on the sample data.

Figure 100: *Sample data set and clusters found by the structure algorithm.*

the spatial distribution of the average signal response. An illustrative example demonstrating the principle of the algorithm is shown in figure 100. The data is generated by the function $f(x,y) = a \cdot (b + \cos(x^r)^2 \cdot \sin(y^r)^2)$ which forms an array of peaks with varying peak width.

In order to find clusters the bins with the highest entries are assigned as seed bins. In the example the seed bins are given by the centre of the peaks. In a second step the remaining bins are each checked, going from bins with high entries to bins with low entries, whether they are adjacent to a seed bin. If so they are assigned to belong to the seed bin to form a cluster, if not the bin is isolated and taken as a new seed bin. After the procedure is completed every bin is assigned to a cluster. The result shown in figure 100b. The resulting clusters are clearly corresponding to the peak structure in the sample data set.

The cluster procedure allows to analyse the data set in terms of number of clusters and cluster size. The structure algorithm was applied to the data of the test detector and resulted in a patch work of irregular patterns shown in figure 101. The average structure size was determined by this method to be $\approx (200\ \ \mu\text{m})^2$.

If the same algorithm is applied to the data-set obtained with a 10 keV photon beam (see section 4.7) a compatible structure size of $\approx (250\ \mu\text{m})^2$ is found. The data and the result of the structure algorithm are shown in figure 102.

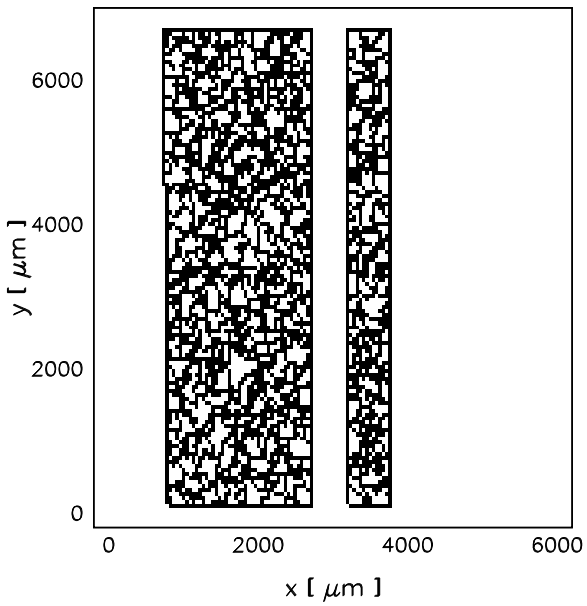

Figure 101: *Clusters found by the structure algorithm explained in the text on the data of the spatial distribution of* ϵ_Q .

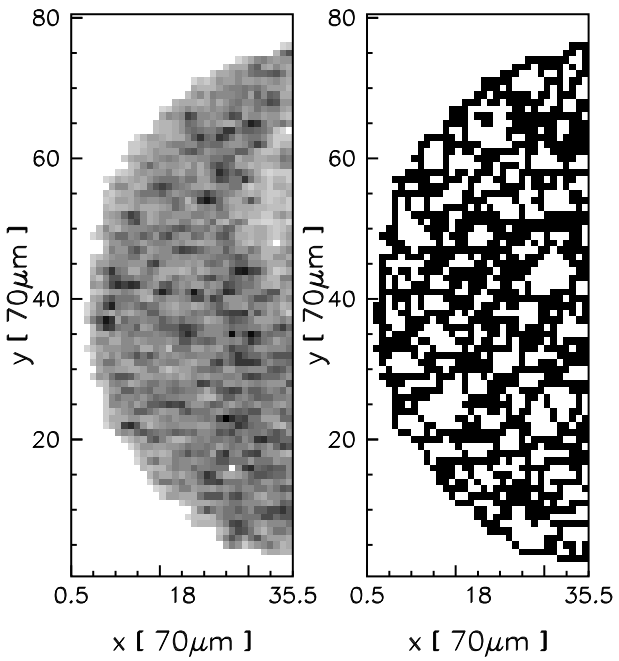

Figure 102: *A spatially resolved measurement of* ϵ_Q *with a 10 keV photon beam (section 4.7) is shown on the left side. The clusters found by the structure algorithm are shown on the right side. The sample was metallised for this measurement with a circular shape of 7 mm diameter.*

8.4.6 Systematic Deviation of Position Reconstruction

In section 8.4.4 the resolutions obtained with the test device for different strip-pitch combinations were discussed. The resolution is not dominated by statistical processes, as for example charge diffusion or delta electrons, but stems from the charge sharing characteristics (see section 8.4.3). Thus the deviation of the reconstructed track position to the real track position is of systematic nature and can be investigated as a function of the position (x, y) on the detector:

$$\bar{s}(x, y) = \langle x - x' \rangle, \tag{82}$$

with x the predicted position, x' the reconstructed position and $\bar{s}$ the average deviation of the reconstructed position relative to the predicted position at (x, y). For a uniform detector material with uniform strips of pitch p running along the y-axis, $\bar{s}(x, y)$ would be a function of modulus(x, p) only. For a material with non-uniformly distributed electrical properties like CVD diamond $\bar{s}$ is dependent on (x, y). The non-uniformity of δ_Q must have a direct effect on $\bar{s}$ as the charge sharing depends on the drift path and length of the generated carriers. The charge induced on one strip is a function of the difference of the strip potential seen by the charge at its creation and stopping point (see appendix A.3). Since the one strip potential, different from the plate capacitor potential, is dependent on z and also x, the fraction of induced charge on one strip is dependent not only on the distance the charge moves but also on the actual path start and end point within the strip potential. In the case of the plate capacitor potential the induced charge is only dependent on the drift length in z.

As the induced charge on a single strip is dependent on x and z also the charge sharing between two strips is dependent on the actual drift path of charge carriers. As a descriptor of the charge sharing the η-value was introduced in section 8.1. It gives the fraction of charge induced on the left strip relative to the charge induced on the left and the right strip next to the particle track. The sharing of the induced charge from a single moving charge as a function of the starting point of the drift path is shown in figure 103. The value of η is plotted as a function of the point of creation of the single charge at (x, z). A uniform drift length of $\delta_x = 10$ μm and a detector thickness of $d = 300$ μm are chosen in the calculation. The drift direction of the charge is towards the strip electrodes which have a pitch $p = 100$ μm and strip width of $\frac{1}{2}p = 50$ μm and are located at $z = 300$ μm. The plot shows a strong dependence of η on (x, z). Noticeably η can become negative and greater than one, due to charges of opposite sign induced on the left and right strip. This is explained by the shape of the single strip weighting potential $V_w(x, z)$ used to calculate the induced charge. The weighting potential is also plotted in figure 103. The derivative $\frac{\partial V_w(x,z)}{\partial z}$ has sometimes negative values. A charge drifting in this area will induce charge of opposite sign on the strip with respect to the total induced charge on both strips. Note that the negative component does not imply a negative electric field since the

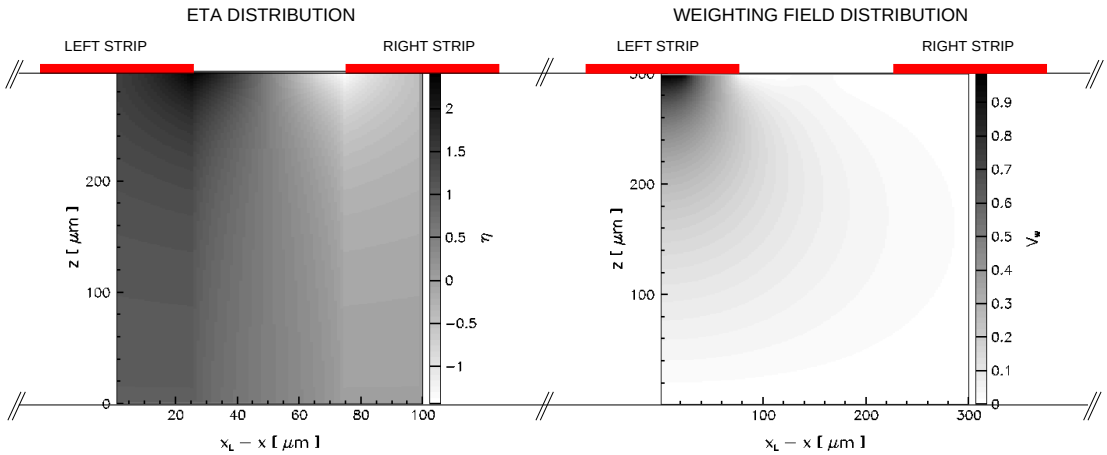

Figure 103: *On the left the calculated dependence of the η-value on the charge initial position relative to a left-sided strip $(x_l - x)$ and the distance to the strip side (z) is shown. The dependence is calculated for a single charge drifting towards the strip side with a drift length of* 10 μm *for strip pitch of* 100 μm *and width of* 50 μm*. The induced charge on the strip is proportional to the difference of the weighting potential V_w (on the right) at the start and end point of the drift path.*

total electric field is composed by the superposition of all strips approximating a plate capacitor field. The dependence of η on z means that the reconstructed position is strongly dependent on the drift length distribution in z. For a uniform ionisation density in z as in the case of MIPs, a non-uniform distribution of the drift length introduces additional systematic variations of the reconstructed track position over the active area.

A second source contributing to the non-uniformity of $\bar{s}$ can be non-uniformly distributed space charge in the crystal. The issue of modelling is addressed in section 8.5 where the influence of space charge on $\bar{s}$ is investigated.

The finite statistics of the experimental data requires to subdivide the detector area into bins of x and y. In analogy to the analysis of the charge collection efficiency (see section 8.4.5) a bin size of $\Delta x = \Delta y = 50$ μm was chosen to investigate the spatial dependence of $\bar{s}$. Figure 104 shows the spatial distribution (a) and the frequency distribution (b) of $\bar{s}$ prepared with the transparent three strip clustering scheme. The spatial distribution has an eye catching strip structure corresponding to the metallisation pattern of the detector. Furthermore, non-uniformities forming clusters are overlaid on top. By comparing the structure with the spatial measurement of ϵ_Q (section 8.4.5) it is seen that the correlation is weak. Cluster areas in ϵ_Q do not necessarily correspond to clusters of $\bar{s}$. However some clusters, i. e. in the 100 μm pitch region, are visible both in $\bar{s}$ and ϵ_Q.

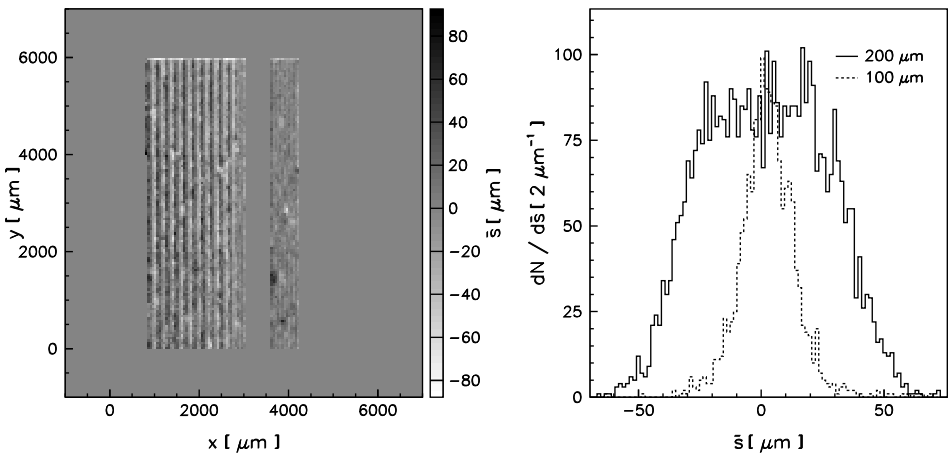

(a) Spatial distribution of $\bar{s}$.

(b) Frequency distribution of $\bar{s}$.

Figure 104: *Spatial representation and frequency distribution of* $\bar{s}$ *for* 200 μm *and* 100 μm *pitch regions. The transparent three strip clustering scheme was used,* U_b = 168 V.

The spectrum in figure 104 shows the frequency distribution of $\bar{s}$ for the 200 μm and 100 μm pitch region separately. In accordance with the resolution plots from section 8.4.4 the distribution of the 100 μm pitch region is narrower with an rms of $\sigma_{rms}(p = 100\ \mu\text{m}) = 11.7\ \mu$m than for the 200 μm pitch variant with $\sigma_{rms}(p = 200\ \mu\text{m}) = 24.3\ \mu$m.

8.5 Numerical Modelling

Introductory Remarks

The aim of the numerical modelling was to understand qualitatively aspects of the behaviour of the prototype device. It is based on the simulation work presented in chapter 7. The simulation considers the crystallite structure of CVD diamond and makes assumptions about the lifetime distribution in the crystal.

The typical crystal structure of CVD diamond is generated with a growth algorithm with the parameters κ_l as the probability of lateral growth, δ_{sat} the saturation drift length of the crystal, and r_0 the life-time length (for details see section 7.1). The result is a non-uniform distribution of traps leading to non-uniform charge collection properties and a non-uniformly distributed space charge, i. e. the space charge density at grain boundaries is higher than within the

grains. The non-uniform charge collection properties influence the signal on the electrodes and the charge sharing between strips. The space charge also disturbs the applied electrical field and introduces additional lateral components. The result is, that the drift path of the charge carriers is no longer determined only by the external field and systematic deviation from the straight drift path (neglecting the effect of thermal diffusion) may occur. This deflection of charge carriers has an impact on the charge sharing between strips and can cause significant variations of $\bar{s}$.

8.5.1 Simulated Device

The material of the simulated device was a two dimensional CVD crystal (thickness $d = 300$ μm, width $l = 1000$ μm) with a lateral growth probability of $\kappa_l = 0.2$, a saturation drift length for electrons and holes of $\delta_{sat} = 100$ μm and a lifetime length of $r_0 = 10$ μm. The average collection distance, $\delta_Q = \delta_e + \delta_h$, for this configuration was determined to $\delta_Q = 113$ μm.

Since the simulation was primarily aimed at a qualitative understanding of the average signal response, the Landau fluctuation of the charge deposition was discarded and a constant ionisation density of $\rho_{mip} = 36$ eh μm^{-1} was used. Furthermore the amplifying electronics were not included in the simulation, thus the intrinsic noiseless signals were used for analysis and track reconstruction.

Nine metallisation configurations according to the patterns used for the prototype device were implemented (see table 18). The read-out strips were placed on the growth side. The signal induced on single strips was calculated using the weighting field method [96, 87] explained in appendix A.3.

To establish the influence of the priming effect on the detector parameters the simulation was run with and without trapped charge. The primed state of the simulated device was achieved by the procedure described in section 7.4.4.

8.5.2 Results of the Simulation

Charge Collection Efficiency

The dependence of ϵ_Q on the track position x is depicted in figure 105b. The large variations in ϵ_Q correspond to the crystallite structure as was already demonstrated in section 7.4.4. The simulation can reproduce qualitatively the variation of ϵ_Q seen on the test device.

The distribution of ϵ_Q (figure 105a) is wider in the simulation than seen experimentally. The ratio of the mean value, μ_Q, over the rms of ϵ_Q , σ_Q, was defined as the charge collection efficiency significance, $S_Q = \frac{\mu_Q}{\sigma_Q}$, and is 2.9 in the data and 2.5 in the model calculation. Taking into account the slightly worse spatial resolution of the experiment of $\sigma = 7$ μm compared to the 1 μm binning of the simulation the agreement is fairly good.

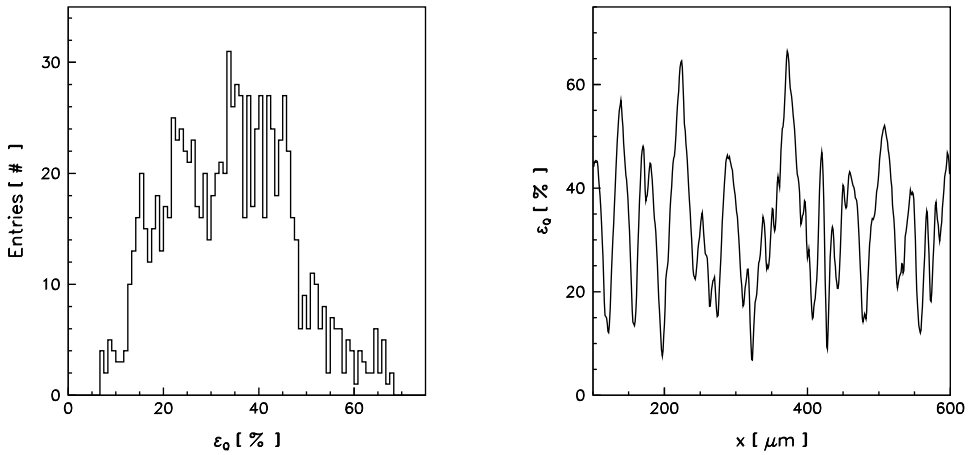

(a) Spectrum of the charge collection efficiency.

(b) Spatial dependence of the charge collection efficiency.

Figure 105: *Simulated spectrum and spatial dependence of the charge collection efficiency, ϵ_Q, of a device with $\kappa_l = 0.2$ and $\delta_{sat} = 100$ μm.*

Charge Sharing

The charge sharing was calculated for the nine different strip geometries for primed and unprimed material. To compare the results with the experimental data the η-distribution and the dependence of η on the track position between the left and the right strip were considered.

The results of the simulation are shown in figure 106 for the unprimed and primed material. The figures have to be compared with the experimental results shown in figure 91 and figure 92. It is recalled that the data showed a tendency to change from a linear to a s-shape of $\eta(x)$ for wider strips. Accordingly the η spectrum changed from a flat distribution to a distribution with two peaks at $\eta \approx 0$ and $\eta \approx 1$. Despite the low statistics the features in the data are well reproduced by the simulation. It is also noticed that the change in shape is most evident for the 200 μm pitch, decreases for 100 μm pitch and is weakly present at 50 μm pitch. The qualitative behaviour is the same for primed and unprimed material, while the primed material shows a tendency to be more s-shaped. This effect is due to the increased lifetime of the carriers by 30% in the primed material.

Resolution

The influence of the structure on the resolution can be discussed in analogy to the discussion of the experimental results in terms of the overall resolution and the systematic deviation of the predicted track position from the true position. Since the amplifier noise and the ionisation density fluctuations are neglected and furthermore the true track position is known the obtained position resolution of the modelled device should be systematically better.

Also here the case of primed and unprimed material is distinguished. It was already speculated that the non-uniformly distributed space-charge could lead to deflection of the charge carriers from the straight path as governed by the external field. Since the internal field is significant for the primed material larger deviations of the reconstructed track positions are expected.

With the model simulation the resolution for the nine strip geometries was determined for primed and unprimed material. The track was reconstructed using the *cog* of the signals of the three next nearest strips to the true track position. The rms of the deviation from the true position to the track position, i. e. the resolution σ_x, is plotted in figure 107. The corresponding experimental data was shown in figure 94. Although the absolute values disagree by a factor of ≈ 1.5 and are higher in the experimental data, the qualitative behaviour is well reproduced by the simulation. The best resolution for a given pitch is obtained with the smallest strip width in agreement with the experimental data. The discrepancy is expected to be due to the neglect of electronic noise and charge deposition fluctuations. The effect of non-uniformly distributed space charge on the resolution can be clearly seen by the increase of σ_x in the case of primed material relative to the unprimed state.

Systematic deviations of the reconstructed position (section 8.4.6) were seen in the experimental data, which were correlated to the strip structure but which also showed uncorrelated deviations similar to the non-uniformities seen in ϵ_Q. The simulation of the spatial dependence of the deviation from true to reconstructed track position shown in figure 108. The black lines indicate the position of the read-out strips. While the variations are clearly correlated to the strip structure in the case of $p = 200$ μm pitch, the correlation is less pronounced for $p = 100$ μm and no clear correlation is seen for p = 50 μm. This result can be compared to the experimental data shown in figure 104. Since the data is binned in $\Delta x = \Delta y = 50$ μm bins the resolution is not sufficient to observe a possible strip correlation for $p = 100$ μm. However, a clear correlation can be seen for $p = 200$ μm in accordance with the simulation. Moreover, the simulation shows systematic deviations of $\bar{s}$, uncorrelated to the strip structure in agreement with the experimental data.

8.6 Summary

A prototype position sensitive detector device made of CVD diamond was successfully constructed and tested. The use of different strip and pitch geometries allowed to investigate the influence of the metallisation geometry on detector parameters like resolution and charge collection.

It was found that the resolution and charge collection showed a non-uniform variation over the active detector area independent of the strip geometry. The non-uniformities of detector properties could be qualitatively reproduced and explained with a computer model based on the close link of crystallite structure and charge carrier lifetime (see section 7 for details).

With low noise read-out electronics the best position resolution ($\sigma_x = 8.4$ μm) was obtained with a strip pitch of 50 μm and a strip width of 16 μm. A detection efficiency of 97% was achieved with a threshold cut of 2 sigma. The signal-to-noise ratio was determined to ≈ 5 with a most probable signal of 1800 e and an average signal of 2500 e for a bias voltage of 168 V.

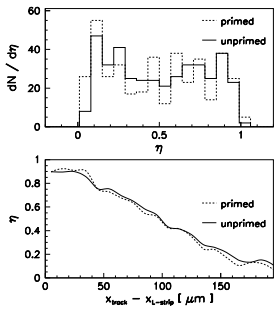

(a) 200 μm pitch, 33% width.

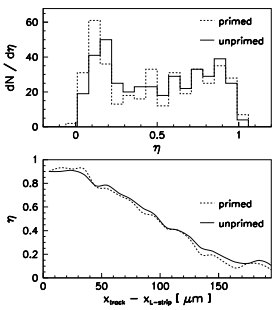

(b) 200 μm pitch, 50% width.

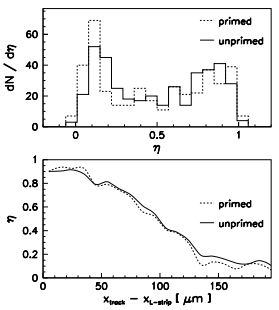

(c) 200 μm pitch, 66% width.

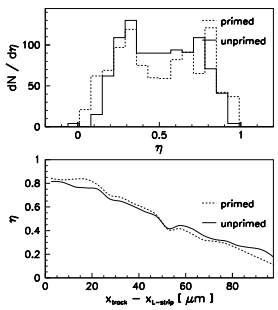

(d) 100 μm pitch, 33% width.

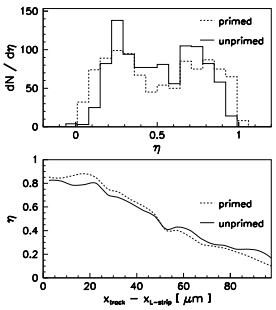

(e) 100 μm pitch, 50% width.

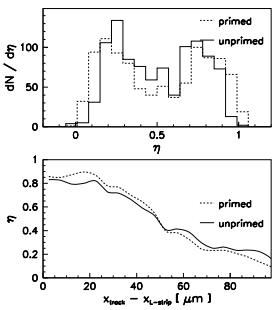

(f) 100 μm pitch, 66% width.

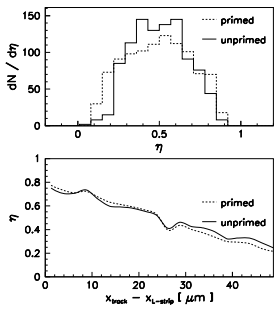

(g) 50 μm pitch, 33% width.

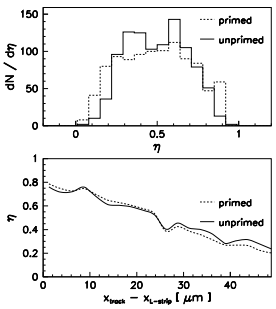

(h) 50 μm pitch, 50% width.

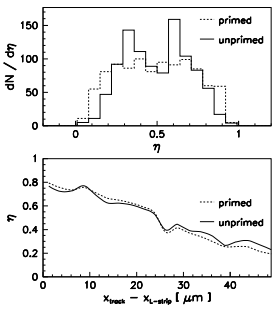

(i) 50 μm pitch, 66% width.

Figure 106: *Simulated η-spectra and $\eta(x)$ dependencies for nine different pitch/width combinations for unprimed and primed material ($\kappa_l = 0.2$ and $\delta_{sat} = 100$ μm).*

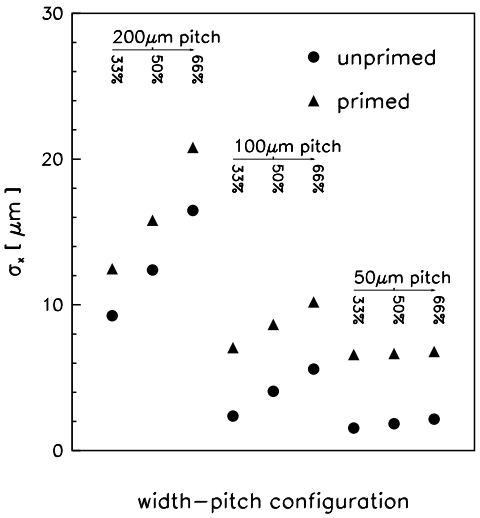

Figure 107: *Obtained resolutions of the device simulation for nine different strip geometries for primed and unprimed material ($\kappa_l = 0.2$ and $\delta_{sat} = 100$ μm).*

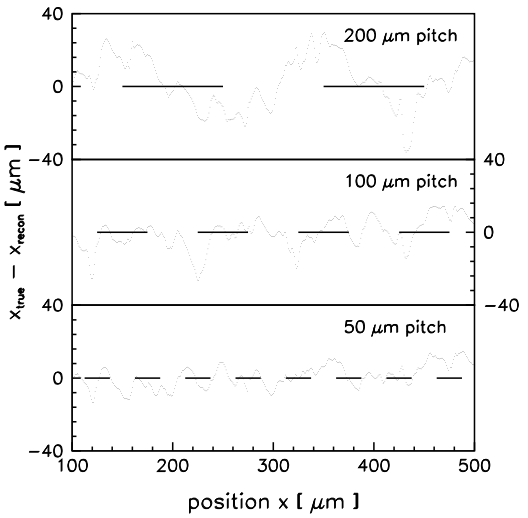

Figure 108: *Simulation of the spatial dependence of the deviation from reconstructed to true track position $x_{true} - x_{recon}$ for three different strip pitches and 50% strip width for primed material ($\kappa_l = 0.2$ and $\delta_{sat} = 100$ μm). The black lines indicate the position of the read-out strips.*

9 Summary

This work presents a study of the applicability of CVD diamond as a material for future particle detection systems. Different characterisation methods of electrical and structural properties were employed and further developed to gain a deeper understanding of the charge collection process in the material. A systematic study of growth parameters of a CVD process was performed with the goal of improving diamond material for the detection of particles. Correlations of growth conditions and detection properties were established. The radiation hardness of diamond was investigated with neutrons. The experimental observations were explained by a damage model. A computer simulation of the charge drifting process and the influence of traps, together with a simple model for the growth of CVD diamond, could explain qualitatively the various experimental data. Finally, a position sensitive prototype detector has been developed and successfully tested. Here also the computer simulation could qualitatively reproduce the experimental data successfully.

The electrical characterisation methods include spatially resolved measurements of the charge collection efficiency with a uniform generation of charge carriers by particle beams (10 keV photons, 5 GeV electrons) and generation of carriers in a thin surface layer (20 keV electrons, 2 MeV protons) as well as non-resolving measurement methods with β and α particles. It was found that the charge collection properties of CVD diamond are distributed non-uniformly in the bulk. The degree of non-uniformity expressed by the charge collection efficiency significance is in good agreement between different measurement methods and typical values of $S_Q \approx 4 \pm 1$ were found with different samples.

Furthermore, due to its incomplete charge collection, polarisation phenomena and trap passivation were observed. While the latter effect increases the lifetime of charge carriers and thus the signal, the former compensates the external electric field and decreases the response. The priming effect has been parametrised with the priming ratio, R_p, and the priming fluence, Φ_0. The priming effect was found to vary strongly depending on the sample quality with ranges of $1.2 < R_p < 4.2$ and $7 \text{ rad} < \Phi_0 < 160 \text{ rad}$. Spectroscopic investigations of defect levels showed the existence of defects with activation energies around 1.8 eV, and therefore explained the persistence of the polarisation and the priming effect at room temperature. Moreover a spatially resolved measurement showed a non-uniform defect concentration laterally across the material, corroborating the findings of the spatially resolved measurements of the charge collection efficiency.

Structural characterisation of CVD diamond with scanning electron microscopy and X-ray diffraction allowed to investigate the growth morphology of the samples and to obtain images of isolated single crystallites within the samples, showing a columnar growth morphology with increasing crystallite size in CVD diamond films. The data are in qualitative agreement with a proposed growth model of CVD diamond.

The main problem hindering the employment of CVD diamond in detection systems is the insufficient signal yield compared to silicon. A systematic growth study with a CVD process could establish correlations of the growth speed with the collection efficiency and the increase of the collection efficiency due to priming of CVD diamond. The best sample with a thickness of 50 μm showed a collection efficiency of 38% at the lowest growth speed of 0.31 μm h^{-1} which is a record value for this quantity reported for CVD diamond. Future improvements of the growth process should be possible and offer the hope for a real alternative to silicon. In terms of signal yield, defined by the product of efficiency and thickness for uniformly ionising particles, better samples were obtained from a commercial manufacturer, grown to thicknesses of the order of 1 mm, from which a prototype detector was build.

The prototype detector was patterned with different strip geometries in order to investigate the influence on the position resolution and the signal. It was found that the resolution and charge collection showed a non-uniform variation over the active detector area independent of the strip geometry. The non-uniformities could be qualitatively reproduced and explained with a computer model based on a close link between crystallite structure and charge carrier lifetime. With low noise read-out electronics the best position resolution ($\sigma_x = 8.4$ μm) was obtained with a strip pitch of 50 μm and a strip width of 16 μm. A detection efficiency of 97% was achieved with a threshold cut of 2 sigma. The signal-to-noise ratio was determined to ≈ 5.

A new approach towards a model of the charge drifting process in CVD diamond was developed. While other models [10] propose a linear relationship between film thickness and the charge collection distance, δ_Q, the new model is based on the growth morphology and proposes a $(1 - e^{-x})$ dependence of δ_Q on the distance to the next grain boundary. This model together with a simple algorithm describing the growth process of CVD diamond films could qualitatively explain the main experimental observations, such as the crystallite shape from X-ray diffraction, priming, polarisation and non-uniformity of charge collection.

The motivation to investigate the particle detection properties of CVD diamond is its supposed radiation hardness. Therefore, the radiation hardness has been considered by irradiation with neutrons to fluences up to several 10^{15} n cm^{-2}. The resistivity, the charge collection and the priming behaviour were recorded as a function of exposure. The change of the latter two properties could be parametrised by a herein proposed damage model and simultaneously fitted with reasonable accuracy. The extracted damage constants were used to predict the change in the signal spectrum of a hypothetical CVD diamond detector with a most probable signal of 7200 e in the ATLAS environment for ten years operation at the LHC. The results show that operation of a pixel device is likely to be uncritical while a strip detector configuration is restricted by its inherent higher noise level.

To conclude the four major subjects of this thesis are listed again: the char-

acterisation of electrical and structural CVD diamond properties, the test of the radiation resistance with neutrons, the simulation of the detection process of ionising particles in CVD diamond, and the construction and test of a position sensitive detector from CVD diamond.

Outlook

The next steps on the road map towards a position sensitive detector device from CVD diamond are given by attempts to improve the material uniformity. While the average signal for a MIP in selected CVD diamond samples is reaching 7200 electrons the poor uniformity effectively spreads the signal spectrum and requires a low threshold cut to achieve reasonable detection efficiency. Another crucial point is a revisiting of the radiation tolerance of CVD diamond. More irradiation experiments with the best material available are needed to establish the radiation hardness and to compare with model predictions. Especially in an envisaged application in future high luminosity particle physics experiments the final decision is made by economics. It is essential to provide cost effective processes to manufacture detector grade CVD diamond while being competitive with silicon in terms of system costs.

A Appendix

A.1 Classification Scheme of Natural Diamond

The predominant impurities in natural diamond are N and B. A scheme was developed to classify natural diamond by its impurity content [97]. Two general classes are distinguished; there are class I diamonds with a prevalent content of aggregated (Ia) or substitutional (Ib) N, and class II diamond with very low N content (< 2 ppm). The two predominant aggregates are called A and B. Aggregate A consists of two neighbouring N atoms in substitutional positions, while aggregate B consists of four substitutional N atoms centred around a vacancy. Diamonds of class II can be semiconducting if B impurities acting as donors are present (IIb). If the concentration of N is comparable to the concentration of B the diamonds are insulating because the B acceptor states are compensated by the N donor states. An overview of the classification scheme is given on table 20.

class	subclass	impurity
I	IaA	predominant N, A-aggregate
	IaB	predominant N, B-aggregate
	Ib	predominant N, substitutional
II	IIa	N $<$ 2 ppm
	IIb	B, N $<$ 2 ppm (semiconducting)

Table 20: *Classification scheme for natural diamond.*

A.2 Signal Amplification

An example of an amplifier layout used to detect signals from CVD diamond samples is shown in fig. 109. The bias voltage (HV) is supplied to the detector (DET) through a filter network to reduce the noise. The example shows an AC coupling of the detector to the amplifier stage via a capacitance. The amplifier consists of a FET[20] followed by an integrating circuit with feedback components (R_f, C_f) which determine the fall time $t = R_f C_f$ of the output pulse and prevent saturation of the amplifier. The output of the charge integrating amplifier is transformed by a shaper to a Gaussian like signal with shaping time τ.

Important parameters of the amplification stage are

- noise level
- gain factor

[20] **F**ield **E**ffect **T**ransistor

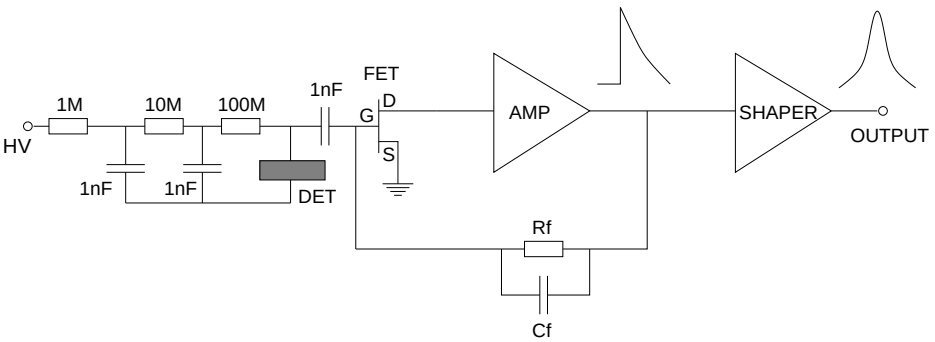

Figure 109: *Layout of a charge integrating amplifier followed by a shaper. The capacitance C_f and the resistor R_f determine the fall time of the output pulse $t = R_f C_f$.*

- shaping time

which define the performance of the device. The single sources of noise in the amplifier can be grouped in [98]

- thermal noise
- shot noise
- $1/f$ noise.

Thermal noise stems from small fluctuations of the voltage in a resistor. The mean square fluctuation in terms of an equivalent current source is given by $\bar{i^2} = 4kTR^{-1}df$ with k Boltzmann constant, T temperature, R resistance and $\mathrm{d}f$ the frequency interval in the noise spectrum. While the thermal noise is caused by the random carrier movement, shot noise originates from fluctuations in the number of carrier in a transport process as for example in the gate current of a FET. The squared fluctuation is independent of temperature and given by $\bar{i^2} = 2eI\ \mathrm{d}f$ with I being the average current. The third source of noise is associated with material properties of the amplifying device, i. e. crystal imperfections or surface states in the case of a FET, and the mean square fluctuation has a $1/f$-frequency dependence with an arbitrary amplitude $\bar{v^2} = A_f \frac{\mathrm{d}f}{f}$.

To determine the total noise for an actual device from the previous expressions, the mean square fluctuations of the different sources have to be integrated over the weighted frequency spectrum according to the amplifier chain. Applying this to a generic FET with gate resistance R_g, equivalent noise resistance of the FET channel R_{eq}, input capacitance C_{in} and shaping time τ of the amplifier one arrives at an expression for the total noise of the device in units of the elementary

charge, the equivalent noise charge ENC:

$$ENC^2 = e^2 \left[\underbrace{\frac{kT}{2R_g}\tau}_{\text{a}} + \underbrace{\frac{eI_g}{4}}_{\text{b}} + \underbrace{\frac{kTR_{eq}C_{in}^2}{2\tau}}_{\text{c}} + \underbrace{\frac{A_f}{2}C_{in}^2}_{\text{d}} \right]. \tag{83}$$

Equation 83 is composed of thermal contributions of gate resistor (a) and FET channel (c), shot noise from the gate current (b) and $1/f$-noise (d). While (a) and (b) scale with τ, (c) scales with τ^{-1} so the noise minimised for a certain τ_{min}. For large τ the shot noise contribution dominates, while for small τ the thermal noise contributions are important. For optimum noise performance the capacitance C_{in} should be kept small.

A.3 Weighting Field Method

The weighting field method[21] [87] allows the charge induced on an arbitrary electrode configuration by a moving charge carrier to be calculated. The method is based on the reciprocity theorem (or Green's theorem) to calculate the induced charge. The theorem defines the relation of potentials and charges in a system of many electrodes. Two states are considered, the state before and the state after the potentials and charges are changed. In the general case the electrodes are allowed to float, i. e. to be connected to infinitely high impedances. In practice the electrodes are connected to a low impedance amplifier or to a bias voltage, which allows a constant potential on the electrodes to be assumed even for moving charges. The reciprocity theorem for many electrodes is given by

$$\sum_i Q_i V_i' = \sum_i Q_i' V_i, \tag{84}$$

where Q_i, V_i and Q_i', V_i' are two values for different states of charge and potential of the electrode system. The summation is over all electrodes.

An example is given for a two electrode configuration where only the potential of one electrode is different from zero in each state by V_1 and V_2'. Then it is

$$Q_1' V_1 = Q_2 V_2' \tag{85}$$

The potential V_1 induces charge Q_2 in the first state, and V_2' induces Q_1' in the second state. By taking the ratio $Q_2/V_1 = Q_1'/V_2' = C_{12}$ the capacitance C_{12} between electrode 1 and electrode 2 is defined. The exercise shows that the partial capacitance between any two electrodes is independent of the direction from which it is measured, or that the electrostatic coupling is independent of the direction of charge displacement.

[21] The discussion of the weighting field method follows the description by Radeka [87].

An electrode configuration is now assumed with electrode 1 as the sensing electrode connected to an amplifier and a charge q_m on an infinitesimal electrode. Then by reciprocity

$$q_m V_m = Q_1 V_1, \tag{86}$$

where q_m is caused by V_1 and Q_1 by V_m. If the charge q_m moves a line segment $\mathrm{d}\vec{l}$ with a velocity $\vec{v} = \mathrm{d}\vec{l}/\mathrm{d}t$ a current is induced on the sensing electrode:

$$I_1 = \frac{\mathrm{d}(q_m V_m)}{\mathrm{d}t} = q_m \frac{\mathrm{d}(V_m/V_1)}{\mathrm{d}\vec{l}} \cdot \frac{\mathrm{d}\vec{l}}{\mathrm{d}t}. \tag{87}$$

As the charge q_m on the imaginary infinitesimal electrode moves away from electrode 1, the ratio V_m/V_1 is decreased which follows from equation (86) and constant q_m. The ratio $V_m/V_1 = V_w$ represents a normalised potential V_w at the position of the charge q_m. The differential term $\mathrm{d}(V_m/V_1)/\mathrm{d}\vec{l}$ can be replaced by

$$\nabla(V_m/V_1) = \nabla(V_w) = -\vec{E_w}. \tag{88}$$

The normalised potential V_w and the normalised field $\vec{E_w}$ are determined by applying a unity potential to the sensing electrode 1 and setting all other electrodes to zero potential. The induced current on electrode 1 is then given by

$$I_1 = -q_m \cdot \vec{E_w}\vec{v} \tag{89}$$

from which the induced charge Q can be calculated with the formalism explained in section 3.3.

The normalised field E_w is in units of cm^{-1}. It expresses the electrostatic coupling between the moving charge and the sensing electrode. An example for a weighting potential calculated for a $d = 300$ μm strip detector with a pitch of 100 μm and a strip width of 50 μm is shown in figure 110.

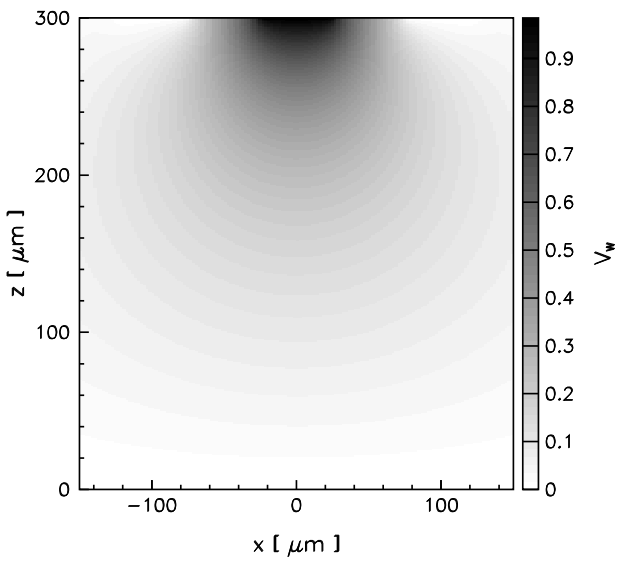

Figure 110: *Weighting potential calculated for a* $d = 300$ μm *thick detector with a strip pitch of* 100 μm *and a strip width of* 50 μm.

References

[1] M. Franklin et al. Development of diamond radiation detectors for SSC and LHC. *NIM A*, 315:39, 1992.

[2] R. J. Tesarek et al. Performance of a diamond-tungsten sampling calorimeter. *NIM A*, 349:96, 1994.

[3] P. Weilhammer et al. Development of diamond tracking detectors for high luminosity experiments at the lhc. CERN/LHCC 98-20, status report RD42, RD42 Collaboration, CERN, 1998.

[4] W. C. Röntgen and A. Joffé. *Ann. Physik*, 41:449, 1913.

[5] P. J. van Heerden. *The Crystal Counter*. PhD thesis, Utrecht, 1945.

[6] G. Stetter. *Verhandl. deut. physik. Ges.*, 22:13, 1941.

[7] H. Bichsel. Straggling in thin silicon detectors. *Rev. of Mod. Physics*, 60(3):663, 1988.

[8] U. Fano. Penetration of protons, alpha particles and mesons. *Ann. Rev. Nucl. Sci.*, 13:1, 1963.

[9] Review of particle physics. *Physical Review D*, 54, 1997.

[10] S. Zhao. *Characterization of the Electrical Properties of Polycrystalline Diamond Films*. PhD thesis, Ohio State University, 1994.

[11] S. M. Seltzer and M. J. Berger. *Nuclear Science Series*, (39):187, 1964.

[12] L. Landau. *J. Phys. (Moscow)*, 8:201, 1944.

[13] K. Kleinknecht. *Detektoren für Teilchenstrahlung*. Teubner, Stuttgart, Germany, 1992.

[14] W. W. M. Allison and J. H. Cobb. Relativistic charged particle identification by energy loss. *Ann. Rev. Nucl. Part. Sci.*, 30:253, 1980.

[15] M. Rogalla et al. Radiation studies for GaAs in the ATLAS inner detector. *NIM*.

[16] G. Hall. Semiconductor particle tracking detectors. *Rep. Prog. Phys.*, 57:481, 1994.

[17] P. J. Dean C. D. Clark and P. V. Harris. Intrinsic edge absorbtion in diamond. *Proc. Roy. Soc. (London)*, A277:312, 1964.

[18] J. R. Chelikowsky and M. L. Cohen. Nonlocal pseudopotential calculations for the electronic structure of eleven diamond and zinc-blende semiconductors. *Phys. Rev.*, B13:556, 1976.

[19] C. F. Fong and B. M. Klein. *Diamond: Electronic Properties and Applications*, page 1. Kluwer Academic Publisher, 1995.

[20] C. Kittel. *Einführung in die Festkörperphysik*. Oldenbourg, München, Germany, 1991.

[21] J. C. Angus and C. C. Hayman. Low pressure, metastable growth of diamond and diamondlike phases. *Science*, 241:913, 1988.

[22] A. T. Collins and W. S. Williams. The nature of the acceptor centre in semiconducting diamond. *J. Phys. C.: Solid State Phys.*, 4:1789, 1970.

[23] A. Mainwood. Substitutional impurities in diamond. *J. Phys. C.: Solid State Phys.*, 12:2543, 1979.

[24] R. G. Farrer. On the substitutional nitrogen donor in diamond. *Solid State Comm.*, 7:685, 1969.

[25] A. T. Collins. *Mat. Res. Soc. Symp. Proc.*, 162:3, 1990.

[26] K. Okano. *Diamond: Electronic Properties and Applications*, page 139. Kluwer Academic Publisher, 1995.

[27] L. S. Pan S. Han and D. R. Kania. *Diamond: Electronic Properties and Applications*, page 241. Kluwer Academic Publisher, 1995.

[28] D. K. Ferry. High-field transport in wide bandgap semiconductors. *Phys. Rev. B*, 12:2361, 1975.

[29] M. Artuso E. Gatti F. Nava, C. Canali and P. F. Manfredi. Transport properties of natural diamond used as a nuclear particle detector for a wide temperature range. *IEEE Trans. Nucl. Sci.*, NS-26(1):308, 1979.

[30] W. Shockley. *Czech. J. Phys. B*, B11:81, 1961.

[31] C. Canali et al. *NIM*, 160:73, 1979.

[32] L. S. Pan et al. Particle and photoinduced conductivity in type IIa diamonds. *J. Appl. Phys.*, 74(2):1086, 1993.

[33] P. Weilhammer et al. *NIM A*, 354:318, 1995.

[34] M. Moll. PhD thesis, University of Hamburg, 1999.

[35] W. G. Eversole. Synthesis of diamond. U.S. Patent No. 3,030,187, 1962.

[36] H. Liander and E. Lundblad. *Ark. Kemi*, 166:139, 1960.

[37] H. A. Will J. C. Angus and W. S. Stanko. Growth of diamond seed crystals by vapor deposition. *J. Appl. Phys.*, 39(6):2915, 1968.

[38] B. V. Deryagin and D. V. Fedoseev. Epitaxial synthesis of diamond in the metastable region. *Russ. Chem. Rev.*, 39(9):783, 1970.

[39] N. D. Polyanskaya B. V. Deryagin, D. V. Fedoseev and E. V. Statenkova.

[40] R. Sussmann. High quality CVD diamond: a material for optical and particle detector applications. *Diam. and Rel. Mat.*, 7.

[41] E. Wörner M. Füner W. Müller-Severt R. Locher P. Koidl, C. Wild. Large area microwave plasma CVD of diamond radiation windows. *Diam. and Rel. Mat.*, 7.

[42] W. J. Zhang X. Jiang and C.-P. Klages. Effect of ion bombardment on the nucleation and growth of diamond films. *Physical Review B*, 58(11):7064, 1998.

[43] W. Müller-Sebert H. Walcher R. Kohl N. Herres C. Wild, P. Koidl and R. Locher. Chemical vapour deposition and characterization of smooth (100)-faceted diamond films. *Diam. and Rel. Mat.*, 2:158, 1993.

[44] C.-P. Klages D. Wittdorf C. L. Jia K. Urban X. Jiang, K. Schiffmann and W. Jäger. Coalescence and overgrowth of diamond grains for improved heteroepitaxy on silicon (001). *J. Appl. Phys.*, 83(5):2511, 1998.

[45] C.-P. Klages. Chemical vapour deposition of diamond. *Applied Physics A*, 56:513, 1993.

[46] D. Meier. *CVD Diamond Sensors for Particle Detection and Tracking*. PhD thesis, Universität Heidelberg, 1999.

[47] S. Ramo. *Proceedings of the I.R.E.*, Sept.:584.

[48] G. Cavalleri et al. *NIM*, 92:137, 1971.

[49] R. Hofstadter. Crystal counters. *Nucleonics*, page 2, 1949.

[50] A. Oh et al. Development of diamond films for particle detector applications. *Diamond and Related Materials*, 7:1553, 1998.

[51] W. Zhu. *Diamond: Electronic Properties and Applications*, page 175. Kluwer Academic Publisher, 1995.

[52] T. L. Nam P. J. Fallon and R. J. Keddy. Trapping levels in pulse-counting synthetic diamond detectors. *Diam. and Rel. Mat.*, 1:1185, 1992.

[53] W. A. Yarbrough and R. Messier. *Science*, 247:688, 1990.

[54] R. Hessmer M. Schreck T. Worblewski, S. Geier and B. Rauschenbach. X-ray imaging of polycrystalline materials. *Rev. Sci. Instrum.*, 66(6):3560, 1995.

[55] P. Polesello E. Vittone C. Manfredotti, F. Fizzotti and F. Wang. A study of polycrystalline CVD diamond by nuclear techniques. *phys. stat. sol. (a)*, 154:327, 1996.

[56] S. M. Seltzer and M. J. Berger. *Stopping powers and ranges of electrons and positrons.* National Bureau of Standards, 1982.

[57] B. Schorr. Programs for the Landau and the Vavilov distributions and the corresponding random numbers. *Comp. Phys. Comm.*, 7:215, 1974.

[58] J. F. Ziegler. *Helium: Stopping Powers and Ranges in All Elemental Matter*, volume 4. Pergamon Press, NY, 1977.

[59] J. F. Ziegler. *Hydrogen: Stopping Powers and Ranges in All Elemental Matter*, volume 3. Pergamon Press, NY, 1977.

[60] J. Piqueras A. Cremades and M. Schreck. Electron beam-induced current imaging of chemical vapour-deposited diamond films. *Diam. and Rel. Mat.*, 6:95, 1997.

[61] M. Maywald L. J. Balk R. Heiderhoff, P. Koschinski and P. K. Bachmann. Correlation of the electrical, thermal, and optical properties of CVD diamond films by scanning microscopy techniques. *Diam. and Rel. Mat.*, 4:951, 1994.

[62] M. G. Buehler. Inpurity centers in pn junctions detemined from shifts in the thermally stmulated current and capacitance response with heating rate. *Solid State Electronics*, 15:69, 1972.

[63] S. Prawer P. Gonon and D. Jamieson. Thermally stimulated currents in polycrystalline diamond films: Application to radiation dosimetry. *Appl. Phys. Lett.*, 70(22):2996, 1997.

[64] H. Feick. *Radiation Tolerance of Silicon Particle Detectors for High-Eneergy Particle Physics Experiments.* PhD thesis, University of Hamburg, 1997.

[65] C. Bowlt. High-temperature thermally stimulated currents in type Ia and type IIa diamonds. *Journal of Physics D*, 6:616, 1973.

[66] *Fraunhofer-Institut für Schicht- und Oberflächentechnik.* Bienroder Weg 54e, 38108 Braunschweig, Germany, 1999.

[67] P. Koidl M. Füner and C. Wild. *Appl. Phys. Lett.*, 72:1149, 1998.

[68] M. Moll G. Lindström and E.Fretwurst. Radiation hardness of silicon detectors - a challenge from high energy physics. In *2nd International Conference on Radiation Effects on Semiconductor Materials, Detectors and Devices*, 1998. To be published in NIM A.

[69] A. Schwarz et al. HERA-B, technical design report. DESY-PRC 95/01, 1995.

[70] S. Amato et al. Lhc-b technical proposal. CERN LHCC 98-4, LHCC/P4, 1998.

[71] J. E. Cunningham. Theoretical modelling of radiation damage in semiconductors, 1996.

[72] S. Beever. Los alamos nuclear data viewer. http://t2.lanl.gov, 1996.

[73] R. Böttger et al. Radiation damage studies of high-resistivity silicon detectors at various neutron energies. to be published, 7 1997.

[74] A. H. B. Benny and F. C. Champion. Neutron bombardment of counting diamonds. *Proc. Royal Soc. London A*, 234:432, 1956.

[75] F. C. Champion. *Proc. Phys. Soc. B*, 65:465, 1952.

[76] F. Hartjes et al. Parameterisation of radiation effects on CVD diamond for proton irradiation. submitted to 6th Int. Conference on Advanced Technology and Particle Physics, Como, 5-9.Oct 1998, 1998.

[77] A. Mainwood et al. Neutron damage of chemical vapour deposition diamond. *J. Phys. D: Appl. Phys.*, 28:1279, 1995.

[78] John Hassard. The neutron radiation hardness of diamond detectors for future particle physics experiments. *NIM A*, 368:217, 1995.

[79] S. Han et al. Radiation damage study of polycrystalline CVD and natural type IIa diamonds using raman and photoluminescence spectroscopies. *NIM B*, 80:1446, 1993.

[80] M. Moll. NIEL scaling factor for the PTB n spectrum. private communication, 1998.

[81] H. Pernegger. *The Silicon Ministrip Detector of the DELPHI Very Forward Tracker*. PhD thesis, HEPHY Vienna, 1996.

[82] P. Polesello C. Manfredotti, F. Fizzotti and E. Vittone. IBIC investigation of radiation-induced effects in CVD and natural diamand. *NIM*, A426:156, 1999.

[83] M. Mishina. Induced charge on diamond detector. RD42 Internal Note 13, RD42 Collaboration, CERN, 1998.

[84] A. Oh. Untersuchungen an CVD diamant mit ionisierender strahlung, 1995.

[85] W. N. Wang C. D. O. Pickard, T. J. Davis and J. W. Steeds. Mapping crystalline quality in diamond films by micro-raman spectroscopy. *Diam. and Rel. Mat.*, 7:238, 1998.

[86] Van der Drift. *Philips Res. Rep.*, 22:267, 1967.

[87] V. Radeka. Low-noise techniques in detectors. *Ann. Rev. Nucl. Part. Sci.*, 38:217, 1988.

[88] E. Belau et al. Charge collection in silicon strip detectors. *NIM*, 214:253, 1983.

[89] *DeBeers Industrial Diamond Division Ltd.* Charters, Sunninghill, Ascot, Berkshire SL5 9PX, UK.

[90] Integrated Detectors & Electronics AS. *Data Sheet VA3.* Oslo, Norway, 1998.

[91] A. Rudge. *The Repeater Card.* CERN, Geneva, Switzerland, 1992.

[92] A. Rudge. *The Timing Unit.* CERN, Geneva, Switzerland, 1992.

[93] R. Meyners. *Beam Information Leaflet*, 1994.

[94] M. Moritz. private communcation, 1998.

[95] K. Ahmet et al. *NIM A*, 305:275, 1991.

[96] D. Fish. Modelling signal generation in CVD diamond detectors. RD42 Internal Note 9, RD42 Collaboration, CERN, 1997.

[97] J. E. Field. *The properties of diamond.* Academic Press, NY, USA, 1979.

[98] C. F. G. Delaney. *Electronics for the Physicist.* Ellis Horwood Publishers, Chichester, England, 1980.

Acknowledgements

I would like to thank Prof. A. Wagner for the opportunity to work in his group on this challenging topic and the support throughout the years of research work. Dr. T. Behnke, Dr. W. Zeuner and Dr. J. Steuerer provided valuable help by discussion, advice and enterprise. It was a great pleasure to work with former diploma student C. Karl and summer students G. Gaycken, K. Prechtel, W. Wohleben and D. Bibitchkov on various topics of diamond. They made important contributions to this work.

The good collaboration with the Fraunhofer Institut für Schicht- und Oberflächentechnik in Braunschweig, namely with L. Schäfer, M. Paul and A. Bluhm, made many material studies possible and allowed an inside view of the growth technology of CVD diamond. Also I acknowledge Dr. R. Sussman and Dr. A. Whitehead of DeBeers Industrial Diamond Division for their uncomplicated and helpful way of providing excellent detector grade CVD diamond.

A valuable source of motivation was the RD42 collaboration and the discussions on the fore-front of diamond detector technology during the collaboration meetings I had with Prof. P. Weilhammer, Prof. H. Kagan, Dr. M. Mishina, Dr. W. Trischuk, Dr. P. Bergonzo, Dr. F. Foulon and many others.

The successful accomplishment of many measurements was made possible by expert support. Here I would like to thank:

- Dr. Fretwurst, U. Pein, Dr. Feick and Dr. Niecke of the Inst. f. Experimentalphysik, Universität Hamburg for the support of the measurements with the proton micro-beam, with alpha particles and the measurements of thermally stimulated currents. Furthermore the neutron irradiations were made possible by the nuclear measurement group (Prof. Lindström, Dr. Fretwurst, Dr. Feick, M. Moll and M. Kuhnke),

- Dr. Wroblewski and Dr. Morgenroth from HASYLAB, DESY,

- Prof. R. Klanner of ZEUS, DESY for allowing me to use the Silicon telescope and jam up the hard discs. M. Milite, M. Moritz and C. Burgard for support in the test-beam and data analysis,

- Prof. Anton of the Inst. f. Experimentalphysik, University of Hamburg for the use of the scanning electron microscope,

- Prof. J. Conway, Dr. B. Stone, Dr. D. Fish of Rutgers University, NJ, USA for stimulating discussions and providing me with the original source code of the simulation and the field generator, plus the necessary computing power.

Finally I want to thank my long term office colleagues Petra Hüntemeyer and Silke Petzold for the nice atmosphere and the celebrated art of making coffee after the daily expedition to the DESY cantine.